RAYLEIGH-TAYLOR INSTABILITY IN VISCOSITY STRATIFIED FLUID MEDIUM

A thesis submitted in partial fulfillment of the requirement
for the degree of

DOCTOR OF PHILOSOPHY

by

SHATRUGHAN PRASAD JAISWAL

DEPARTMENT OF MECHANICAL ENGINEERING
INDIAN INSTITUTE OF TECHNOLOGY GUWAHATI
GUWAHATI-781039, INDIA

FEBRUARY 2023

DECLARATION

This is to declare that the work presented in the thesis entitled "Rayleigh-Taylor instability in viscosity stratified fluid medium" submitted by me to the Indian Institute of Technology Guwahati for the award of the degree of **Doctor of Philosophy** is a bonafide record of research work carried out by me under the supervision of **Dr. Madhusudhana G.** . Hereby I declare that the contents of this thesis, in full or in parts, have not been submitted elsewhere to any other university or institute for the award of any degree.

Shatrughan Prasad Jaiswal
Roll no. 156103028
Department of Mechanical Engineering
Indian Institute of Technology Guwahati

Date: February 2022
Place: IIT Guwahati

Abstract

In the present work, study of Rayleigh-Taylor instability in viscosity stratified fluid medium is carried out. The instability is studied for two dimensional rectangular as well as axisymmetric coordinate configurations using numerical simulations. In both the configurations, two viscous fluid layers, a heavier fluid layer is superposed over a lighter fluid layer, are sandwiched between two parallel isothermal horizontal solid walls. Out of the two walls, one wall is isothermally heated, while the other wall is isothermally cooled. In particular, the effect of stratification due to viscosity varying exponentially with temperature on the instability is studied. Marangoni effect on the instability is studied under the influence of viscous stratification for both the configurations. The studies carried out in the present work consist six parts.

In the first part, Rayleigh-Taylor instability is studied in viscosity stratified fluid layers in 2-D rectangular coordinate configuration. Study of viscosity stratification effect on the instability is carried out for exponentially varying viscosity with temperature. Effect of different parameters such as viscosity ratio, temperature ratio, Weber number, Prandtl number and hot and cold wall locations on the instability is studied under the influence of viscosity stratification. For variable viscosity, spike deformation is found to be higher and spike movement is found to be faster compared to that of constant viscosity. Increase in viscosity ratio is found to show reduced deformation of spike and stabilizing effect on the instability. Increase in temperature ratio is found to show destabilizing effect on the instability with irregular spike-arm structure for higher temperature ratios. For top heated configuration, the spike deforms more and moves faster than that of bottom heated configuration. The instability is found to be unaffected by variation of Prandtl number. For Weber number less than critical value, the configuration does not undergo instability. Beyond the critical value, increasing Weber number shows destabilizing effect on the instability. A range of Weber numbers exist in which spatial periodicity of the instability is higher than spatial periodicity of the initial perturbation, unlike for the other remaining ranges of Weber number.

In the second part, the effect of functional variation of viscosity with temperature on the instability is studied in 2-D rectangular coordinate configuration for four types of viscosity variations, which are constant, linear, power law and exponential variations. The study of effect of functional variation of viscosity on the instability is carried out for various viscosity ratios and density ratios. Type of viscosity variation shows strong effect on the instability at low viscosity ratios and low density ratios. At high viscosity ratios, the spike is formed as a fluid column structure, irrespective of type of viscosity variation. At high density ratios, viscosity variation effect on the instability is found to be smeared out in the dominance of inertial forces. Overall, rate of spike movement is in decreasing order of sequence of exponential, linear, constant and power law variations, for all viscosity ratios and density ratios.

In the third part, Marangoni effect due to temperature varying surface tension on the instability is studied in 2-D rectangular coordinate configuration. Marangoni effect is studied for three types of functional dependencies of surface tension with temperature, which are constant, linear and parabolic dependencies. Effect of Weber number and Froude number on the instability is studied in the presence of Marangoni effect. Rate of spike movement for the three types of surface tension dependencies is

in increasing order of sequence of constant, parabolic and linear dependencies as overall effective surface tension decreases in the above sequence. Critical value of Weber number is found, below which the configuration does not undergo instability, and beyond which increasing Weber number shows destabilizing effect on the instability. Increasing Froude number shows stabilizing effect on the instability. Critical Froude number is found above which the configuration is stable.

In the fourth part, Rayleigh-Taylor instability is studied in viscosity stratified fluid layers in axisymmetric configuration. Viscosity stratification effect on the instability is studied for viscosity varying exponentially with temperature. Effect of viscosity ratio, temperature ratio, Prandtl number, Weber number and hot and cold wall locations on the instability is studied in the presence of viscosity stratification. For variable viscosity, the configuration becomes more unstable and spike undergoes larger deformation compared to that of constant viscosity. It is found that increasing viscosity ratio shows stabilizing effect. Increasing temperature ratio shows destabilizing effect on the instability and irregular spike-skirt structure is formed for high temperature ratios. In top wall heating configuration, formation of mushroom shaped spike occurs earlier compared to that in bottom wall heating configuration. Prandtl number variation is found to show negligible effect on the instability. For Weber number less than critical value, the configuration does not undergo instability, beyond which increasing Weber number shows destabilizing effect on the instability.

In the fifth part, effect of functional variation of viscosity with temperature on the instability is studied in axisymmetric configuration for four types of viscosity variations, which are constant, linear, power law and exponential variations. The study of effect of functional variation of viscosity on the instability is carried out for various viscosity ratios and density ratios. The functional variation of viscosity is found to show strong influence on the instability at low viscosity ratios and low density ratios. For high viscosity ratios as well as high density ratios, dynamics of instability becomes independent of type of viscosity variation. Rate of spike movement is in increasing order of sequence of power law, constant, linear and exponential variations due to that the overall effective viscosity is in the decreasing order of the above sequence.

In the sixth part, Marangoni effect due to temperature varying surface tension on axisymmetric Rayleigh-Taylor instability is studied in viscous stratified fluid layers. Marangoni effect is studied for constant, linear and parabolic variations of surface tension with temperature. The instability is also studied for the effect of Weber number, temperature ratio and Froude number in the presence of Marangoni effect. Rate of spike movement is lowest for parabolic and highest for linear dependency of surface tension. With increasing temperature ratio up to a certain value, rate of spike movement increases, beyond which it decreases. For temperature ratio more than critical temperature ratio, the configuration does not undergo instability. The critical Weber number is found below which the configuration is stable, and beyond the critical value, increasing Weber number shows destabilizing effect on the instability. For Weber number approaching infinity, surface tension approaching zero, multiple roll up structures form on the stem of the spike. Increase in Froude number shows stabilizing effect on the instability, and beyond critical value of Froude number the configuration is found to be stable.

Contents

Nomenclature

Symbols

c_p	dimensionless heat capacity of the fluid
c_{p_r}	ratio of heavier to lighter fluid heat capacity, $\tilde{c}_{p_1}/\tilde{c}_{p_2}$
$\mathbf{e}_j$	unit direction vector
$\mathbf{F}$	dimensionless body force vector
Fr	Froude number, $\tilde{V}_{\text{ref}}^2/\tilde{g}\,\tilde{L}$
f	volume fraction
$\tilde{g}$	gravitational acceleration, (m/s^2)
H	dimensionless height of the domain and heaviside function in governing equation
H_1	dimensionless height at which interface is located
$\mathbf{j}$	unit vector in vertical direction
k	dimensionless thermal conductivity
k_r	ratio of heavier to lighter fluid thermal conductivity, $\tilde{k}_1/\tilde{k}_2$
L	dimensionless width of the domain
M_1, M_2	dimensionless constants in dimensionless surface tension expression given in Eq. (2.31)
m	ratio of heavier to lighter fluid viscosity, $\tilde{\mu}_1(\tilde{T}_2)/\tilde{\mu}_2(\tilde{T}_2)$
Ma	Marangoni number, $\beta_1\,\tilde{T}_2\,\tilde{\rho}_2\,\tilde{c}_{p_2}\,\tilde{L}/\tilde{\mu}_2\,\tilde{k}_2$
$\mathbf{n}$	unit normal vector
p	dimensionless pressure
Pr	Prandtl number, $\tilde{c}_{p_2}\,\tilde{\mu}_2/\tilde{k}_2$
Re	Reynolds number, $\tilde{\rho}_{\text{ref}}\,\tilde{V}_{\text{ref}}\,\tilde{L}_{\text{ref}}/\tilde{\mu}_{\text{ref}}$
r_T	temperature ratio, $(\tilde{T}-\tilde{T}_{\text{ref}})/\tilde{T}_{\text{ref}}$
S	sign function
t	dimensionless time
$\tilde{T}$	temperature, (K)
$\mathbf{u}$	dimensionless velocity vector
u, v	dimensionless velocities in x and y–directions or r and z–directions, respectively
$\tilde{V}$	reference velocity, (m/s)
We	Weber number, $\tilde{\rho}_2\,\tilde{g}\,\tilde{L}_{\text{ref}}^2/\sigma_{\text{ref}}$
$\tilde{x}, \tilde{y}$	coordinates in x and y–directions, respectively (m)
x, y	dimensionless coordinates in x and y–directions, respectively
$\tilde{r}, \tilde{z}$	coordinates in radial and axial directions, respectively (m)
r, z	dimensionless coordinates in radial and axial directions, respectively

Greek Symbols

β_1, β_2	constants in dimensional surface tension expression given in Eq. (2.28)
δ	Dirac delta function and perturbation of interface
δ_0	amplitude of initial interface perturbation

ϵ	epsilon
κ	curvature
μ	dimensionless dynamic viscosity
$\omega_1, \omega_2, \omega_3$	weight function in WENO discretization
ϕ	level set function
ρ	dimensionless density
ρ_r	ratio of heavier to lighter fluid density, $\tilde{\rho}_1/\tilde{\rho}_2$
σ	dimensionless surface tension
$\tilde{\sigma}_0$	surface tension value at reference temperature, (N/m)
θ	dimensionless temperature, $(\tilde{T} - \tilde{T}_{\text{ref}})/\tilde{T}_{\text{ref}}$

Subscripts

i,j	nodes in x and y-coordinates, respectively
n	normal component of surface tension force
ref	reference quantities
s	surface gradient
t	tangential component of surface tension force
T	corresponds to temperature ratio
x, y	derivative with respect to x and y, respectively
0	reference quantities correspond to reference temperature
1	corresponds to quantities of 'Fluid 1'
2	corresponds to quantities of 'Fluid 2'

Superscripts

$\tilde{(\ )}$	corresponds to dimensional quantities
n, $n+1$	time step level

Abbreviations

2-D	Two dimensional
3-D	Three dimensional
ENO	Essentially Non Oscillatory Scheme
FVM	Finite Volume Method
LS	Level Set
RTI	Rayleigh-Taylor Instability
TDMA	Tri-Diagonal Matrix Algorithm
TVD	Total Variation Diminishing
VoF	Volume of Fluid
WENO	Weighted Essentially Non Oscillatory Scheme

List of Figures

List of Tables

Chapter 1

Introduction and literature review

In this chapter, introduction and literature review are presented. Conclusions from the literature review and objectives of the work are presented.

1.1 Introduction to Rayleigh-Taylor instability

Rayleigh-Taylor instability is one of the classic interfacial instabilities. When a high density fluid layer is placed over a low density fluid layer, the configuration may become unstable and it can undergo instability. Such instability is called Rayleigh-Taylor instability. The instability in the fluid layers with increasing density in vertically upward direction was first investigated by Rayleigh [16]. Accelerated fluid layers in vertically downward direction also exhibit Rayleigh-Taylor instability, which was investigated in various past studies [17–19].

A simple form of Rayleigh-Taylor instability can be seen when water droplets drip from ceiling. To explain this, take an example of water layer with a thickness of 1 m which is plastered to the ceiling of a room, as shown in Fig. 1.1. Below the water layer, a layer of air is present. As the instability arises in the interface of water and air, the water layer falls down from the ceiling. Reason of the fall down is not because of the air layer can not hold the water layer as the pressure of atmosphere is about ten meters of water column, and the pressure is sufficient enough to hold the 1 m thick water layer. The water layer falls down as a heavier fluid is placed over a lighter fluid, and any small disturbance in the interface grows which makes the configuration unstable. The growing disturbance leads to falling of water from ceiling. However, when the same water layer is kept on the floor, the small disturbances introduced in the water-air interface decay which leads to a stable configuration.

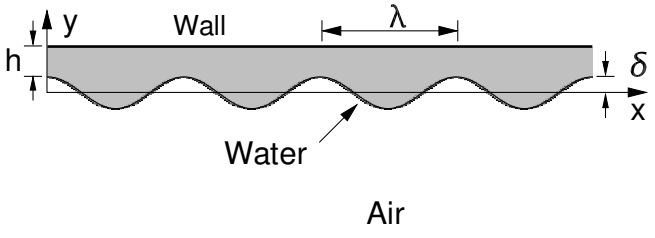

Figure 1.1: Schematic of water layer.

The occurrence of Rayleigh-Taylor instability can be stated as "*If the heavy fluid pushes the light fluid, the interface is stable, if the light fluid pushes the heavy fluid, the interface is unstable* [18]." Rayleigh-Taylor instability takes place in a wide range of applications in nature and industry such as dripping of water from ceilings [20], mushroom clouds formation, suspended water over oil [21], inertial confinement fusion of plasma, volcanic eruptions, surface of the Sun, Earth's mantle, supernovae explosions [22–25], crab nebula [26], plasma physics [27], inertia induced fusion reaction, solar corona [28], etc. Technological applications of Rayleigh-Taylor instability can be found in various processes such as implosion of electromagnetic waves on a metal liner [29, 30], mushroom shape formation in metal boiling [18], laser implosion driven fusion of Tritium-Deuterium [18], etc.

In Rayleigh-Taylor instability, spikes, curtains and bubbles are usually formed. Kelvin-Helmholtz instability like-structure on the side interface of spike is found to form for certain range of parameter values. Competition among the bubbles and spikes leading to bubble amalgamation, formation of droplets, entrainment and turbulent mixing are also associated with Rayleigh-Taylor instability. Under certain conditions, the instability can display chaotic mixing with fractalized interface. The process of Rayleigh-Taylor instability evolution can be broadly categorized into four stages.

Stage-1: When the perturbations in the interface are extremely small, the disturbance grows in a linear regime. In the linear regime, nonlinear effects are negligibly small compared to linear effects. Here, the amplitude of the perturbation of wavelength λ grows exponentially with time. The assumption of the linear growth is valid when the amplitudes of the initial perturbation are less than order of 0.1λ.

Stage-2: In this stage, the amplitude of the perturbation grows non-linearly to a size of order of λ. In this stage, development of the instability is strongly affected by three dimensional effects. Here, value of density ratio or Atwood number (A) plays an important role. Atwood number is defined as $(\tilde{\rho}_1 - \tilde{\rho}_2)/(\tilde{\rho}_1 + \tilde{\rho}_2)$. If Atwood number is such that $A \leq 1$, the fluid of lower density moves upward in a form of bubble and fluid of higher density moves downward in a form of spike. Heavier fluid forms spikes and lighter fluid forms bubbles. If a section is cut horizontally including multiple spikes and bubbles, the cross section would form a honey comb pattern. If Atwood number is such that $A \geq 0$, the pictures of bubbles and spikes are different from those simple patterns of bubbles and spikes present in two dimensions. The interpenetration of spikes and bubbles represents two sets of bubbles penetrating into each other.

Stage-3: Here, development of interface structures and interactions among the bubbles and the spikes are found to occur. In this stage, nonlinear interactions between initial perturbations of different frequencies can take place. The interface commonly forms into mushroom shaped spike. With time, increasing drag forces on spike and bubble and shear force along the interface can lead to formation of Helmholtz instability like structure. This phenomena can be generated due to several sources and such effect is prominent at lower values of density ratio and surface tension. In some instances, bubble amalgamation occurs in which large bubbles absorb small bubbles resulting into formation of a larger bubble at faster rate. When heterogeneities in various physical quantities is present, shape and movement of bubbles and spikes are modified. The degree of modification of bubbles and spikes depends on strength and scales of the heterogeneities.

Stage-4: In this stage of the instability, complicated behaviors of the instability such as breakup of spikes by various mechanisms and penetration of bubbles through a slab of fluid of finite thickness can take place. Larger spikes and bubbles envelope smaller spikes and bubbles which eventually leads to a region of chaotic mixing. In general, it is assumed that the chaotic mixing results into self-similar mixing effects. The complications of the instability lead to a turbulent or chaotic mixing of two fluids.

This four stage development of the instability can be affected largely due to change in various influencing parameters. These parameters and state of the equation can control the interfacial structure and the growth of the instability. The factors which influence Rayleigh-Taylor instability are discussed next.

1.1.1 Factors which influence the evolution of Rayleigh-Taylor instability

Many factors can affect the development of Rayleigh-Taylor instability. Fluid properties such as surface tension, density, viscosity can influence the growth of the instability. Converging geometry and three dimensional effects influence the instability significantly. Time dependence of the driving acceleration, equation of the state of the fluids and heterogeneity in different form are the influential factors on the instability. Compressibility effect and shock formation show strong influence on the instability. The change of phase leads to change in several components of the material which results into influencing factor on the instability largely. The presence of heat transfer can play an influential role on the development of Rayleigh-Taylor instability.

In fluid properties, density ratio or Atwood number is one of the strongly influencing factors on the growth of the instability and perturbation amplitude. For lower Atwood number, formation of spiral or roll-up structure like Helmholtz instability can become prominent [31, 32]. Whereas for higher Atwood number, approaching to 1, free falling interface structure can be observed [33–35]. Fluid viscosity shows strong effect on the disturbance growth of the instability. With increased viscosity effect, increased viscous drag force delays the interfacial disturbance growth. With the delay in disturbance growth, rate of instability reduces which results into suppression effect on the instability [36]. Viscosity affects the interface shape structure as well. For example, for high viscosity fluids, Helmholtz instability like structure can be avoided due to the delayed growth of the instability [32, 37, 38].

Surface tension shows an influential effect on the instability and its growth. For surface tension value higher than critical value, the configuration is found to be stable which was reported in different analytical studies [21, 36, 39] and numerical simulations [9, 32]. However, below the critical value of surface tension, the configuration is found to be unstable, and decrease in surface tension value results into destabilizing effect on the instability. Kelvin-Helmholtz instability like structure in the nonlinear stage is expected to form when the surface tension is low [18]. Compressibility effect shows a strong effect on the growth rate of initial perturbations. In the presence of compressibility effect, disturbance growth rate of the unstable interface was reduced which results into stabilizing effect on the instability [40–43]. The nature of initial perturbation shows strong influence on the instability. For example, for single mode disturbance interface evolution was found to be of symmetric nature, and for multimode disturbance interface evolution was found to be of asymmetric nature with chaotic mixing effect [44]. Presence of electric and magnetic fields show influence on Rayleigh-Taylor insta-

bility. Effect of electric and magnetic fields on the instability were reported in past studies [45–47]. Effect of the above mentioned influencing factors on Rayleigh-Taylor instability are studied using different analytical, quasi-analytical, experimental and numerical methods. The linear stability and weakly nonlinear stability regimes are usually studied using analytical and semi analytical methods. Numerical methods are used to solve the governing equations in complete form.

Stratification of fluid layers affects Rayleigh-Taylor instability. Stratification of the fluid layers can takes place due to variation of density, viscosity, concentration, etc. Stratification of fluid layers due to density and gravity shows strong influence on Rayleigh-Taylor instability [48, 49]. Varying surface tension (Marangoni effect) along the interface of the fluid layers shows a significant effect on dynamics of interfacial flows in general. Hence, such Marangoni effect can also influence Rayleigh-Taylor instability to a large extent. The effect of stratification of fluid layers and the effect of variable surface tension on the instability are some of the important focus points of the present study. Hence, the details of stratification of fluid layers, viscosity variation in fluids and surface tension variation with temperature along the interface are discussed next.

1.1.2 Stratification in fluid layers

Stratification in the fluid layers can arise due to various factors such as variation of density, viscosity, concentration, etc. Gravitational acceleration may also create a stratification effect on fluid layers [48, 49]. Flow in stratified fluid layers are known as stratified flows. Atmospheric air flowing over still water is one example of stratified flow. Some other examples are flow of two fluid layers with distinct density in the atmosphere, such as cloud movement, ocean currents, microfluidics, etc. The cloud wave formation is one of the best examples of instability in stratified flow which is also known as Kelvin-Helmholtz instability. Density stratification occurs in the atmosphere due to gravity where density is stratified in decreasing order with increasing altitude. Thermal stratification are inherent in nature and various industrial processings. Thermal stratification may affect the density, viscosity and concentration largely [50–53]. The common examples are mixing of fluids, multiphase flow in pipes and channels, desalination plants, solar salt, petrochemical engineering, etc. Due to variation in density, viscosity and other fluid properties, an instability arises at the interface of the stratified fluid layers in the flow. Classical examples of instability in stratified flows are Rayleigh-Taylor instability, Kelvin-Helmholtz instability, shear flows, etc.

When interfacial instability takes place in stratified flows due to accelerating heavier fluid layer through lighter fluid layer leads to Rayleigh-Taylor instability, unlike other instabilities which are mainly due to velocity difference between two consecutive layers. Interfacial instability in stratified fluid layers has a wide range of applicability in various natural processes and industrial applications. Some examples are plasma formations, fusion reactions, volcanic eruption, glaciers, internal gravity waves [54], natural oil reservoirs [55], supernovae or star explosions [22,56], crab nebula [26], Earth's mantle [57, 58], etc. Viscous stratification effect can be experienced in the atmosphere of Earth while re-entry of space shuttle. Due to presence of viscosity stratification, interfacial instability may occur at a large scale as well as at a small scale such as blood flow in veins, sugar syrup, Earth's mental, atmospheric and oceanic movement, etc. Viscosity variation is affected significantly by various factors

which are discussed in next subsection.

1.1.3 Viscosity variation in fluids

Viscosity of fluid is affected by various factors such as temperature, pressure, solute concentration, etc [59–63]. Temperature is one of the factors which influences the fluid viscosity largely. In the present study, for viscous stratification effect, viscosity is specified to vary with temperature. Hence, fluid viscosity variation with temperature is discussed in more details.

Variation of viscosity with temperature: Viscosity of different liquids and gases vary differently with temperature. In general, increase in temperature results into increased viscosity of most of the gases. This is due to fact that with increase in temperature, rate of the collision between two consecutive molecule increases which results into increased viscosity of gases. Some examples of gases in which viscosity increases with temperature are air, nitrogen, oxygen, etc. In general, an increase in temperature results into decreased viscosity of most of the liquids. Some example of such liquids are syrups, honey, mercury, water, oils, hydrocarbons. There are various empirical models based on the experimental studies which are used to find an approximate value of viscosity of liquids. Viscosity variation of fluids are used based on the different empirical correlations in past studies [7,12, 32,37,52,53,64–75]. Different types of functional variations for viscosity variation with temperature are used in the past studies such as constant, linear, exponential and power-law functions. Constant viscosity of fluid is used in many past studies [7, 32, 37, 71, 72, 74]. A linearly varying temperature dependent viscosity variation, which was used in the studies by Wall and Wilson [67], Dhiman and Sharma [76] and Tripathi et al. [73], is given by

$$\tilde{\mu} = A + B\,(\tilde{T} - \tilde{T}_{\text{ref}}) \tag{1.1}$$

Power law variation of viscosity with temperature was used in the studies by Tripathi and Sahu [12], Nahme [64] and Balla et al. [75] which can be expressed as

$$\tilde{\mu} = A + B\left(\frac{\tilde{T} - \tilde{T}_{\text{ref}}}{\tilde{T}_{\text{ref}}}\right)^{3/2} \tag{1.2}$$

Exponential variation of viscosity with temperature was used in different past studies [52,53,64–67, 69,70,77], is given by

$$\tilde{\mu} = A + B\,\exp^{\frac{\tilde{T}_{\text{ref}} - \tilde{T}}{\tilde{T}_{\text{ref}}}} \tag{1.3}$$

Common example of fluids whose viscosity show an exponential variation with temperature are water and alcohol [52,53]. Here, A and B are different combinations of constants such that fluid viscosity ($\tilde{\mu}$) is always positive.

Variation of viscosity with pressure: In general, pressure does not show significant effect on fluid viscosity [61–63]. However, pressure affect the fluid viscosity under certain conditions such as at high pressure. Fluid viscosity increases weakly with increase in pressure [61,63]. The viscosity of oil and lubricant varies with pressure in high pressure and high temperature operating conditions. For

such oil and lubricant, equation of the fluid viscosity variation with pressure, which was used in past studies [78, 79], is given by

$$\tilde{\mu} = \tilde{\mu}_0 \exp^{(A\,\tilde{p})} \tag{1.4}$$

Here, A is the Barus coefficient and $\tilde{p}$ is the fluid pressure. $\tilde{\mu}_0$ is the fluid viscosity defined at zero pressure.

Variation of viscosity with solutal concentration: The viscosity of fluid varies with the concentration of solvents in multi-component solutions. Some examples of solutions whose viscosity varies with concentration are aqueous solutions of amino acids, sugar solutions, etc. In general, the viscosity of the solution increases with an increase in concentration. Concentration dependent viscosity variation of binary solution, as used in the past studies [80–82], is expressed as

$$\tilde{\mu} = \tilde{\mu}_0 + A\,c + Bc^2 \tag{1.5}$$

Here, A and B are constant coefficients. $\tilde{\mu}_0$ is viscosity of the solution at zero concentration value. c is solutal concentration.

Stratification in fluid layers due to temperature dependent fluid properties shows significant effect on interfacial instabilities. In general, fluid viscosities vary with temperature in nature and industrial processing. Temperature differences can vary or exist up to the order of 10^4-10^7 K in the nature such as nuclear explosions, solar corona prominence [28], crab nebula, plumes of plasma [27], neutron star, etc. In the presence of thermal stratification, viscosity variation can be affected largely and it can show an influential effect on stratified flows. Viscous stratification has a large scale applications in engineering and industrial fields. Such examples are chemical and food processing plants, tribology, petrochemical engineering, polymer processing [83], printing press, lubrication process, metal boiling [18], combustion [84], etc. The variation of viscosities with temperature can affect Rayleigh-Taylor instability to a large extent as compared to the instability in fluid layers with constant viscosity.

1.1.4 Surface tension variation along the interface between fluid layers

Surface tension exhibits influential effect on multiphase flows in a wide range of applications. However, presence of surface tension gradient at the interface between two fluid layers plays an important role in many industrial and natural phenomena. Due to presence of surface tension variation, additional stresses along the interface is generated which are called Marangoni stresses. The surface tension can vary with concentration variation [85] and temperature [10, 12, 15, 73, 86–92]. Some of the studies, such as in Muradoglu and Tryggvason [93] and Adami and Caps [94], also considered surface tension variation with space. The effect of Marangoni stresses is also known as Maranoni effect or thermocappilary effect. In most of the Marangoni effect studies, surface tension was considered to vary linearly with temperature [10, 12, 15, 86–91], and the expression of surface tension variation with temperature is given by

$$\tilde{\sigma}(\tilde{T}) = \tilde{\sigma_0} + \beta_1(\tilde{T} - \tilde{T}_{\text{ref}}) \tag{1.6}$$

A more generalized form of surface tension variation with temperature in quadratic form, which was also used in past studies of [73, 92], can be written as

$$\tilde{\sigma}(\tilde{T}) = \tilde{\sigma_0} + \beta_1(\tilde{T} - \tilde{T}_{\text{ref}}) + \beta_2(\tilde{T} - \tilde{T}_{\text{ref}})^2 \tag{1.7}$$

Here, $\tilde{\sigma_0}$ is the reference value of surface tension at the reference temperature ($\tilde{T}_{\text{ref}}$). β_1 and β_2 are the constants such that value of the surface tension ($\tilde{\sigma}(\tilde{T})$) is always positive. Example of fluids which exhibit linearly varying temperature-dependent surface tension are the combination of fluids such as water-oil, water-air, etc [86]. But, fluids which show non-monotonically variation such as parabolically varying temperature-dependent surface tension are known as self-rewetting fluids. Non-azeotropic and diluted aqueous solutions of high carbon alcohol behave as self-rewetting fluids [12, 73,75,95,96]. Marangoni effect in these fluids plays an important role in the fields of flight, space and aviation technology [95–97]. Marangoni effect has a wide range of applications such as beading of water drops on a leaf, floating of striders or objects on a liquid surface, tears formation of wine [98], liquid foam, bubble rise in soda bottles [86], flight and space technology [97], etc.

1.2 Literature review

In the literature, Rayleigh-Taylor instability was studied by various methods such as experimental study, linear stability, nonlinear stability and numerical simulations. Those studies are reviewed in the following subsections.

1.2.1 Linear stability studies on Rayleigh-Taylor instability

Linear stability analysis on Rayleigh-Taylor instability in constant viscosity fluid layers was carried out to find out the effect of various parameters such as density, viscosity, surface tension at interface, electric and magnetic fields, etc., in the linear regime. Plesset and Whipple [99] studied viscous effects on Rayleigh-Taylor instability using linear stability analysis in the linear regime. Linear stability of Rayleigh-Taylor instability in an ablative plasma was studied by Takabe et al. [100]. The authors presented an expression for growth rate of ablative plasma. Orozco and Rosas [101] studied linear stability analysis of continuously stratified fluid layers under a general rotation field. An upper bound of the growth rate of instability was found in the study. Alon et al. [33] studied linear evolution of large structure in Rayleigh-Taylor and Richtmyer-Meshkov instabilities of interface between two inviscid fluids. They presented growth rate of bubble and spike fronts for Rayleigh-Taylor and Richtmyer-Meshkov instabilities for all Atwood numbers. They provided theoretical explanations for dependence of the scaling laws and parameters on initial conditions and Atwood number. Oron et al. [34] performed a three dimensional Rayleigh-Taylor and Richtmyer-Meshkov instabilities for random initial perturbation. Sohn [36] presented a potential flow model for Rayleigh-Taylor (RT) and Richtmyer-Meshkov (RM) instabilities for arbitrary density ratio. They presented a generalized model for bubble velocity for both the instabilities. The asymptotic growth rate of bubble in RT and RM instabilities were obtained in two and three dimensions for finite density ratios.

Banerjee et al. [102] studied combined effect of vorticity and viscosity on bubble growth of single mode Rayleigh-Taylor instability. The upper and lower layer fluids were taken as irrotational and rotational, respectively. The vorticity on the lower lighter fluid reduced the viscous drag on the bubble. Sohn and Baek [38] studied Rayleigh-Taylor instability in inviscid fluid layers using potential theory for the effect of surface tension. They presented an expression for asymptotic velocity and the curvature of a single bubble in the presence of surface tension. In the presence of surface tension, the rate of instability for the single bubble was decreased, and the rate of mixing of multiple bubbles at the self-similar stage was increased. Kord and Capecelatro [103] performed Rayleigh-Taylor instability for multi-mode interfacial perturbations based on the most sensitive wave number to enhance the mixing effect. The calculated value of the most sensitive wave number showed a good match with the predicted value of the most unstable wave number using linear stability theory. The optimized function of interfacial perturbations was extended to three dimensional study of the instability. The optimized function of the wave number enhanced the mixing effect.

Presence of viscosity and surface tension shows stabilizing effect on the instability unlike density effect. Menikoff et al. [104] carried out a linear stability analysis of Rayleigh-Taylor instability in viscous fluids. They found the growth rate of the disturbance to depend on density weighted average viscosity, effective acceleration and surface tension. The scaled growth rate was found to be insensitive to the values of fluid density and viscosity. Clavin and Williams [105] presented a solution for asymptotic behavior of descending spike in Rayleigh-Taylor instability of an incompressible fluid bounded by vacuum in the absence of surface tension. The study was carried out for both 2-D rectangular and axisymmetric spikes. A self similar solution was obtained for the shape of the free surface at the tip of the spike. The evolution of surface curvature at the tip was presented. The free fall acceleration of the spike was found to follow the inverse power law with time variation. Gerashchenko and Livescu [106] carried out linear stability on compressible Rayleigh-Taylor instability in the presence of background temperature gradient. The effect of temperature gradient on the instability was studied with inviscid-inviscid, viscous-viscous and viscous-inviscid fluid layers for different Atwood numbers. The dispersion relation for growth rate was presented for several limiting cases. For viscous-inviscid case, dispersion relation was obtained in the limit of incompressible flow and zero temperature gradient. In the presence of viscosity rate of instability was decreased. Viscous effect strongly influenced the instability when viscosity was a function of temperature. Sohn [107] presented an analytical model for unstable interfaces in single mode Rayleigh-Taylor and Richtmyer-Meshkov instabilities for arbitrary viscosity. Linear and nonlinear asymptotic relations were found for growth rate of the disturbance. Surface tension and viscosity decreased asymptotic bubble velocity in Rayleigh-Taylor instability. However, in Richtmyer-Meshkov instability, the decay in rate of bubble velocity was found to be dependent on relative strength of surface tension and viscosity. Mikaelian [108] carried out linear stability analysis of Rayleigh-Taylor and Richtmyer-Meshkov instabilities in two fluid layers in which one of both the fluid might be viscous fluid. An exact analytical expression for amplitude of disturbance with time was presented for only one fluid was viscous. Comparison of exact solution of initial value problem with an approximate Eigenvalue problem was made. They proposed a hybrid model which was an improvement of an approximate model.

Rudraiah et al. [109] carried out linear stability analysis on Rayleigh-Taylor instability in viscosity stratified fluid layers. For viscosity stratification effect, viscosity of fluid layers were specified to vary exponentially with space in vertical upward direction. Dispersion relations were obtained for the thickness of the bottom lighter fluid layer, surface tension and viscosity stratification. The rate of instability increased with increasing bottom layer thickness. With viscosity stratification, the instability rate was relatively higher than that of constant viscosity fluid layers. Piriz [110] presented a new approach to find an exact and approximate analytic solutions involving viscous fluids. The Newton second law based approach gave a way to intuitive and physically appealing explanation for the physics resulting the instability. Xie et al. [111] presented a modified approximate analytical solution for the growth rate of Rayleigh-Taylor instability. The accuracy of the modified analytical solution was significantly higher than those of previous existing analytical solutions for different viscosity ratios and Weber numbers in the whole range. Inclusion of diffusion effects was much easier due to the explicit and ease of use nature of the solutions. The authors demonstrated the extension of analytical solutions of growth rate to include concentration diffusion effects on the stability of viscous Rayleigh-Taylor instability. The analytical expression extended to include more effects such as thermal diffusion effect and electromagnetic effect.

Silveira and Orlandi [112] analyzed viscous resistive layer in Rayleigh-Taylor instability in magnetic confined plasma. They derived using scaling laws for temporal growth rate of Rayleigh-Taylor instability including plasma resistivity, kinematic viscosity and electron number density. They presented a dispersion relation for the temporal growth rate in terms of viscous resistivity. Sun and Wang [113] studied viscous Rayleigh-Taylor and Richtmyer-Meshkov instabilities for the influence of horizontal magnetic field. The study revealed that the presence of horizontal magnetic field caused generation of vorticity in the flow, thereby causing additional distortion in the velocity field. This result differed from the previous viewpoint that presence of horizontal magnetic fields show effect as surface tension like force that does not produce any vorticity in the inviscid flow. The study showed presence of viscosity and magnetic fields both play fundamental role in Richtmyer-Meshkov instability. Linear stability analysis was presented on Rayleigh-Taylor instability in the presence of magnetic field for electrically conducting fluid film by Yang et al. [47]. The magnetic field showed suppression effect on the interfacial growth rate for finite thickness of small conducting fluid film. Whereas for large conductive fluids the range of unstable modes become narrowed down under the effect of magnetic field. Awasthi et al. [46] carried out a linear stability analysis on Rayleigh-Taylor instability in the presence of electric field. A dispersion relation was obtained for the rate of instability with the electric field. A comparison was made using inviscid and viscous potential flow analysis, and the rate of instability decreased in the presence of viscosity. The rate instability was affected strongly by tangentially acting electric field in the flow direction.

Linear stability study on Rayleigh-Taylor instability in a cylindrical domain was carried by various authors. Yu and livescu [114] performaed linear stability analysis of Rayleigh-Taylor instability in a cylindrical geometry filled with two inviscid immiscible fluid layers. Lister et al. [115] studied stability analysis on Rayleigh-Taylor instability of an inclined cylinder of highly viscous fluid rising in another surrounding fluid due to density difference. The authors performed linear stability analysis,

numerical analysis and experimental studies. The flow was studied for the Stokes condition in polar coordinates using linear stability analysis. For small inclination and viscosity ratio, the most unstable wave number corresponded to a longer wave. With the increased inclination, the axisymmetric growth rate was decreased, and an upward propagation rate of disturbance was increased. For inclination angles more than 70, disturbance growth was found to be propagated. Their results of linear stability, numerical simulations and experimental observation were found to agree with each other for the viscosity of the cylinder equal to the viscosity of the outer fluid. Their experiments showed that non-linear interaction between two plumes in a cylinder was important for inclination angle 20. Experiment results showed that disturbances might propagate out of the system for an inclination angle greater than 40 without considerable growth. Balestra et al. [116] studied Rayleigh-Taylor instability of a thin liquid film coated on the inner side of a cylindrical shell whose axis was orthogonal to gravity. The gravity was found to be destabilizing force at the beginning of the instability which leads to stretching and progressive drainage of coating at the wall of cylinder. This flow was found to be stable in linear regime of infinitesimal perturbation. However, algebraic growth of these infinitesimal perturbations for short span of time was found to lead to formation of distinctive patterns. The nature of these patterns were found to depend on the relative strength of capillary strength and gravity force. Their experiment showed that a traverse instability assisting over time was found to take place for moderate wave number. Liquid accumulated into rivulets of equal space which resulted into drainage of liquid at faster rate from top to bottom compared to that of uniform drainage of liquid. For higher value of Bond numbers stretched lattice of droplets was found to form in two dimension nature on the cylinder top part. The transition between the two types of patterns can be examined by an optimal linear growth analysis. Zheng et al. [117] studied Rayleigh-Taylor instability in an elastic soft gel confined in a cylindrical rigid wall. Authors performed linear stability analysis and numerical simulations to examine the interfacial instability in soft solids. Linear stability analysis and nonlinear numerical simulation revealed that critical load and instability pattern was found to be affected strongly by cylindrical gel aspect ratio. Their theoretical prediction and experimental results showed good match.

Linear stability analysis on Rayleigh-Taylor instability with heat transfer was carried out in various linear stability studies [118–123]. Hsieh [118] carried out linear stability analysis of Rayleigh-Taylor instability in a liquid vapor system including heat and mass transfer. Presence of heat and mass transfer reduced the growth rate which made the system more stable when the vapor was at higher temperature. Ho [119] studied linear stability of Rayleigh-Taylor instability with heat and mass transfer in the presence of viscosity for finite thickness of layers. The study showed that critical wave number was different from the classical wave number value due to the presence of surface tension, kinematic viscosity and heat and mass transfer. The stabilizing effect of the surface tension was found to be independent of which fluid layer was at upper and lower locations, and also independent of direction of temperature gradient. However, effect of viscosity and gravity forces on the instability were found to be influenced by the fluid arrangement and the direction of temperature gradient. Parhi and Nath [120] obtained sufficient condition for linear stability of Rayleigh-Taylor instability of viscous incompressible three fluid layers. The sufficient condition was found to depend on viscosity ratio of

fluid layers, wave number, surface tension ratio and middle layer thickness.

Khodaparast et al. [121] studied linear stability of Rayleigh-Taylor instability on liquid-vapor interface with viscosity and phase change. Rayleigh-Taylor and Kelvin-Helmholtz instabilities for viscous liquid and inviscid vapor is studied and the dispersion relation was obtained. The viscosity phase change effect was found to be destabilizing on Kelvin-Helmholtz instability. The liquid was stationary and vapor was taken to be with uniform horizontal velocity. Awasthi and Srivastava [122] performed linear stability analysis of Rayleigh-Taylor instability in two die-electric viscous fluid layers with heat and mass transfer across the interface in the presence of tangential electric field. The study was carried out using viscous potential flow analysis. The authors presented critical wave number and critical electric field for the instability. The effect of electric field, heat transfer coefficients, vapor fraction on the instability were studied. Presence of both heat transfer and electric fields showed stabilizing effect. Konovalov et al. [123] studied linear stability analysis of Rayleigh-Taylor instability in horizontal liquid layer and vapor layer of the liquid sandwiched between an upper and a lower solid walls. The temperature of the lower wall was kept higher than the saturation temperature of liquid, and temperature of the upper wall was kept lower that than the saturation temperature of liquid, so that phase change along the interface could take place. The critical value of heat flux which was required to completely suppress Rayleigh-Taylor instability by the phase transition was obtained for the absence of natural convection of fluid layers. The results showed that the pressure in the medium showed influential effect on the phase transitions which can significantly increase the growth of long wave disturbances.

1.2.2 Weakly nonlinear stability study on Rayleigh-Taylor instability

Goncharov [124] presented analytical model for single mode Rayleigh-Taylor instability at arbitrary Atwood numbers for nonlinear bubble evolution regime. This model was developed based on Lyzer's theory [125] which was applied only for an interface of a fluid in vacuum space associated to infinite density ratio. A model was used for starting from the linear regime till the nonlinear regime where bubble velocity saturated at $U_b = \sqrt{2\,A/(1+A)(g/C_g\,k)}$. Here, A, k and g were denoted for Atwood number, wave number of the perturbation and acceleration of the interface, respectively. The value of constant C_g was taken equal to 3 for two dimension and 1 for three dimensional geometries. Awasthi [126] carried out viscous correction for viscous potential flow analysis of Rayleigh-Taylor instability of liquid water layer over water vapor layer in which both heat and mass transfer were present across the interface. Critical value of wave number was presented. Heat and mass transfer showed stabilizing effect and increase of vapor fraction and density ratio showed destabilizing effect. Viscosity ratio showed stabilizing effect.

Hsieh [127] performed weaky nonlinear analysis of Rayleigh-Taylor instability of a finite liquid layer over a finite vapor layer using method of multiple scales. The study showed that for strong enough heat transfer rate, system was found to be linearly stable with reduced nonlinear effects. The estimation of size of bubbles which detaches from the interface was presented. Hsieh and Ho [128] carried out a weakly nonlinear analysis of Rayleigh-Taylor instability of liquid water layer superposed over a water vapor layer including heat and mass transfer using method of multiple scale expansion.

The authors presented stability criteria in terms of equilibrium heat flux, vapor pressure, surface tension, gravity, latent heat of evaporation, fluid thermal properties and densities of fluid. The study showed, under strong enough heat flux and under sufficient enough heat transfer mechanism, the nonlinearity of the system can be stabilized in the region where the system is linearly unstable. The effect of boiling heat transfer was also analyzed. Awasthi et al. [129] carried out analysis of weakly nonlinear Rayleigh-Taylor instability in a liquid water layer over a water vapor layer using viscous potential flow theory. The water and vapor were considered incompressible and viscous fluids of different kinematic viscosities. The presence of heat and mass transfer was found to be stabilizing factors in weakly nonlinear regime.

Seadawy and Rashidy [130] carried out weakly nonlinear analysis of Rayleigh-Taylor instability of a cylindrical interface between vapor and liquid phases of the fluid in the presence of heat ans mass transfer across the interface. The analysis was carried out using multiple expansion method and they derived Ginzburg–Landau equation for the growth rate of disturbance amplitude. The results showed that presence of heat and mass transfer result into stabilizing effect on the instability. Gupta et al. [131] studied the influence of magnetic field on the nonlinear disturbance growth of Rayleigh-Taylor instability. The magnetic field was assumed to be parallel to the interface of the two fluids and in the perpendicular direction to the wave number vector. When magnetic field was applied only on one side, presence of magnetic field showed unstable and stable effects, respectively, depending on whether magnetic pressure is in the same or opposing direction to the driving pressure difference. When magnetic field was present on the both the sides of interface, stabilization taken place when the forces due to magnetic pressure act in the opposite directions.

1.2.3 Rayleigh-Taylor instability in fully nonlinear regime

Rayleigh-Taylor instability has been an interesting field of study in physics and fluid mechanics. Authors have been studied the instability and its physics extensively using the different methods and reported. The instability in stratified fluid layer with density increasing in vertical direction was first observed and studied by Rayleigh [16] experimentally. Later, Taylor [17] presented an experimental study the interfacial instability with liquid layers accelerated in downward direction which showed occurrence of Rayleigh-Taylor instability. Top heavier density fluid spike showed accelerating movement while bottom lighter fluid bubble showed decelerating movement. Similar experimental studies were presented by various authors in various studies [17–19, 132, 133]. The instability effect was found to generated by various experimental techniques such as by removing the lid placed between superposed heavier fluid over lighter fluid, giving motion to a tank filled with higher density fluid superposed over lower density liquid, etc. in various experimental studies [19, 132, 134–142]. These studies were reported for various parameters effect on the instability such as density ratio, viscosity ratio, surface tension, electric and magnetic fields effect, etc. The growth rate of the instability was found to be affected significantly with these parameters. Numerical studies were carried out by many authors on the instability in past [9, 37, 40, 143–152] to find out the effect of various parameters such as density ratio, viscosity ratio, interfacial surface tension, heat transfer, magnetic and electric fields effect, etc.

Some of these studies were focused on Rayleigh-Taylor instability study in inviscid fluid layers. Daly [37] presented a numerical study on the instability evolution for various density ratio in inviscid fluid layers. In this study, it was observed that for low density ratio, heavier density fluid showed a spike-arm structure with a vortex formation, and for high density ratio, heavier density fluid showed a spike without any arm in fluid column form. In the study of Baker et al. [153], the instability was simulated for Atwood number effect on the instability in inviscid fluid layers. Results showed good agreement with the linear stability theory [154]. The spike acceleration showed non-linear growth with time for the larger time duration of the flow instability. Ramaprabhu and Dimonte [155] studied single mode Rayleigh-Taylor instability taking place with periodic arrays of bubbles and spikes of wavelength λ for any density ratios using three dimensional numerical simulations. The non-dimensional velocities of bubble and spike were found to vary with Atwood number. The asymptotic radius of curvature at the bubble tip was found to be independent of Atwood number, which was inline with potential flow predictions. Ramaprabhu et al. [71] studied in compressible inviscid single mode Rayleigh-Taylor instability in nonlinear regime for high aspect ratios. The simulations showed re-acceleration of Froude number beyond 1. Froude number values increase beyond 1 which is asymptotic Froude number predicted by potential theory. The deviation of Froude number from potential theory was found due to appearance of secondary Helmholtz structure. Formation of secondary Helmholtz instability was found to be affected to several parameters such as Helmholtz instability structure was found to suppressed at large Atwood number and viscosity with the bubble spike velocity in each case reverting the potential flow value. For low Atwood number spike behavior was found to be similar to bubble while for large Atwood number spike behavior approached to free fall. The numerical and experimental studies showed good agreement with those of the analytical studies such as Alon et al. [33] and Sohn [36] to find the disturbance growth rate with inviscid conditions.

Li et al. [146] performed 2-D and 3-D simulations to study Rayleigh-Taylor instability at various Atwood numbers. The study revealed that the disturbance amplitude growth of the instability showed nonlinear variation with time for Atwood numbers. He et al. [31] simulated for 3-D Rayleigh-Taylor instability for various Atwood numbers and Reynolds numbers. Heavy-fluid roll-ups were observed at the saddle point and at the tip of the spike. Interfacial instability become complicated with the secondary instability in parallel planes. Spike front and bubble tip growth rate found to increased with density ratio. Spike of the higher density fluid become slender with the increasing density ratio. Numerical study carried out by Ramaprabhu and Dimonte [155] on Rayleigh-Taylor instability showed spike with bigger head for low Atwood numbers, and showed spike with free fall behavior and smaller head for Atwood number approaching to 1. The spike velocity showed good agreement with other analytical studies [33–35]. In 3-D case, interface perturbation growth in linear and nonlinear stages were found to be faster than that in 2-D case. Rayleigh-Taylor instability problem of two immiscible fluids was studied for small Atwood number by Celani et al. [148]. Amplitude of perturbation was found to be grow linearly with time. 2-D and 3-D simulations were performed to study Rayleigh-Taylor instability in a solid rectangular box by Anuchina et al. [156]. With 3-D case, for same initial amplitude of perturbation the instability growth rate was found to be higher compared

to that with 2-D case. Lee and Kim [157] performed 3-D simulation on Rayleigh-Taylor instability in a rectangular box for various Atwood and Reynolds numbers. Interface spike and bubble growth with time was found to grow asymmetrically for high Atwood number and high Reynolds number. Ramaprabhu et al. [72] numerically studied single mode Rayleigh-Taylor instability with application of time dependent acceleration for density ratio in two and three dimensional configurations. Study was carried out for various form of time dependent accelerations. For two dimensional case, results obtained from numerical simulations showed good agreement with the 2-D potential flow model. Study showed that the spikes undergo free fall regime at large Atwood number. Free falling behavior of spike was found when Atwood number is more 0.5. For three dimensional case, results obtained from numerical simulations showed good agreement with the linear stability analysis presented by Mikaelian [158] for growth rates of spike and bubble. For three-dimensional Rayleigh-Taylor instability experimental studies, Wilkinson and Jacobs [159] found symmetric vortices formation with the upward and downward movement for low Atwood number cases. Growth rate of the disturbance amplitude at the initial stage followed an exponential nature and showed better agreement with the linear stability theory. Morgan et al. [142] performed 2-D and 3-D experiments to study Rayleigh-Taylor instability for various Atwood number cases. The spike and bubble velocity showed a better match with the study of Mikaelian [158] compared to the Goncharov's model [124] for the moderate Atwood number.

To understand the different stages involved in the interfacial instability, reviews on Rayleigh-Taylor instability were presented in past [18, 160–166]. Kull [160] reviewed on different analytical and stability analysis method used to study Rayleigh-Taylor instability for various affecting parameters. Boffetta and A. Mazzino [162] presented a review on Rayleigh-Taylor instability with turbulence. The focus of the review was on the effect of miscible and buoyancy which showed enhanced effect on Rayleigh-Taylor leading to turbulence which as supported through different experimental and numerical studies. Zhou [163] presented review on early experimental and analytical studies on Rayleigh-Taylor instability for singlemode and multimode disturbances. The analytical studies carried out for multi-scale modelings for single and multi-mode disturbances, and the evolution of the instability was studied in detail. Zhou [164] presented review on initial disturbance effect on Rayleigh-Taylor instability mixing effect in multi layer fluids. The review emphasized on the main difference between two and three dimensional studies in Rayleigh-Taylor and Richtmyer-Meshkov instability instabilities. Caulfield [165] presented a review on study of density stratification effect on interfacial instbility with turbulent flow. Banerjee [166] carried out a review on various experimental designs used to perform experiments to study Rayleigh-Taylor instability. The measurement techniques and designs parameters used in the experimental studies were focused in the review. Their reviews discussed the different stages of the instability. Some of the experimental studies also discussed on the mixing of top heavier fluid and bottom lighter fluid layers in the various past studies [136, 138, 158, 167]. They categorized the instability in three stages for lower Atwood number cases. In the first stage, inertial force affected the fluid mixing and interfacial disturbance growth. In the second stage, self-similar fluid mixing occurred for a short span of time with decaying inertial forces. However, in the third stage, late time decay in fluid mixing was observed with reduced inertial

effects leading to stable stratification. The released kinetic energy was due to inertial force, which was converted into potential energy. Later, the potential energy got released with dissipation effects.

Elgowainy and Ashgriz [168] performed numerical simulations to study Rayleigh–Taylor instability in density stratified fluid layers with finite thickness. Effects of initial perturbation of the interface, surface tension and viscosity on the instability growth rate was studied. The most unstable wave number was found to be at lower the Weber number which corresponded higher wavelength of the interface. Instability growth delayed with lower Reynolds numbers and spikes growth was found to be slower and thicker compared to the higher Reynolds numbers. Salih and Maullik [9] presented numerical study on the effect of surface tension in viscous fluid layers. Their study showed stabilizing effect on the instability for a critical value of surface tension. Rayleigh-Taylor instability was studied for various density ratios and surface tension effect in viscous fluid layers by Yakovenko [32]. At the initial state, instability development was found to be independent of density ratio. For density ratio less than 2, the instability shows symmetry for long time before asymmetry appears. Asymmetry was also found at lower times for larger density ratios. Suppression of interfacial disturbance was found to take place due to presence of surface tension and viscosity. These finding can be supported from the linear stability analysis [21, 39, 107]. Sweeney et al. [169] performed experimental and linear stability study on Rayleigh-Taylor instability for different parameters such as aspect ratio of cylinder, viscosity ratio, density ratio and surface tension effect. For large viscosity ratio and low Reynolds number value case, flow pattern showed axisymmetric fingering from the axis of cylinder, and for low viscosity ratio and high Reynolds number value case, flow pattern showed asymmetric fingering the side walls of cylinder. Linear stability studies performed by themselves were found to consistent with the experimental studies carried out by themselves. Experimental study results showed asymmetric and axisymmetric instability flow patterns in cylindrical domain.

Andrews and Spalding [134] performed Rayleigh-Taylor instability with the mixing of two fluids with different density. Experimental studies revealed that region of mixing zone was found to be reduced for two dimensional Rayleigh-Taylor instability compared to that of one-dimensional cases. Mixing effect of Rayleigh-Taylor instability on stratified fluid layers was investigated using experimental studies for various density ratios by Dimonte and Schneider [135]. Rayleigh-Taylor instability of two stratified fluid layers at low Atwood number cases were experimentally investigated by Waddell et al. [170] for the initial single mode disturbances. Spike and bubble velocity variation was observed to be more constant compared to the previous numerical and experimental analysis for lower Atwood number cases. Amplitude growth was found to be uniform with time. Initial instability growth rate showed good match with linear stability theory studied by Alon et al. [33]. Experimental study on mixing effect of Rayleigh-Taylor instability in density stratified fluid layers is carried out by Wykes and Dalziel [171]. Stably stratified fluid layers showed better mixing effect compared to that of two constant fluid layers. Wang et al. [172] performed 3-D simulation for Rayleigh-Taylor instability problem. Time-dependent density field and pressure boundary condition implemented for the study of the instability. The interface profiles at instantaneous dimensionless time, interface positions and velocity versus time were plotted in this study.

An experimental study on Rayleigh-Taylor instability was performed by Read [132] to analyze

mixing effect for turbulent flow. Initial disturbance of the interface showed significant effect on Rayleigh-Taylor instability. Instability growth rate was found to be increased more for the longer wavelength disturbances compared to that of the density difference. Mixing effect was found to be affected with interfacial movement due to Rayleigh-Taylor instability in the study of Dalziel et al. [136]. Olson and Jacobs [137] performed an experimental analysis to study Rayleigh-Taylor instability with the complex initial disturbance provided by accelerated tank. Growth rate of the fluid mixing zone was found to be in better agreement with the numerical study compared with the previous experimental analysis. Aspect ratio increased with increasing the width of the system resulted into better mixing effect. Hartmann and Colonius [44] studied Rayleigh-Taylor instability for single and multimode disturbances in a rectangular domain. With single mode disturbance symmetric interface evolution was observed and with multimode disturbances asymmetric interface evolution was observed which resulted into chaotic mixing of the fluids. Lee et al. [151] presented a numerical study on Rayleigh-Taylor instability for multimode disturbances in viscous fluid layers. Presence of multimode disturbance resulted into asymmetric behavior of interface evolution in the configuration. Similar effects were observed on Rayleigh-Taylor instability for single mode and multi mode initial perturbations of the interface in the study presented by Walters and Forbes [173]. With single and multi mode disturbance, interfacial instability showed symmetric and asymmetric evolution of spike and bubble growth, respectively. The interfacial growth was found be exponential for linear and nonlinear models of density variations. Nonlinear variation of density and viscosity showed damping effect on the roll-up structure formation and rate of instability. Bian et al. [174] performed 2-D and 3-D simulation for growth of Rayleigh-Taylor instability problem for various Reynolds number. The growth of the interface was found to be uniform or say constant at lower Reynolds number. The interface development showed unstable behavior with the increased Reynolds number.

In some of theoretical and experimental studies on Rayleigh-Taylor instability flow with differential wall heating have shown significant effect on two-fluid layer interface [20, 118, 119]. Young et al. [175] performed 2-D and 3-D simulations on Rayleigh-Taylor instability for miscible flow. Cold fluid was place over warmer fluid with the finite temperature difference. The instability was studied with random spatial disturbances in 3-D rectangular domain filled with top cold and bottom heated fluid layers. Rayleigh-Taylor instability problem with single and multi-mode disturbance was studied by Hartmann and Colonius [44] for temperature dependent density stratified fluids layer in a domain with top heated and bottom cooled conditions. Li et al. [176] performed numerical study on the interfacial instability in three layered viscous fluid fluid layers for heat transfer and fluid flow analysis. Effect of different parameters such as surface tension, gravitational force, velocity and viscosity ratio on the interfacial instability were considered for the study. With the increased conductivity and viscosity ratio, heat rate at the upper layer was found to be decreased and increased for lower layer. Rayleigh-Taylor instability was studied in the presence of temperature gradient for temperature independent viscous and inviscid fluid layers by Gerashchenko and Livescu [106], showed destabilizing effect on its interface. Overall, presence of temperature resulted into destabilizing effect on the instability. Manu et al. [177] performed the numerical study on Rayleigh-Taylor instability in a molten salt storage. The effect of temperature and velocity disturbance, penetration length and time duration

on the flow were studied. Density of the fluid was taken as function of temperature. Yuan et al. [178] simulated for Rayleigh-Taylor instability at high Reynolds number ($Re = 3000$) in a rectangular domain. With the gravity force effect, light fluid went up in the form of bubble and heavier fluid went down in the form of spike with bubble roll ups. Vortices formed in the domain with rotating in opposite direction and grew with time. For higher Atwood and large Reynolds numbers spike formed with a roll-up structure in 2-D numerical studies [174, 178, 179]. It was also observed that with single mode disturbance symmetric nature of interface formed whereas the multi-mode disturbance showed asymmetric nature of interface which resulted in chaotic nature of flow.

1.2.4 Rayleigh-Taylor instability in turbulence regime

Linear stability analysis predicts the growth of Rayleigh-Taylor instability in the linear stages of the instability. In the linear stage, interfacial disturbance grows linearly and at infinitesimally smaller scales. In the later stage, the disturbance grows with weakly nonlinearity. In the nonlinear stage of the instability, interfacial disturbance grows nonlinearly and at a larger scales in the order of unstable wavelength. Propagation of interfacial disturbance into larger scale is mainly due to nonlinear interactions between spikes and bubbles. These nonlinear interactions between the spikes and the bubbles results into growth of the mixing layer region between two fluids. With the increase in mixing length of the the mixing fluids turns into chaotic nature of the instability. The evolution of Rayleigh-Taylor instability can lead to turbulent regime under such increasing scales of nonlinear interactions and chaotic mixing conditions. When the fluids are miscible it results into relatively more faster mixing effects which leads to turbulent regime of the instability. Rayleigh-Taylor instability with turbulent flow was studied using different methods such as reported in various past studies [132, 133, 162–164, 180–183]. The mixing effect of top to bottom layer fluid with interfacial instability growth was studied and observed for turbulent flow by various authors. An experimental study on multimode Rayleigh-Taylor instability was performed by Read [132] to analyze mixing effect for turbulent flow. Initial interfacial perturbation provided with multi-modes showed better mixing effect. Rayleigh-Taylor instability was studied using numerical simulation for interfacial perturbation growth subjected to a uniform acceleration by Youngs [133]. Study showed that mixing effect was found to be better with the flow becoming turbulent for Rayleigh-Taylor instability.

Youngs [180] performed 3-D simulations to study the effect of density ratio on Rayleigh-Taylor instability. The study revealed that mixing of two fluid layers resulted into relatively more dissipation of kinetic energy and density fluctuation in the domain. Turbulent flow of Rayleigh-Taylor instability showed three-dimensionality in nature such as merging bubbles, roll-up and breakup structures of spike, and mixing effect of the fluid layers. The growth of interfacial instability was of nonlinear nature. Guermond and Quartapelle [181] studied Rayleigh-Taylor instability for various Atwood numbers and Reynolds numbers. At low Atwood number values, single roll-up structure of the bubble was found to be formed, irrespective of Reynolds number value. Whereas at high Atwood number values, two roll-up structures of the bubbles were found to be formed for higher Reynolds number value. Chiu and Lin [182] also found a single roll-up structure in the study of Rayleigh-Taylor instability at high Reynolds number. Wang et al. [172] performed 3-D simulation for Rayleigh-Taylor instability

problem. First roll-up structure formed near saddle point for the heavy fluid while second roll-up structure formed at the bubble spike of the lighter fluid. Wang et al. [184] performed simulations for multiphase flows of high Reynolds number and high density ratios with constant viscosity across the interface. Roll-up structures with secondary vortices formation observed for different Reynolds number values.

The instability was studied for various Atwood numbers in the presence of viscous effect by Ramaprabhu et al. [71]. For low Atwood number values, spike-arm structure was formed, and for high Atwood number values, a single free falling fluid like spike structure was formed. The late time evolution of the spike resulted into chaotic nature of fluid mixing. In the presence of higher viscous effect, the Kelvin-Helmholtz vortex formation was found to be suppressed. Ramaprabhu et al. [72] performed transient analysis on the instability for various Atwood numbers. The spike and bubbles showed linear growth at higher Atwood number cases while it showed nonlinear growth for lower Atwood number cases. Liu and Guo [185] performed the numerical simulations to study the mixing effect on Rayleigh-Taylor instability for various Prandtl numbers with the Boussinesq approximation. Density of the fluid was considered to be a linear function of temperature with top cold and bottom hot wall. Increase in Prandtl number showed decreased mixing effect, and initial perturbation showed increased mixing effect. Chou et al. [186] carried out 3-D simulations on the instability to examine the mixing effect of the suspended particles for concentration ratio. Their study showed that high concentration results into increased mixing effect. Direct numerical simulations of single and multi mode disturbances Rayleigh-Taylor instability was carried out in 2-D and 3-D rectangular domains by Hamzehloo [187]. Effects of Reynolds number, Atwood number, initial disturbance amplitude and surface tension on the instability were studied. Kelvin-Helmholtz type instability structure formation was prevented for high Reynolds number values in the presence of high surface tension. 3-D multi-mode instability showed qualitative similarity compared with that of single-mode instability.

1.2.5 Stratification effect on Rayleigh-Taylor instability

The stratified fluid layers with variable fluid properties can affect the instability to a large extent as compared to that of fluid layers with constant fluid properties. In past, authors studied for various stratification effects on different types of interfacial instabilities. However, stratification effect on specifically on Rayleigh-Taylor was focused for density, thermal and gravitational variations. Dimonte and Schneider [135] performed experimental study on Rayleigh-Taylor instability in density stratified fluid layers. The experiment was carried out to find density stratification effect on the instability mixing efficiency. Lawrie and Dalziel [188] studied Rayleigh-Tayor instablity in density stratified fluid layers. In their study, they found that self similarity mixing showed better mixing effect in density stratified fluid layers. Wykes and Dalziel [171] performed experimental study on Rayleigh-Taylor instability to find the mixing effect in the presence of density stratification. The two stable density stratified fluid layers showed relatively better mixing effect comparing with that of two homogeneous fluid layers. Gonzalez and Gutierrez [189] carried out linear stability study on Rayleigh-Taylor instability for semi-inifnite medium with density stratification. The upper fluid layer density was considered to vary exponentially with space. The decay of perturbation growth was found

to be more with exponential density stratification compared to that of constant fluid density. Aslangil et al. [51] studied for Reynolds and Atwood numbers effect on the instability in density stratified fluid layers. Flow phenomena was found to be more sensitive to Reynolds and Atwood numbers in variable density fluid layers compared sensitivity to other parameters. Aslangil et al. [190] studied the instability for various Atwood numbers with density varying initial disturbances. For low Atwood number values, initial density disturbances effect was found to be limited. Whereas for high Atwood number values, initial density disturbances effect leads to better mixing of fluid layers.

Snider and Andrews [191] experimentally studied Rayleigh-Taylor instability in fluid layers with density stratification. The density stratification was provided with temperature gradient in the presence of unstable thermal stratification. Shearing and buoyancy effect on mixing growth rate and vortices formation were studied in the presence of thermal stratification. Buoyancy had shown dominating effect on mixing with large plumes vortices formation. Livescu [50] studied Rayleigh-Taylor instability in thermal stratified fluid layers which cause density variation. Due to such density variation, mixing of fluid layers lead to compositional changes and inhomogeneities in fluid mixing. The effect acceleration stratification on Rayleigh-Taylor instability was analyzed in several studies such as [48, 49, 192, 193]. These studies showed mixing in Rayleigh-Taylor instability shows strong sensitivity to initial disturbance of initial acceleration stratification. Reversal of the acceleration direction had shown stronger destabilizing effect compared to the destabilizing effect due to density stratification. Wieland et al. [194] studied Rayleigh-Taylor instability in the presence of stratified compressibility effect. Compressibility stratification effect showed strong influence on the instability. For weaker stratification, instability growth rate showed a decelerating and accelerating nature. Whereas for stronger stratification the growth rate showed decelerating nature which turns into stabilizing effect on the instability. For higher Reynolds number values secondary vortices formation was observed. Gibbon [195] showed the effect of variable density stratification on Rayleigh-Taylor instability which lead to miscible mixing in two fluid layers. A model was used to find the mixing turned into inhomogeneous mixing of fluid layers in the presence of density stratification. It was found that buoyancy forces control the mixing effect in the fluid layers.

Many studies, such as the above mentioned studies, addressed the stratification effect on Rayleigh-Taylor instability due to density variation and gravity variation. However, the stratification effect due to viscosity variation on Rayleigh-Taylor instability was studied in fewer studies. However, viscosity stratification can show interesting phenomena on the instability in two fluid layers. Rudraiah et al. [109] studied viscosity stratification effect on Rayleigh-Taylor instability using a linear stability analysis. Viscosity of fluid layers were subjected to vary with space in vertically upward direction exponentially to get the viscosity stratified fluid layers. In the presence of viscosity stratification, increased thickness of bottom lighter fluid layer showed destabilizing effect on the interfacial instability. For viscosity stratified fluid layer, the instability growth rate was found to be higher than that of constant viscosity fluid layer. Various studies had been performed with viscosity stratification due to temperature varying viscosity on other interfacial instabilities, other than Rayleigh-Taylor instability. Viscosity of fluids were taken as a function of temperature in many past studies [52, 53, 65, 65–67, 69, 76, 77, 196–201]. Temperature dependent viscosity stratification effect was limited to linear

stability analysis on parallel flow in the past studies [52, 53, 65, 65, 66, 69, 77, 196, 199–201]. Some of these studies were focused on stratified shear flows and channel flows [202–212]. In the presence of viscosity stratification, the flow was found to be relatively unstable with faster disturbance growth. But, Rayleigh-Taylor instability in viscosity stratified fluid layers was given less attentions in the past studies.

1.2.6 Marangoni effect on Rayleigh-Taylor instability

Presence of thermocapillary or Marangoni effect shows significant effect on Rayleigh-Taylor instability in heated fluid layers or thin films. In the study of Deissler and Oron [213] Marangoni effect showed stabilizing effect against the destabilizing gravitational force on Rayleigh-Taylor instability in heated the liquid films. In their study, it was found that for a wide range of parameters, thin films of air-liquid interface on the bottom of a cooled horizontal plate showed localized pattern formation of axisymmetric nature. In the study of Krishnamoorthy et al. [214], interface deformation was found to be higher with increased thermocapillary effect in thin liquid films. Burgess et al. [20] performed an experimental and linear stability analysis on dripping of oil from ceiling in the presence of Marangoni effect. It was found that decreased instability growth rate with increased temperature gradient results into suppression effect on dripping of oil from ceiling. Heating and cooling show significant effect on the interfacial instability in liquid films with Marangoni effect. Kabova et al. [215] found that heating results in thinning and destabilizing effect on liquid film interface, whereas cooling results in thickening and stabilizing effect on liquid film interface in the presence of thermocapillary effect. Adami and Caps [94] carried out experimental studies for the capillary effect on thin liquid films with spatially varying surface tension. Presence of the capillary effect resulted into a damping effect on the interfacial instability of thin liquid films, and the results were found to be in line with the theoretical analysis carried out by themselves. The dynamics of liquid film forming on a substrate of a curved shape was studied for Rayleigh-Taylor instability using linear stability analysis by Trinh et al. [216]. The interfacial instability growth studied for various liquid film thickness and radius of curvature for substrate. For curvature less than the critical value, Rayleigh-Taylor instability became stable. Shabalina et al. [217] carried out a study on Rayleigh-Taylor instability in liquid foam layers. The authors found that thickness of the film and unstable wavelength of disturbance showed a significant effect on the disturbance growth rate. They also found that the instability growth rate decreases with gravitation acceleration. Overall, from the above studies it was observed that the presence of Marangoni effect can strongly affect Rayleigh-Taylor instability.

1.3 Conclusions from the literature review

Rayleigh-Taylor instability is one of the classic interfacial instability phenomena for which many studies were carried out in the past. Rayleigh-Taylor instability was studied using linear stability analysis in various past studies [33, 36, 74, 99–108, 113, 121]. Linear stability analysis of Rayleigh-Taylor instability with compressibility effect was also addressed in past studies [40–43]. Some of the analytical and semi-analytical studies on the instability were carried out with inviscid fluid layers

assumption. Weakly nonlinear studies on the instability were carried out for with and without heat and mass transfer [126–131]. Rayleigh-Taylor instability in incompressible fluid layers were studied numerically for the effect of various influencing parameters such as density, viscosity, surface tension effect, etc. [32, 37, 143–150, 153]. The instability in miscible and immiscible fluid layers were also studied and mixing effects were analyzed for conditions of with and without heating [148, 175, 195]. The turbulence aspects of the instability at late stage were considered in many numerical studies [132, 133, 180–182]. The effect of viscous stratification was mainly focused on channel flow and parallel flow instability [52, 53, 65, 66, 69]. Some studies on Rayleigh-Taylor instability were carried out using weakly nonlinear analysis including heat transfer with viscous and inviscid fluid layers [126–129]. The influence of heat transfer on Rayleigh-Taylor instability in fully nonlinear regime was not addressed.

In most of the past studies, Rayleigh-Taylor instability was studied for fluid layers of constant viscosity. However, Rayleigh-Taylor instability in viscosity stratified fluid layers, in which fluid layers are stratified due to viscosity variation with temperature, was not studied. Rayleigh-Taylor instability in viscosity stratified fluid layers due to viscosity variation with temperature has many important practical applications such as metal boiling [18], lubrication process, polymer processing [83], combustion [84], etc. From the studies found in literature, it is concluded that Rayleigh-Taylor instability in viscosity stratified fluid layers with heat transfer has not been reported sufficiently. Hence, study of such instability is important.

Marangoni effect, in which surface tension varies along the interface between different fluids layers, was found to show an influential effect on interfacial instability such as in thin films and liquid films, etc. [20, 94, 213–217]. Hence, in general Marangoni effect can show a significant effect on Rayleigh-Taylor instability. Influence of such important effect on Rayleigh-Taylor instability was not addressed in the literature.

Many of the numerical simulation studies were addressed for Rayleigh-Taylor instability in 2-D and 3-D rectangular coordinates. However, numerical studies on Rayleigh-Taylor instability in axisymmetric configuration were not addressed in literature. Also, the effect of viscous stratification of fluid layers due to temperature variation and Marangoni effect on axisymmetric Rayleigh-Taylor instability were not addressed in literature. The present study is aimed to address the above gaps in the literature.

1.4 Objectives of the work

The present work is aimed to study Rayleigh-Taylor instability in viscosity stratified fluid medium in 2-D rectangular as well as axisymmetric coordinate configurations. The following objectives are set for the study from the above literature review.

1. To study Rayleigh-Taylor instability in 2-D rectangular coordinates with viscosity stratification. The study includes the effect of viscosity ratio, temperature ratio, surface tension and hot and cold wall locations on the instability under the influence of viscosity stratification.

2. To study the effect of functional variation of viscosity with temperature on Rayleigh-Taylor instability in 2-D rectangular coordinates.

3. To study Marangoni effect due to surface tension variation with temperature on Rayleigh-Taylor instability in 2-D rectangular coordinates. Study on effect of gravity and surface tension on the instability in the presence of Marangoni effect is also aimed.

4. To study Rayleigh-Taylor instability in viscosity stratified fluid layers in axisymmetric configuration. The study in viscosity stratified fluid layers also includes the effect of viscosity ratio, hot and cold wall locations, temperature ratio and surface tension on the instability.

5. To study the effect of functional variation of viscosity with temperature on Rayleigh-Taylor instability in axisymmetric configuration.

6. To study Marangoni effect due to temperature varying surface tension on Rayleigh-Taylor instability in axisymmetric configuration. The study includes effect of different parameters such as temperature ratio, gravity effect and surface tension on the instability in the presence of Marangoni effect.

1.5 Organization of the thesis

The thesis is organized in nine chapters. In chapter 1, the introduction and literature review of Rayleigh-Taylor instability in stratified flow is presented. The conclusions form the literature and objectives of the present work are also presented in this chapter. In chapter 2, details of the physical system, mathematical model, numerical methodology and validations of the used solvers are presented. In chapter 3, Rayleigh-Taylor instability in viscosity stratified fluid layers in 2-D rectangular coordinates is simulated and results are presented for various parameters. In chapter 4, effect of various functional variations of viscosity with temperature on Rayleigh-Taylor instability in 2-D rectangular coordinates is studied and results are presented for various parameters. In chapter 5, Rayleigh-Taylor instability with Marangoni effect due to surface tension variation with temperature is simulated in 2-D rectangular coordinates and results are presented for various parameters in the presence of Marangoni effect. In chapter 6, axisymmetric Rayleigh-Taylor instability in viscosity stratified fluid layers is simulated and results are presented for various parameters. In chapter 7, effect of different functional variations of viscosity with temperature on Rayleigh-Taylor instability is studied for axisymmetric configuration and results are presented for various parameters. In chapter 8, axisymmetric Rayleigh-Taylor instability with Marangoni effect due to temperature varying surface tension is simulated and results are presented for various parameters in the presence of Marangoni effect. In chapter 9, conclusions of the present work and future scope are presented.

Chapter 2

Physical system and mathematical treatment

In this chapter, physical system of the present study is presented which is followed by description of mathematical model. Governing equations along with initial and boundary conditions are presented. Numerical methodology used to solve the governing equations is presented.

2.1 Physical system

In this study, Rayleigh-Taylor instability in viscosity stratified fluid medium is studied in two types of physical systems, which are in 2-D rectangular and axisymmetric coordinate configurations. The physical systems are described in the next subsections.

2.1.1 Physical system for configuration in 2-D rectangular coordinates

Fig. 2.1 shows a schematic diagram of two superimposed viscous stratified fluid layers sandwiched between two infinite differentially heated parallel walls. Both the fluid layers are assumed to be immiscible. A representative repetitive portion of the above mentioned system is the domain of analysis in 2-D rectangular coordinates. The physical system consists of a higher density fluid layer superimposed over a lower density fluid layer sandwiched between top and bottom walls as shown in Fig. 2.2. The side boundaries are of symmetric nature. The top heavier and bottom lighter density fluid layers are represented as 'Fluid 1' and 'Fluid 2', respectively. Top and bottom walls are isothermally maintained at two different temperatures $\tilde{T}_1$ and $\tilde{T}_2$, respectively. The density, thermal conductivity and heat capacity in the individual fluid layers are assumed to be constant. Viscosities of both the fluid layers vary with temperature. 'Fluid 1' layer fluid properties such as density, viscosity, heat capacity and thermal conductivity are denoted with $\tilde{\rho}_1$, $\tilde{\mu}_1$, $\tilde{c_{p_1}}$, $\tilde{k}_1$, respectively. 'Fluid 2' layer fluid properties such as density, viscosity, heat capacity and thermal conductivity are denoted with $\tilde{\rho}_2$, $\tilde{\mu}_2$, $\tilde{c_{p_2}}$, $\tilde{k}_2$, respectively. Acceleration due to gravity, $\tilde{g}$, acts in the downward $\tilde{y}-$ direction. Initially, interface between the two fluid layers is located at $\tilde{y} = \tilde{H}_1$. At initial state, the interface is perturbed using a disturbance function with an amplitude of δ_0. Initially, temperature is specified to vary linearly from cold wall temperature to hot wall temperature.

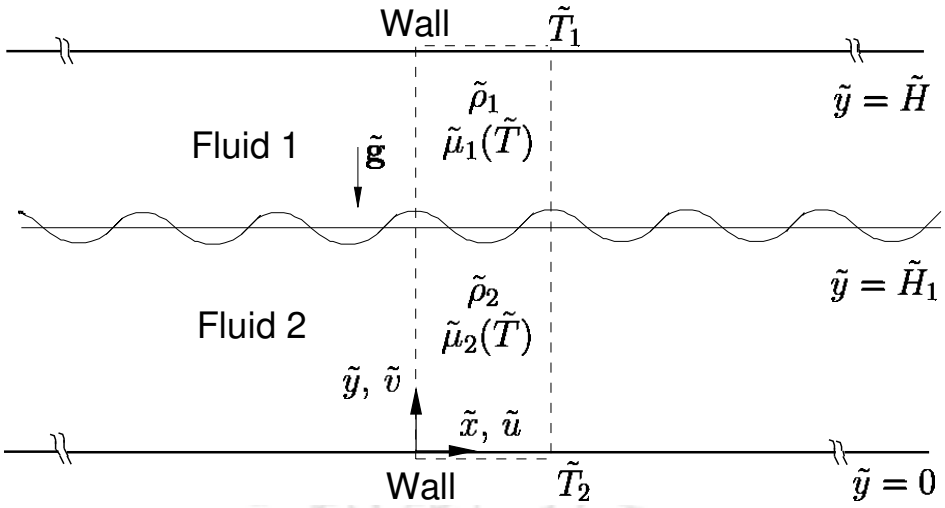

Figure 2.1: Schematic of two fluid layers sandwiched between two infinite parallel walls.

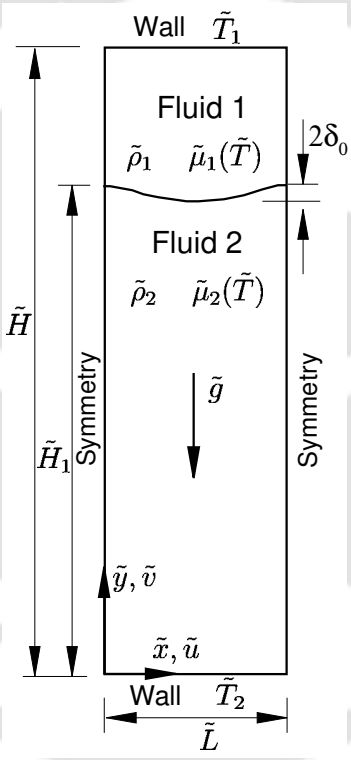

Figure 2.2: Schematic of physical system for 2-D rectangular coordinate configuration.

2.1.2 Physical system for configuration in axisymmetric coordinates

Physical system consists of a superposed heavier fluid layer over a lighter fluid layer, as shown in Fig. 2.3. The system is of axisymmetric configuration in which top and bottom boundaries are solid walls maintained at different isothermal temperatures. The upper heavier fluid is denoted with 'Fluid 1' and the lower lighter fluid is denoted with 'Fluid 2'. The top and bottom walls are isothermally maintained at constant temperatures $\tilde{T}_1$ and $\tilde{T}_2$, respectively. Viscosities of both the fluid layers vary with temperature. Fluid properties such as density, heat capacity, viscosity and thermal conductivity of 'Fluid 1' layer are denoted with $\tilde{\rho}_1$, $\tilde{c}_{p_1}$, $\tilde{\mu}_1$ and $\tilde{k}_1$, respectively. In 'Fluid 2' layer, density, heat capacity, viscosity and thermal conductivity are denoted with $\tilde{\rho}_2$, $\tilde{c}_{p_2}$, $\tilde{\mu}_2$ and $\tilde{k}_2$, respectively. Accel-

eration due to gravity, $\tilde{g}$, acts in the downward $\tilde{z}-$direction. Initially, the two fluid layers are separated by an interface located at $\tilde{z} = \tilde{H}_1$. At the initial state, the interface is perturbed with an axisymmetric form of disturbance with a finite amplitude δ_0. Initially, temperature is specified to vary linearly from cold wall temperature to hot wall temperature.

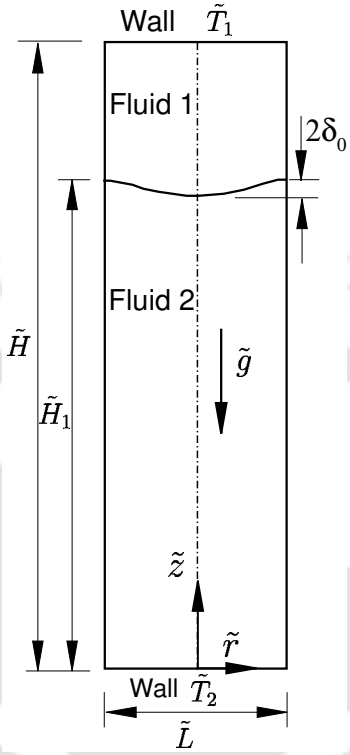

Figure 2.3: Schematic of physical system for axisymmetric coordinate configuration.

2.2 Mathematical model

The flow is assumed to be incompressible. Density and thermal conductivity in the individual fluid layers are invariant of temperature variation. With the above assumptions, the governing equations are as following

Continuity equation

$$\tilde{\nabla}\cdot\tilde{\mathbf{u}} = 0 \tag{2.1}$$

Momentum equation

$$\tilde{\rho}\left(\frac{\partial\tilde{\mathbf{u}}}{\partial\tilde{t}} + \tilde{\mathbf{u}}\cdot\tilde{\nabla}\tilde{\mathbf{u}}\right) = -\tilde{\nabla}\tilde{p} + \tilde{\nabla}\cdot\tilde{\mu}\left(\tilde{\nabla}\tilde{\mathbf{u}} + \tilde{\nabla}\tilde{\mathbf{u}}^{\mathrm{T}}\right) + \tilde{\mathbf{F}} \tag{2.2}$$

Energy equation

$$\tilde{\rho}\,\tilde{c}_p\left(\frac{\partial\tilde{T}}{\partial\tilde{t}} + \tilde{\mathbf{u}}\cdot\tilde{\nabla}\tilde{T}\right) = \tilde{\nabla}\cdot(\tilde{k}\tilde{\nabla}\,\tilde{T}) \tag{2.3}$$

In the governing equations, $\tilde{\mathbf{u}}$, $\tilde{p}$ and $\tilde{T}$ represent the velocity, pressure and temperature fields in the domain, respectively. Time is denoted with $\tilde{t}$. Fluid properties such as density, heat capacity, thermal conductivity and viscosity are denoted with $\tilde{\rho}$, $\tilde{c_p}$, $\tilde{k}$ and $\tilde{\mu}$, respectively. Term $\tilde{\mathbf{F}}$ represents body force term. The body force term is combination of surface tension force ($\tilde{\mathbf{F}}_{\tilde{\sigma}}$) and gravitational force ($\tilde{\mathbf{F}}_{\tilde{\mathbf{g}}}$) given by

$$\tilde{\mathbf{F}} = \tilde{\mathbf{F}}_{\sigma} + \tilde{\mathbf{F}}_{\tilde{g}} \tag{2.4}$$

Surface tension force term ($\tilde{\mathbf{F}}_{\tilde{\sigma}}$) can be expressed in normal and tangential components as following.

$$\tilde{\mathbf{F}}_{\sigma} = \tilde{\mathbf{F}}_{\sigma_\mathbf{n}} + \tilde{\mathbf{F}}_{\sigma_\mathbf{t}} = \tilde{\sigma}\,\tilde{\kappa}\,\delta\,\tilde{\mathbf{n}} + \tilde{\nabla}_s\,\tilde{\sigma}\,\delta_s \tag{2.5}$$

Here, $\tilde{\mathbf{F}}_{\sigma_\mathbf{n}}$ and $\tilde{\mathbf{F}}_{\sigma_\mathbf{t}}$ are the normal and tangential surface tension force, respectively, acting along the interface. In the above, $\tilde{\sigma}$ is the surface tension coefficient, $\tilde{\kappa}$ is the interface curvature, $\tilde{\mathbf{n}}$ is the unit normal and δ is the dirac delta function. Value of δ is zero throughout the domain except along the interface. Substituting the term $\tilde{\mathbf{F}}_{\tilde{\sigma}}$ in Eq. (2.4), we get

$$\tilde{\mathbf{F}} = \tilde{\mathbf{F}}_{\sigma_\mathbf{n}} + \tilde{\mathbf{F}}_{\sigma_\mathbf{t}} + \tilde{\mathbf{F}}_{\tilde{g}} = \tilde{\sigma}\,\tilde{\kappa}\,\delta\,\tilde{\mathbf{n}} + \tilde{\nabla}_s\,\tilde{\sigma}\,\delta_s - \tilde{\rho}\tilde{g}\,\mathbf{e}_j \tag{2.6}$$

Here, $\mathbf{e}_j$ is the unit vector. The tangential surface tension force term, $\tilde{\mathbf{F}}_{\sigma_\mathbf{t}}$, represents Marangoni force which is generated due to the variable surface tension. For constant surface tension case or say in the absence of Marangoni effect the term $\tilde{\mathbf{F}}_{\sigma_\mathbf{t}}$ becomes zero. Hence, for constant surface tension case the body force term becomes

$$\tilde{\mathbf{F}} = \tilde{\sigma}\,\tilde{\kappa}\,\delta\,\tilde{\mathbf{n}} - \tilde{\rho}\tilde{g}\,\mathbf{e}_j \tag{2.7}$$

The viscosity variation in both the fluid layers are taken to be temperature dependent, which is according to [52, 53, 64–66, 69]. Fluid viscosity variation with temperature is taken in the form of

$$\tilde{\mu}_1(\tilde{T}) = \tilde{\mu}_1(\tilde{T}_{\text{ref}})\,e^{\left[-\frac{(\tilde{T}-\tilde{T}_{\text{ref}})}{\tilde{T}_{\text{ref}}}\right]} \quad \text{and} \quad \tilde{\mu}_2(\tilde{T}) = \tilde{\mu}_2(\tilde{T}_{\text{ref}})\,e^{\left[-\frac{(\tilde{T}-\tilde{T}_{\text{ref}})}{\tilde{T}_{\text{ref}}}\right]} \tag{2.8}$$

Here, $\tilde{\mu}_1(\tilde{T}_{\text{ref}})$ and $\tilde{\mu}_2(\tilde{T}_{\text{ref}})$ are top heavier and bottom lighter fluid viscosities at reference temperature ($\tilde{T}_{\text{ref}}$).

In the present study, a code is developed for simulations of multiphase flows in 2-D rectangular coordinates using Finite Volume Method (FVM). Simulations of some parts of the study are carried out using a present developed code, while the remaining simulations are carried out using an open source software Basilisk. The present code is developed using level set method. In level set method, an additional equation of the level set function is solved to find the interface location. At any point in the domain, the value of level set function represents the distance of the interface from that particular point. Hence, the contour along which the level set function is zero represents the curve of interface. The normal distance with positive value on one side of the interface represents 'Fluid 1' and negative value on other side of the interface represents 'Fluid 2'. The equation of level set function is given by

$$\frac{\partial\tilde{\phi}}{\partial t} + \tilde{\mathbf{u}}\cdot\tilde{\nabla}\tilde{\phi} = 0 \tag{2.9}$$

In level set method, fluid properties such as density, viscosity, thermal conductivity and heat capacity are calculated using the expressions

$$\begin{aligned}\tilde{\rho} &= \tilde{\rho}_2 + (\tilde{\rho}_1 - \tilde{\rho}_2)\, H \\ \tilde{\mu} &= \tilde{\mu}_2 + (\tilde{\mu}_1 - \tilde{\mu}_2)\, H \\ \tilde{k} &= \tilde{k}_2 + (\tilde{k}_1 - \tilde{k}_2)\, H \\ \tilde{c_p} &= \tilde{c_{p2}} + (\tilde{c_{p1}} - \tilde{c_{p2}})\, H\end{aligned} \tag{2.10}$$

Where, H is defined as heaviside function. Heaviside function (H), in Ghost Fluid Method (GFM), is defined as per past studies [218–220] as following

$$\begin{aligned}H(\phi) &= 1 \qquad \text{if} \quad \phi > 0 \\ &= 0 \qquad \text{if} \quad \phi \leq 0\end{aligned} \tag{2.11}$$

Simulations of some parts of the study are carried out using an open source software Basilisk. The software uses Volume of Fluid (VoF) framework for solutions of multiphase flows. In VoF, the interface between two fluids is captured using volume fraction (f). The volume fraction (f) value varies from 0 to 1 in the fluid layers. The volume fraction value and in a control volume which is fully occupied with 'Fluid 1' fluid will be 1, and control volume which is occupied by other fluid 'Fluid 2' will be 0. The value of f in control volumes which are occupied of both the fluids will be between 0 to 1, representing the volume of fraction of the 'Fluid 1'. The equation of volume fraction (f) is given by

$$\frac{\partial f}{\partial t} + \tilde{\mathbf{u}} \cdot \tilde{\nabla} f = 0 \tag{2.12}$$

In volume of fluid method, fluid properties such as density, thermal conductivity, heat capacity and viscosity of two fluid layers are computed as a function of f using expressions given by

$$\begin{aligned}\tilde{\rho} &= \tilde{\rho}_1 f + \tilde{\rho}_2 (1 - f) \\ \tilde{k} &= \tilde{k}_1 f + \tilde{k}_2 (1 - f) \\ \tilde{c_p} &= \tilde{c_{p_1}} f + \tilde{c_{p_2}} (1 - f) \\ \tilde{\mu} &= \tilde{\mu}_1 f + \tilde{\mu}_2 (1 - f)\end{aligned} \tag{2.13}$$

The dimensionless variables used to non-dimensionalize the governing equations, for 2-D rectangular coordinates and axisymmetric coordinates, are as following

$$\begin{aligned}\rho = \frac{\tilde{\rho}}{\tilde{\rho}_{\text{ref}}},\ \mu = \frac{\tilde{\mu}}{\tilde{\mu}_{\text{ref}}},\ k = \frac{\tilde{k}}{\tilde{k}_{\text{ref}}},\ c_p = \frac{\tilde{c_p}}{\tilde{c_p}_{\text{ref}}},\ x = \frac{\tilde{x}}{\tilde{L}_{\text{ref}}},\ y = \frac{\tilde{y}}{\tilde{L}_{\text{ref}}},\ r = \frac{\tilde{r}}{\tilde{L}_{\text{ref}}},\ z = \frac{\tilde{z}}{\tilde{L}_{\text{ref}}}, \\ \nabla = \frac{\tilde{\nabla}}{\tilde{L}_{\text{ref}}},\ t = \frac{\tilde{t}}{(\tilde{L}_{\text{ref}}/\tilde{V}_{\text{ref}})},\ \mathbf{u} = \frac{\tilde{\mathbf{u}}}{\tilde{V}_{\text{ref}}},\ p = \frac{\tilde{p}}{\tilde{\rho}_{\text{ref}}\, \tilde{V}^2_{\text{ref}}},\ \theta = \frac{\tilde{T} - \tilde{T}_{\text{ref}}}{\tilde{T}_{\text{ref}}},\ \sigma = \frac{\tilde{\sigma}}{\tilde{\sigma}_{\text{ref}}},\ \phi = \frac{\tilde{\phi}}{\tilde{L}_{\text{ref}}},\end{aligned} \tag{2.14}$$

In the above, variables with subscript 'ref' represent reference quantities. The reference quantities in different studies are chosen differently based on the physics and appropriate scales of the study. Non-dimensionalized form of the governing equations are given as following

Continuity equation

$$\nabla\cdot\mathbf{u} = 0 \tag{2.15}$$

Momentum equation

$$\rho\left(\frac{\partial\mathbf{u}}{\partial t} + \mathbf{u}\cdot\nabla\mathbf{u}\right) = -\nabla p + \frac{1}{Re}\nabla\cdot\mu\left(\nabla\mathbf{u} + \nabla\mathbf{u}^{\mathrm{T}}\right) + \mathbf{F} \tag{2.16}$$

Energy equation

$$\rho\, c_p\left(\frac{\partial\theta}{\partial t} + \mathbf{u}\cdot\nabla\theta\right) = \frac{1}{Re\,Pr}\nabla\cdot(k\nabla\theta) \tag{2.17}$$

Level set equation

$$\frac{\partial\phi}{\partial t} + \mathbf{u}\cdot\nabla\phi = 0 \tag{2.18}$$

Volume of fraction (f) equation

$$\frac{\partial f}{\partial t} + \mathbf{u}\cdot\nabla f = 0 \tag{2.19}$$

Here, dimensional quantities are represented with "~" (tilde) notation and non-dimensional quantities are represented without any tilde. θ represents the dimensionless temperature. Here, dimensionless body force term, $\mathbf{F}$, in the momentum equation is the combination of surface tension force and gravitational force given by

$$\mathbf{F} = \mathbf{F}_\sigma + \mathbf{F}_\mathbf{g} \tag{2.20}$$

Surface tension force term ($\mathbf{F}_\sigma$) is, the combination of normal ($\mathbf{F}_{\sigma_\mathbf{n}}$) and tangential ($\mathbf{F}_{\sigma_\mathbf{t}}$) components, expressed as

$$\mathbf{F}_\sigma = \mathbf{F}_{\sigma_\mathbf{n}} + \mathbf{F}_{\sigma_\mathbf{t}} = \frac{\delta}{We}\left(\sigma\,\kappa\,\mathbf{n} + \nabla_s\,\sigma\right) \tag{2.21}$$

Substituting the above expression in Eq. (2.20), we get

$$\mathbf{F} = \frac{\delta}{We}\left(\sigma\,\kappa\,\mathbf{n} + \nabla_s\,\sigma\right) - \frac{\rho}{Fr}\,\mathbf{e}_j \tag{2.22}$$

The tangential component ($\mathbf{F}_{\sigma_\mathbf{t}}$) represents Marangoni force which is generated due to variable surface tension. Surface tension force can vary with different parameters such as space, temperature or solute concentration as given in past studies [10, 12, 15, 73, 75, 86, 86–91, 93]. For the case of constant surface tension, the tangential component ($\mathbf{F}_{\sigma_\mathbf{t}}$) becomes zero. Hence, the dimensionless body force term for flows with constant surface tension becomes

$$\mathbf{F} = \frac{\delta}{We}\,\kappa\,\mathbf{n} - \frac{\rho}{Fr}\,\mathbf{e}_j \tag{2.23}$$

In the above, dimensionless numbers Reynolds number (Re), Froude number (Fr), Weber number (We) and Prandtl number (Pr) are defined as following.

$$Re = \frac{\tilde{\rho}_{\text{ref}}\,\tilde{V}_{\text{ref}}\,\tilde{L}_{\text{ref}}}{\tilde{\mu}_{\text{ref}}};\quad Fr = \frac{\tilde{V}_{\text{ref}}}{\tilde{g}\,\tilde{L}_{\text{ref}}};\quad We = \frac{\tilde{\rho}_{\text{ref}}\,\tilde{g}\,\tilde{L}^2_{\text{ref}}}{\tilde{\sigma}_{\text{ref}}};\quad Pr = \frac{\tilde{\mu}_{\text{ref}}\,\tilde{c}_{p_{\text{ref}}}}{\tilde{k}_{\text{ref}}} \tag{2.24}$$

Viscosity variation with temperature in dimensionless form becomes

$$\mu_1 = m\, e^{-\theta} \qquad \text{and} \qquad \mu_2 = e^{-\theta} \tag{2.25}$$

Here, $m = \tilde{\mu}_1(\tilde{T}_{\text{ref}})/\tilde{\mu}_2(\tilde{T}_{\text{ref}})$ is top to bottom layer fluid viscosity ratio at reference temperature. In level set method, dimensionless fluid properties such as density, viscosity, thermal conductivity and heat capacity are calculated as a function of H, which is given by

$$\begin{aligned} \rho &= \rho_1\, H + \rho_2\,(1 - H) \\ \mu &= \mu_1\, H + \mu_2\,(1 - H) \\ k &= k_1\, H + k_2\,(1 - H) \\ c_p &= c_{p_1}\, H + c_{p_2}\,(1 - H) \end{aligned} \tag{2.26}$$

Here, ρ_1, μ_1, k_1, c_{p_1} denotes dimensionless properties of 'Fluid 1' such as density, viscosity, thermal conductivity and heat capacity, respectively. ρ_2, μ_2, k_2, c_{p_2} denotes dimensionless properties of 'Fluid 2' such as density, viscosity, thermal conductivity and heat capacity, respectively.

In volume of fluid method, dimensionless fluid properties such as density, viscosity, heat capacity and thermal conductivity are expressed, as a function of f, in the dimensionless form as

$$\begin{aligned} \rho &= \rho_1\, f + \rho_2\,(1 - f) \\ \mu &= \mu_1\, f + \mu_2\,(1 - f) \\ c_p &= c_{p_1}\, f + c_{p_2}\,(1 - f) \\ k &= k_1\, f + k_2\,(1 - f) \end{aligned} \tag{2.27}$$

2.2.1 Marangoni effect due to surface tension variation with temperature

Surface tension can vary with various parameters such as temperature [10, 12, 15, 73, 75, 86–91], solute concentration [85], etc. There are some studies, such as Muradoglu and Tryggvason [93] and Adami and Caps [94], in which surface tension was taken to be varying with space. The Marangoni effect due to temperature dependent surface tension on different multiphase flows was studied in past studies [10, 12, 15, 73, 75, 86–91]. Common examples of interfaces of combination of fluids in which surface tension vary linearly or parabolically with temperature are interface between water and oils, interface between oil and air and interface between high-carbon alcohol solutions. A linear variation of surface tension with temperature was used in the various studies [10, 12, 15, 90, 91]. However, a more general quadratic function for surface tension variation with temperature was used in studies [73, 75]. In the present study, quadratic form of temperature dependent surface tension variation is considered, which is also used in the studies of [73, 75], which is as following

$$\tilde{\sigma}(\tilde{T}) = \tilde{\sigma_0} + \beta_1(\tilde{T} - \tilde{T}_{\text{ref}}) + \beta_2(\tilde{T} - \tilde{T}_{\text{ref}})^2 \tag{2.28}$$

Here, $\beta_1 \equiv -d\tilde{\sigma}/d\tilde{T}|_{\tilde{T}_{\text{ref}}}$ and $\beta_2 \equiv (1/2)d^2\tilde{\sigma}/d\tilde{T}^2|_{\tilde{T}_{\text{ref}}}$ are the surface tension coefficients dependent on temperature. Substituting the above expression for surface tension variation with temperature, the

body force term in momentum equation which is given by Eq. (2.6) becomes

$$\tilde{\mathbf{F}} = \tilde{\sigma}(\tilde{T})\,\tilde{\kappa}\,\delta\,\tilde{\mathbf{n}} + \tilde{\nabla}_s\,\tilde{\sigma}(\tilde{T})\,\delta_s - \tilde{\rho}\tilde{g}\,\mathbf{e}_j \tag{2.29}$$

The above body force term in dimensionless form becomes

$$\mathbf{F} = \frac{\delta}{We}\left[\sigma(\theta)\,\kappa\,\mathbf{n} + \nabla_s\,\sigma(\theta)\right] - \frac{\rho}{Fr}\,\mathbf{e}_j \tag{2.30}$$

The expression of temperature dependent surface tension, given in Eq. (2.28), is non-dimesionalized as following

$$\sigma(\theta) = \tilde{\sigma}(\tilde{T})/\tilde{\sigma_0} = 1 - M_1\,\theta + M_2\,\theta^2 \tag{2.31}$$

Here, the dimensionless constants M_1 and M_2 are defined as $\beta_1\,\tilde{T}_{\text{ref}}/\tilde{\sigma_0}$ and $\beta_2\,\tilde{T}^2_{\text{ref}}/\tilde{\sigma}$, respectively. Substituting the expression of dimensionless surface tension ($\sigma(\theta)$) in Eq. (2.22), we get the dimensionless body force ($\mathbf{F}$) as

$$\mathbf{F} = \frac{1}{We}\left[\kappa(1 - M_1\,\theta + M_2\theta^2)\,\delta\,\mathbf{n}\right] - \frac{(M_1 - 2\,M_2\theta)}{We}\left[\nabla\theta - (\nabla\theta\cdot\mathbf{n})\,\mathbf{n}\right]\delta_s - \frac{\rho}{Fr}\mathbf{e}_j \tag{2.32}$$

2.2.2 Initial and boundary conditions for 2-D rectangular coordinate configuration

Computational domain for 2-D rectangular coordinates varies from $x = 0$ to L and $y = 0$ to H in x and y-coordinates, respectively, as shown in Fig. 2.4. No slip and no penetration boundary conditions are imposed on top and bottom solid walls. Symmetry boundary conditions are imposed on both the side vertical boundaries. The top wall is maintained isothermally at dimensionless temperature θ_1, and the bottom wall is maintained isothermally at dimensionless temperature θ_2. The values of θ_1 and θ_2 are set according to the heating configuration. For example, with top heated and bottom cooled configuration, top and bottom walls are set to the dimensionless temperatures of $\theta_1 = r_T$ and $\theta_2 = 0$, respectively. For top cooled and bottom heated configuration, top and bottom walls are set to the dimensionless temperatures of $\theta_1 = 0$ and $\theta_2 = r_T$, respectively. Here, r_T is the dimensionless temperature ratio defined equal to $(\tilde{T} - \tilde{T}_{\text{ref}})/\tilde{T}_{\text{ref}}$. Dimensionless height of the domain is taken $H = 4$ and width of the domain is taken $L = 1$. At initial state, $t = 0$, the interface is located at dimensionless vertical distance of $y = H_1 = 3$ from the bottom wall of the domain, which is perturbed according to $\delta = \delta_0\cos(2\pi x/)$. Here, δ_0 is defined as amplitude of the perturbation, which is taken equal to 0.01. At the initial condition, temperature is specified to vary linearly from cold wall to hot wall. The initial and boundary conditions are expressed in mathematical form as following.

Initial conditions

At $t = 0$, $\quad 0 \le x \le L$ and $0 \le y \le H$

$$u = 0, \qquad v = 0, \qquad \theta = \theta_2 + (\theta_1 - \theta_2)y/H$$

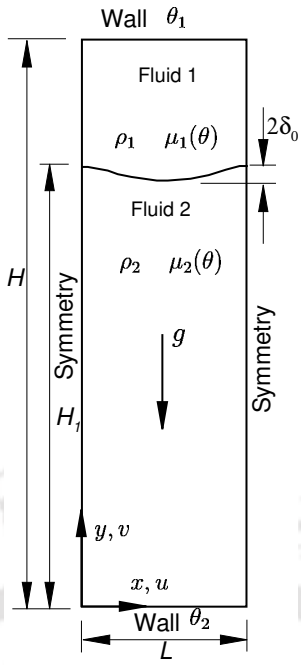

Figure 2.4: Schematic of boundary conditions for 2-D rectangular coordinate configuration.

Boundary conditions

At left and right side boundaries:

$$u = 0, \qquad \frac{\partial v}{\partial x} = 0, \qquad \frac{\partial \theta}{\partial x} = 0, \qquad \frac{\partial p}{\partial x} = 0, \qquad \frac{\partial \phi}{\partial x} = 0$$

At top wall:

$$u = 0, \qquad v = 0, \qquad \theta = \theta_1 \qquad \frac{\partial p}{\partial y} = 0, \qquad \frac{\partial \phi}{\partial y} = 0$$

At bottom wall:

$$u = 0, \qquad v = 0, \qquad \theta = \theta_2, \qquad \frac{\partial p}{\partial y} = 0, \qquad \frac{\partial \phi}{\partial y} = 0$$

2.2.3 Initial and boundary conditions for axisymmetric coordinate configuration

Computational domain varies from $r = 0$ to $L/2$ in the radial direction and $z = 0$ to H in the axial direction, as shown in Fig. 2.5. The top and bottom solid walls are imposed with no slip and no penetration conditions. Axisymmetric condition is applied along the vertical axis ($r = 0$). On the outer vertical boundary, the Neumann boundary condition is applied for axial velocity and temperature, and the Dirichlet boundary condition is applied for radial velocity ($r = L/2$). The top and bottom walls are maintained at different dimensionless isothermal temperatures based on the heating or cooling conditions. For example, for top heating and bottom cooling walls condition, the top and bottom walls are maintained isothermally at dimensionless temperature $\theta_1 = r_T$ and $\theta_2 = 0$, respectively. For bottom heating and top cooling walls condition, the top and bottom walls are maintained isothermally at dimensionless temperature $\theta_1 = 0$ and $\theta_2 = r_T$, respectively. Where, r_T is the temperature ratio defined equal to $(\tilde{T} - \tilde{T}_{\text{ref}})/\tilde{T}_{\text{ref}}$. In the present study, dimensionless height of domain (H) is chosen

equal to 4 and dimensionless width of domain (L) is chosen equal to 1. At initial state ($t = 0$), interface is located at dimensionless axial distance of $z = H_1 = 3$ from the bottom wall. At the initial state, the interface is perturbed according to $\delta = \delta_0 \cos(2\pi r/L)$. Here, δ_0 is defined as amplitude of the perturbation, which is taken equal to 0.01. Initially, dimensionless temperature is specified to vary linearly from the cold wall to the hot wall. The initial and boundary conditions are expressed in mathematical form as following.

Initial conditions

At $t = 0$, $\quad 0 \leq r \leq L$ and $0 \leq z \leq H$

$$u = 0, \qquad v = 0, \qquad \theta = \theta_2 + (\theta_1 - \theta_2)z/H$$

Boundary conditions

Outer radial boundary (at $r = L/2$):

$$u = 0, \qquad \frac{\partial v}{\partial r} = 0, \qquad \frac{\partial \theta}{\partial r} = 0, \qquad \frac{\partial f}{\partial r} = 0$$

At top wall:

$$u = 0, \qquad v = 0, \qquad \theta = \theta_1, \qquad \frac{\partial f}{\partial z} = 0$$

At bottom wall:

$$u = 0, \qquad v = 0, \qquad \theta = \theta_2, \qquad \frac{\partial f}{\partial z} = 0$$

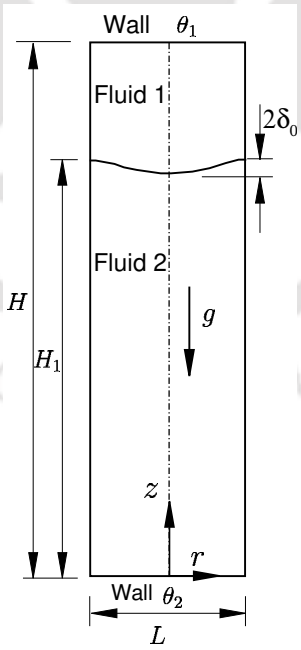

Figure 2.5: Schematic of boundary conditions for axisymmetric coordinate configuration.

2.2.4 Mathematical formulation for the developed code in 2-D rectangular coordinates

In the present work, some parts of the studies are simulated using a developed code for multiphsae flows in 2-D rectangular coordinates. The code is developed based on level set method. In level set method, an additional advection equation for level set function is solved. The flow is assumed to be incompressible. Density and thermal conductivity in the individual fluid layers are invariant of temperature variation. With the above assumptions, dimensional form of governing equations in 2-D rectangular coordinates can be written as following.

Continuity equation

$$\frac{\partial \tilde{u}}{\partial \tilde{x}} + \frac{\partial \tilde{v}}{\partial \tilde{y}} = 0 \tag{2.33}$$

$\tilde{x}$-momentum equation

$$\tilde{\rho}\left(\frac{\partial \tilde{u}}{\partial \tilde{t}} + \tilde{u}\frac{\partial \tilde{u}}{\partial \tilde{x}} + \tilde{v}\frac{\partial \tilde{u}}{\partial \tilde{y}}\right) = -\frac{\partial \tilde{p}}{\partial \tilde{x}} + \frac{\partial}{\partial \tilde{x}}\left(2\tilde{\mu}\frac{\partial \tilde{u}}{\partial \tilde{x}}\right) + \frac{\partial}{\partial \tilde{y}}\left[\tilde{\mu}\left(\frac{\partial \tilde{u}}{\partial \tilde{y}} + \frac{\partial \tilde{v}}{\partial \tilde{x}}\right)\right] + \tilde{\sigma}\tilde{\kappa}\frac{\partial H}{\partial \tilde{x}} \tag{2.34}$$

$\tilde{y}$-momentum equation

$$\tilde{\rho}\left(\frac{\partial \tilde{v}}{\partial \tilde{t}} + \tilde{u}\frac{\partial \tilde{v}}{\partial \tilde{x}} + \tilde{v}\frac{\partial \tilde{v}}{\partial \tilde{y}}\right) = -\frac{\partial \tilde{p}}{\partial \tilde{y}} + \frac{\partial}{\partial \tilde{x}}\left[\tilde{\mu}\left(\frac{\partial \tilde{u}}{\partial \tilde{y}} + \frac{\partial \tilde{v}}{\partial \tilde{x}}\right)\right] + \frac{\partial}{\partial \tilde{y}}\left(2\tilde{\mu}\frac{\partial \tilde{v}}{\partial \tilde{y}}\right) - \tilde{\rho}\,\tilde{g} + \tilde{\sigma}\tilde{\kappa}\frac{\partial H}{\partial \tilde{y}} \tag{2.35}$$

Energy equation

$$\tilde{\rho}\tilde{c}_p\left(\frac{\partial \tilde{T}}{\partial \tilde{t}} + \tilde{u}\frac{\partial \tilde{T}}{\partial \tilde{x}} + \tilde{v}\frac{\partial \tilde{T}}{\partial \tilde{y}}\right) = \frac{\partial}{\partial \tilde{x}}\left(\tilde{k}\frac{\partial \tilde{T}}{\partial \tilde{x}}\right) + \frac{\partial}{\partial \tilde{y}}\left(\tilde{k}\frac{\partial \tilde{T}}{\partial \tilde{y}}\right) \tag{2.36}$$

Level set equation

$$\frac{\partial \tilde{\phi}}{\partial \tilde{t}} + \tilde{u}\frac{\partial \tilde{\phi}}{\partial \tilde{x}} + \tilde{v}\frac{\partial \tilde{\phi}}{\partial \tilde{y}} = 0 \tag{2.37}$$

Expression for interface curvature ($\tilde{\kappa}$), which is used in the past studies [221–223], is given by

$$\tilde{\kappa}(\tilde{\phi}) = \tilde{\nabla}\cdot\mathbf{n} = \tilde{\nabla}\cdot\frac{\tilde{\nabla}\tilde{\phi}}{|\tilde{\nabla}\tilde{\phi}|} = \frac{\tilde{\phi}_{\tilde{x}\tilde{x}}\,\tilde{\phi}_{\tilde{y}}^2 - 2\tilde{\phi}_{\tilde{x}}\,\tilde{\phi}_{\tilde{y}}\,\tilde{\phi}_{\tilde{x}\tilde{y}} + \tilde{\phi}_{\tilde{y}\tilde{y}}\,\tilde{\phi}_{\tilde{x}}^2}{(\tilde{\phi}_{\tilde{x}}^2 + \tilde{\phi}_{\tilde{y}}^2)^{3/2}} \tag{2.38}$$

In level set method, fluid properties such as density, viscosity, thermal conductivity and heat capacity are calculated using the expressions

$$\begin{aligned}
\tilde{\rho} &= \tilde{\rho}_2 + (\tilde{\rho}_1 - \tilde{\rho}_2)\,H \\
\tilde{\mu} &= \tilde{\mu}_2 + (\tilde{\mu}_1 - \tilde{\mu}_2)\,H \\
\tilde{k} &= \tilde{k}_2 + (\tilde{k}_1 - \tilde{k}_2)\,H \\
\tilde{c_p} &= \tilde{c_{p_2}} + (\tilde{c_{p_1}} - \tilde{c_{p_2}})\,H
\end{aligned} \tag{2.39}$$

Here, H is the heaviside function and expressed as given by Eq. (2.11).

Here, the contour line corresponds to $\tilde{\phi} = 0$ represents interface between two fluids. The interface

is captured by integrating the level set equation for the given velocity field in the domain. In this method, level set function needs to be reinitialized after every time step. The reinitilization of level set is carried out by the the following equation. Since the level set function represents the distance from the interface, the value of $\tilde{\nabla}\phi$ should be 1 in the domain. However, after the integration of level set equation, the numerical value of $\tilde{\nabla}\tilde{\phi}$ may be different than one. To reset the values of $\tilde{\nabla}\phi$ to one, the level set function is reinitialized using the following equation.

$$\begin{aligned} &\frac{\partial\tilde{\phi}}{\partial\tilde{t}} = S(\tilde{\phi}_0)\left(1 - |\tilde{\nabla}\tilde{\phi}|\right)\tilde{u}_0 \\ &\tilde{\phi}(\tilde{x},0) = \tilde{\phi}_0(\tilde{x}) \end{aligned} \tag{2.40}$$

Where, $S(\tilde{\phi}_0)$ is sign function which is calculated as

$$\begin{aligned} S(\tilde{\phi}_0) &= 0 && \text{if} \quad |\tilde{\phi}| \leq 1.5d \\ &= \frac{\tilde{\phi}_0}{\sqrt{\tilde{\phi}_0^2 + d^2}} && \text{otherwise} \end{aligned} \tag{2.41}$$

Where, d is grid spacing. The governing equation are made dimensionless using the different reference parameters which are given in Eq. (2.14). The dimensionless form of governing equations are written as following.

Continuity equation

$$\frac{\partial u}{\partial x} + \frac{\partial v}{\partial y} = 0 \tag{2.42}$$

x-momentum equation

$$\begin{aligned} \rho\left(\frac{\partial u}{\partial t} + u\frac{\partial u}{\partial x} + v\frac{\partial u}{\partial y}\right) = &-\frac{\partial p}{\partial x} + \frac{1}{Re}\frac{\partial}{\partial x}\left(2\mu\frac{\partial u}{\partial x}\right) + \frac{1}{Re}\frac{\partial}{\partial y}\left[\mu\left(\frac{\partial u}{\partial y} + \frac{\partial v}{\partial x}\right)\right] \\ &+ \frac{1}{We}\kappa\frac{\partial H}{\partial x} \end{aligned} \tag{2.43}$$

y-momentum equation

$$\begin{aligned} \rho\left(\frac{\partial v}{\partial t} + u\frac{\partial v}{\partial x} + v\frac{\partial v}{\partial y}\right) = &-\frac{\partial p}{\partial y} + \frac{1}{Re}\frac{\partial}{\partial x}\left[\mu\left(\frac{\partial u}{\partial y} + \frac{\partial v}{\partial x}\right)\right] + \frac{1}{Re}\frac{\partial}{\partial y}\left(2\mu\frac{\partial v}{\partial y}\right) \\ &- \frac{1}{Fr}\rho + \frac{1}{We}\kappa\frac{\partial H}{\partial y} \end{aligned} \tag{2.44}$$

Energy equation

$$\rho c_p\left(\frac{\partial\theta}{\partial t} + u\frac{\partial\theta}{\partial x} + v\frac{\partial\theta}{\partial y}\right) = \frac{1}{Re\,Pr}\left[\frac{\partial}{\partial x}\left(k\frac{\partial\theta}{\partial x}\right) + \frac{\partial}{\partial y}\left(k\frac{\partial\theta}{\partial y}\right)\right] \tag{2.45}$$

Level set equation

$$\frac{\partial\phi}{\partial t} + u\frac{\partial\phi}{\partial x} + v\frac{\partial\phi}{\partial y} = 0 \tag{2.46}$$

Here, the dimensionless numbers such as Froude number (Fr), Prandtl number (Pr), Reynolds num-

ber (Re) and Weber number (We) are expressed as

$$Fr = \frac{\tilde{V}_{\text{ref}}^2}{\tilde{g}\,\tilde{L}_{\text{ref}}}, \quad Pr = \frac{\tilde{\mu}_{\text{ref}}\,\tilde{c}_{p_{\text{ref}}}}{\tilde{k}_{\text{ref}}}, \quad Re = \frac{\tilde{\rho}_{\text{ref}}\,\tilde{V}_{\text{ref}}\,\tilde{L}_{\text{ref}}}{\tilde{\mu}_{\text{ref}}}, \quad We = \frac{\tilde{\rho}_{\text{ref}}\,\tilde{g}\,\tilde{L}_{\text{ref}}^2}{\tilde{\sigma}_{\text{ref}}} \tag{2.47}$$

The curvature (κ) is non-dimensionlized as

$$\kappa = -\frac{1}{L}\nabla \cdot \frac{\nabla\phi}{|\nabla\phi|} = -\frac{1}{L}\frac{\phi_{xx}\,\phi_y^2 - 2\phi_x\,\phi_y\,\phi_{xy} + \phi_{yy}\,\phi_x^2}{(\phi_x^2 + \phi_y^2)^{3/2}} \tag{2.48}$$

Fluid properties in dimensionless form are calculated, as a function of heaviside function (H), using expressions as following.

$$\begin{aligned} \rho &= \rho_2 + (\rho_1 - \rho_2)\,H \\ \mu &= \mu_2 + (\mu_1 - \mu_2)\,H \\ k &= k_2 + (k_1 - k_2)\,H \\ c_p &= c_{p2} + (c_{p1} - c_{p2})\,H \end{aligned} \tag{2.49}$$

2.2.5 Numerical methodology for the developed code in 2-D rectangular coordinates

The code is developed based on Finite Volume Method (FVM). A staggered Marker And Cell (MAC) grid is used for discretization of governing equations. The scalar variables such as pressure (p), temperature (T), level set (ϕ) are located at cell centers. Velocities are forward staggered with respect to scalar control volumes. The continuity, momentum, energy and level set equations are discretized in their respective control volumes. In multiphase flow computations using level set method uniform grid is used in both the coordinate directions. In momentum and energy equations, the diffusion term is treated with central difference scheme. The convective terms are treated with fifth-order Weighted Essentially Non-Oscillatory (WENO) scheme. For energy and momentum equations, the temporal and diffusion terms are treated implicitly. In moving interface problems accurate prediction of interface is very important for overall accuracy of the simulations. Hence, to capture the interface, level set equation is integrated using third order time accurate Total Variation Diminishing (TVD) method. The convective terms in the level set equation are treated using WENO scheme [224–228]. Since in momentum and energy equations, temporal and diffusion terms are treated implicitly, the discretization equations result in a system of linear algebraic equations. The linear system is solved using Tri-Diagonal Matrix Algorithm (TDMA). TDMA sweeps are performed till a specified convergence criteria is reached. Details of the FVM can be found in books of Patankar [229] and Versteeg and Malalasekera [230].

Numerical treatments of governing equations

Temporal terms of governing equation are discretized with fully first order explicit scheme. The source terms are treated using fully implicit scheme, where convection terms are treated with fully

explicit scheme. The discretization carried out are expressed as following. Continuity equation

$$\nabla \cdot \mathbf{u}^{n+1} = 0 \tag{2.50}$$

Momentum equation

$$\frac{\mathbf{u}^{n+1} - \mathbf{u}^{*}}{\Delta t} = \frac{1}{\rho}\nabla p^{n+1} \tag{2.51}$$

Energy equation

$$\frac{T^{n+1} - T^{n}}{\Delta t} = -\mathbf{u}^{n+1} \cdot \nabla T^{n} + \frac{1}{\rho c_p}\nabla(k\,\nabla \cdot T^{n}) \tag{2.52}$$

Level set equation

$$\frac{\phi^{n+1} - \phi^{n}}{\Delta t} = -\mathbf{u}^{n+1} \cdot \nabla \phi^{n} \tag{2.53}$$

Projection method

In the developed code, flow field is solved using the projection method by decoupling of velocity and pressure fields [218, 219]. In projection method, flow field is solved in two steps. In the first step, the velocity is computed excluding the pressure gradient term. In the calculation of intermediate velocity all the terms are treated explicitly. In the second step, the velocity field is corrected using the pressure gradient term. The projection method followed can be expressed as following.

Step-1: Intermediate velocity, $\mathbf{u}^{*}$, calculation

$$\frac{\mathbf{u}^{*} - \mathbf{u}^{n}}{\Delta t} = -\mathbf{u}^{n} \cdot \mathbf{u}^{n} + \frac{1}{\rho}\left(\nabla \cdot \mu \nabla \mathbf{u}^{n} + \mathbf{S}_{\mathbf{u}}\right)$$

Step-2: Final velocity, $\mathbf{u}^{n+1}$, calculation

$$\frac{\mathbf{u}^{n+1} - \mathbf{u}^{*}}{\Delta t} = \frac{1}{\rho}\nabla p^{n+1}$$

Pressure equation

$$\nabla \cdot \frac{\nabla p^{n+1}}{\rho}(\Delta t) = \nabla \mathbf{u}^{*} \tag{2.54}$$

Here, superscript value of n and $(n+1)$ represents the n^{th} and $(n+1)^{\text{th}}$ time step quantities, respectively.

Integration of level set method

In level set method, the interface between two fluid layers is captured by solving the level set function (ϕ), given in Eq. (2.46). The equation is discretized on a uniform grid using the finite difference method which can be written in the following form

$$\left(\frac{\delta \phi}{\delta t}\right)_{i,j} + \left(u^{+}\phi_x^{-} + u^{-}\phi_x^{+} + v^{+}\phi_y^{-} + v^{-}\phi_y^{+}\right) = 0 \tag{2.55}$$

Here, $(\delta\phi/\delta t)$ represents discretized form of the temporal term of the level set function, and velocity gradient terms ($u^+, u^-, v^+,$ and v^-) which are associated with the convection terms are given as following.

$$\begin{aligned} u^+ &= \max(u_{i,j}, 0) \qquad & u^- &= \min(u_{i,j}, 0) \\ v^+ &= \max(v_{i,j}, 0) \qquad & v^- &= \min(v_{i,j}, 0) \end{aligned} \tag{2.56}$$

The gradient terms such as ϕ_x^+, ϕ_x^-, ϕ_y^+ and ϕ_y^- in the advection equation can be approximated using different schemes. Accuracy of calculations of level set function mainly depends on the schemes used to discretize these terms. Second order Essentially Non-Oscillatory (ENO 2) scheme and fifth order Weighted Essentially Non-Oscillatory (WENO 5) schemes are commonly used in the multiphase flow problems. In the present study, 'WENO 5' is used due to its higher accuracy and higher mass conservation properties. The expressions for ϕ_x^+, ϕ_x^-, ϕ_y^+ and ϕ_y^- terms for 'ENO 2' and 'WENO 5' are given as follows.

Essentially Non-Oscillatory (ENO) scheme

The expressions of the terms ϕ_x^+, ϕ_x^-, ϕ_y^+ and ϕ_y^- in second order ENO scheme, which are also used in past [1, 224, 226–228], are given by

$$\begin{aligned} \phi_x^- &= \frac{\phi_{i,j} - \phi_{i-1,j}}{\Delta x} + \frac{\Delta x}{2}\text{minmod}\left(\frac{\phi_{i+1,j} - 2\phi_{i,j} + \phi_{i-1,j}}{\Delta x^2}, \frac{\phi_{i,j} - 2\phi_{i-1,j} + \phi_{i-2,j}}{\Delta x^2}\right) \\ \phi_x^+ &= \frac{\phi_{i+1,j} - \phi_{i,j}}{\Delta x} - \frac{\Delta x}{2}\text{minmod}\left(\frac{\phi_{i+1,j} - 2\phi_{i,j} + \phi_{i-1,j}}{\Delta x^2}, \frac{\phi_{i+2,j} - 2\phi_{i+1,j} + \phi_{i,j}}{\Delta x^2}\right) \\ \phi_y^- &= \frac{\phi_{i,j} - \phi_{i,j-1}}{\Delta y} + \frac{\Delta y}{2}\text{minmod}\left(\frac{\phi_{i,j+1} - 2\phi_{i,j} + \phi_{i,j-1}}{\Delta y^2}, \frac{\phi_{i,j} - 2\phi_{i,j-1} + \phi_{i,j-2}}{\Delta y^2}\right) \\ \phi_y^+ &= \frac{\phi_{i,j+1} - \phi_{i,j}}{\Delta y} - \frac{\Delta y}{2}\text{minmod}\left(\frac{\phi_{i,j+1} - 2\phi_{i,j} + \phi_{i,j-1}}{\Delta y^2}, \frac{\phi_{i,j+2} - 2\phi_{i,j+1} + \phi_{i,j}}{\Delta y^2}\right) \end{aligned} \tag{2.57}$$

where, the *minmod* function is defined as

$$\text{minmod}\,(a, b) = \begin{cases} S(a)\min(|a|, |b|) & \text{if} \quad a \cdot b > 0 \\ 0, & \text{otherwise} \end{cases} \tag{2.58}$$

and $S(a)$ is defined as

$$S(a) = \begin{cases} -1 & \text{if } a < 0 \\ 1 & \text{if } a > 0 \\ 0 & \text{if } a = 0 \end{cases} \tag{2.59}$$

Weighted Essentially Non-Oscillatory (WENO) scheme

An improved form of ENO scheme is Weighted Essentially Non-Oscillatory (WENO) scheme, which was first developed by Liu et al. [225]. In WENO scheme, the terms $(\phi_x^+)_{i,j}$ and $(\phi_x^-)_{i,j}$ are approxi-

mated using Hamiltonian-Jacobi techniques.

$$v_1 = \frac{\phi_{i-2,j} - \phi_{i-3,j}}{\Delta x}$$
$$v_2 = \frac{\phi_{i-1,j} - \phi_{i-2,j}}{\Delta x}$$
$$v_3 = \frac{\phi_{i,j} - \phi_{i-1,j}}{\Delta x}$$
$$v_4 = \frac{\phi_{i+1,j} - \phi_{i,j}}{\Delta x}$$
$$v_5 = \frac{\phi_{i+2,j} - \phi_{i+1,j}}{\Delta x}$$

and

$$\phi_x^1 = \frac{1}{3}v_1 - \frac{7}{6}v_2 + \frac{11}{3}v_3$$
$$\phi_x^2 = -\frac{1}{6}v_2 + \frac{5}{6}v_3 + \frac{1}{3}v_4$$
$$\phi_x^3 = \frac{1}{3}v_3 + \frac{5}{6}v_4 - \frac{1}{6}v_5$$

convex combination of the above three approximation gives the fifth-order WENO approximation of (ϕ_x^-) which is given by

$$\phi_x^- = \omega_1\phi_x^1 + \omega_2\phi_x^2 + \omega_3\phi_x^3$$

Where, the weights are defined as $0 \leq \omega_k \leq 1$ and $\omega_1 + \omega_2 + \omega_3 = 1$. Optimal weights are calculated with the normalization of α_k and given by

$$\omega_1 = \frac{\alpha_1}{\alpha_1 + \alpha_2 + \alpha_3}$$
$$\omega_2 = \frac{\alpha_2}{\alpha_1 + \alpha_2 + \alpha_3}$$
$$\omega_3 = \frac{\alpha_3}{\alpha_1 + \alpha_2 + \alpha_3}$$

Here, α_1, α_2 and α_3 are defined as

$$\alpha_1 = \frac{0.1}{(S_1 + \epsilon)^2}$$
$$\alpha_2 = \frac{0.6}{(S_2 + \epsilon)^2}$$
$$\alpha_3 = \frac{0.3}{(S_3 + \epsilon)^2}$$

In the above, definition of the α_k, term ϵ is included with a very small value of 10^{-99} to avoid division by zero. The term ϵ is defined as

$$\epsilon = 10^{-6}\max(v_1^2, v_2^2, v_3^2, v_4^2, v_5^2) + 10^{-99}$$

The smoothness estimation is given by

$$S_1 = \frac{13}{12}(v_1 - 2v_2 + v_3)^2 + \frac{1}{4}(v_1 - 4v_2 + v_3)^2$$
$$S_2 = \frac{13}{12}(v_2 - 2v_3 + v_4)^2 + \frac{1}{4}(v_2 - v_4)^2$$
$$S_3 = \frac{13}{12}(v_3 - 2v_4 + v_5)^2 + \frac{1}{4}(3v_3 - 4v_4 + v_5)^2$$

In a similar way, using the subset of $\{\phi_{i-2,j}, \phi_{i-1,j}, \phi_{i,j}, \phi_{i+1,j}, \phi_{i+2,j}, \phi_{i+3,j}\}$, the term $(\phi_x^+)_{i,j}$ in advection equation is calculated. The other terms of the advection equation in $y-$direction, $(\phi_y^+)_{i,j}$ and $(\phi_y^-)_{i,j}$, are also approximated in a dimension-by-dimension manner using the Hamiltonian-Jacobi techniques [1, 224–228]. In the present code, the gradient terms in the level set reinitiaization equation are discretized using WENO scheme.

TVD scheme used for level set method

The level set function is integrated with time using third order Total Variation Diminishing (TVD) scheme [231, 232]. The TVD scheme is performed in three steps which can be written as following.
Step-1:

$$L(\phi^n) = \phi^1 = \phi^n + \Delta t\, L(\phi^n)$$

Step-2:

$$\phi^2 = \frac{3}{4}\phi^n + \frac{1}{4}L(\phi^1)$$
$$\phi^2 = \frac{3}{4}\phi^n + \frac{1}{4}\left[\phi^1 + \Delta t\, L(\phi^1)\right]$$

Step-3:

$$\phi^{n+1} = \frac{1}{3}\phi^n + \frac{2}{3}L(\phi^2)$$

2.2.6 Numerical methodology used in Basilisk software

In the present work, some parts of numerical study are simulated using an open source software Basilisk [233]. The software uses FVM method. In the software, two phase flows are handled using Volume of Fluid (VoF) method by finding volume of fraction (f) to capture the interface. Multigrid method is adopted in the software to accelerate the convergence rate of the solution. Dynamic adaptation of grid is performed based on the function of the velocity fields and the volume fraction. Domain in each direction is divided into 2^n number of cells, where n is defined as grid refinement level. The software provides a maximum of 12 levels of adaptive grid refinement near the interface, which makes the solution more accurate and efficient. Imbalanced forces which arise at the interface of two fluids due to presence of surface tension are efficiently minimized using continuum surface tension model [152, 221, 234]. The continuum approach eliminates the need of the interface reconstruction by enabling the accurate modeling with simplified calculations for surface tension forces. The numerical treatments used in the software are given in detail in past studies [7, 152, 220–222, 233, 234].

2.3 Validation of the developed code in 2-D rectangular coordinates to solve multiphase flows

In this section, validation of the developed code is carried out to verify its ability to solve the multiphase flow related problems. The validation is carried out for different benchmark multiphase flows such as rising bubble, splashing over liquid interface, dam breaking flows, etc. The validation of the code for numerical simulations of Rayleigh-Taylor instability, which is the topic of the present study, is also presented.

2.3.1 Mass conservation test

In level set method for computation of multiphase flows, an advection equation is solved for level set function. The equation consists of temporal and convection terms. Hence, the scheme used to solve the convection term plays a major role in the accuracy of interface capturing. The scheme should be accurate and preserve mass conservation. Hence, convection schemes should be tested for the mass conservation property of the schemes.

Mass conservation is tested using a well known trans-rotation of circle test. In the trans-rotation test, a circle of radius $0.2\,\pi$ is kept inside a square domain of size $\pi \times \pi$ such that the center of the circle is located at $0.5\,\pi, 0.2\,(\pi + 1)$. The initial shape of the circle is given by

$$[x - 0.5\,\pi]^2 + [y - 0.2\,(\pi + 1)]^2 = 0.4\,\pi^2 \tag{2.60}$$

The fluid in the domain is rotated in one direction for the time period of $0 \leq t \leq T/2$ using specific expressions for u and v velocities. Then, the fluid is rotated in the opposite direction for the time period of $T/2$ to T. The expressions for rotation of the fluid in clockwise and anti-clockwise directions are as following.

For the first half of time period (anti-clockwise rotation): $0 \leq t \leq T/2$

$$\begin{aligned} u(x, y, t) &= +\sin(x)\cos(y) \\ v(x, y, t) &= -\cos(x)\sin(y) \end{aligned} \tag{2.61}$$

For the second half of time period (clockwise rotation) : $T/2 < t \leq T$

$$\begin{aligned} u(x, y, t) &= -\sin(x)\cos(y) \\ v(x, y, t) &= +\cos(x)\sin(y) \end{aligned} \tag{2.62}$$

According to the above expressions for velocity for both the half time periods, the circle should resume back to its original shape after the time period of T. Shape of the circle, after the time period of $T = 8$, obtained using the present code is compared with that of initial shape of the circle given by analytical expression which is given by Eq. (2.60).

Fig. 2.6 shows the comparison of final shape of the circle obtained using the present code and

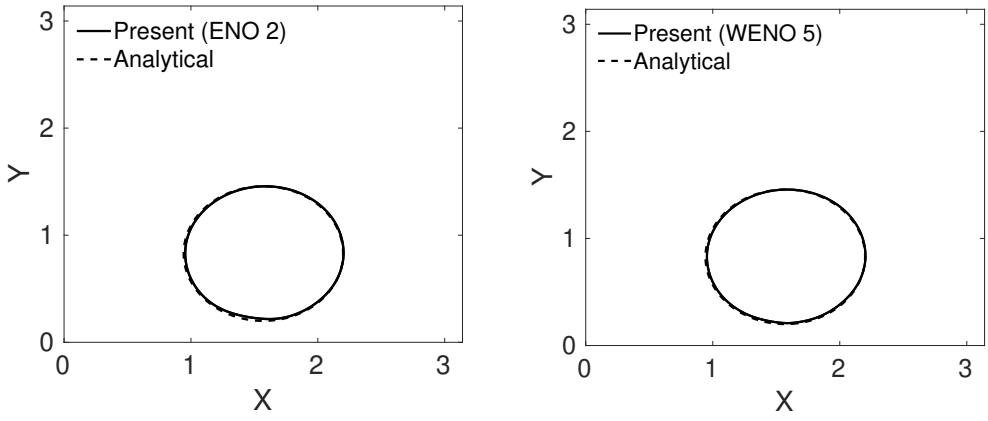

(1) ENO 2 (2) WENO 5

Figure 2.6: The comparison of final shape of the bubble after rotation obtained by numerical simulation using present code with that of initial shape of the bubble given by analytical expression for $T = 8$. The profiles are compared for both 'ENO 2' and 'WENO 5' schemes.

initial shape of the circle using the analytical expression. The results obtained from the present code show good agreement with the shape from the analytical expression.

The variation of normalized mass of circle with time is compared for 'ENO 2' and 'WENO 5' schemes in Fig. 2.7. The comparison of mass variation is carried out for total time rotation of $T = 8$ and $T = 24$. The normalized mass of the circle is the ratio of mass of the circle at any point of time normalized with the mass of the initial circular shape. Mass conservation test results show loss of mass less than 0.5% and 0.01% for 'ENO 2' and 'WENO 5' schemes, respectively. From this we can see that 'WENO 5' scheme performs much better than 'ENO 2' scheme for mass conservation.

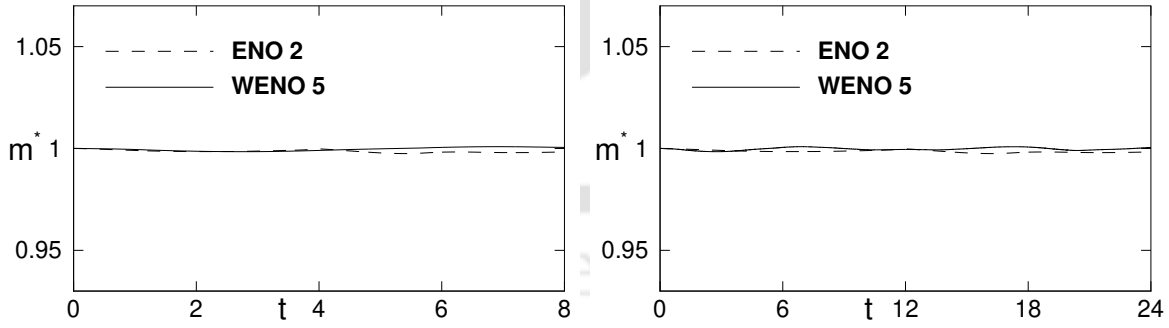

(1) $T = 8$ (2) $T = 24$

Figure 2.7: The comparison of the normalized mass of final shape with that of the initial mass of the circle obtained from both 'ENO 2' and 'WENO 5' schemes. The normalized mass is compared for a total time period of $T = 8$ and 24.

Salih and Moulic [1] presented, numerical solution of the trans-rotation problem. Fig. 2.8 and Fig. 2.9 show the comparison of the shape of the curve obtained using the present code with those presented by Salih and Moulic [1] for time periods of $T = 8$ and $T = 24$, respectively. The figures show the curve at time instances of $t = T/2$ and $t = T$. From the comparison, it is confirmed that the results obtained from the present code agree well with those of Salih and Moulic [1].

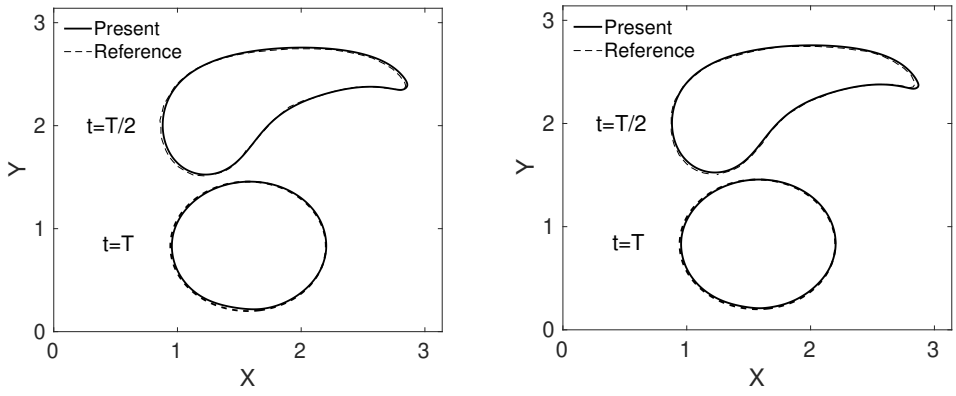

(1) ENO 2 (2) WENO 5

Figure 2.8: Comparison of present study results for 'ENO 2' and 'WENO 5' schemes with those of Salih and Moulic [1] for the case of time period of $T = 8$.

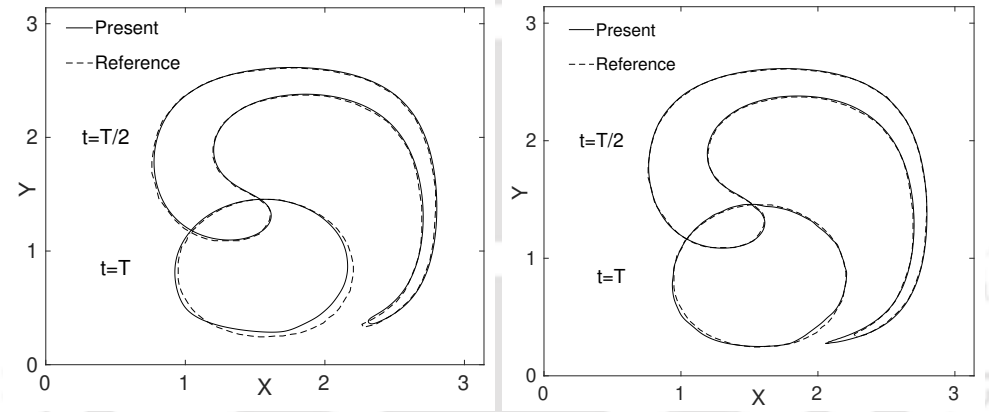

(1) ENO 2 (2) WENO 5

Figure 2.9: Comparison of present study results for 'ENO 2' and 'WENO 5' schemes with those of Salih and Moulic [1] for the case of time period of $T = 24$.

2.3.2 Spurious currents test

In multiphase flow computations, non-physical numerically generated spurious currents are present in the solutions. The simulation is carried out for an inviscid static drop surrounded by a different inviscid medium without gravity to examine the generated spurious currents in the present code. Physically, the drop does not move and velocities in the domain should be zero everywhere which would not vary with time. Velocity fields should remain zero in the cavity and Laplace pressure jump should be followed across the interface which would not vary with time. The numerical code should replicate this fact and give zero velocity everywhere throughout the domain with time integration of governing equation. However, numerical codes develop non-physical spurious currents with time integration.

Physical system of the test case consists of a square domain with dimension of 8×8. An inviscid drop of diameter of 4 is placed in the domain so that the center is located at $(4, 4)$. Free-slip boundary conditions are applied on all four boundaries of the domain. Density of the droplet fluid is set equal to 1 and density of the outer fluid is set equal to 0.1. The problem is simulated for a high surface tension case with dimensionless surface tension coefficient value of 73. Similar tests were performed

in different spurious test studies [221,235]. After the initial state, the governing equations, continuity, momentum and level set equations, are integrated with a time step size of Δt. The norm of spurious current values at the time instance of total time $t = \Delta t$ and $t = 50\,\Delta t$ are computed. The spurious currents are measured using the L_∞ norm of the velocity field which is given by

$$L_\infty = |\mathbf{u}|_{\max} = \max(||\mathbf{u}||) \tag{2.63}$$

Spurious current values (L_∞) generated using the present code are compared with those of presented by Francois et al. [235] for the same test case, in Table 2.1. The table shows that the spurious currents generated from the present code are much less than those of the reference study. Fig. 2.10 shows velocity vectors at total time of $t = \Delta t$ and $t = 50\,\Delta t$.

Table 2.1: Comparison of spurious currents (L_∞) for the static droplet in inviscid fluid.

Total time	Present	Reference [235]
Δt	6.9817×10^{-4}	0.00406
$50\Delta t$	0.02588	0.146

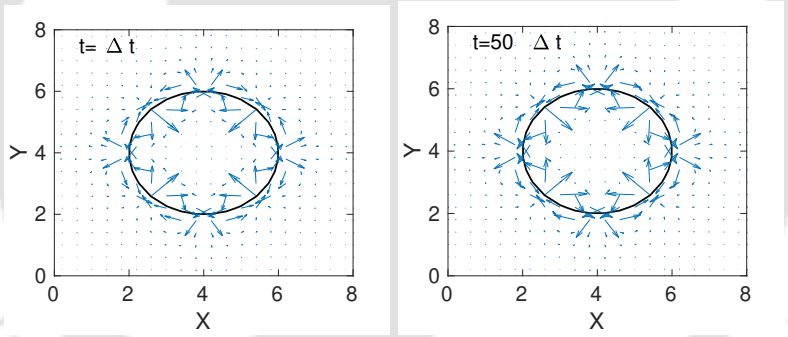

(1) $|\mathbf{u}|_{\max} = 6.9817 \times 10^{-4}$ (2) $|\mathbf{u}|_{\max} = 0.02588$

Figure 2.10: Velocity vectors and shape of the drop after $t = \Delta t$ and $t = 50\,\Delta t$ for the inviscid static drop in equilibrium.

2.3.3 Validation test-1: dam-break flow on dry ground

Physical system for dam break validation consists of a rectangular domain, as shown in Fig. 2.11. Top and bottom boundaries are solid walls. Left and right vertical side boundaries represent symmetry planes. At the initial state, a rectangular water column of height h and width $L/2$ is placed in the domain, which is represented as 'Fluid 1'. The remaining part of the domain is occupied with air, which is represented as 'Fluid 2'.

The width (L) and height (H) of the domain are set to 1.2 m and 0.14 m, respectively. Height of the water column (h) is set to 0.1 m. Densities of water and air are set to 1000 kg/m^3 and 1.1768 kg/m^3, respectively. Viscosities of water and air are set to 10^{-3} Pa·s and 10^{-5} Pa·s, respectively. The

gravitational constant (g) is set to 9.81 m/s^2. Present work of dam-break analysis on a dry ground is validated with the results of Vincent and Caltagirone [2].

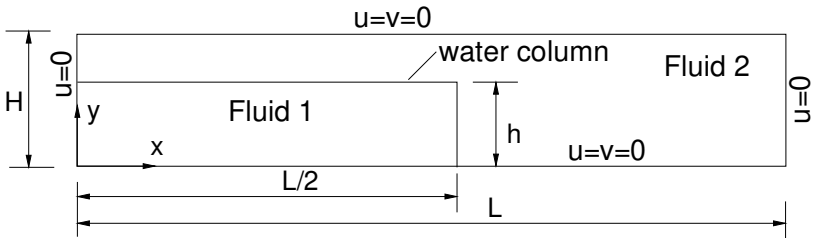

Figure 2.11: Schematic of the physical system of dam break flow.

2.3.3.1 Initial and boundary conditions

No slip and no penetration conditions are imposed on top and bottom walls. The left and right vertical boundaries are specified with symmetry conditions. The applied boundary conditions in mathematical form are expressed as

Initial conditions

At $t = 0$, $\quad 0 \leq x \leq L$ and $0 \leq y \leq H$

$$u = 0, \qquad v = 0$$

Boundary conditions

At left and right boundaries:

$$u = 0, \qquad \frac{\partial v}{\partial x} = 0, \qquad \frac{\partial p}{\partial x} = 0, \qquad \frac{\partial \phi}{\partial x} = 0$$

At top and bottom walls:

$$u = 0, \qquad v = 0, \qquad \frac{\partial p}{\partial y} = 0, \qquad \frac{\partial \phi}{\partial y} = 0$$

The instantaneous interface profiles obtained from the present code are compared with those presented by Vincent and Caltagirone [2], in Fig. 2.12. The interface profiles predicted with the present code show good agreement with those of the reference.

2.3.4 Validation test-2: droplet splash over water surface

Physical system consists of a rectangular domain with a thin water layer at the bottom, as shown in Fig. 2.13. Bottom and top boundaries of the domain are solid walls. Side vertical boundaries of the domain are symmetry planes. At initial state, a droplet of water of diameter D is centrally placed just over the thin water layer and released. The shape of the droplet and water layer at the bottom vary

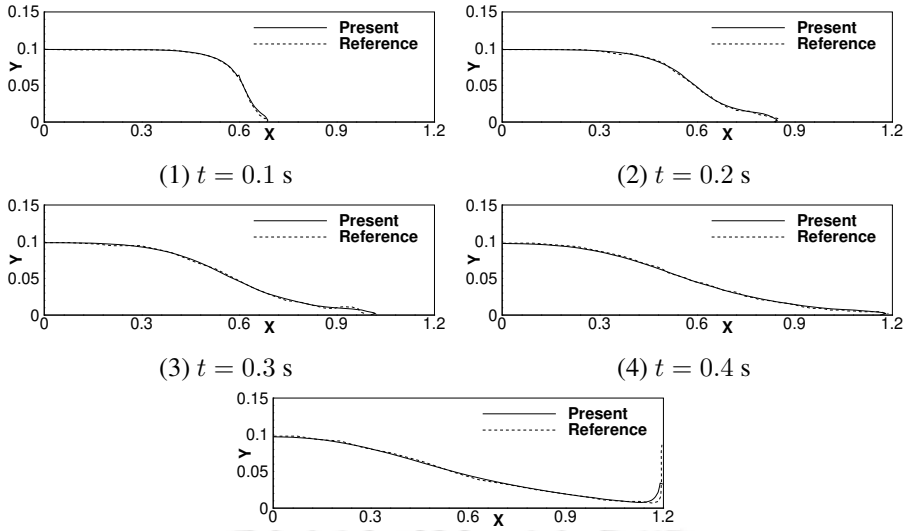

(1) $t = 0.1$ s (2) $t = 0.2$ s

(3) $t = 0.3$ s (4) $t = 0.4$ s

(5) $t = 0.5$ s

Figure 2.12: Validation of dam-break problem: the comparison of present code interface profiles at different time instances with those of Vincent and Caltagirone [2].

with time as the droplet splashes over the water surface. Instantaneous interface profiles are obtained using the present code and compared with those presented in Patel and Natarajan [3].

In the computation, dimensionless height and width of the domain are set to H =2 and L = 6, respectively. The dimensionless diameter of the bubble (D) is taken equal to 1. Dimensionless thickness of water layer (h) is taken equal to 0.2. Water to air density ratio and viscosity ratio are taken equal to 815 and 55, respectively. Dimensionless numbers such as Reynolds number (Re) and Weber number (We) are taken equal to 66 and 0.126, respectively. At initial state, water droplet is located just above the water surface. Center of the water droplet is at (3,0.7).

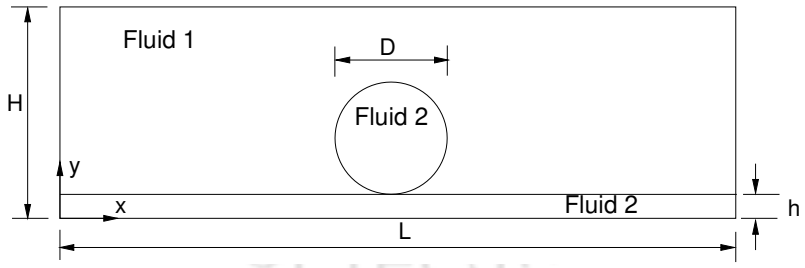

Figure 2.13: Physical system of splash over liquid surface.

2.3.4.1 Initial and boundary conditions

Top and bottom wall boundaries are specified with no slip and no penetration conditions. Side vertical boundaries are specified with symmetry conditions. The initial and boundary conditions are expressed in mathematical form as following.

Initial conditions

At $t = 0, \quad 0 \leq x \leq L \quad$ and $\quad 0 \leq y \leq H$

$$u = 0, \qquad v = 0$$

Boundary conditions

At left and right boundaries :

$$u = 0, \qquad \frac{\partial v}{\partial x} = 0, \qquad \frac{\partial p}{\partial x} = 0, \qquad \frac{\partial \phi}{\partial x} = 0$$

At top and bottom walls:

$$u = 0, \qquad v = 0, \qquad \frac{\partial p}{\partial y} = 0, \qquad \frac{\partial \phi}{\partial y} = 0$$

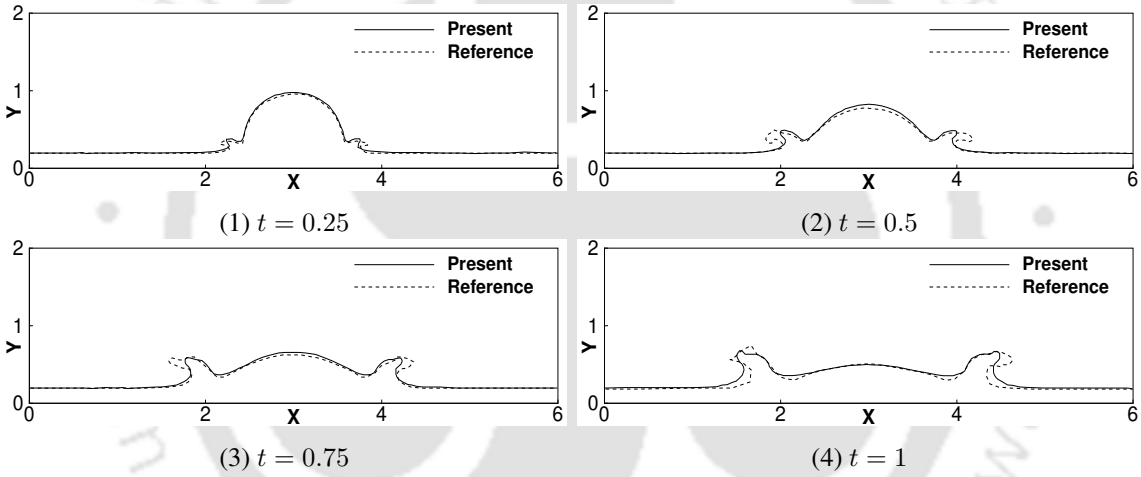

Figure 2.14: Comparison of instantaneous interface profiles of droplet splashing on a thin liquid layer of water obtained in the present study with those of Patel and Natarajan [3].

Instantaneous interface profiles obtained using the present code are compared with those presented in Patel and Natarajan [3], as shown in Fig. 2.14. Present code results show good agreement with those of reference results [3].

2.3.5 Validation test-3: dynamics of bubble rise (without surface tension)

Physical system consists of a square cavity filled with fluid containing a rising bubble, as shown in Fig. 2.15. The top and bottom boundaries are walls, and the vertical side boundaries are symmetry planes. A bubble (Fluid 2) of diameter D is placed on the bottom wall and the remaining domain is filled with surrounding fluid (Fluid 1). The density of bubble is less than that of surrounding fluid, and hence, the bubble starts rising. While rising in the domain upwards, the shape of the bubble changes with time.

Height and width of the domain, both are set equal to 1 m. Diameter of the bubble is taken equal

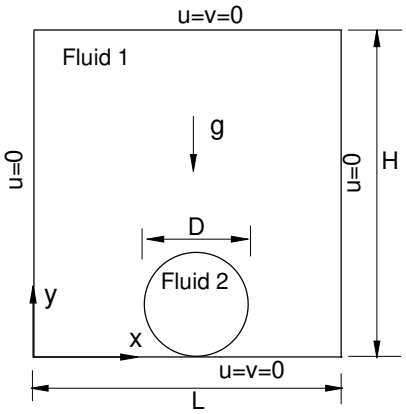

Figure 2.15: Schematic of rising bubble in surrounding fluid medium.

to $D = 0.314$ m. Density and viscosity of the bubble fluid are taken equal to 1 kg/m^3 and 10^{-3} Pa·s, respectively. Density and viscosity of the surrounding fluid are taken equal to 5 kg/m^3 and 10^{-3} Pa·s, respectively. Surface tension between bubble and surrounding fluid is set to zero. For validation, the results obtained from the code are compared with those presented in Sussman et al. [4].

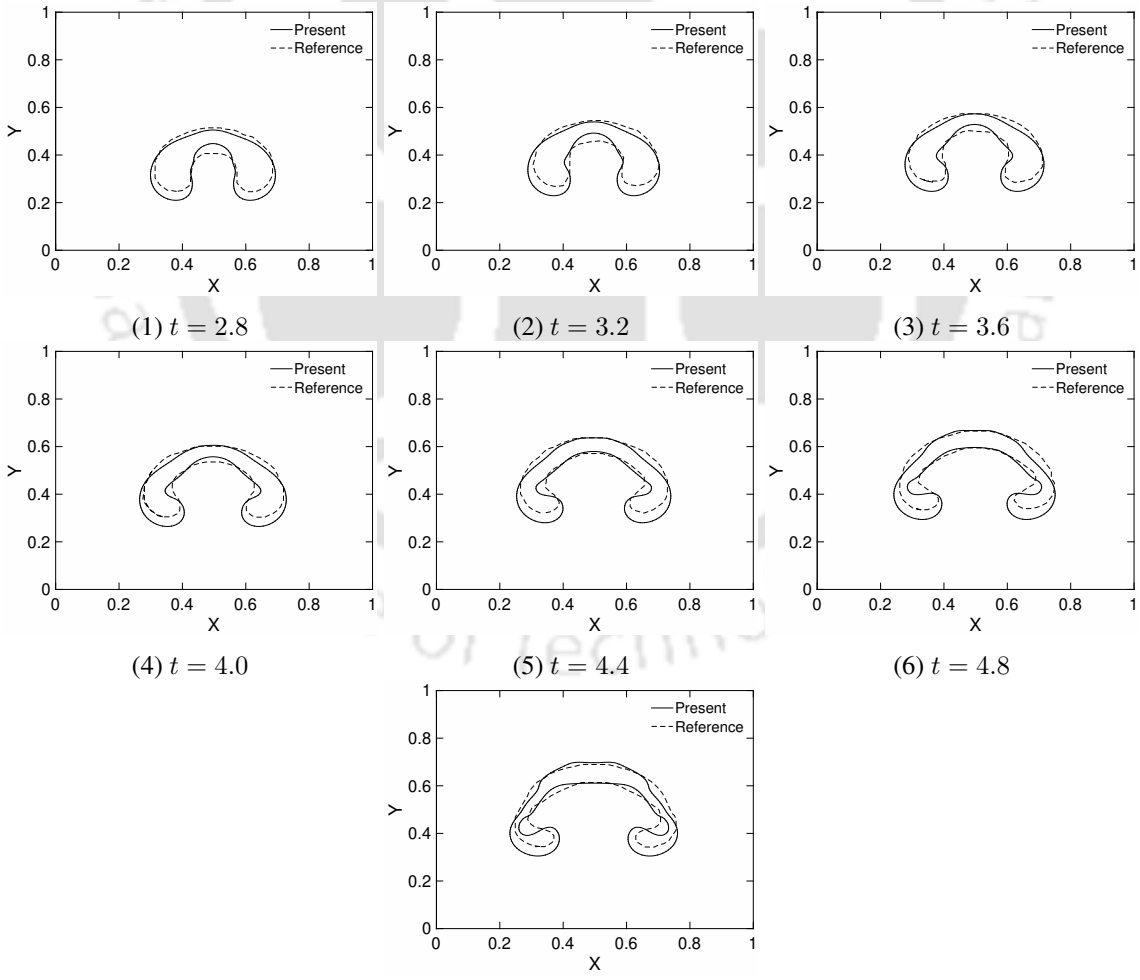

(1) $t = 2.8$ (2) $t = 3.2$ (3) $t = 3.6$

(4) $t = 4.0$ (5) $t = 4.4$ (6) $t = 4.8$

(7) $t = 5.2$

Figure 2.16: Validation for rising bubble: comparison of instantaneous interface profiles of present study results with those of Sussman et al. [4].

2.3.5.1 Initial and boundary conditions

No slip and no penetration conditions are imposed on top and bottom walls, whereas left and right side boundaries are specified with symmetry condition. The applied initial and boundary conditions, in mathematical form, are expressed as following.

Initial conditions

At $t = 0, \quad 0 \leq x \leq L \quad$ and $0 \leq y \leq H$

$$u = 0, \qquad v = 0$$

Boundary conditions

At left and right bondaries:

$$u = 0, \qquad \frac{\partial v}{\partial x} = 0, \qquad \frac{\partial p}{\partial x} = 0, \qquad \frac{\partial \phi}{\partial x} = 0$$

At top and bottom walls:

$$u = 0, \qquad v = 0, \qquad \frac{\partial p}{\partial y} = 0, \qquad \frac{\partial \phi}{\partial y} = 0$$

The interface profiles obtained at various time instances using the present code are compared with those presented by Sussman et al. [4], in Fig. 2.16. The figure shows that the present study results match well with the reference study results.

2.3.6 Validation test-4: dynamics of bubble rise (with surface tension)

Physical system consists of a rectangular domain, as shown in Fig. 2.17. Top and bottom boundaries are solid walls and side vertical boundaries are symmetric. A bubble of lower density fluid is placed with the center located at $(0.5, 0.5)$ in the domain. Since the density of the bubble (Fluid 2) is less than surrounding fluid (Fluid 1), the bubble rises in the upward direction and its shape varies with time. The numerical values of different dimensions are shown in Fig. 2.17.

The present bubble rise study is carried out for two cases, case-1 and case-2. Each case is taken to be of different combinations of numerical values for properties. The numerical values set, for bubble rise validation with surface tension, are same as presented by Hysing et al. [5]. The initial and applied boundary conditions are set to be same, as given in subsection 2.3.5.1.

- **Case-1:** Fluid properties are, $\tilde{\rho}_1 = 1000$ kg/m^3, $\tilde{\rho}_2 = 100$ kg/m^3, $\tilde{\mu}_1 = 10$ Pa·s, $\tilde{\mu}_2 = 1$ Pa·s, surface tension $\tilde{\sigma} = 24.5$ N/m.
- **Case-2:** Fluid properties are, $\tilde{\rho}_1 = 1000$ kg/m^3, $\tilde{\rho}_2 = 1$ kg/m^3, $\tilde{\mu}_1$=10 Pa·s, $\tilde{\mu}_2 = 0.1$ Pa·s, surface tension $\tilde{\sigma} = 1.96$ N/m.

The shapes of the bubble obtained using the present code are compared with those presented by

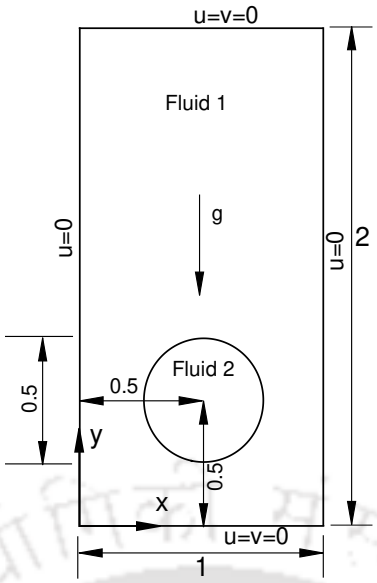

Figure 2.17: Physical system for bubble rise dynamics.

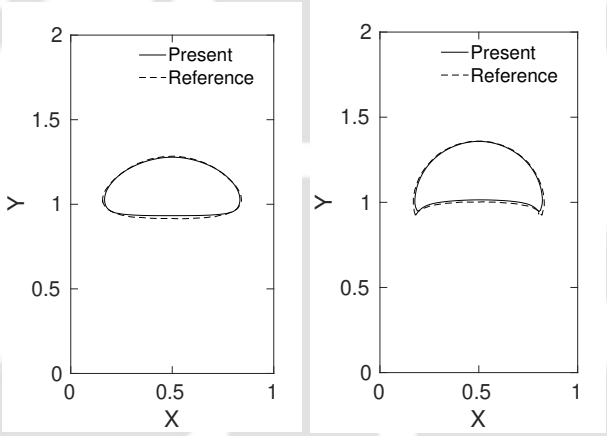

(1) case-1 (2) case-2

Figure 2.18: Comparison of instantaneous profiles of present result with those of Hysing et al. [5] for both the cases of bubble rise at dimensionless time $t = 3$.

Hysing et al. [5], in Fig. 2.18. The present simulation results show good match with the benchmark results.

2.3.7 Validation for Rayleigh-Taylor instability

The developed code is validated for Rayleigh-Taylor instability. The validations are carried out using the solution of the instability presented in various past studies. The physical configurations used in various studies are similar. However, values of fluid properties and geometric parameters are different in different studies. Fig. 2.19 shows schematic of Rayleigh-Taylor instability. A heavier fluid layer (Fluid 1) is placed over a lighter fluid layer (Fluid 2). Here, H and L represent height and width of the domain, respectively. H_1 represents the location of interface from the bottom wall. At the initial

state, the interface is perturbed using a cosine function which is expressed as

$$\delta = \delta_0 \cos\left(\frac{2\pi x}{L}\right); \qquad 0 \leq x \leq L \tag{2.64}$$

Here, δ_0 is the amplitude of the initial perturbation.

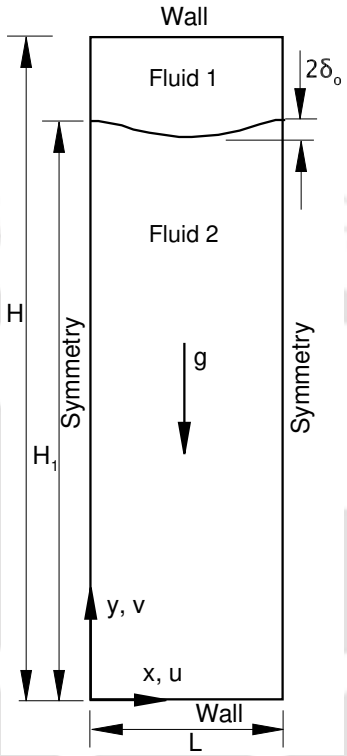

Figure 2.19: Schematic of Rayleigh-Taylor instability.

2.3.7.1 Initial and boundary conditions

No slip and no penetration conditions are imposed on top and bottom boundaries of the domain. Symmetry condition is implied on left and right side boundaries of the domain. The applied initial and boundary conditions in mathematical form are given by

Initial conditions

At $t = 0$, $\quad 0 \leq x \leq L$ and $0 \leq y \leq H$

$$u = 0, \qquad v = 0$$

Boundary conditions

At left and right boundaries:

$$u = 0, \qquad \frac{\partial v}{\partial x} = 0, \qquad \frac{\partial p}{\partial x} = 0, \qquad \frac{\partial \phi}{\partial x} = 0$$

At top and bottom walls:

$$u = 0, \qquad v = 0, \qquad \frac{\partial p}{\partial y} = 0, \qquad \frac{\partial \phi}{\partial y} = 0$$

2.3.7.2 Rayleigh-Taylor instability-1

The developed code is validated against Rayleigh-Taylor instability study carried out by Strubelj and Tiselj [6]. Simulations are performed to study the instability in a rectangular domain, as given in Fig. 2.19. The boundaries at the top and bottom locations are set to be walls, while the boundaries at the right and left locations are set to be symmetric. A heavier fluid layer (Fluid 1) is superposed over a lighter fluid layer (Fluid 2). The heavier fluid density and viscosity are taken equal to 3 kg/m^3 and 0.03 Pa·s, respectively. The lighter fluid density and viscosity are taken equal to 1 kg/m^3 and 0.01 Pa·s. Height (H) and width (L) of the domain are taken equal 5 m and 1 m, respectively. At initial state, interface between both the fluid layers is located at $H_1 = 4.5$ m from the bottom wall. At the initial state ($t = 0$), the interface is perturbed by a cosine wave function, according to Eq. (2.64), with an amplitude value of $\delta_0 = 10^{-3}$ m. The boundary conditions are as mentioned in subsection 2.3.7.1.

For the validation, the instantaneous interface profiles obtained from the present code are compared with those presented in Strubelj and Tiselj [6]. From Fig. 2.20, it is evident that the present study results show good match with the reference study results.

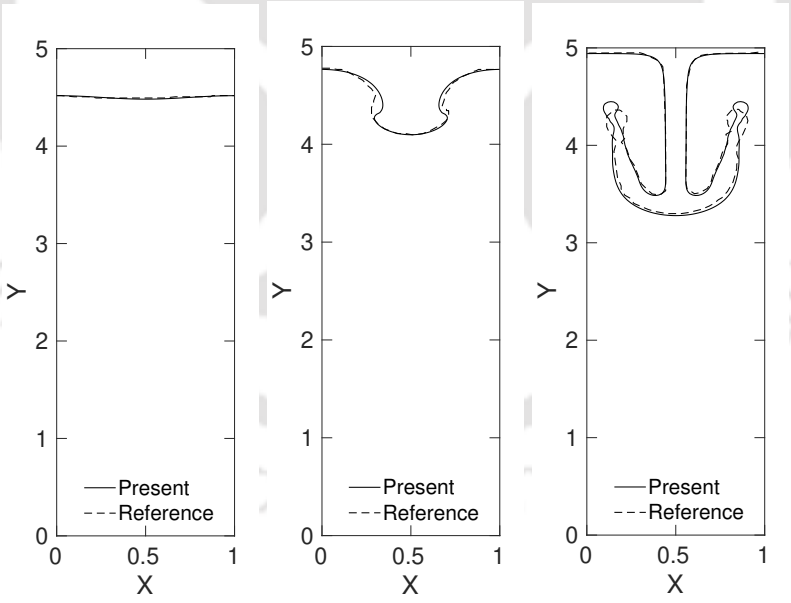

(1) $t = 1/8$ (2) $t = 2/8$ (3) $t = 3/8$

Figure 2.20: Comparison of present results with Strubelj and Tiselj [6] for Rayleigh-Taylor instability problem at various dimensionless time instances $t = 1/8$, 2/8, 3/8 .

2.3.7.3 Rayleigh-Taylor instability-2

Present code is validated for Rayleigh-Taylor instability in a rectangular domain and by comparing the obtained results with those reported in Popinet and Zaleski [7]. The rectangular domain used to study

the instability is shown in Fig. 2.19. Upper and lower portions of the domain are occupied with 'Fluid 1' and 'Fluid 2', respectively. Both the fluid layers are sandwiched between two parallel solid walls. Vertical side planes are specified with symmetry condition. The upper and lower fluid densities are taken equal to 1.225 and 0.1694 kg/m^3, respectively. The upper and lower fluid viscosities are taken to be of same value, equal to 0.00313 Pa·s. The height and width of the domain are set equal to $H = 4$ m and $L = 1$ m, respectively. Interface between 'Fluid 1' and 'Fluid 2' layers is located at vertical distance of $H_1 = 2$ m from the bottom wall. The interface between two fluid layers is perturbed according to Eq. (2.64), and amplitude of the perturbation is taken equal to $\delta_0 = 0.05$ m. The boundary conditions are set same as given in subsection 2.3.7.1.

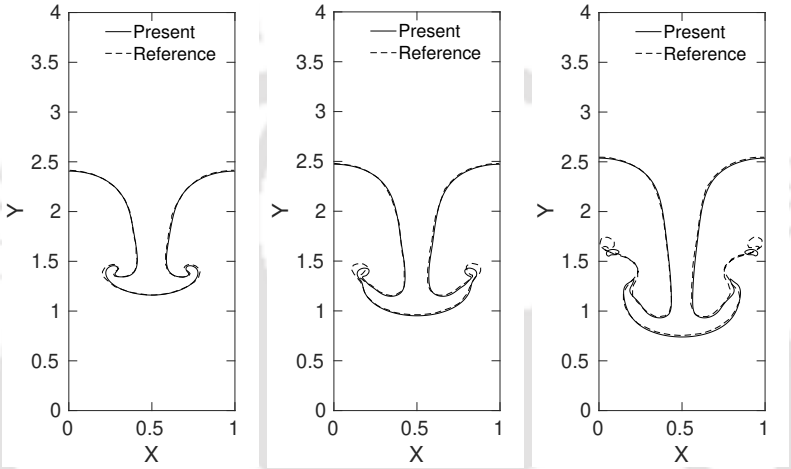

(1) $\tilde{t} = 0.7$ s (2) $\tilde{t} = 0.8$ s (3) $\tilde{t} = 0.9$ s

Figure 2.21: Comparison of present results with Popinet and Zaleski [7] for Rayleigh-Taylor instability at given time instances.

Interface profiles obtained from the present code are validated with those presented in Popinet and Zaleski [7], as shown in Fig. 2.21. The present study results show good match with those of the reference study results.

2.3.7.4 Rayleigh-Taylor instability-3

Fig. 2.19 represents a rectangular domain of two fluid layers bounded between two parallel solid walls which are placed at top and bottom locations. Right and left vertical side planes are of symmetry nature. Here, 'Fluid 1', which is a heavier fluid, is superposed over 'Fluid 2', a lighter fluid, in the domain. The 'Fluid 1' and 'Fluid 2' represent the air and helium, respectively. The developed code is validated for Rayleigh-Taylor instability, in the above domain, by comparing the present results with those presented by Puckett et al. [8].

Density and viscosity of air are taken equal to 1.225 kg/m^3 and 1.77625×10^{-5} Pa·s, respectively. Density and viscosity of helium are taken equal to 0.1694 kg/m^3 and 1.941×10^{-5} Pa·s, respectively. Height and width of the domain are taken equal to $H = 0.04$ m and $L = 0.01$ m, respectively. The interface is located at $H_1 = 0.02$ m from the bottom wall. At the initial state, the interface is perturbed with a perturbation of cosine wave form with an amplitude of $\delta_0 = 0.0005$ m, according to

Eq. (2.64). The initial and boundary conditions for the present test case are taken same as given in subsection 2.3.7.1. Present simulation results are validated by comparing the instantaneous interface

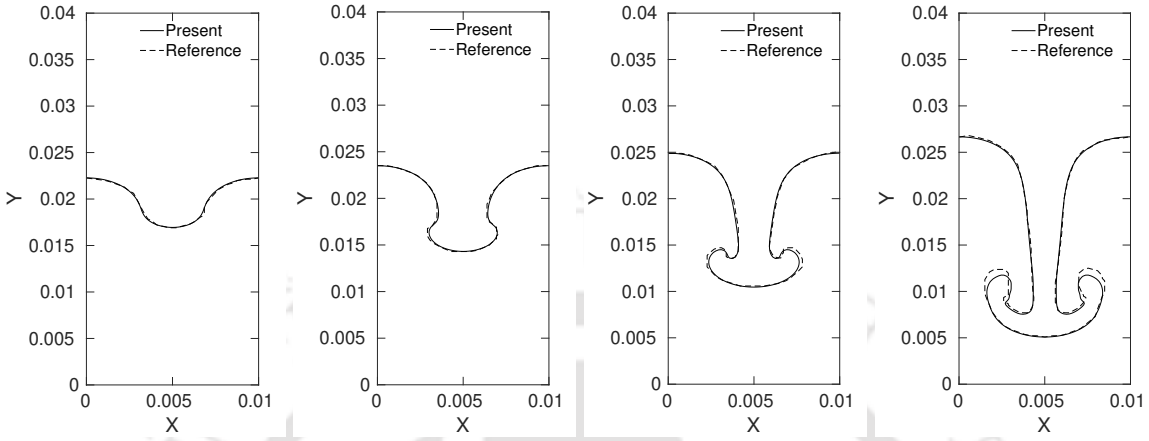

(1) $\tilde{t} = 0.047$ s (2) $\tilde{t} = 0.066$ s (3) $\tilde{t} = 0.088$ s (4) $\tilde{t} = 0.118$ s

Figure 2.22: Comparison of present results with Puckett et al. [8] for Rayleigh-Taylor instability at different time instances.

profiles obtained using the present code with those of Puckett et al. [8], in Fig. 2.22. From the figure, it is concluded that present study results show good match with reference study results.

2.3.7.5 Rayleigh-Taylor instability-4

In this test case, present simulation results for the instability are validated for with and without surface tension case with those of Salih and Maullik [9]. Physical system consists of a rectangular domain filled with a heavier fluid layer (Fluid 1) over a lighter fluid layer (Fluid 2), as shown in Fig. 2.19. Top and bottom boundaries are considered to be solid walls. Vertical side boundaries are considered to be symmetric.

The ratio of the heavier to lighter fluid density and viscosity ratio are taken equal to 5 and 10, respectively. The dimensionless height and width of domain are set to $H = 3$ and $L = 1$, respectively. Atwood number A is defined by $(\rho_1 - \rho_2)/(\rho_1 + \rho_2)$. Reynolds number ($Re$) and Weber number ($We$) are defined based on the heavier fluid properties. Width of the domain is taken as reference length. The values of Re and A are set equal to 156.6 and 0.6667, respectively. At initial state, the interface is set to be located at dimensionless height of $H_1 = 1.83$ from the bottom wall. The amplitude of the interface perturbation in Eq. (2.64) is set to $\delta_0 = 0.03$. Initial and boundary conditions are set same as mentioned in subsection 2.3.7.1.

The Weber number represents a reciprocal of surface tension. Hence, simulations are carried out for different Weber numbers and the present code results are compared with those of Salih and Maullik [9]. For zero surface tension case Weber number (We) value is set to ∞. Whereas for non zero surface tension case, simulations are carried out for three different Weber number values We =40, 80 and 144.

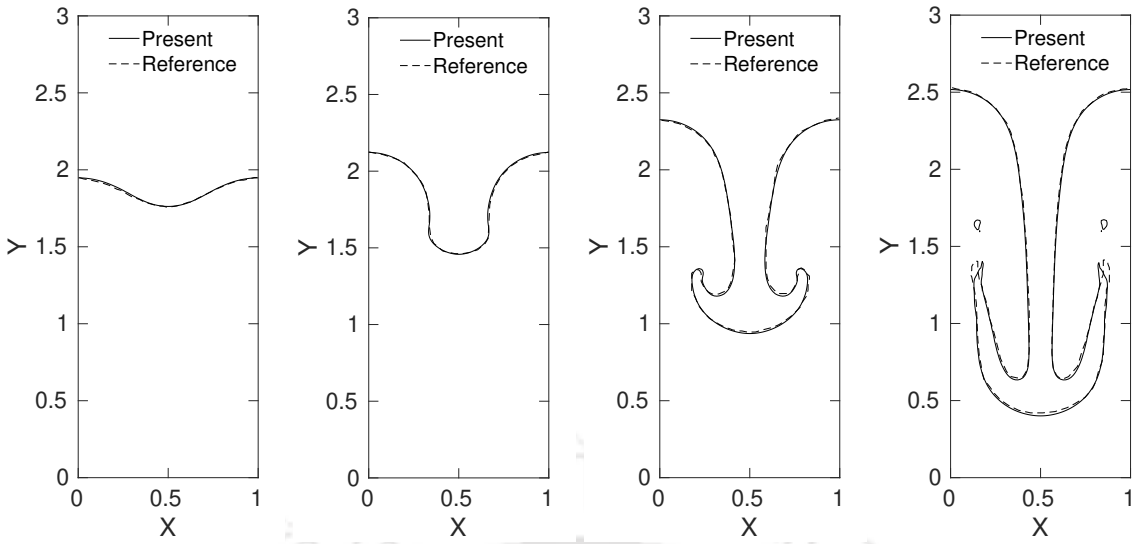

(1) $t = 1$ (2) $t = 2$ (3) $t = 3$ (4) $t = 4$

Figure 2.23: Comparison of present study results at various dimensionless time instances with Salih and Maullik [9] for Rayleigh-Taylor instability for Weber number value $We = \infty$.

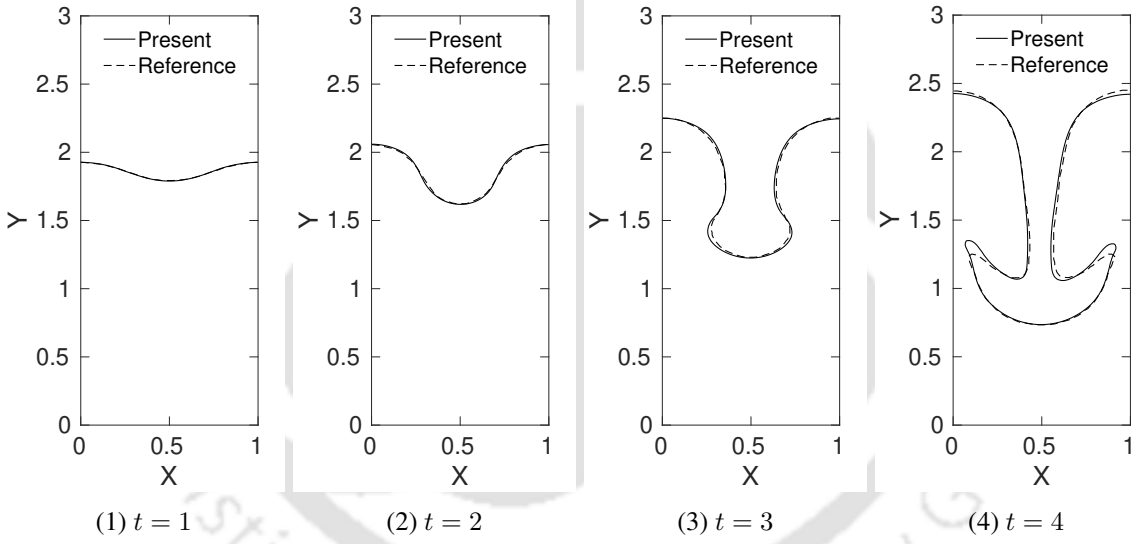

(1) $t = 1$ (2) $t = 2$ (3) $t = 3$ (4) $t = 4$

Figure 2.24: Comparison of present study results at various dimensionless time instances with Salih and Maullik [9] for Rayleigh-Taylor instability for Weber number value $We = 144$.

The instantaneous interface profiles obtained from the present code are compared with those of Salih and Maullik [9]. Figs. 2.23-2.25, show comparison of the present study results with the reference study results for different Weber number values. The comparison shows that the present code results agree well with those of the reference results.

2.3.8 Validation of the developed code using the results obtained from Basilisk software

Before performing simulations of Rayleigh-Taylor instability for the present thesis, the present code is validated against the results of the open source code. For the validation, the present problem of

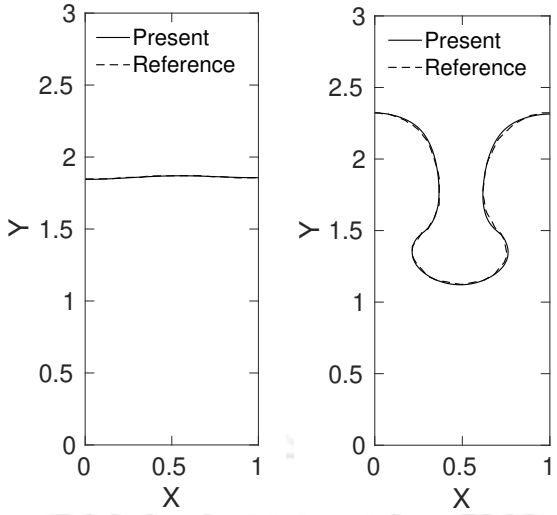

(1) $We = 40$ (2) $We = 80$

Figure 2.25: Comparison of present study results at dimensionless time $t = 4$ with those of reference [9] study results for Rayleigh-Taylor instability for various We values.

the thesis is solved for a set of parameters. The results are obtained with the present code and the open source software, and compared. The schematic of physical system, initial and boundary conditions of Rayleigh-Taylor instability of the present work are presented in sections 2.2.2. The validation simulations are carried out for dimensionless width of $L = 1$, dimensionless height of $H = 4$ and dimensionless distance of the interface from the bottom $H_1 = 3$. Dimensionless amplitude of initial perturbation is set to $\delta_0 = 0.01$. The validation is carried out for the instability with constant viscosity and viscosity varying temperature configurations. Simulations are carried out for density ratio $\rho_r = 2$, viscosity ratio $m = 2$, heat capacity ratio $c_{p_r} = 2$, thermal conductivity ratio $k_r = 2$, temperature ratio $r_T = 3$, Reynolds number $Re = 50$ and Weber number $We = 150$ and Prandtl number $Pr = 1$. For both cases, simulations are carried out by solving governing equation along with equation for temperature. For constant viscosity fluid layers, the temperatures of upper and lower walls are set equal to zero. In the simulations, viscosities of both the fluid layers are taken to be varying exponentially with temperature according to Eq. (2.25). For temperature varying viscosity fluid layers, the top and bottom walls are isothermally maintained at constant dimensionless temperatures of $\theta_1 = r_T$ and $\theta_2 = 0$, respectively. Here, r_T is set equal to 3.

Rayleigh-Taylor instability in two fluid layers with constant viscosity

With the above mentioned baseline parameters, the results obtained from the present code are compared with results obtained with Basilisk, in Fig. 2.26. Time variation of spike front and bubble tip locations is also compared in Fig. 2.27. The present code results show good agreement with those of obtained using Basilisk software.

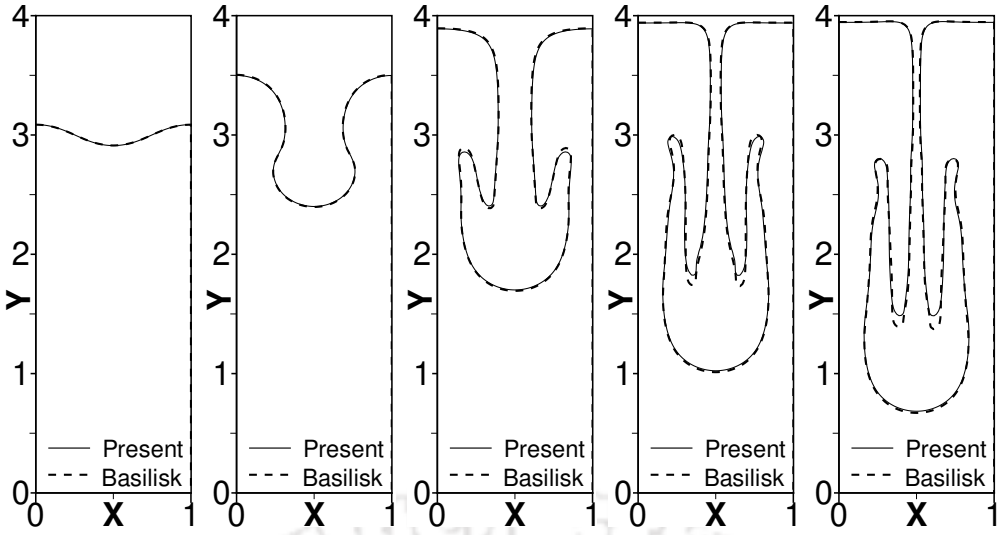

(1) $t = 4$ (2) $t = 8$ (3) $t = 12$ (4) $t = 16$ (5) $t = 18$

Figure 2.26: Comparison of instantaneous interface profiles of the instability obtained using the present code with those of Basilisk software for constant viscosity fluid layers (rest of the parameters are: $\rho_r = 2$, $m = 2$, $k_r = 2$, $c_{p_r} = 2$, $Re = 50$, $We = 150$, $Pr = 1$ and $r_T = 0$).

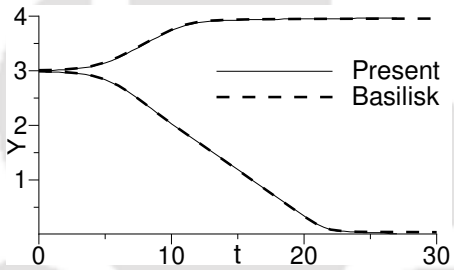

Figure 2.27: Comparison of time variation of spike front and bubble tip locations for constant viscosity fluid layers (rest of the parameters are: $\rho_r = 2$, $m = 5$, $k_r = 2$, $c_{p_r} = 2$, $Fr = 1$, $Re = 50$, $Pr = 1$, $We = 150$ and $r_T = 0$).

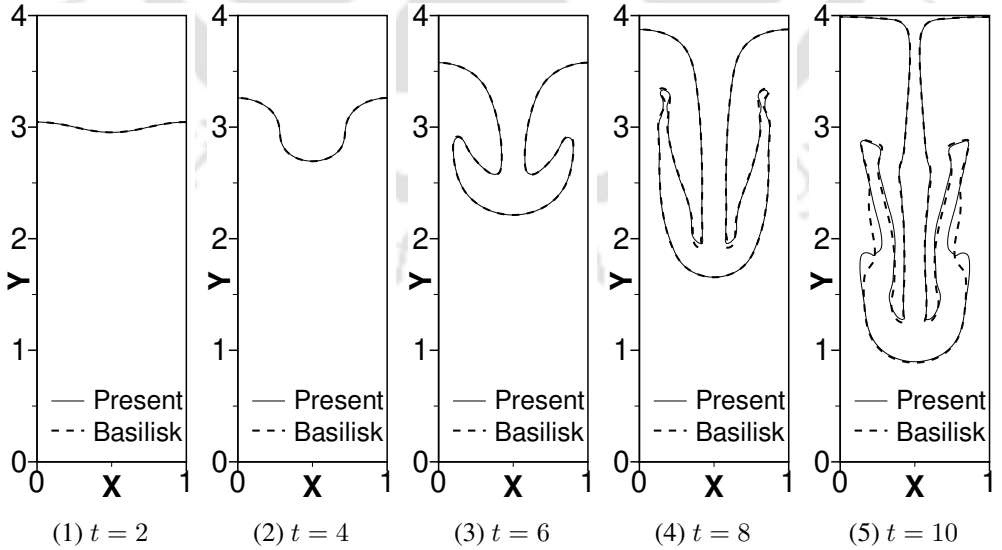

(1) $t = 2$ (2) $t = 4$ (3) $t = 6$ (4) $t = 8$ (5) $t = 10$

Figure 2.28: Comparison of instantaneous interface profiles of the instability obtained using the present code with those of Basilisk software for variable viscosity fluid layers (rest of the parameters are: $\rho_r = 2$, $m = 2$, $k_r = 2$, $c_{p_r} = 2$, $Re = 50$, $We = 150$, $Pr = 1$ and $r_T = 3$).

Rayleigh-Taylor instability in viscosity stratified two fluid layers

Fig. 2.28 shows the comparison of present code results with those of Basilisk software results, in the form of instantaneous interface profiles for variable viscosity fluid layers. Time variation of spike front and bubble tip locations is also compared in Fig. 2.29. From both the figures, it is concluded that the present code results show good agreement with those of the Basilisk software results.

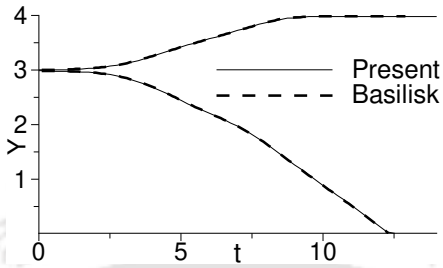

Figure 2.29: Comparison of time variation of spike front and bubble tip locations for variable viscosity fluid layers (rest of the parameters are: $\rho_r = 2$, $m = 5$, $k_r = 2$, $c_{p_r} = 2$, $Fr = 1$, $Re = 50$, $Pr = 1$, $We = 150$ and $r_T = 0$).

2.4 Validation of usage of Basilisk software in 2-D rectangular and axisymmetric coordinate configurations

Usage of Basilisk software is validated by solving and comparing the results obtained from the software with those of presented in past studies. The validations of Basilisk software are performed by solving the multiphase flow problem in 2-D rectangular and axisymmetric coordinate configurations. The relevant validations, based on the study in respective chapter, are solved and presented in the corresponding chapters. For 2-D rectangular coordinates, usage of the Basilisk software to perform simulations to study multiphase flow is validated by solving Rayleigh-Taylor instability in 2-D rectangular configuration with and without surface tension effects in subsection 5.2.5.1 of Chapter 5. For Marangoni effect validation, a 2-D bubble rising in an ambient fluid medium is solved using the software and comparison is presented in subsection 5.2.5.2 of Chapter 5. Usage of Basilisk software in axisymmetric coordinates is also validated for multiphase flow problems in axisymmetric configuration, and the corresponding validations are presented in subsection 6.2.5 of Chapter 6. Similarly, for Marangoni flow in axisymmetric configuration, the validations are presented in subsection 8.2.5 of Chapter 8.

Chapter 3

Rayleigh-Taylor instability in viscosity stratified medium in 2-D rectangular coordinates

In this chapter, study of Rayleigh-Taylor instability in viscosity stratified medium in 2-D rectangular coordinates is carried out. Viscosity of both the fluid layers are specified to vary with temperature exponentially. The effect of viscosity ratio, temperature ratio, Weber number, Prandtl number and hot and cold wall locations on the instability is studied under the influence of viscosity stratification.

3.1 Physical system

Physical system used in the study of present chapter is described in subsection 2.1.1. Schematic of the physical system is shown in Fig. 2.2.

3.2 Mathematical treatment

In this chapter, simulations are carried out using the developed code which is written based on level set method. In level set method, an additional equation for level set variable is solved. Hence, the governing equations consist of continuity, momentum and energy equations along with level set equation.

3.2.1 Scaling parameters

For the study presented in this chapter, the following reference scales are chosen for non dimensionalization of the governing equations. The reference scales for length, velocity, time, pressure, temperature and surface tension are taken as $\tilde{L}_{\text{ref}}$, $\tilde{V}_{\text{ref}}$, $\tilde{L}_{\text{ref}}/\tilde{V}_{\text{ref}}$, $\tilde{\rho}_{\text{ref}}\,\tilde{V}_{\text{ref}}^2$, $\tilde{T}_{\text{ref}}$ and $\tilde{\sigma}_{\text{ref}}$, respectively. Reference length ($\tilde{L}_{\text{ref}}$) is chosen equal to width of the domain ($\tilde{L}$). Reference velocity ($\tilde{V}_{\text{ref}}$) is chosen equal to $\left(\tilde{g}\,\tilde{L}_{\text{ref}}\right)^{1/2}$. Reference surface tension value ($\tilde{\sigma}_{\text{ref}}$) is chosen equal to $\tilde{\sigma}_0$, which is surface

tension value at reference temperature. The reference temperature is chosen to be of cold wall temperature ($\min(\tilde{T}_1, \tilde{T}_2)$). The reference fluid properties are chosen to be the properties of lighter fluid, 'Fluid 2'. The reference variables are as following.

$$\begin{aligned} &\tilde{\rho}_{\text{ref}} = \tilde{\rho}_2, \quad \tilde{\mu}_{\text{ref}} = \tilde{\mu}_2, \quad \tilde{k}_{\text{ref}} = \tilde{k}_2, \quad \tilde{c_p}_{\text{ref}} = \tilde{c_p}_2, \quad \tilde{L}_{\text{ref}} = \tilde{L}, \\ &\tilde{T}_{\text{ref}} = \min(\tilde{T}_1, \tilde{T}_2), \quad \tilde{\sigma}_{\text{ref}} = \tilde{\sigma}_0, \quad \tilde{V}_{\text{ref}} = \sqrt{\tilde{g}\,\tilde{L}}, \quad \tilde{\phi}_{\text{ref}} = \tilde{L} \end{aligned} \tag{3.1}$$

Definitions of dimensionless variables, which are given by Eq. (2.14), become

$$\begin{aligned} &\rho = \frac{\tilde{\rho}}{\tilde{\rho}_2}, \quad \mu = \frac{\tilde{\mu}}{\tilde{\mu}_2}, \quad k = \frac{\tilde{k}}{\tilde{k}_2}, \quad c_p = \frac{\tilde{c_p}}{\tilde{c_p}_2}, \quad x = \frac{\tilde{x}}{\tilde{L}}, \quad y = \frac{\tilde{y}}{\tilde{L}}, \quad t = \frac{\tilde{t}}{\sqrt{\tilde{L}/\tilde{g}}}, \\ &\mathbf{u} = \frac{\tilde{\mathbf{u}}}{\sqrt{\tilde{g}\,\tilde{L}}}, \quad p = \frac{\tilde{p}}{\tilde{\rho}_2\,\tilde{g}\,\tilde{L}}, \quad \theta = \frac{\tilde{T} - \min(\tilde{T}_1, \tilde{T}_2)}{\min(\tilde{T}_1, \tilde{T}_2)}, \quad \phi = \frac{\tilde{\phi}}{\tilde{L}}, \quad \sigma = \frac{\tilde{\sigma}}{\tilde{\sigma}_0} \end{aligned} \tag{3.2}$$

3.2.2 Governing equations

With the above choice of dimensionless variables, the dimensionless form of governing equations are as follows.

Continuity equation

$$\nabla\cdot\mathbf{u} = 0 \tag{3.3}$$

Momentum equation

$$\rho\left(\frac{\partial\mathbf{u}}{\partial t} + \mathbf{u}\cdot\nabla\mathbf{u}\right) = -\nabla p + \frac{1}{Re}\nabla\cdot\mu\left(\nabla\mathbf{u} + \nabla\mathbf{u}^{\mathrm{T}}\right) + \mathbf{F} \tag{3.4}$$

Energy equation

$$\rho\, c_p\left(\frac{\partial\theta}{\partial t} + \mathbf{u}\cdot\nabla\theta\right) = \frac{1}{Re\,Pr}\nabla\cdot(k\nabla\theta) \tag{3.5}$$

Level set equation

$$\frac{\partial\phi}{\partial t} + \mathbf{u}\cdot\nabla\phi = 0 \tag{3.6}$$

The dimensionless body force term $\mathbf{F}$ in the momentum equation for constant surface tension is given by Eq. (2.23), which is

$$\mathbf{F} = \frac{1}{We}\,\kappa\,\delta\,\mathbf{n} - \frac{\rho}{Fr}\,\mathbf{e}_j \tag{3.7}$$

Expressions of dimensionless numbers in the above governing equations, which are given by Eq. (2.24), are as following.

$$Re = \frac{\tilde{\rho}_2\,\tilde{g}^{1/2}\,\tilde{L}^{3/2}}{\tilde{\mu}_2}, \quad Fr = 1, \quad We = \frac{\tilde{\rho}_2\,\tilde{g}\,\tilde{L}^2}{\tilde{\sigma}_0}, \quad Pr = \frac{\tilde{\mu}_2\tilde{c_p}_2}{\tilde{k}_2} \tag{3.8}$$

Viscosities in both the fluid layers vary with temperature exponentially, as given by Eq. (2.25), according to the following expressions

$$\mu_1 = m\, e^{-\theta} \qquad \text{and} \qquad \mu_2 = e^{-\theta} \tag{3.9}$$

Here, m is top heavier fluid to bottom lighter fluid viscosity ratio ($\mu_1(\tilde{T}_2)/\mu_2(\tilde{T}_2)$) at reference temperature. Dimensionless fluid properties such as density (ρ), viscosity (μ), thermal conductivity (k) and heat capacity (c_p) are calculated using heaviside function (H), as given by Eq. (2.26), according to the following expressions

$$\begin{aligned} \rho &= \rho_2 + (\rho_1 - \rho_2)\, H \\ \mu &= \mu_2 + (\mu_1 - \mu_2)\, H \\ k &= k_2 + (k_1 - k_2)\, H \\ c_p &= c_{p_2} + (c_{p_1} - c_{p_2})\, H \end{aligned} \tag{3.10}$$

3.2.3 Initial and boundary conditions

The initial and boundary conditions used for the study carried out in this chapter are as discussed in subsection 2.2.2. The dimensions of the domain used for the study are given in the same subsection.

3.2.4 Numerical methodology

The numerical methodology and validations of the developed code are presented in subsections 2.2.4-2.2.5 and section 2.3, respectively. The governing equations along with the initial and boundary conditions are solved numerically.

3.2.5 Grid independent test

Grid independence test is carried out before performing the numerical simulations to study Rayleigh-Taylor instability in viscosity stratified fluid medium in 2-D rectangular coordinate configuration. The grid independent test is carried out for the parameters of $\rho_r = 2$, $m = 2$, $k_r = 2$, $c_{p_r} = 2$, $Re = 50$, $Fr = 1$,$Pr = 1$, $We = 150$ and $r_T = 3$, which is the baseline parameters of the studies carried out in the present chapter. Rayleigh-Taylor instability in viscosity stratified fluid medium is studied for four different grid sizes with uniform grid spacing ($\Delta = \Delta_x = \Delta_y$) in both x and $y-$coordinate directions. For the test, the four different grid sizes of 64×256, 72×288, 80×320, and 88×352 are used which correspond to the uniform grid spacing of 0.0156, 0.0138, 0.0125 and 0.011, respectively, in both x and y coordinate directions. The details of the grid size and the corresponding grid spacing are given in Table 3.1. Fig. 3.1 shows the comparison of instantaneous interface profiles of Rayleigh-Taylor instability obtained with different grids. Fig. 3.2 shows the comparison of spike front and bubble tip locations for different grids. From the figures, it is observed that for the grid spacing of 0.0138 or lower, the solutions do not vary significantly. Hence, for the studies carried out in the present chapter, the numerical simulations are performed with the grid spacing of 0.0125 for which the grid size of

Table 3.1: Grid spacing corresponds to different grids used in the present simulations present developed code

Grid size	64×256	72×288	80×320	88×352
Grid spacing ($\Delta = \Delta_x = \Delta_y$)	0.0156	0.0138	0.0125	0.0113

80×320.

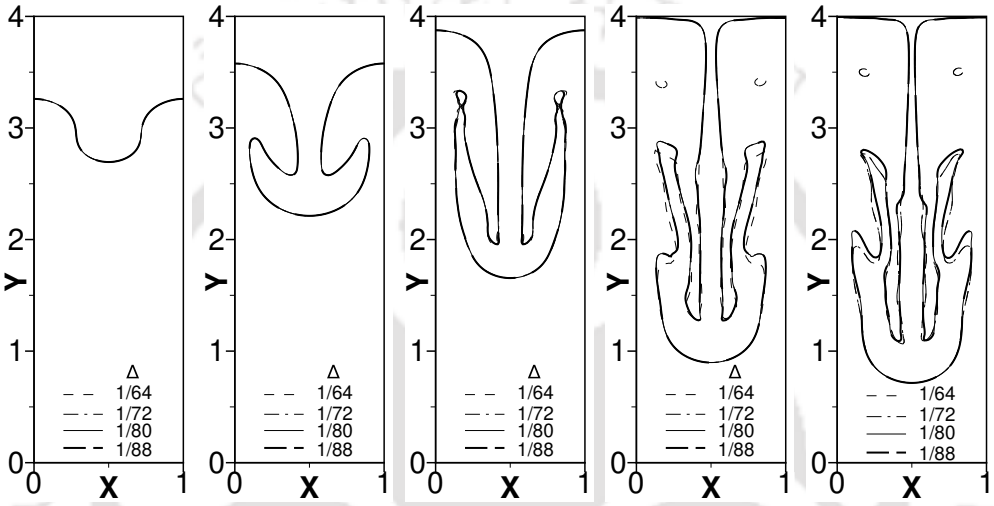

(1) t =4 (2) t =6 (3) t =8 (4) t =10 (5) t =10.5

Figure 3.1: Comparison of instantaneous interface profiles of Rayleigh-Taylor instability in viscosity stratified fluid layers in 2-D rectangular coordinate configuration obtained with different grid sizes (rest of the parameters are: $\rho_r = 2$, $m = 2$, $k_r = 2$, $c_{p_r} = 2$, $Re = 50$, $Pr = 1$, $Fr = 1$, $We = 150$ and $r_T = 3$).

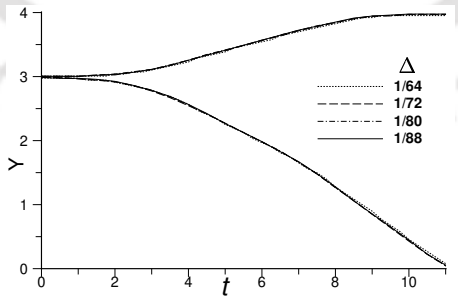

Figure 3.2: Comparison of time variation of spike front and bubble tip locations for various grid sizes (rest of the parameters are: $\rho_r = 2$, $m = 2$, $k_r = 2$, $c_{p_r} = 2$, $Re = 50$, $Pr = 1$, $Fr = 1$, $We = 150$ and $r_T = 3$).

3.3 Results and discussion

3.3.1 Baseline parameter values

In this part of the present work, effect of various parametric studies on the instability are carried out at a set of baseline parameter values. The chosen baseline parameters are as following. Top heavier fluid to bottom lighter fluid density ratio (ρ_r), viscosity ratio (m), thermal conductivity ratio (k_r) and heat capacity ratio (c_{p_r}), all are set equal to 2. For the baseline configuration, the top wall is isothermally heated at dimensionless temperature $\theta = r_T$ and the bottom wall is isothermally cooled at dimensionless temperature $\theta = 0$. Here, r_T is temperature ratio which is taken equal to 3. The dimensionless numbers such as Fr, Pr, Re and We are taken equal to 1, 1, 50 and 150, respectively. The study of the effect of a particular parameter is carried out by varying the value of that particular parameter and keeping all the other parameter values fixed at the corresponding above baseline values.

3.3.2 Effect of stratification due viscosity variation with temperature

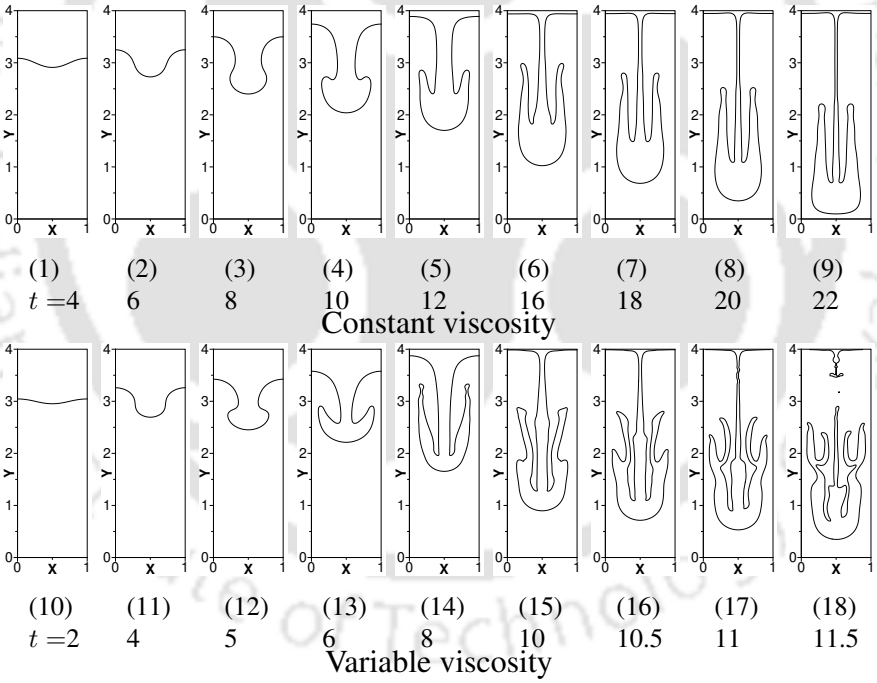

Figure 3.3: Instantaneous interface profiles for variable viscosity and constant viscosity of fluid layers for viscosity ratio $m = 2$ (rest of the parameters are: $\rho_r = 2$, $k_r = 2$, $c_{p_r} = 2$, $Re = 50$, $Pr = 1$, $Fr = 1$, $We = 150$ and $r_T = 3$).

Effect of stratification due to viscosity variation with temperature on Rayleigh-Taylor instability is studied in this section. For the study, fluid viscosity is specified to vary exponentially with temperature in both the fluid layers according to Eq. (3.9) and the instability is compared to that of constant viscosity fluid layers. For variable viscosity, viscosities of the fluid layers vary in the domain, unlike for constant viscosities of fluid layers. Due to the viscosity variation, the instability in variable viscosity fluid layers is expected to be different from that of constant viscosity fluid layers.

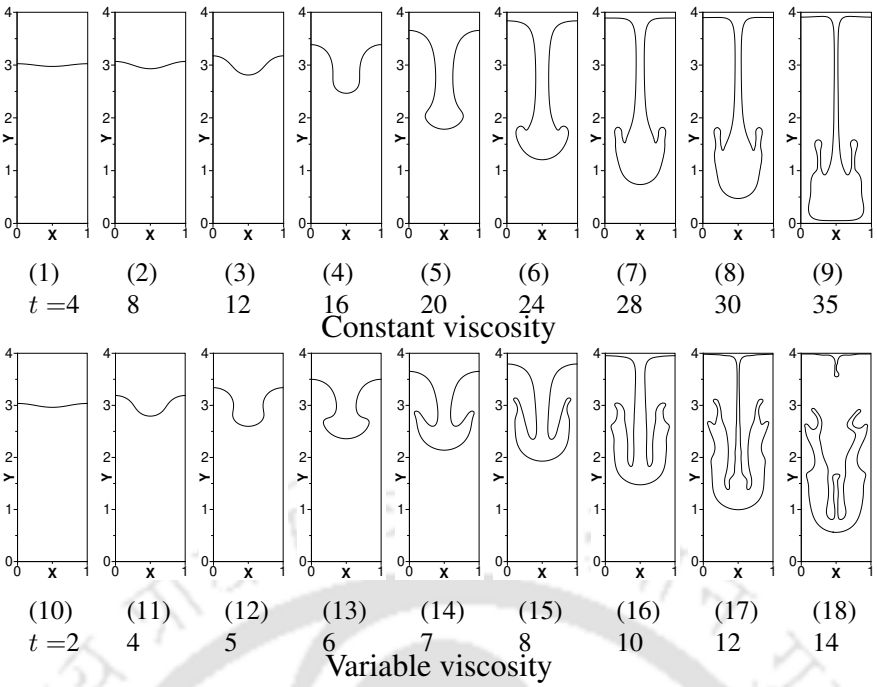

Figure 3.4: Instantaneous interface profiles for variable viscosity and constant viscosity of fluid layers for viscosity ratio $m = 10$ (rest of the parameters are: $\rho_r = 2$, $k_r = 2$, $c_{p_r} = 2$, $Re = 50$, $Pr = 1$, $Fr = 1$, $We = 150$ and $r_T = 3$).

Fig. 3.3 shows the instability evolution in constant and variable viscosity fluid layers for viscosity ratio 2. In initial stage, growth of the disturbance is small, and instability shows qualitative similarity for both constant and variable viscosity fluid layers. Whereas in later stage, growth of the disturbance is large, and with time, a mushroom shape spike forms with arms on both sides of spike head which shows qualitative difference for both types of viscosities of fluid layers. For constant viscosity, the arm on the spike head elongates more as the spike moves towards the bottom wall. For variable viscosity, the arm on the spike head elongates and undergoes large deformation as spike moves towards the bottom wall. Further with time, the elongated arm splits into two branches and stem of the spike breaks before striking the bottom wall. Whereas for constant viscosity, the spike forms with smoother arms and stem of the spike does not break, unlike for variable viscosity. Viscosity stratification also affects rate of the instability. For example, for variable viscosity, top heavier fluid penetrates into bottom lighter fluid relatively faster than that of constant viscosity. For viscosity ratio 10, instability evolution in both constant and variable viscosity fluid layers are presented in Fig. 3.4. For constant viscosity, the heavier fluid forms into a bigger head mushroom shaped spike with a suppressed arm. For variable viscosity, the heavier fluid forms into a mushroom shaped spike with an elongated wavy arm. For viscosity ratio 20, the instability is presented in Fig. 3.5 for the both types of viscosity variations. For constant viscosity, a mushroom shape spike forms without any arm and found to be attached to the top wall without breaking of stem. For variable viscosity, a mushroom shape spike forms with thick arm on both sides of the spike head which eventually elongates more and become wavy. With time, stem of the spike breaks and the spike comes down in the form of spike-arm

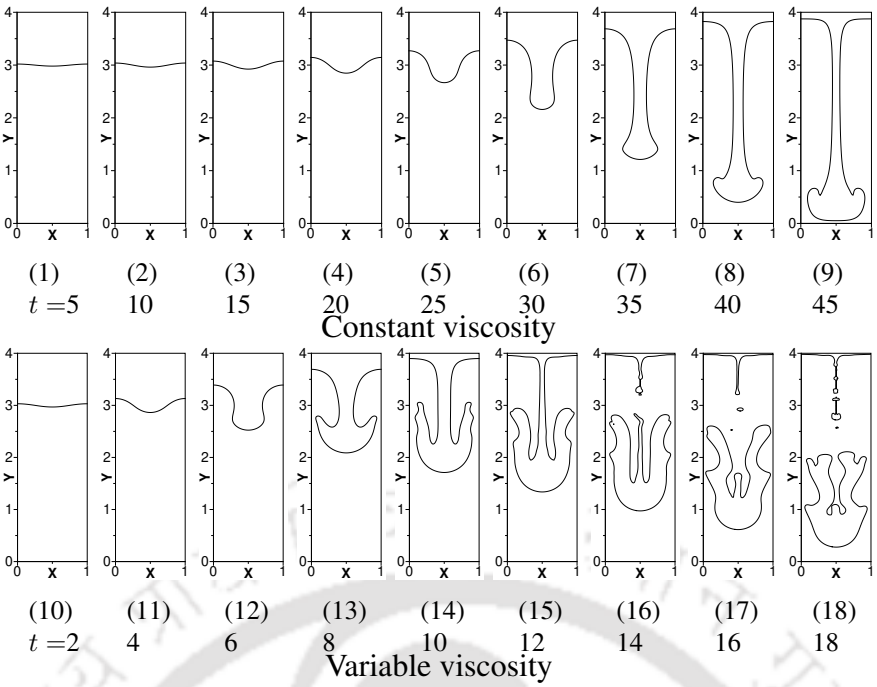

Figure 3.5: Instantaneous interface profiles for variable viscosity and constant viscosity of fluid layers for viscosity ratio $m = 20$ (rest of the parameters are: $\rho_r = 2$, $k_r = 2$, $c_{p_r} = 2$, $Re = 50$, $Pr = 1$, $Fr = 1$, $We = 150$ and $r_T = 3$).

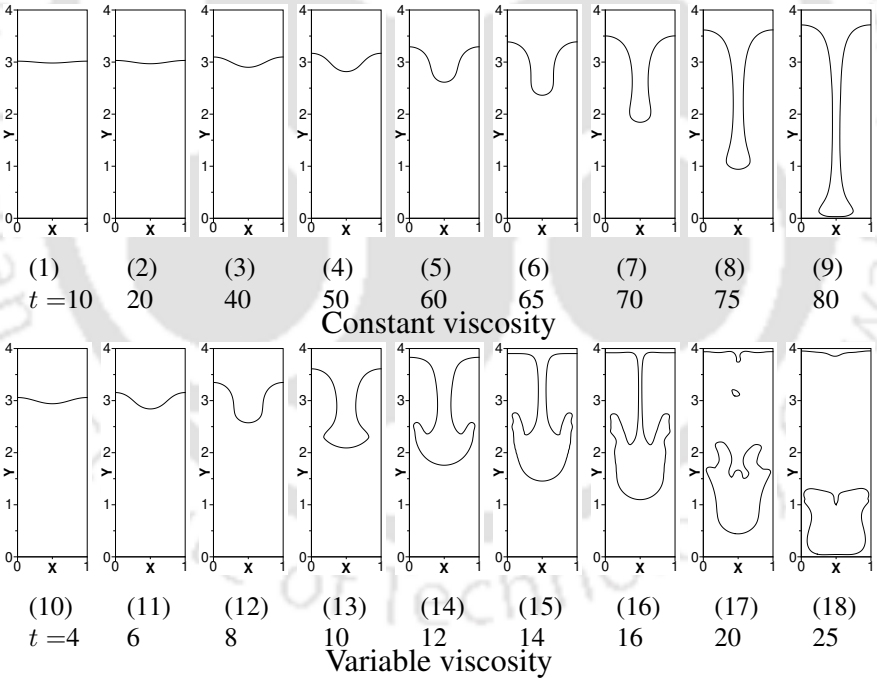

Figure 3.6: Instantaneous interface profiles for variable viscosity and constant viscosity of fluid layers for viscosity ratio $m = 50$ (rest of the parameters are: $\rho_r = 2$, $k_r = 2$, $c_{p_r} = 2$, $Re = 50$, $Pr = 1$, $Fr = 1$, $We = 150$ and $r_T = 3$).

structure.

With increasing viscosity ratio, spike forms relatively more smoother and simpler, irrespective of

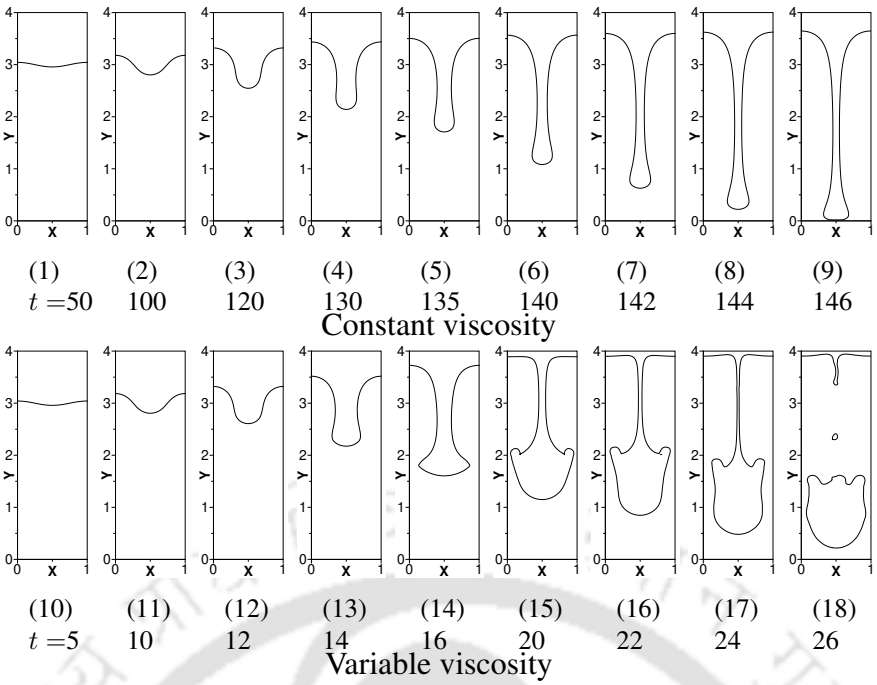

Figure 3.7: Instantaneous interface profiles for variable viscosity and constant viscosity of fluid layers for viscosity ratio $m = 100$ (rest of the parameters are: $\rho_r = 2$, $k_r = 2$, $c_{p_r} = 2$, $Re = 50$, $Pr = 1$, $Fr = 1$, $We = 150$ and $r_T = 3$).

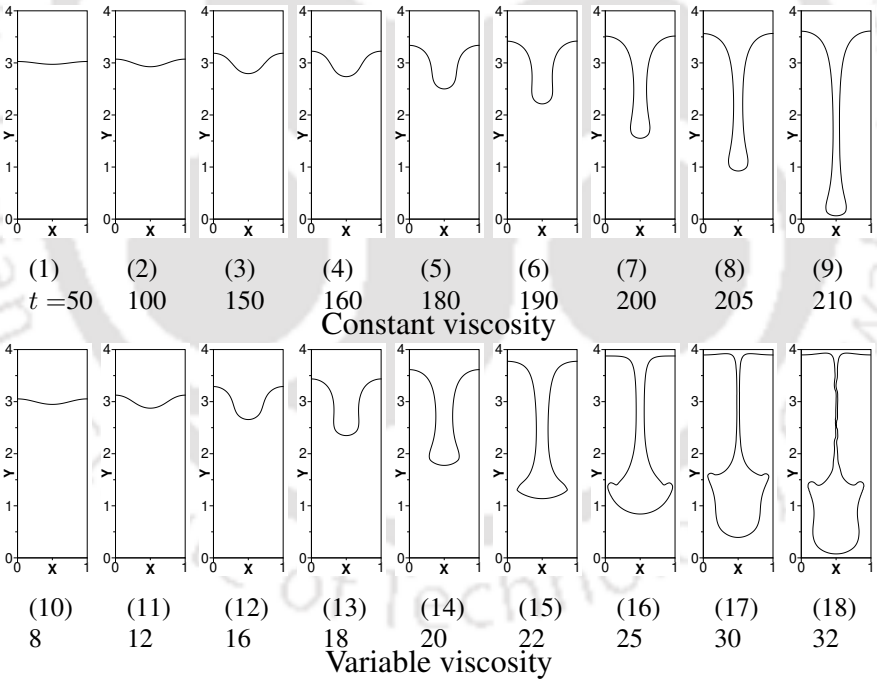

Figure 3.8: Instantaneous interface profiles for variable viscosity and constant viscosity of fluid layers for viscosity ratio $m = 150$ (rest of the parameters are: $\rho_r = 2$, $k_r = 2$, $c_{p_r} = 2$, $Re = 50$, $Pr = 1$, $Fr = 1$, $We = 150$ and $r_T = 3$).

viscosity variations. Fig. 3.6 represents the instability evolution for both types of viscosities of fluid layers for viscosity ratio 50. For constant viscosity, spike forms a fluid column like structure and stem of the spike does not break even after striking the bottom wall. Whereas, for variable viscosity, spike forms a thick and short arm on both sides of the spike head which eventually becomes a fluid droplet upon breaking of stem as the spike moves towards the bottom wall, unlike constant viscosity. When

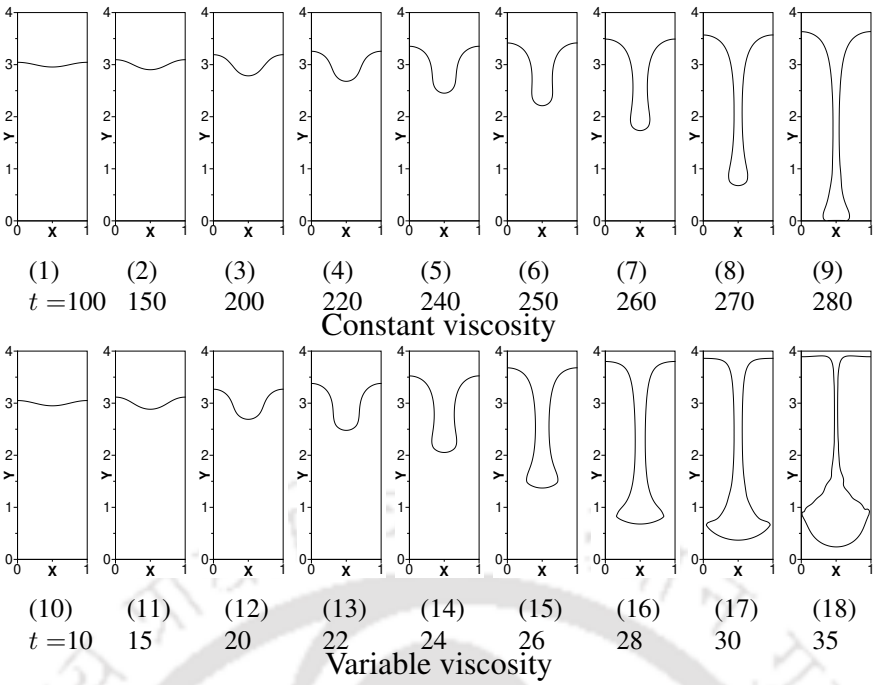

Figure 3.9: Instantaneous interface profiles for variable viscosity and constant viscosity of fluid layers for viscosity ratio $m = 200$ (rest of the parameters are: $\rho_r = 2$, $k_r = 2$, $c_{p_r} = 2$, $Re = 50$, $Pr = 1$, $Fr = 1$, $We = 150$ and $r_T = 3$).

viscosity ratio is increased to 100, the spike forms without any arm showing a qualitative similarity for both types of viscosity variations, as shown in Fig. 3.7. However, for variable viscosity, the spike forms with relatively bigger head than that of constant viscosity. For variable viscosity, stem of the spike is found to break and the spike forms into a fluid droplet before striking the bottom wall, unlike for constant viscosity. The instability for both variable and constant viscosity variations is presented in Fig. 3.8 and Fig. 3.9 for viscosity ratio 150 and 200, respectively. With increased viscosity ratio from 150 to 200, the instability shows qualitative similarity for both constant and variable viscosity fluid layers. For the both types of viscosity variations, the spike forms into a fluid column like structure and stem of the spike does not break throughout the spike movement. However, with variable viscosity the spike is formed with bigger head compared to that with constant viscosity. For variable viscosity, formation of spike into a fluid column like structure takes place at higher viscosity ratio compared to that of constant viscosity. Similar mushroom shape spikes are formed at about $t = 200$ and 20 for constant and variable viscosity fluid layers, respectively, for viscosity ratio 200. This is due to the fact that fluid viscosity is found to be decreased with increasing temperature which results into relatively more unstable flow for variable viscosity fluid layers. The decreased resistive viscous force results into relatively faster spike movement. Overall, relatively more destabilizing effect on the instability can be observed with temperature varying viscosity than that of constant viscosity fluid layers.

Figs. 3.10-3.11 show temperature contours at different time instances for various viscosity ratios ($m = 2$-200) with temperature varying viscosity fluid layers. Initially, the temperature contours form parallel to the horizontal walls, irrespective of the value of viscosity ratio. These parallel temperature contours represent that initially heat transfer takes place across the fluid layers through conduction mode. This is due to the fact that the velocities in the domain are extremely small in initial stage

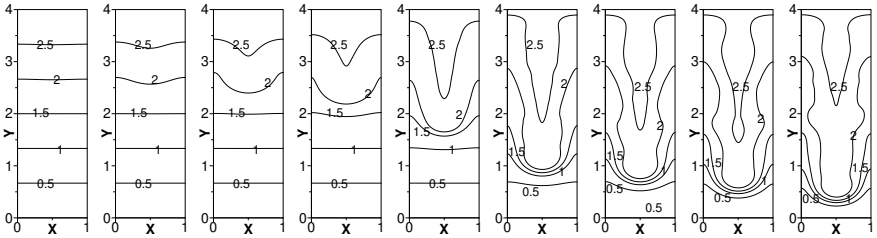

(1) (2) (3) (4) (5) (6) (7) (8) (9)
t =2 4 5 6 8 10 10.5 11 11.5

Viscosity ratio $m = 2$

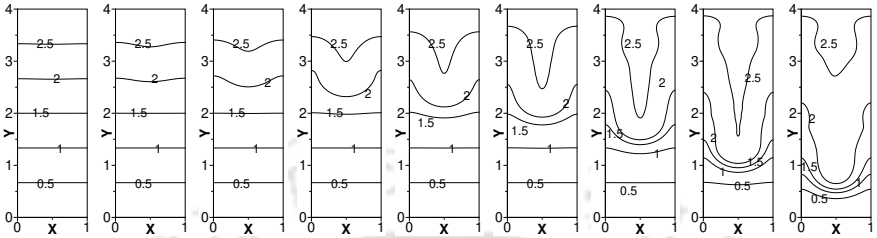

(10) (11) (12) (13) (14) (15) (16) (17) (18)
t =2 4 5 6 7 8 10 12 14

Viscosity ratio $m = 10$

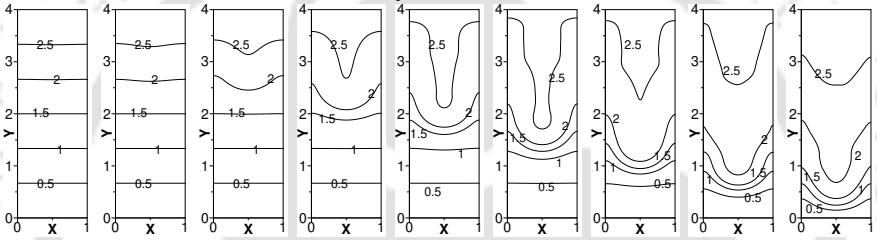

(19) (20) (21) (22) (23) (24) (25) (26) (27)
t =2 4 6 8 10 12 14 16 18

Viscosity ratio $m = 20$

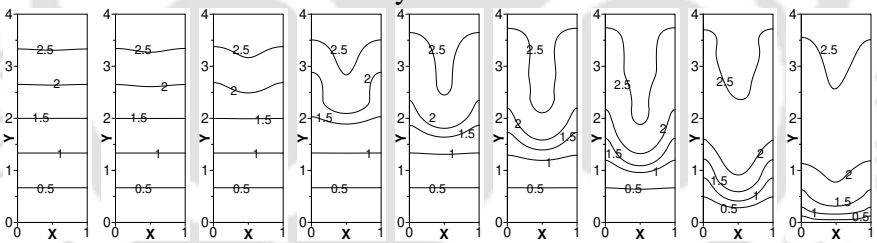

(28) (29) (30) (31) (32) (33) (34) (35) (36)
t =4 6 8 10 12 14 16 20 25

Viscosity ratio $m = 50$

Figure 3.10: Temperature contours at different time instances for various viscosity ratios $m = 2-50$ (rest of the parameters are: $\rho_r = 2$, $k_r = 2$, $c_{p_r} = 2$, $Re = 50$, $Pr = 1$, $Fr = 1$, $We = 150$ and $r_T = 3$).

resulting into heat transfer through conduction mode. With time, the contours bend in the downward direction due to increasing spike penetration in later stage. With increasing viscosity ratio, the temperature contours stay horizontal for relatively longer duration of time compared to that of lower viscosity ratios. This is due to the fact that heavier fluid penetration into lighter fluid is delayed with increasing viscosity ratio.

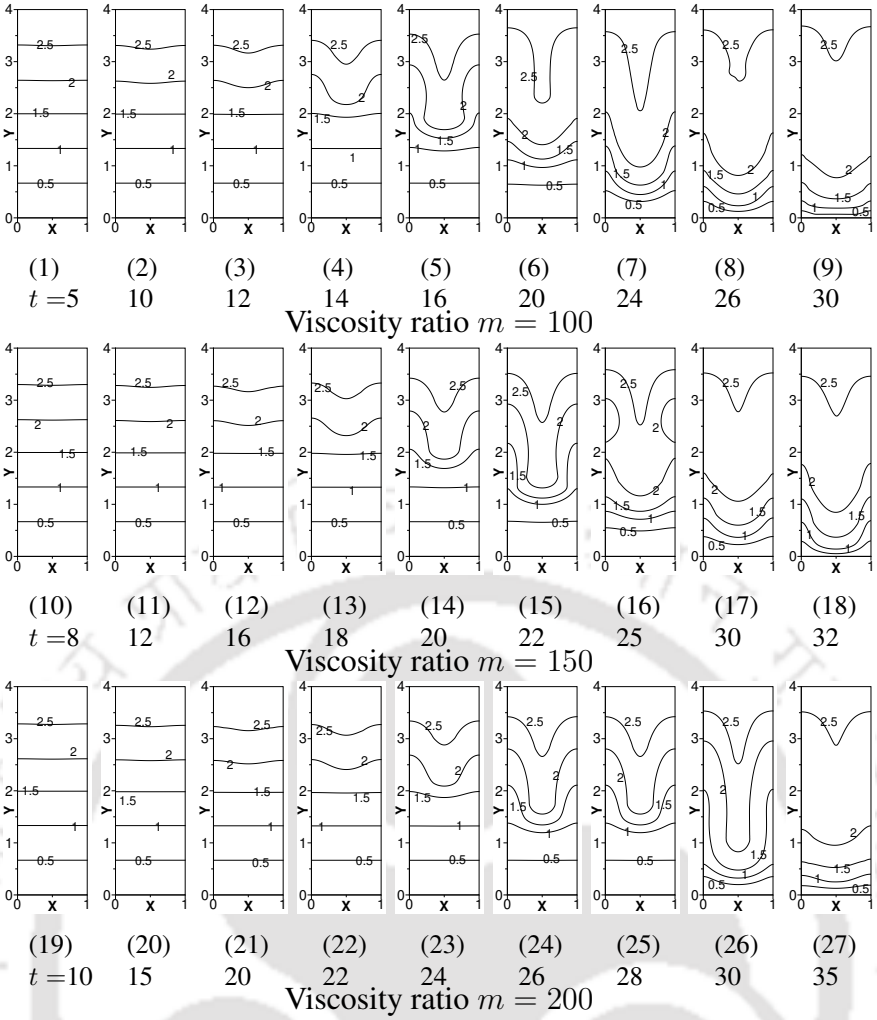

Figure 3.11: Temperature contours at different time instances for various viscosity ratios $m = 100-200$ (rest of the parameters are: $\rho_r = 2$, $k_r = 2$, $c_{p_r} = 2$, $Re = 50$, $Pr = 1$, $Fr = 1$, $We = 150$ and $r_T = 3$).

3.3.3 Effect of viscosity ratio

The instability in viscosity stratified fluid layers is studied for various viscosity ratios in the range of 1 to 200 and instability evolution is presented in Figs. 3.12-3.13. In initial stage of the instability, the heavier fluid forms a mushroom shaped spike, almost similar for all the viscosity ratios. In later stage of the instability, the mushroom shaped spike moves towards the bottom wall which eventually deforms more, and with time, the instability differs largely from each other as viscosity ratio is varied.

Fig. 3.12 shows the instability for viscosity ratio varying from 1 to 10. For viscosity ratio 1, the mushroom shaped spike deforms into an arm attached to the spike head, and with time, the arm elongates more as spike moves in the downward direction. The elongated arm undergoes large deformation which splits into two branches as the spike moves towards the bottom wall. This is due to the fact that velocity shearing effect along the arm is increased which results into large deformation of the spike. For viscosity ratio 2, the instability shows qualitative similarity with that of viscosity ratio 1. With further increase in viscosity ratio, the spike-arm structure becomes smoother at higher viscosity ratio. For example, for viscosity ratio in the range of 5 to 10, the spike forms with relatively thicker and smoother arm than that of lower viscosity ratio. With time, the arm does not splits into branches,

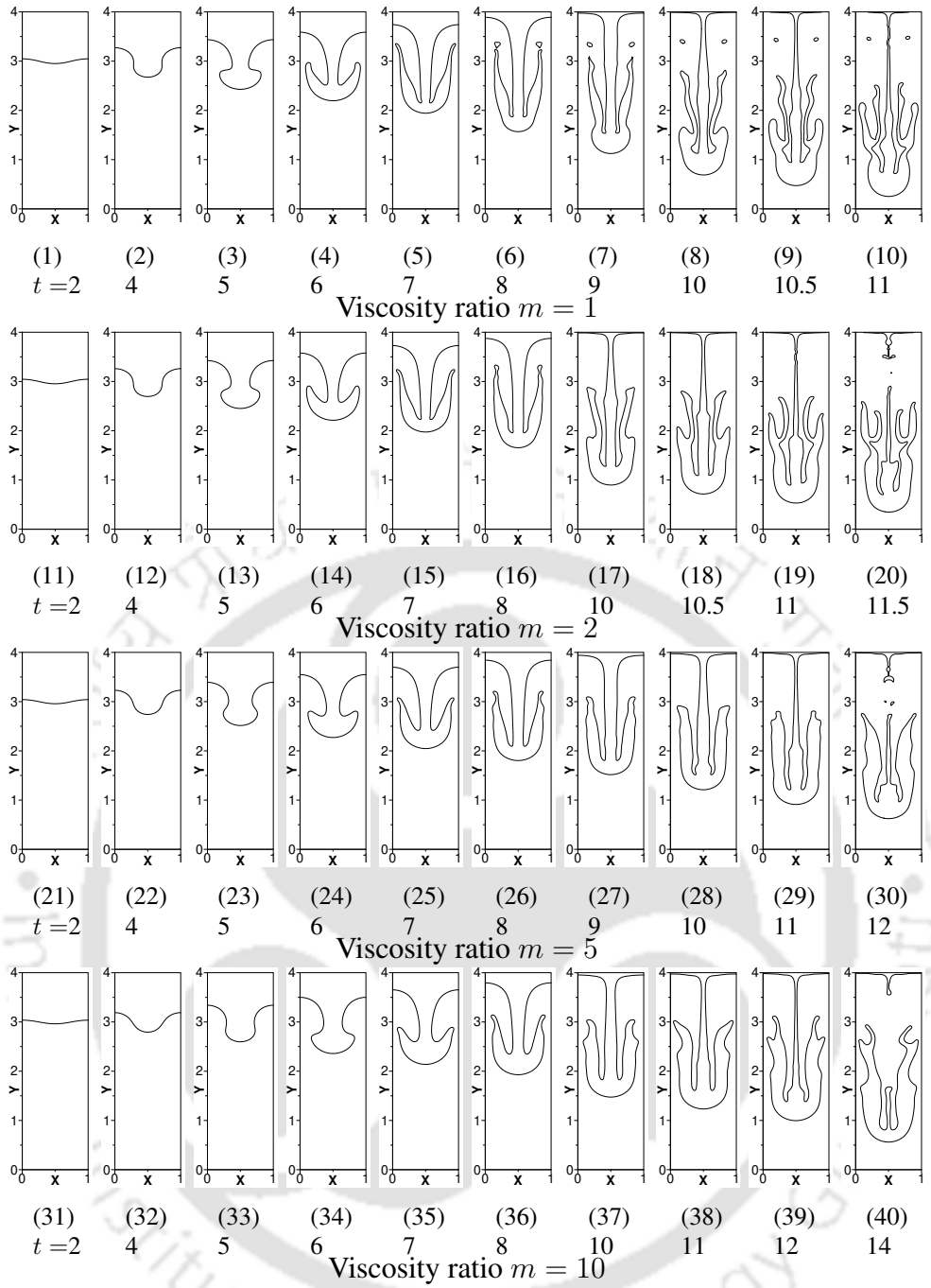

Figure 3.12: Instantaneous interface profiles for various viscosity ratios in the range of m = 1-10 (rest of the parameters are: $\rho_r = 2$, $k_r = 2$, $c_{p_r} = 2$, $Re = 50$, $Fr = 1$, $We = 150$, $Pr = 1$ and $r_T = 3$).

unlike for viscosity ratio 2. This is due to the fact that with increased viscosity ratio, relative viscosity of heavier fluid increases which results into reduced deformation of the spike.

With further increase in viscosity ratio, the arms on the spike head become shorter and the spike moves towards the bottom wall at slower rate. This can be evident from the instability evolution presented in Fig. 3.13 for viscosity ratio in the range of 20 to 200. For viscosity ratio 20, the spike forms with relatively thicker and shorter arms. With further increase in viscosity ratio to 50, the arms on the spike head form with shorter length and relatively simpler than that of viscosity ratio 20. For viscosity ratio 100, the arms on both sides of the spike head become shorter, and the spike moves

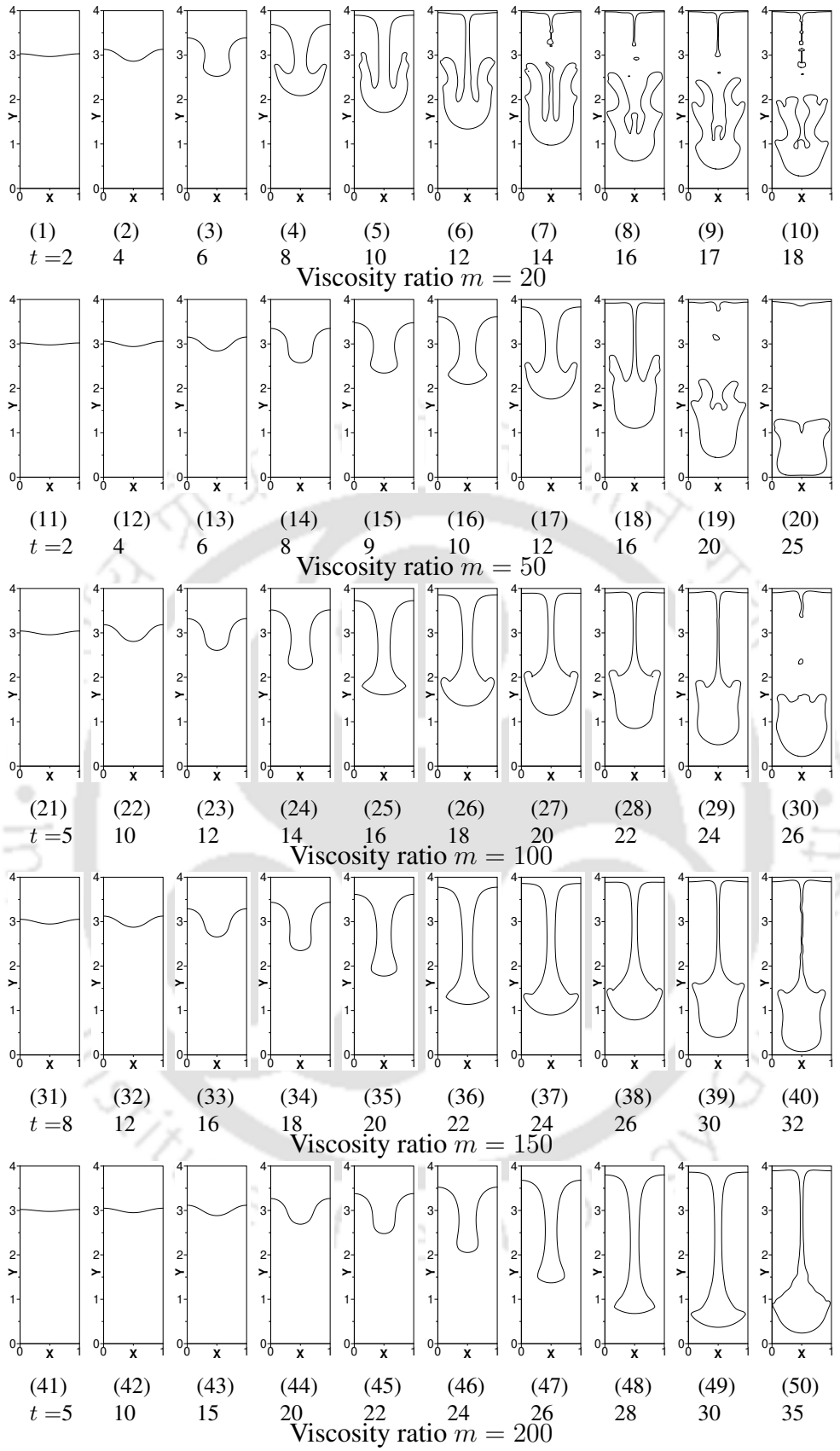

Figure 3.13: Instantaneous interface profiles for various viscosity ratios in the range of $m = 20$-100 (rest of the parameters are: $\rho_r = 2$, $k_r = 2$, $c_{p_r} = 2$, $Re = 50$, $Fr = 1$, $We = 150$, $Pr = 1$ and $r_T = 3$).

towards the bottom wall in a thick finger like pattern with bigger head. With time, stem of the spike breaks resulting into detachment of the spike head from the top wall, and the spike moves towards the bottom wall in a form of a fluid drop. With further increase in viscosity ratio from 150 to 200, the spike forms into a fluid column like structure. This means that with increased viscosity ratio viscous drag on the spike is found to be increased which turns into slower spike movement and relatively less spike deformation. Overall, it can be observed that the instability is found to be affected significantly with viscosity ratio, and increase in viscosity ratio shows stabilizing effect on the instability. The results of formation of spike into a fluid column structure for high viscosity ratios in Rayleigh-Taylor instability are inline with the results of past studies [9, 32, 168].

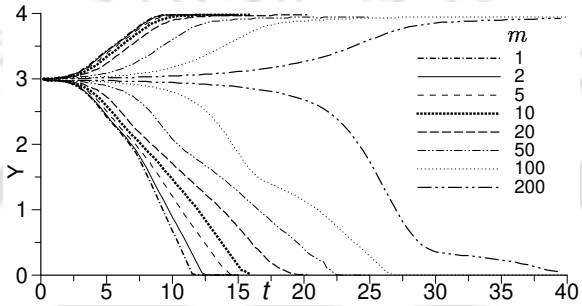

Figure 3.14: Time variation of spike front and bubble tip locations for various viscosity ratios $m = 1$-200 (rest of the parameters are: $\rho_r = 2$, $k_r = 2$, $c_{p_r} = 2$, $Re = 50$, $Fr = 1$, $We = 150$, $Pr = 1$ and $r_T = 3$).

Fig. 3.14 shows time variation of spike front and bubble tip locations for various viscosity ratios. From the figure it can be observed that the spike movement becomes slower with increasing viscosity ratio. For viscosity ratio 1, the spike strikes the bottom wall at about dimensionless time $t = 11$, and for viscosity ratio 200, the spike strikes the bottom wall at about dimensionless time $t = 40$, almost 4 times slower. An increase in viscosity ratio shows stabilizing effect on the instability. Present study result of increasing viscosity showing stabilizing effect on the instability is inline with the results of past studies presented in [107, 168].

3.3.4 Effect of temperature ratio

Study on effect of temperature ratio (r_T) on the instability is carried out for temperature ratio in the range of 0 to 3. Fig. 3.15 shows the instability evolution for various temperature ratios. For the study of temperature ratio, the bottom wall is kept at '0' dimensionless temperature and the top wall is varied from 0 to 3. With increasing temperature ratio, the fluid viscosity decreases exponentially in both the fluid layers, and due to such effect the instability at higher temperature ratio differs largely compared to that of lower temperature ratio.

Temperature ratio 0 represents the fluid layers of constant viscosities. For temperature ratio 0, heavier fluid forms into a mushroom shaped spike with a bigger head, and eventually an arm forms on both sides of the spike head. With time, the arm elongates more and the spike is found to be attached to the top wall all the time. When temperature ratio is increased to a value in the range of 1 to 2, the arm

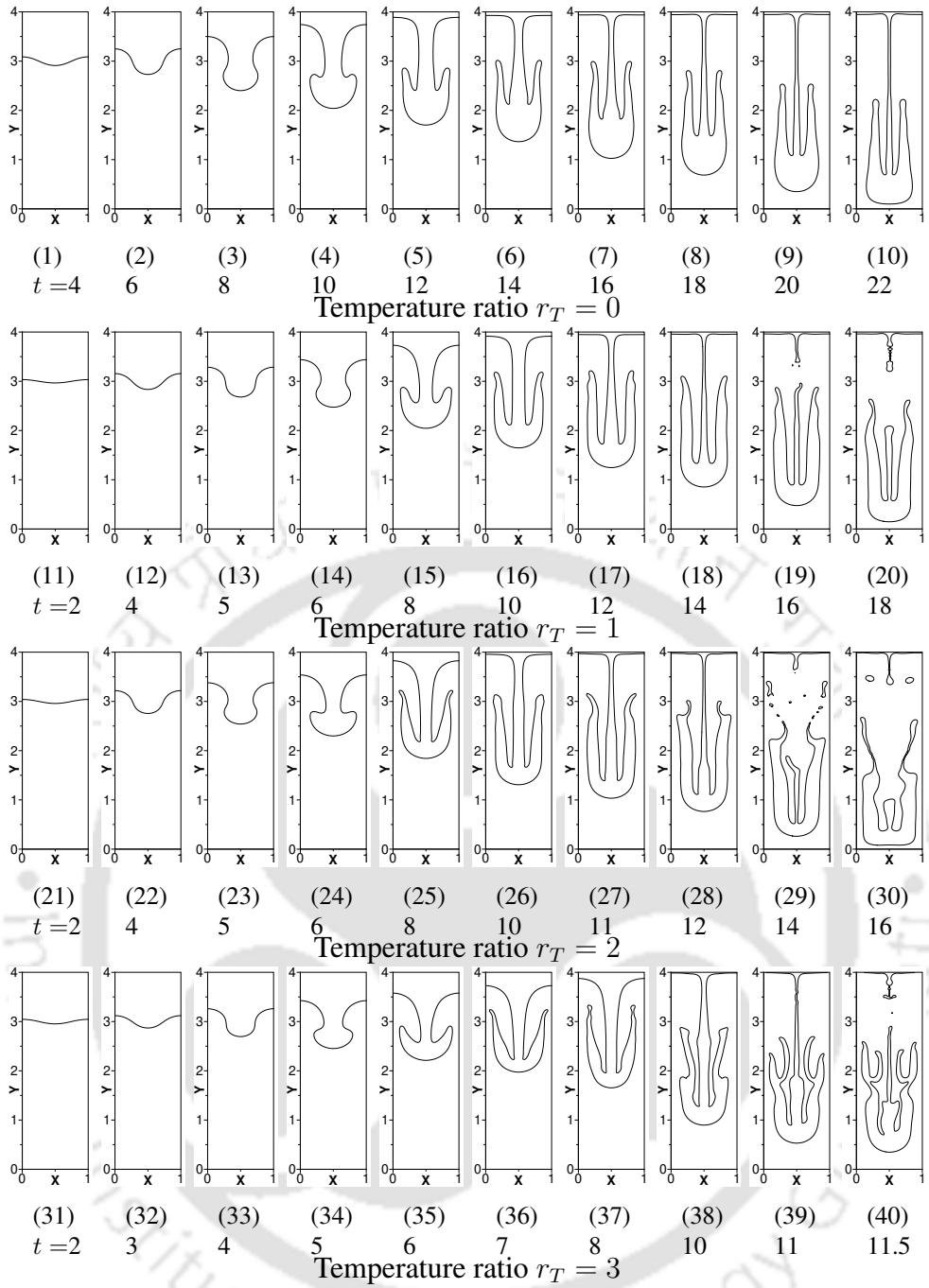

Figure 3.15: Instantaneous interface profiles for various temperature ratios in the range of r_T = 0-3 (rest of the parameters are: $\rho_r = 2$, $m = 2$, $k_r = 2$, $c_{p_r} = 2$, $Re = 50$, $Fr = 1$, $We = 150$ and $Pr = 1$).

elongates more and becomes thinner. With time, the stem of the spike breaks and the spike detaches from the top wall before striking the bottom wall. With further increase in temperature ratio, the spike undergoes large deformation and irregular spike-arm structure forms at higher temperature ratio. For example, for temperature ratio 3, the arm attached to the spike head becomes longer and thinner which eventually splits into two branches. With time, the splitted branches elongate more as the spike moves towards the bottom wall. At this stage, stem of the spike breaks before striking the bottom wall. At higher temperature ratios, the spike undergoes relatively larger deformation compared to that of lower temperature ratios. This is because with increasing temperature ratio, the viscosity decreases within

the fluid layers which makes the flow more unstable.

Fig. 3.16 shows time variation of spike front and bubble tip locations for various temperature ratios. For temperature ratio 0, spike strikes the bottom wall at about dimensionless time $t = 22$, and, for temperature ratio 3, spike strikes the bottom wall at about dimensionless time $t = 12$, almost two times faster. An increase in temperature ratio shows destabilizing effect on the instability.

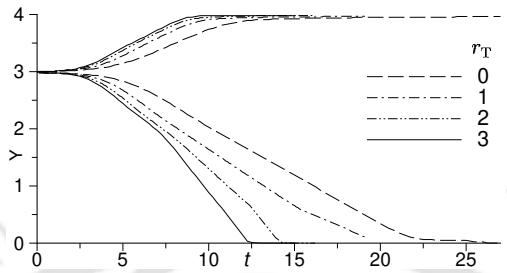

Figure 3.16: Time variation of spike front and bubble tip locations for various temperature ratios r_T = 0-3 (rest of the parameters are: $\rho_r = 2$, $m = 2$, $k_r = 2$, $c_{p_r} = 2$, $Re = 50$, $Fr = 1$, $We = 150$ and $Pr = 1$).

3.3.5 Effect of hot and cold wall locations

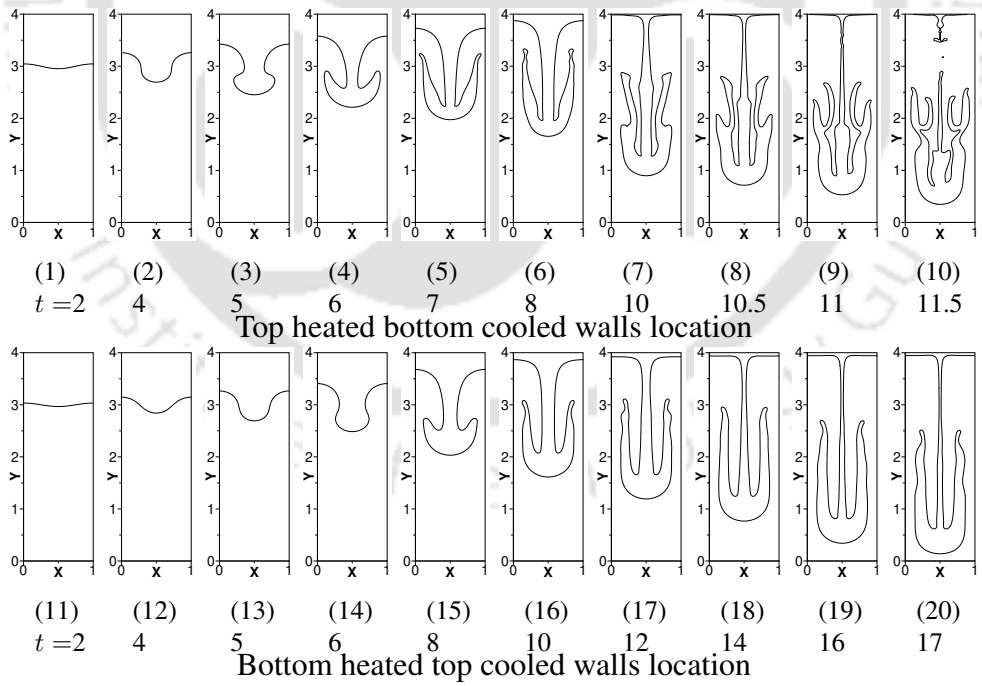

Figure 3.17: Instantaneous interface profiles for both the cases of heating and cooling walls location (rest of the parameters are: $\rho_r = 2$, $m = 2$, $k_r = 2$, $c_{p_r} = 2$, $Re = 50$, $Fr = 1$, $We = 150$, $Pr = 1$ and $r_T = 3$).

The effect of hot and cold wall locations on the instability is studied for two types of configurations. For the first configuration, the hot wall is located at the bottom while the cold wall is located

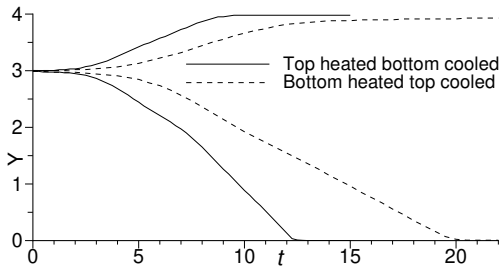

Figure 3.18: Time variation of spike front and bubble tip locations for two different hot and cold wall locations.

at the top. For the second configuration, locations of hot and cold walls are interchanged such that the hot and cold walls are located at the top and bottom, respectively. In both the cases, hot and cold walls are kept at dimensionless temperatures $\theta = r_T = 3$ and $\theta = 0$, respectively. For both the configurations, fluid viscosity is specified to vary exponentially with temperature. In bottom heated configuration, fluid viscosity in bottom layer increases from the bottom heated wall to the interface and fluid viscosity in top layer increases from the interface to the top cooled wall. In top heated configuration, fluid viscosity in bottom layer decreases from the bottom cooled wall to the interface and fluid viscosity in top layer decreases from the interface to the top heated wall. Due to such differences in viscosity variation in both the fluid layers, the instability may differ from each other as the heating configuration is changed.

Fig. 3.17 shows the instability evolution for both the configurations. For the bottom heated configuration, top denser fluid forms a mushroom shaped spike which eventually deforms, and with time, an elongated arm forms on both sides of the spike head. The spike is found to be attached to the top wall with spike stem throughout the spike movement. For the top heated configuration, a mushroom shaped spike forms with an elongated arm attached on both sides of the spike head. With time, both the elongated arms split into two branches and the spike detaches from the top wall upon breaking of stem of the spike. It can be observed that change in location of hot and cold walls shows a significant effect on the instability. For the bottom heated configuration, the spike forms with relatively simpler arms compared to that of the top heated configuration.

Time variation of spike front and bubble tip locations is presented in Fig. 3.18 for both the configurations. For the bottom heated configuration, the spike strikes the bottom wall at about dimensionless time $t = 20$, and for the top heated configuration, the spike strikes the bottom wall at about dimensionless time $t = 12$, almost two times faster. Overall, the bottom heated configuration shows relatively more stabilizing effect on the instability than that of the top heated configuration.

3.3.6 Effect of Prandtl number

Prandtl number effect on instability is studied for various Prandtl numbers in the range of 0.01 to 100 and the instability is presented in Fig. 3.19. It can be observed from the figure that the spike forms with splitted arm on both sides of the spike, showing qualitative similarity for all the Prandtl numbers. Unlike for the other Prandtl numbers, for Prandtl number 100, the arm adjacent to the spike stem

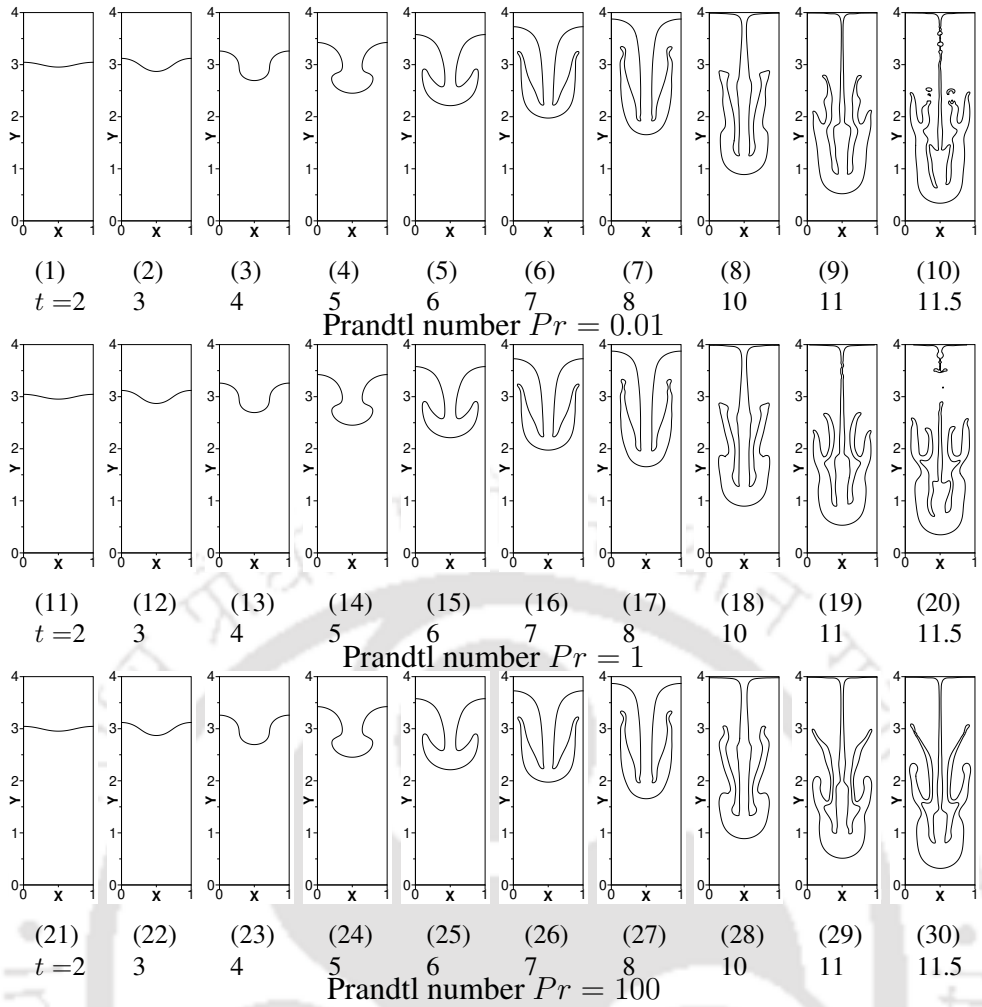

Figure 3.19: Instantaneous interface profiles for various Prandtl numbers in the range of $Pr = 0.01$-100 (rest of the parameters are: $\rho_r = 2$, $m = 2$, $k_r = 2$, $c_{p_r} = 2$, $Re = 50$, $Fr = 1$, $We = 150$ and $r_T = 3$).

forms relatively longer than that of the outer arm. Overall, the instability is almost same and found to be almost unaffected by Prandtl number variation. This is due to the fact that hydrodynamics of the instability happens within short span of time such that influence of heat diffusion on the instability is insignificant. Fig. 3.20 shows the time variation of spike front and bubble tip locations for various Prandtl numbers. The figure also reconfirms that the effect of Prandtl number on the instability is negligibly small. The time variation of spike front and bubble locations are found to be almost same, and the spike strikes the bottom wall at about dimensionless time $t = 12$ for different Prandtl numbers.

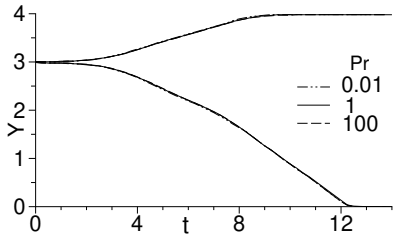

Figure 3.20: Time variation of spike front and bubble tip locations for various Prandtl numbers $Pr =$ 0.01-100 (rest of the parameters are: $\rho_r = 2$, $m = 2$, $k_r = 2$, $c_{p_r} = 2$, $Re = 50$, $We = 150$, $Fr = 1$ and $r_T = 3$).

3.3.7 Effect of Weber number

Rayleigh-Taylor instability is studied for the effect of Weber number in viscosity stratified two fluid layers. The study is carried out for various Weber numbers, inversely proportional to the surface tension, in the range of 0 to infinity. The instability evolution is presented in Figs. 3.21-3.22. For the set of parameters of study, a critical value of Weber number 0.1 is found below which the configuration does not undergo instability. Surface tension along the interface acts similar to an elastic membrane. For Weber number less than the critical value, the strength of the elastic nature is sufficient enough to hold the heavier fluid layer over the lighter fluid layer. As Weber number increases, the strength of elastic nature of the interface decreases and the configuration undergoes instability. For Weber numbers in the range of 0.1 to 39 (for example, see Fig. 3.21, for $We = 20$), the spike comes down along one of the side boundaries of the domain, instead of coming down along the mid vertical plane of the domain. To find more about the results, for Weber number in the range of 0.1 to 39, simulations are carried out with domain of dimensionless width higher than unit width. With higher domain width, simulations are carried out with symmetry condition on left and right side vertical boundaries, and the initial perturbation is specified according to $0.01\cos(2\pi x/L)$ (dimensionless spatial periodicity of the initial perturbation is of one unit). When the dimensionless domain width is increased to greater than a certain value, the solutions of the instability are found with spike coming down through mid vertical plane of the domain. For example, for Weber number 39, when a domain of dimensionless width of about 1.15 or higher is used, the spike comes down through the mid vertical plane of the domain. Similarly for Weber number 30, when a domain of dimensionless width of about 1.25 or higher is used, the spike comes down through the mid vertical plane. This means that for Weber number 30, spatial periodicity of the instability is more than 1.25 times that of the initial perturbation. For Weber number 20, the spike comes down through the mid vertical plane in a domain of dimensionless width of about 1.5 or higher. This shows that the spatial periodicity of the instability is more than 1.5 times that of the initial perturbation. This infers that for Weber number in this range ($We = 0.1$-39), the spatial periodicity of the instability is higher than the spatial periodicity of the initial perturbation.

For Weber number more than 39, the spike comes down through mid vertical plane of the domain (for example, see Fig. 3.21, for $We = 40$). This means the spatial periodicity of the instability is same as that of the spatial periodicity of the initial perturbation. For Weber number 40, the spike

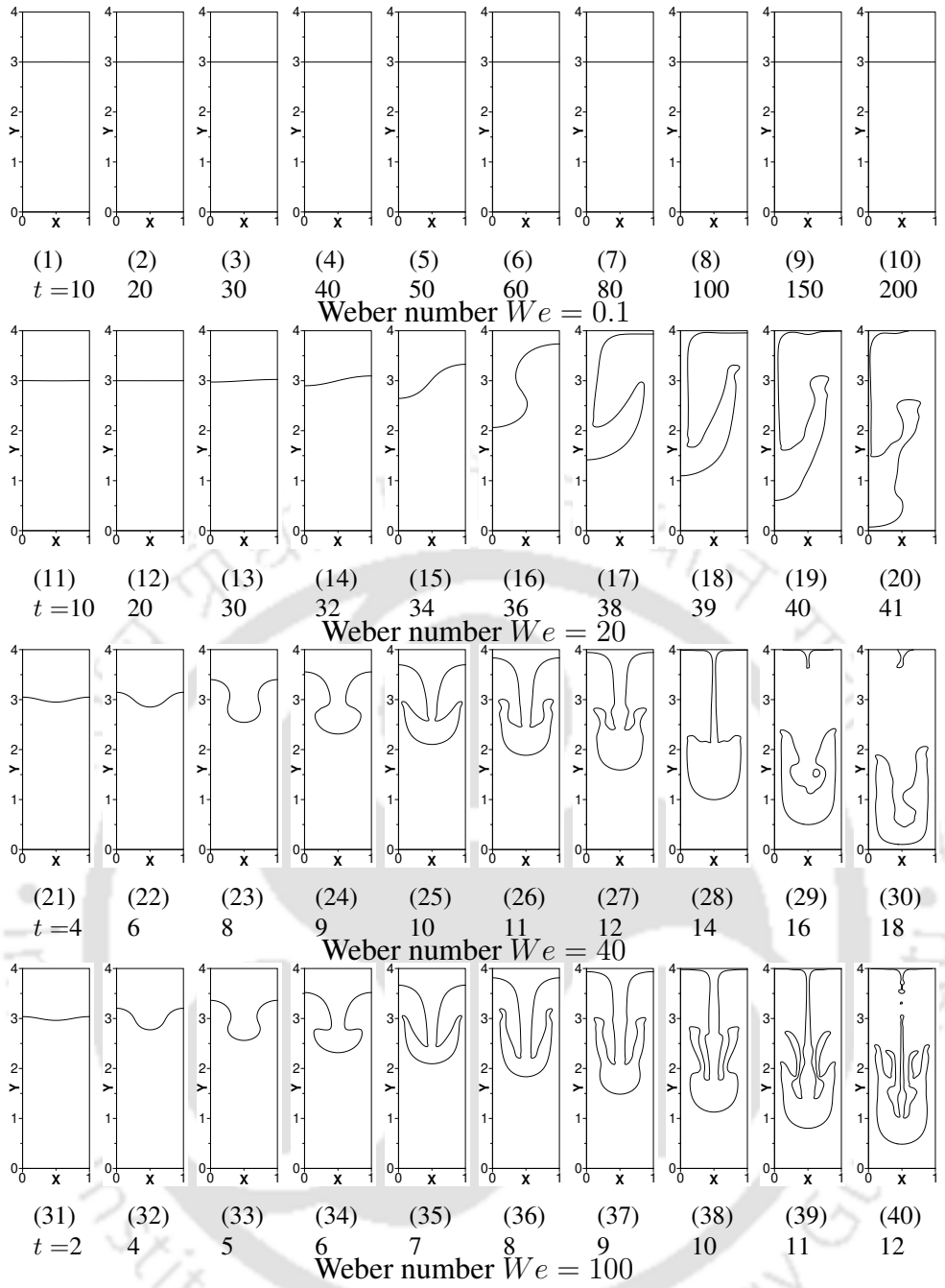

Figure 3.21: Instantaneous interface profiles for various Weber numbers in the range of $We = 10$-100 (rest of the parameters are: $\rho_r = 2$, $m = 2$, $k_r = 2$, $c_{p_r} = 2$, $Re = 50$, $Fr = 1$, $Pr = 1$ and $r_T = 3$).

forms into a mushroom shape which eventually deforms, and with time, an arm forms on both sides of the spike head. As the spike comes down towards the bottom wall, stem of the spike breaks, and the spike strikes the bottom wall in the form of a fluid droplet. With increasing Weber number, the spike-arm structure deforms more and the spike moves relatively faster. For Weber number in the range of 100–150, the arm attached to the spike head on both sides is splitted into two branches, and the branches stretch apart as spike moves towards the bottom wall. For Weber number 500-1000, the arm attached to the spike head becomes relatively thinner, longer and smoother. For Weber number tends to infinity, surface tension tends to zero, spike deforms more and thin elongated arm is formed on the spike head. With time, end portion of the thin elongated arm breaks as spike moves faster

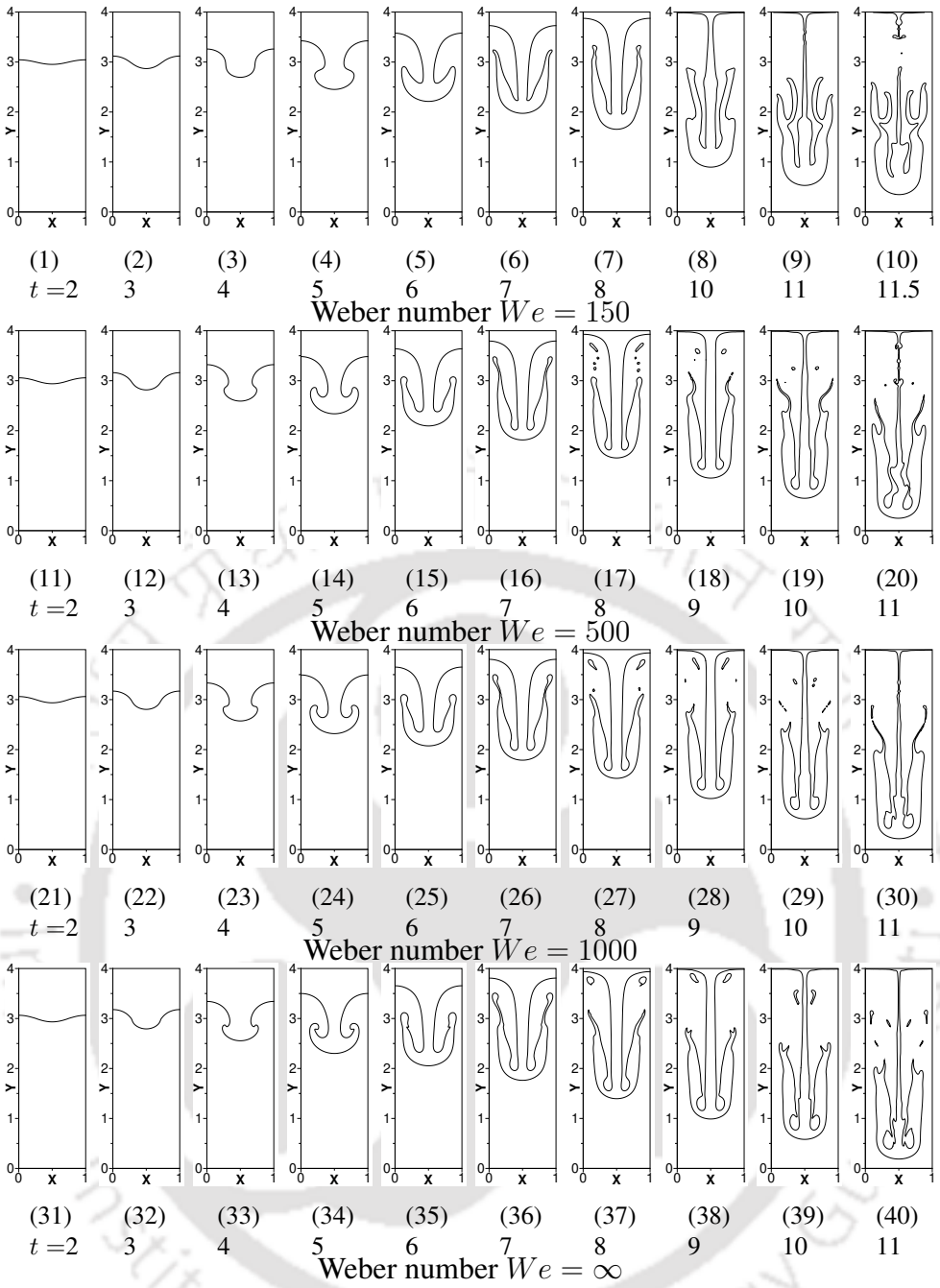

Figure 3.22: Instantaneous interface profiles for various Weber numbers in the range of $We = 150$ to ∞ (rest of the parameters are: $\rho_r = 2$, $m = 2$, $k_r = 2$, $c_{p_r} = 2$, $Re = 50$, $Fr = 1$, $Pr = 1$ and $r_T = 3$).

towards the bottom wall. It is observed that increasing Weber number results in larger deformation of the spike with faster spike movement. The present study results are inline with results of analytical study of Drazin and Reid [236] and numerical study of Strubelj and Tiselj [237].

Fig. 3.23 shows time variation of spike front and bubble tip locations for various Weber numbers. Presence of surface tension affects the rate of spike and bubble movement significantly. For Weber number 20, the heavier fluid spike strikes the bottom wall at about dimensionless time $t = 41$, and for Weber number tends to infinity, the heavier fluid spike strikes the bottom wall at asymptotic minimum value of dimensionless time $t = 11$, almost four times faster. For Weber number more than the critical

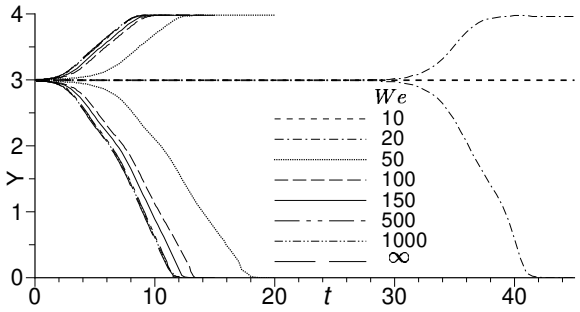

Figure 3.23: Time variation of spike front and bubble tip locations for various Weber number in the range of $We = 10$ to ∞ (rest of the parameters are: $\rho_r = 2$, $m = 2$, $k_r = 2$, $c_{p_r} = 2$, $Re = 50$, $Pr = 1$, $Fr = 1$ and $r_T = 3$).

value, increasing Weber number shows destabilizing effect on the instability.

3.4 Conclusions

Rayleigh-Taylor instability is studied in viscous stratified fluid layers in 2-D rectangular coordinates. Viscosity in both the fluid layers are specified to vary exponentially with temperature. For variable viscosity fluid layers, formation of spike into a fluid column like structure occurs at higher viscosity ratio compared to that of constant viscosity fluid layers. Increasing viscosity ratio shows stabilizing effect on the instability. For viscosity ratio 200, time taken by spike to strike the bottom wall is increased to almost 4 times compared to that of viscosity ratio 1. With increasing temperature ratio, spike undergoes larger deformation with faster spike movement than that of lower temperature ratios. For temperature ratio 3, time taken by spike to strike the bottom wall is reduced to half compared to that of temperature ratio 0. Top heated configuration is relatively more unstable than that of bottom heated configuration. Effect of Prandtl number variation on the instability is negligible. For Weber number less than critical value of 0.1, the configuration does not undergo instability, and beyond the critical value, increasing Weber number shows destabilizing effect on the instability. For Weber number in the range of 0.1 to 39, the spike comes down through one of the side vertical boundaries of the domain representing higher value of spatial periodicity of the instability than that of the initial perturbation. For Weber number more than 39, the spike comes down through mid vertical plane representing spatial periodicity of the instability is same as that of the initial perturbation.

Chapter 4

Effect of functional variation of viscosity with temperature on Rayleigh-Taylor instability in 2-D rectangular coordinates

In the present chapter, effect of functional variation of viscosity with temperature on Rayleigh-Taylor instability is studied in 2-D rectangular coordinates. The effect of functional variation of viscosity with temperature on the instability is studied for four types of functional variations of viscosity with temperature.

4.1 Physical system

The physical system described in subsection 2.1.1 is used for the study presented in this chapter. Schematic of the physical system is shown in Fig. 2.2.

4.2 Mathematical treatment

For the study presented in this chapter, numerical simulations are carried out using the present developed code which is based on level set method. In level set method, an additional level set equation is solved to find the interface location. The governing equations consist of continuity, momentum, energy and level set equations.

4.2.1 Scaling parameters

For the present study, different reference scales are chosen to non-dimensionalize the governing equations. The reference scales for time, length, velocity, pressure, temperature and surface tension are taken equal to $\tilde{L}_{\text{ref}}/\tilde{V}_{\text{ref}}$, $\tilde{L}_{\text{ref}}$, $\tilde{V}_{\text{ref}}$, $\tilde{\rho}_{\text{ref}}\,\tilde{V}_{\text{ref}}^2$, $\tilde{T}_{\text{ref}}$ and $\tilde{\sigma}_{\text{ref}}$, respectively. Reference length is chosen equal to width of the domain ($\tilde{L}$). Reference velocity is chosen equal to $\tilde{V}_{\text{ref}} = \left(\tilde{g}\,\tilde{L}_{\text{ref}}\right)^{1/2}$. Reference temperature is chosen equal to cold wall temperature ($\tilde{T}_2$). Reference surface tension is taken equal to $\tilde{\sigma}_0$, which is surface tension value at reference temperature. Reference fluid properties such as density,

viscosity, thermal conductivity and heat capacity are chosen equal to respective fluid properties of 'Fluid 2' which are equal to $\tilde{\rho}_2$, $\tilde{\mu}_2$, $\tilde{k}_2$ and $\tilde{c}_{p_2}$, respectively. The reference variables chosen are given as following.

$$\begin{gathered}\tilde{L}_{\text{ref}} = \tilde{L}, \quad \tilde{\rho}_{\text{ref}} = \tilde{\rho}_2, \quad \tilde{k}_{\text{ref}} = \tilde{k}_2, \quad \tilde{\mu}_{\text{ref}} = \tilde{\mu}_2, \quad \tilde{c}_{p_{\text{ref}}} = \tilde{c}_{p_2}, \\ \tilde{V}_{\text{ref}} = \sqrt{\tilde{g}\,\tilde{L}}, \quad \tilde{T}_{\text{ref}} = \tilde{T}_2, \quad \tilde{\sigma}_{\text{ref}} = \tilde{\sigma}_0, \quad \tilde{\phi}_{\text{ref}} = \tilde{L}\end{gathered} \tag{4.1}$$

With the above choice of reference values, definitions of dimensionless variables, which are given by Eq. (2.14), become

$$\begin{gathered}x = \frac{\tilde{x}}{\tilde{L}}, \quad y = \frac{\tilde{y}}{\tilde{L}}, \quad \rho = \frac{\tilde{\rho}}{\tilde{\rho}_2}, \quad k = \frac{\tilde{k}}{\tilde{k}_2}, \quad \mu = \frac{\tilde{\mu}}{\tilde{\mu}_2}, \quad c_p = \frac{\tilde{c_p}}{\tilde{c}_{p_2}}, \\ t = \frac{\tilde{t}}{\sqrt{\tilde{L}/\tilde{g}}}, \quad \mathbf{u} = \frac{\tilde{\mathbf{u}}}{\sqrt{\tilde{g}\,\tilde{L}}}, \quad p = \frac{\tilde{p}}{\tilde{\rho}_2\,\tilde{g}\,\tilde{L}}, \quad \theta = \frac{\tilde{T} - \tilde{T}_2}{\tilde{T}_2}, \quad \phi = \frac{\tilde{\phi}}{\tilde{L}}, \quad \sigma = \frac{\tilde{\sigma}}{\tilde{\sigma}_0}\end{gathered} \tag{4.2}$$

4.2.2 Governing equations

With the use of the above dimensionless variables, the governing equations are non-dimensionalized and given as following.

Continuity equation

$$\nabla\cdot\mathbf{u} = 0 \tag{4.3}$$

Momentum equation

$$\rho\left(\frac{\partial\mathbf{u}}{\partial t} + \mathbf{u}\cdot\nabla\mathbf{u}\right) = -\nabla p + \frac{1}{Re}\nabla\cdot\mu\left(\nabla\mathbf{u} + \nabla\mathbf{u}^{\mathrm{T}}\right) + \mathbf{F} \tag{4.4}$$

Energy equation

$$\rho\, c_p\left(\frac{\partial\theta}{\partial t} + \mathbf{u}\cdot\nabla\theta\right) = \frac{1}{Re\,Pr}\nabla\cdot(k\nabla\theta) \tag{4.5}$$

Level set equation

$$\frac{\partial\phi}{\partial t} + \mathbf{u}\cdot\nabla\phi = 0 \tag{4.6}$$

Here, dimensionless body force term ($\mathbf{F}$) used in the momentum equation for constant surface tension, as given by Eq. (2.23), is expressed as

$$\mathbf{F} = \mathbf{F}_\sigma - \frac{\rho}{Fr}\mathbf{e}_j = \frac{1}{We}\,\kappa\,\delta\,\mathbf{n} - \frac{\rho}{Fr}\,\mathbf{e}_j \tag{4.7}$$

Different dimensionless numbers used in the governing equations, as given by Eq. (2.24), are defined as following.

$$Re = \frac{\tilde{\rho}_2\,\tilde{g}^{1/2}\,\tilde{L}^{3/2}}{\tilde{\mu}_2}, \quad Fr = 1, \quad We = \frac{\tilde{\rho}_2\,\tilde{g}\,\tilde{L}^2}{\tilde{\sigma_0}}, \quad Pr = \frac{\tilde{\mu}_2\tilde{c}_{p_2}}{\tilde{k}_2} \tag{4.8}$$

4.2.3 Functional variations of viscosity with temperature in the fluid layers

In the present study, four different types of functional variations of viscosity with temperature are considered for the fluid layers, which are constant, linear, power law and exponential variations. These functional variations of viscosity with temperature are based on the past studies [12, 52, 53, 64–72, 74–76], which are given as following. Constant viscosity, which was also used in the studies of [7, 32, 37, 71, 72], is expressed as

$$\mu_1 = m \qquad \text{and} \qquad \mu_2 = 1 \tag{4.9}$$

Linearly varying temperature dependent viscosity, which was also used in the studies of Wall and Wilson [67], Tripathi et al. [73] and Dhiman and Sharma [76], is expressed as

$$\mu_1 = m\,(a + b\,\theta) \qquad \text{and} \qquad \mu_2 = (a + b\,\theta) \tag{4.10}$$

Here, values of a and b are constants taken equal to 1 and -0.2, respectively. Power law varying temperature dependent viscosity, which was also used in the studies of Tripathi and Sahu [12], Nahme [64] and Balla et al. [75], is expressed as

$$\mu_1 = m\,(a + b\,\theta^{3/2}) \qquad \text{and} \qquad \mu_2 = (a + b\,\theta^{3/2}) \tag{4.11}$$

Here, $a = 1$ and $b = 0.2$. In Eq. (4.10) and Eq. (4.11), the value of a and b are chosen such that viscosities of fluids in both the layers (μ_1 and μ_2) are always positive. Exponentially varying temperature dependent viscosity, which was also used in the studies of [52, 53, 64–67, 69, 70], is expressed as

$$\mu_1 = m\,e^{-\theta} \qquad \text{and} \qquad \mu_2 = e^{-\theta} \tag{4.12}$$

In the above viscosity variations, m is viscosity ratio ($\mu_1(\tilde{T}_2)/\mu_2(\tilde{T}_2)$) which is ratio of top heavier fluid to bottom lighter fluid viscosities at reference temperature. In level set method, fluid properties such as density (ρ), thermal conductivity (k), heat capacity (c_p) and viscosity (μ) in dimensionless form are calculated using heaviside function (H), as given by Eq. (2.26), according to the following expressions

$$\begin{aligned} \rho &= \rho_2 + (\rho_1 - \rho_2)\,H \\ \mu &= \mu_2 + (\mu_1 - \mu_2)\,H \\ k &= k_2 + (k_1 - k_2)\,H \\ c_p &= c_{p2} + (c_{p1} - c_{p2})\,H \end{aligned} \tag{4.13}$$

4.2.4 Initial and boundary conditions

For the study presented in this chapter, the initial and boundary conditions given in subsection 2.2.2 are used. Dimensions of the domain used for the present study are given in the same subsection.

4.2.5 Numerical methodology

The numerical methodology of the present developed code are presented in subsections 2.2.4–2.2.5. The validations of the developed code for simulation of multiphase flow in 2-D rectangular coordinates are given in section 2.3.

4.3 Results and discussions

4.3.1 Baseline parameter values

Study on effect of functional variations of viscosity on Rayleigh-Taylor instability is carried out in 2-D rectangular coordinates for the four types of viscosity variations with temperature. The four types of functional variations of viscosity with temperature are constant, linear, power law and exponential variations. A set of baseline parameter values are chosen for the study, which are given as following. The baseline values for top heavier fluid to bottom lighter fluid density ratio (ρ_r), viscosity ratio (m), heat capacity ratio (c_{p_r}), thermal conductivity ratio (k_r), all are chosen equal to 2. Temperature ratio (r_T) is chosen equal to 3. Values of Reynolds number (Re), Weber number (We), Froude number (Fr) and Prandtl number (Pr) are chosen equal to 50, 150, 1 and 1, respectively. Study on the effect of functional variations of viscosity with temperature on the instability is carried out for various viscosity ratios and various density ratios. Effect of a particular parameter is studied by varying that particular parameter while the rest of the parameter values are kept at the corresponding above baseline parameter values.

4.3.2 Effect of functional variation of viscosity with temperature for various viscosity ratios

Effect of functional variation of viscosity with temperature on Rayleigh-Taylor instability is studied for various viscosity ratios in the range of 2 to 200 for the four types of functional variations. For the different types of viscosity variations, fluid viscosities in both top and bottom layers vary differently with temperature based on the type of viscosity variation. For example, for constant viscosity, viscosities of top and bottom layer fluids are constant, independent of temperature. For linearly varying viscosity, fluid viscosity decreases linearly with increasing temperature according to Eq. (4.10). For power law varying viscosity, fluid viscosity increases with increasing temperature according to Eq. (4.11). For exponentially varying viscosity, fluid viscosity decreases exponentially with increasing temperature according to Eq. (4.12). Since, top and bottom walls are maintained at higher and lower temperatures, respectively, the temperature decreases from the top wall to interface and it again decreases from interface to the top wall. Since, viscosity decreases with temperature in linear and exponential viscosity variations. For these variations, viscosity in bottom layer decreases from the bottom wall to interface and it again decreases from interface to the top wall. As viscosity increases with temperature in power law viscosity variation, fluid viscosity in bottom layer increases from the bottom wall to interface and it again increases from interface to the top wall. Due to such difference in

viscosity variations for different types of functional variations of viscosity, the instability may largely differ for different viscosity variations.

In initial stage of the instability, a mushroom shaped spike forms for all the four types of viscosity variations. In later stage of the instability, the shape of the spike and evolution of the instability differs significantly for different types of viscosity variations. For viscosity ratio 2, the instability evolution for the four types of viscosity variations is presented in Fig. 4.1. For constant viscosity, a mushroom shaped spike forms with an arm on both sides of the spike which deforms further, and with time, the arm elongates as the spike moves towards the bottom wall. For linear variation, the spike-arm structure shows qualitative similarity compared with that of constant viscosity. However, for linear variation, the arm elongates more and stem of the spike breaks before the spike strikes the bottom wall, unlike for constant viscosity. For power law variation, the mushroom shaped spike forms with relatively shorter arm compared to that of constant viscosity. For exponential variation, an elongated arm forms on both sides of the spike head. With time, the arm splits into two branches and stem of the spike is broken before striking the bottom wall. Spike deformation for the exponential viscosity variation is relatively higher compared to those of the other three types of viscosity variations. Time variation of spike front and bubble tip locations is presented in Fig. 4.2 for viscosity ratio 2. The figure shows that for exponential, linear, constant and power law variations, the spike strikes the bottom wall at about dimensionless time $t = 12$, 18, 22 and 26, respectively. For power law variation, rate of spike movement is almost half of that of exponential variation.

Fig. 4.3 shows the instability evolution for the four types of viscosity variations for viscosity ratio 10. For both constant and linear viscosity variations, spike-arm structure is similar with a shorter arms. For power law viscosity variation, the spike forms without any arm. For exponential viscosity variation, the spike stem is broken before the spike front reaches the bottom wall, unlike, whereas the breaking of the spike stem does not take place for the other three types of variations. For exponential variation, the spike forms with relatively thicker and longer arms on both sides of the spike head. As spike moves towards the bottom wall, the stem of the spike breaks and both the arms become more wavy. Time variation of spike front and bubble tip locations is presented in Fig. 4.4 for viscosity ratio 10. For exponential, linear, constant and power law variations, spike strikes the bottom wall at about dimensionless time $t = 15$, 25, 35 and 45, respectively. For exponential variation, rate of spike movement is almost 3 times compared to that of power law variation.

For viscosity ratio 20, the instability evolution is presented in Fig. 4.5 for the four types of viscosity variations. For both constant and power law viscosity variations, the spike form into thick finger like pattern. For power law variation, shape of the spike head is relatively smaller compare to that of constant viscosity. For linear variation, a spike with bigger head is formed which eventually deforms and a short arm forms on both sides of the spike. For exponential variation, a spike with an attached arm on both the sides is formed. With time, both the arms become thicker, eventually become longer and more wavy. The stem of the spike breaks before the spike head strikes the bottom wall, unlike for the other types of viscosity variations. The time variation of spike front and bubble tip locations

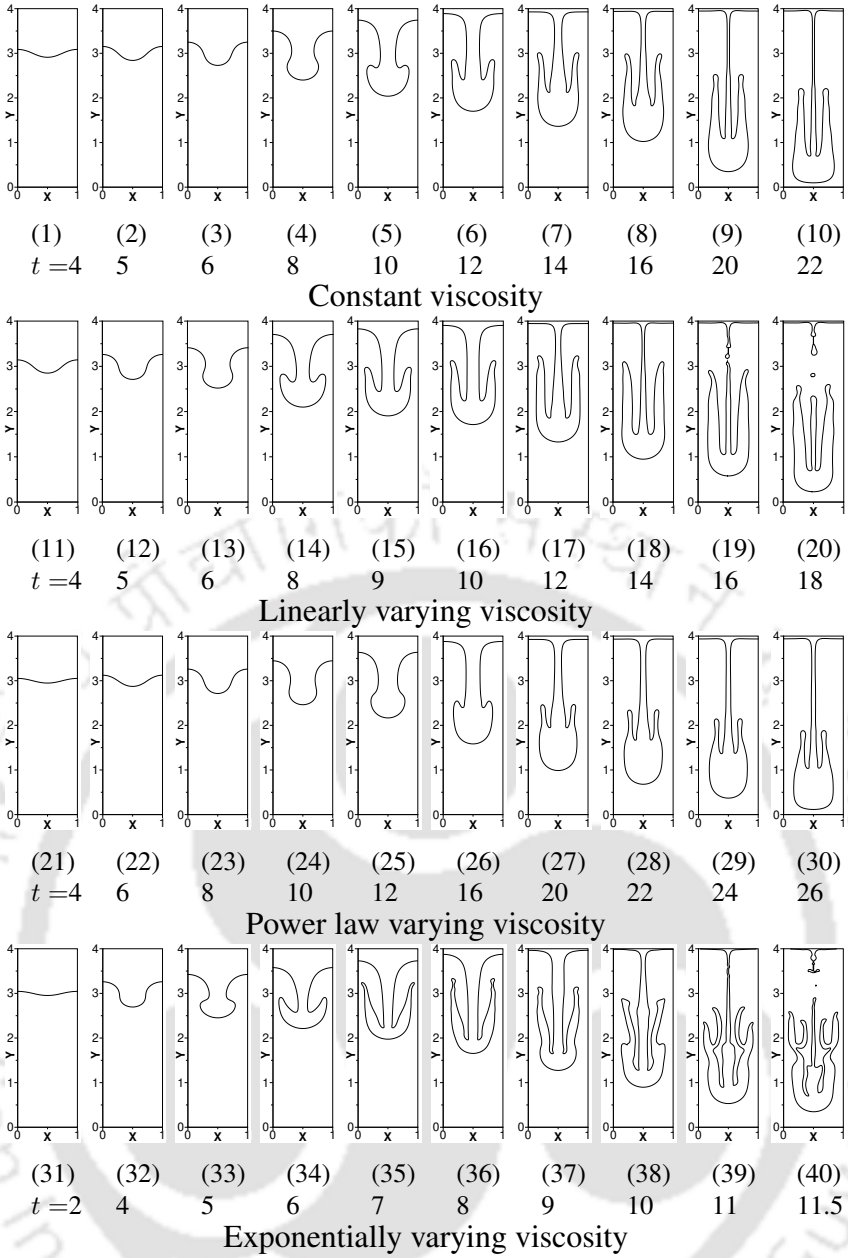

Figure 4.1: Instantaneous interface profiles for the four types of viscosity variations with viscosity ratio $m = 2$ (rest of the parameters are: $\rho_r = 2$, $c_{p_r} = 2$, $k_r = 2$, $Re = 50$, $Pr = 1$, $Fr = 1$, $We = 150$ and $r_T = 3$).

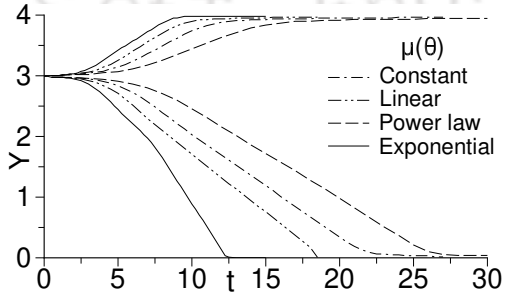

Figure 4.2: Time variation of spike front and bubble tip locations for the four types of viscosity variations with viscosity ratio $m = 2$ (rest of the parameters are: $\rho_r = 2$, $c_{p_r} = 2$, $k_r = 2$, $Re = 50$, $Pr = 1$, $Fr = 1$, $We = 150$ and $r_T = 3$).

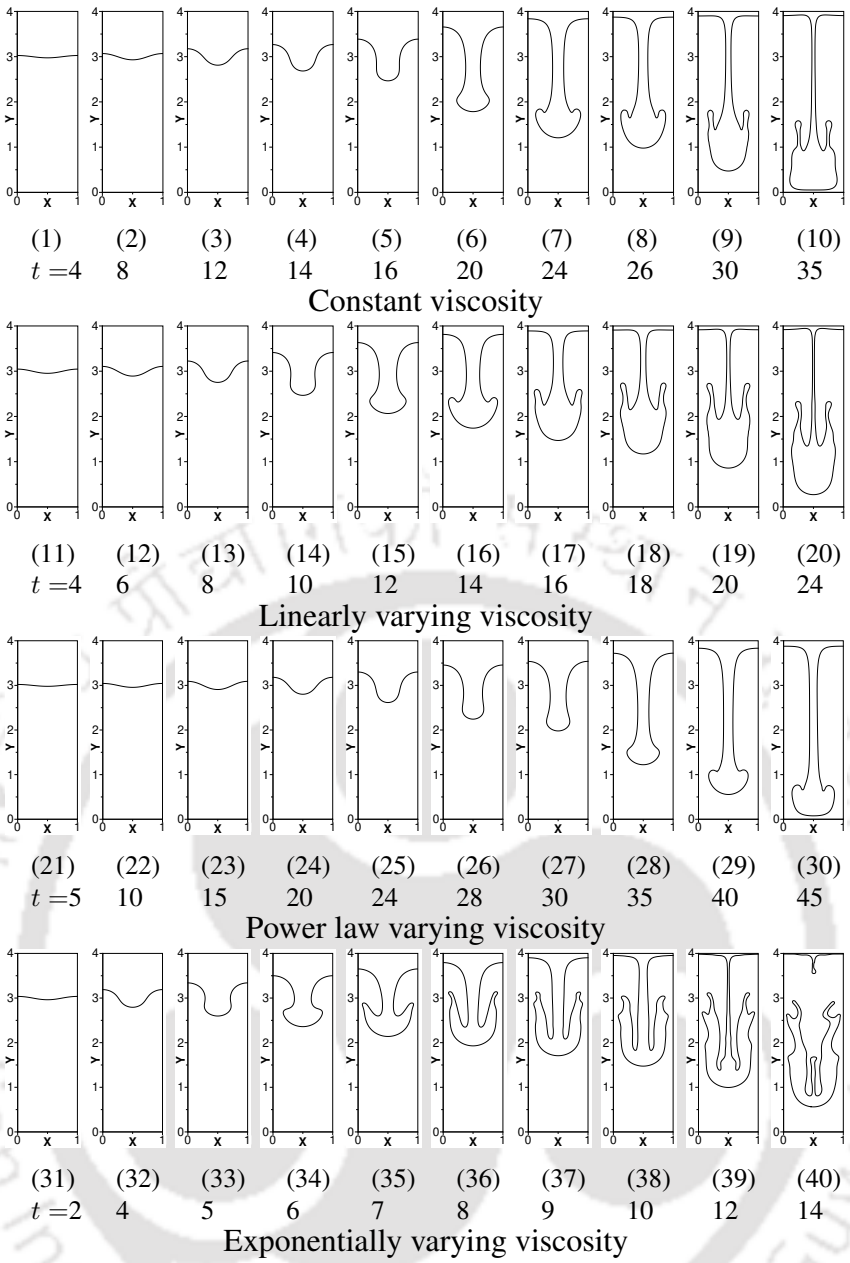

Figure 4.3: Instantaneous interface profiles for the four types of viscosity variations with viscosity ratio $m = 10$ (rest of the parameters are: $\rho_r = 2$, $c_{p_r} = 2$, $k_r = 2$, $Re = 50$, $Pr = 1$, $Fr = 1$, $We = 150$ and $r_T = 3$).

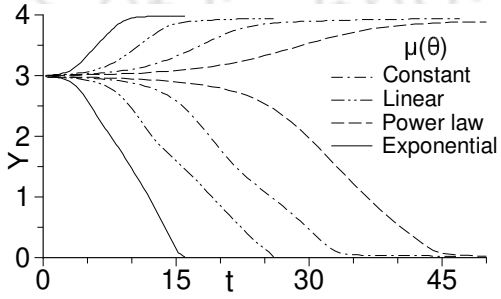

Figure 4.4: Time variation of spike front and bubble tip locations for the four types of viscosity variations with viscosity ratio $m = 10$ (rest of the parameters are: $\rho_r = 2$, $c_{p_r} = 2$, $k_r = 2$, $Re = 50$, $Pr = 1$, $Fr = 1$, $We = 150$ and $r_T = 3$)

is presented in Fig. 4.6 for viscosity ratio 20. From the figure, it can be observed that for exponential, linear, constant and power law variations, the spike front strikes the bottom wall at about dimensionless time $t = 18$, 35, 45 and 65, respectively. For power law variation, time taken by the spike to strike the bottom wall is almost 3.5 times compared to that of exponential variation.

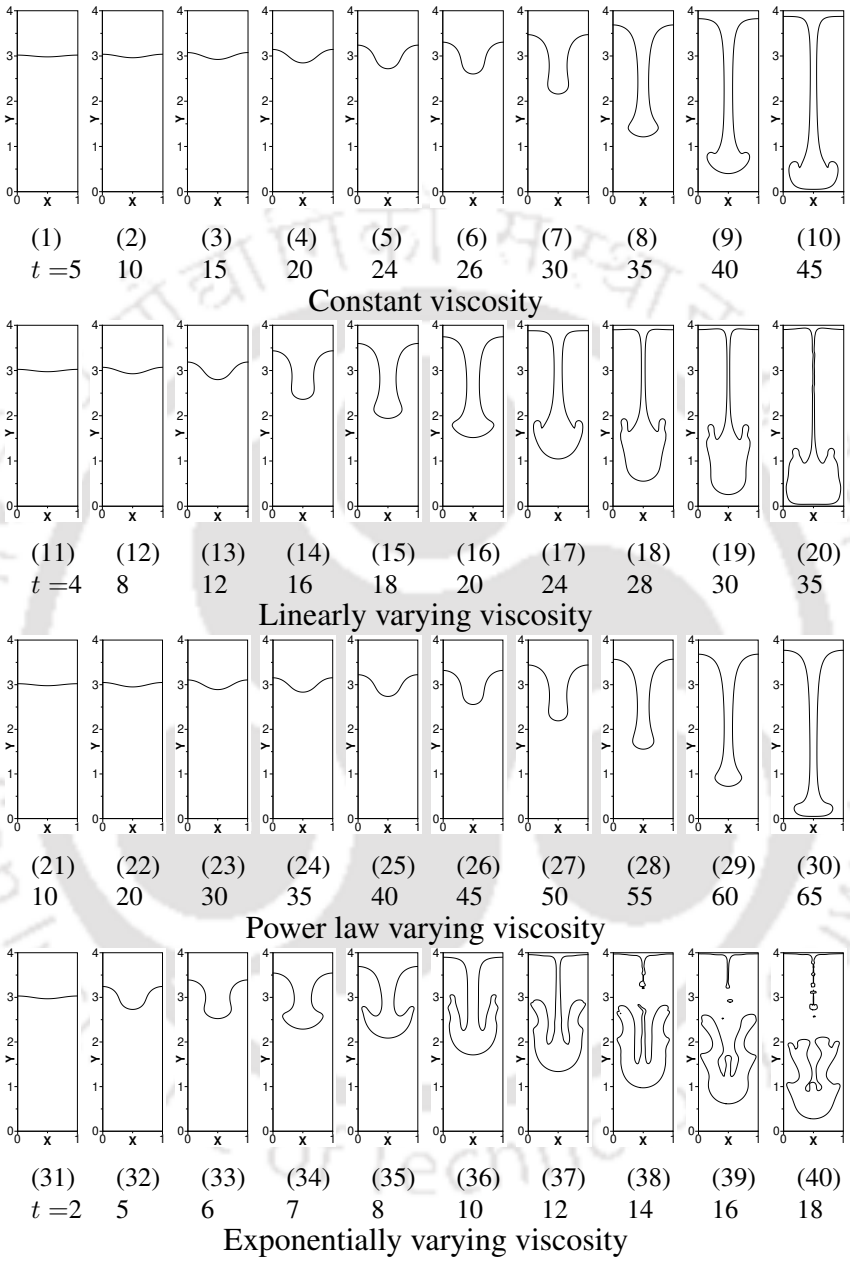

Figure 4.5: Instantaneous interface profiles for the four types of viscosity variations with viscosity ratio $m = 20$ (rest of the parameters are: $\rho_r = 2$, $c_{p_r} = 2$, $k_r = 2$, $Re = 50$, $Pr = 1$, $Fr = 1$, $We = 150$ and $r_T = 3$).

Fig. 4.7 shows the instability evolution for the four types of viscosity variations for viscosity ratio 50. As the viscosity ratio increases, spike forms in a thick finger like pattern without any arm which shows qualitative similarity for constant, power law and linear variations. The finger like pattern of the spike represents fluid column structure. Whereas for exponential variation, a mushroom shaped spike forms which eventually deforms and a thick arm forms on both sides of the spike. With time,

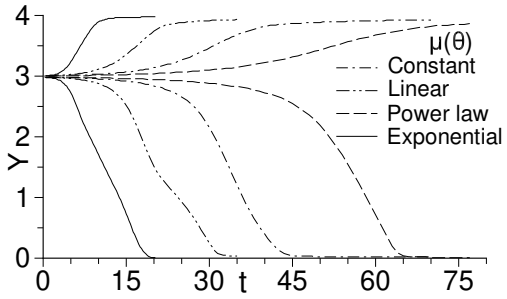

Figure 4.6: Time variation of spike front and bubble tip locations for the four types of viscosity variations with viscosity ratio $m = 20$ (rest of the parameters are: $\rho_r = 2$, $c_{p_r} = 2$, $k_r = 2$, $Re = 50$, $Pr = 1$, $Fr = 1$, $We = 150$ and $r_T = 3$).

stem of the spike breaks and the spike moves towards the bottom wall in the form of a droplet. Time variation of spike and bubble tip locations is shown in Fig. 4.8 for viscosity ratio 50. For exponential, linear, constant and power law variations, the spike strikes the bottom wall at about dimensionless time $t = 24$, 45, 80 and 130, respectively. For exponential variation, rate of spike movement is almost 5 times compared to that of power law variation.

Fig. 4.9 shows the instability evolution for the four types of viscosity variations for viscosity ratio of 100. With increased viscosity ratio, the spike forms into a fluid column like structure, showing a qualitative similarity for all the four types of viscosity variations. For exponential variation, the spike forms with bigger head compared to the other three types of viscosity variations. However, for exponential variation, stem of the spike breaks before striking the bottom wall, unlike the other three types of viscosity variations. After breaking of the stem, the spike moves towards the bottom wall in a form of a droplet. Time variation of spike front and bubble tip locations is shown in Fig. 4.10. The figure shows that the spike front strikes the bottom wall at about dimensionless time $t = 28$, 75, 146 and 235 for exponential, linear, constant and power law variations, respectively. For exponential variation, rate spike movement is almost 8 times compared to that of power law variation.

Instability evolution for viscosity ratio 200 is plotted in Fig. 4.11 for the four types of viscosity variations. From the figure it can observed that instability shows a qualitative similarity and the spike forms into fluid column like structure with non breaking stem, for the four types of viscosity variations. For exponential variation, the spike is found to form with relatively bigger head compared to that of the other three types of variations. Time variation of spike front and bubble tip locations is plotted in Fig. 4.12 for viscosity ratio 200. Even though shape of interface is qualitatively similar for all the four types of viscosity variation, but, the time taken by the heavier fluid spike to strike to the bottom wall differs largely for different types of viscosity variations. From the figure, it can be observed that for exponential, linear, constant and power law variations, the spike strikes the bottom wall at about dimensionless time $t = 36$, 130, 280 and 405, respectively. This is due to the fact that overall effective viscosity variation is arranged in the reverse order of rate of spike movement.

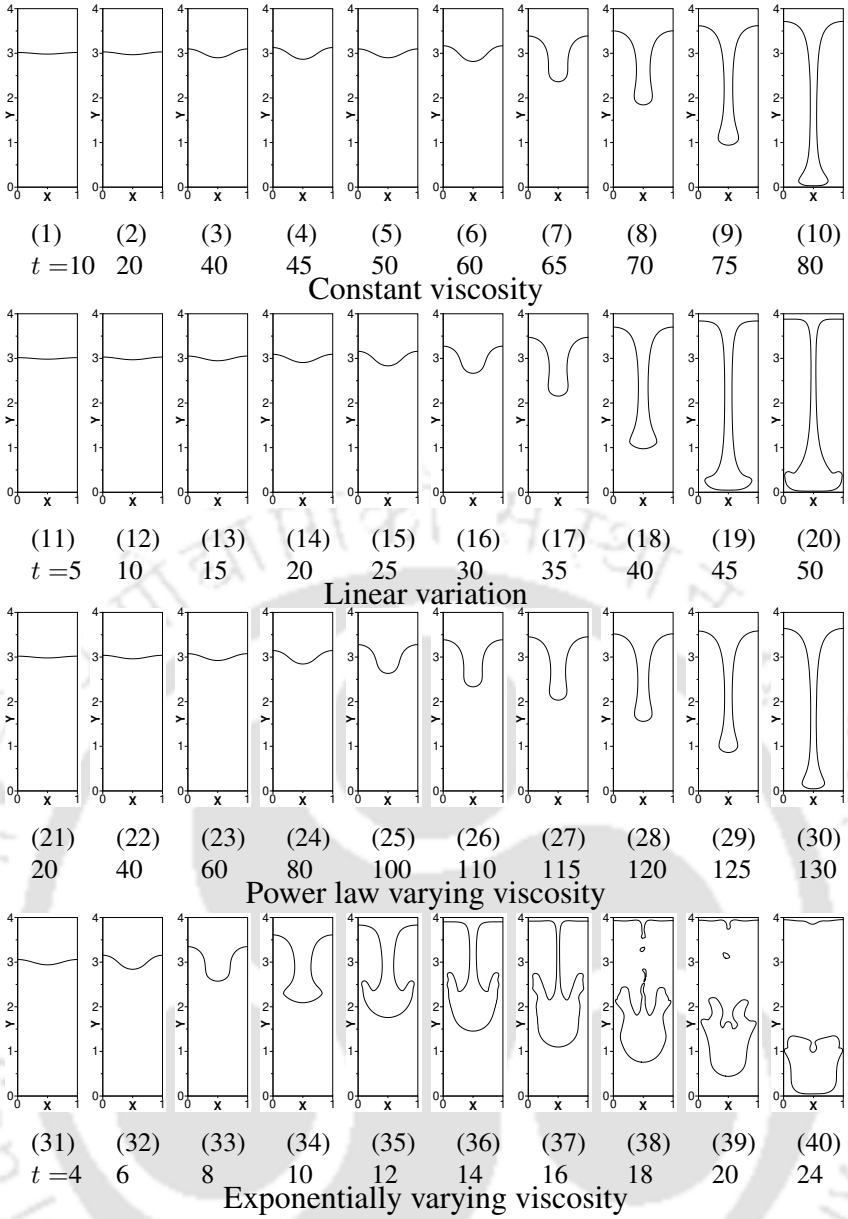

Figure 4.7: Instantaneous interface profiles for the four types of viscosity variations with viscosity ratio $m = 50$ (rest of the parameters are: $\rho_r = 2$, $c_{p_r} = 2$, $k_r = 2$, $Re = 50$, $Pr = 1$, $Fr = 1$, $We = 150$ and $r_T = 3$).

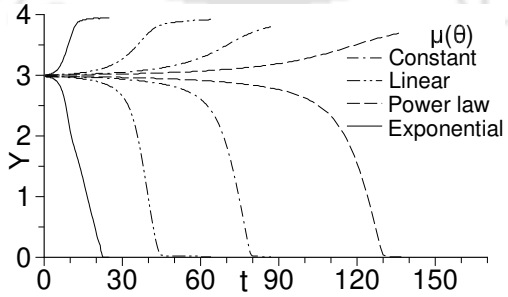

Figure 4.8: Time variation of spike front and bubble tip locations for the four types of viscosity variations with viscosity ratio $m = 50$ (rest of the parameters are: $\rho_r = 2$, $c_{p_r} = 2$, $k_r = 2$, $Re = 50$, $Pr = 1$, $Fr = 1$, $We = 150$ and $r_T = 3$).

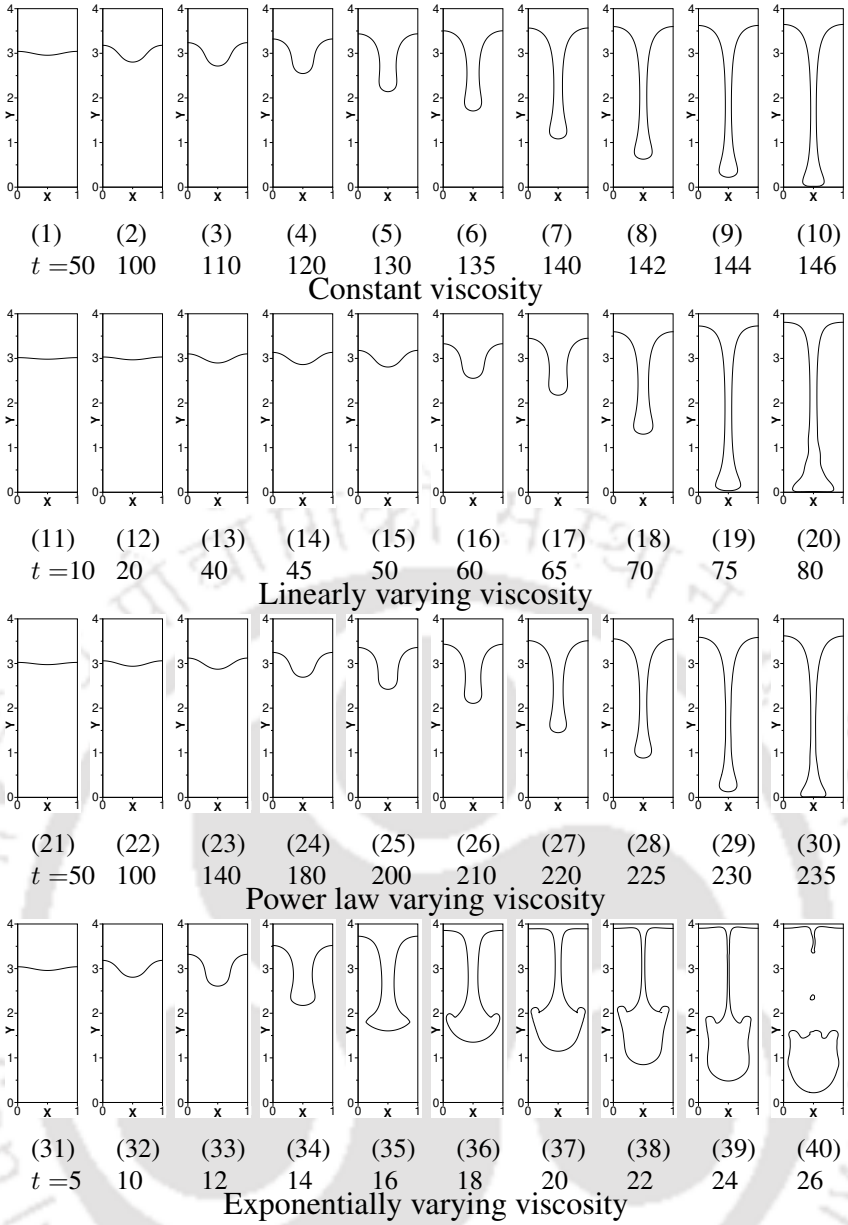

Figure 4.9: Instantaneous interface profiles for the four types of viscosity variations with viscosity ratio $m = 100$ (rest of the parameters are: $\rho_r = 2$, $c_{p_r} = 2$, $k_r = 2$, $Re = 50$, $Pr = 1$, $Fr = 1$, $We = 150$ and $r_T = 3$).

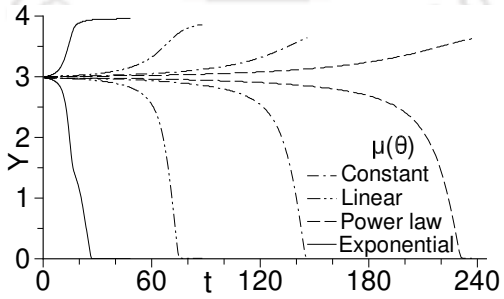

Figure 4.10: Time variation of spike front and bubble tip locations for the four types of viscosity variations with viscosity ratio $m = 100$ (rest of the parameters are: $\rho_r = 2$, $c_{p_r} = 2$, $k_r = 2$, $Re = 50$, $Pr = 1$, $Fr = 1$, $We = 150$ and $r_T = 3$).

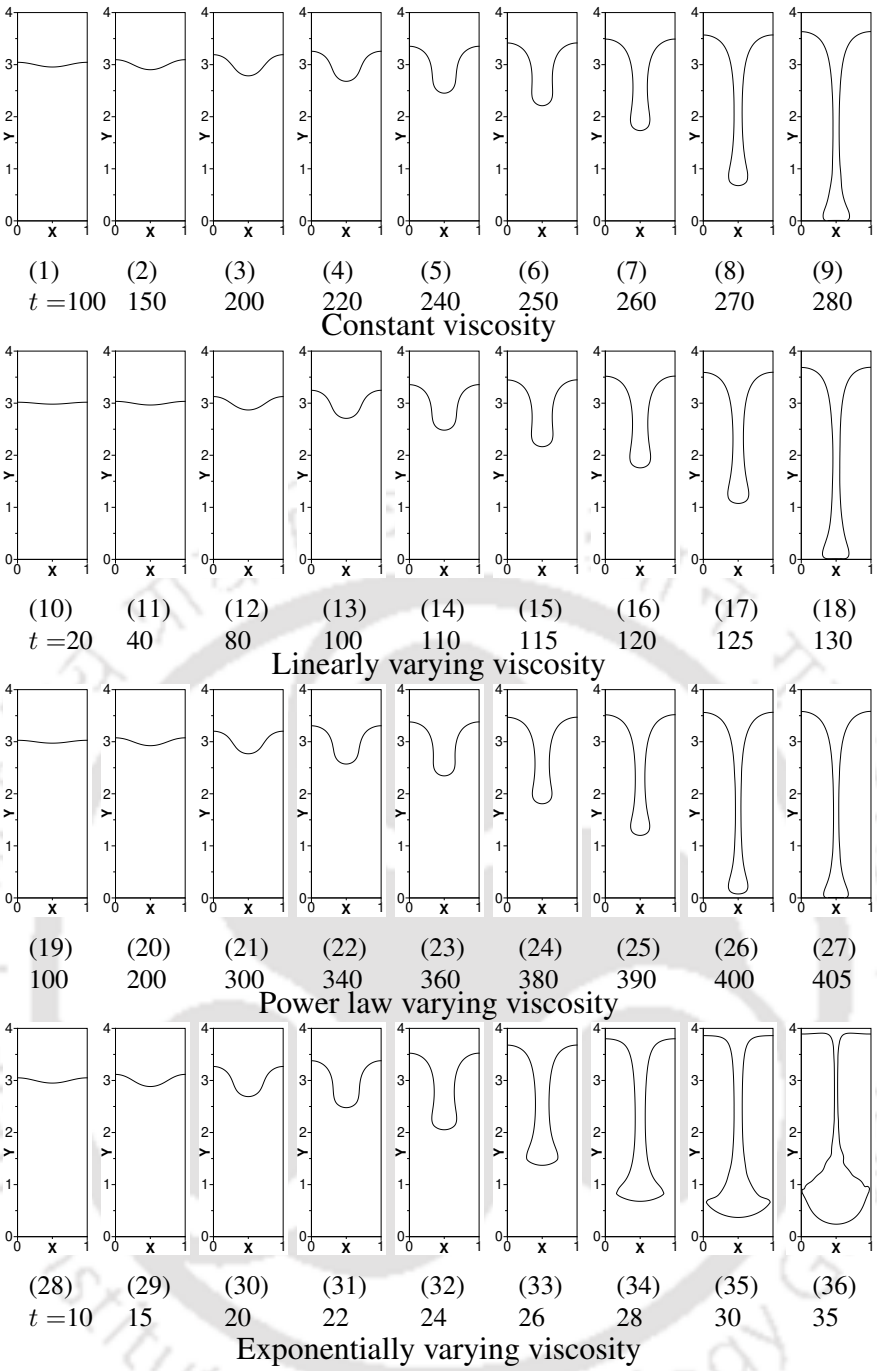

Figure 4.11: Instantaneous interface profiles for the four types of viscosity variations with viscosity ratio $m = 200$ (rest of the parameters are: $\rho_r = 2$, $c_{p_r} = 2$, $k_r = 2$, $Re = 50$, $Pr = 1$, $Fr = 1$, $We = 150$ and $r_T = 3$).

For exponential variation, rate of spike movement is almost 11 times compared to that of power law variation. Overall, exponential viscosity variation shows highest destabilizing effect and power law viscosity variation shows lowest destabilizing effect on the instability.

Fig. 4.13 shows time variation spike front and bubble tip locations for exponentially varying viscosity for various viscosity ratios. From the figure, it can be observed that time taken by the spike to strike the bottom wall increases with increasing viscosity ratio. For ratio 200, rate of spike movement becomes almost 4 times slower than that of viscosity ratio 2. For increasing viscosity ratio, it can be

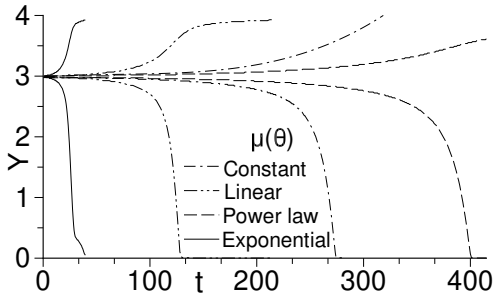

Figure 4.12: Time variation of spike front and bubble tip locations for the four types of viscosity variations with viscosity ratio $m = 200$ (rest of the parameters are: $\rho_r = 2$, $c_{p_r} = 2$, $k_r = 2$, $Re = 50$, $Pr = 1$, $Fr = 1$, $We = 150$ and $r_T = 3$).

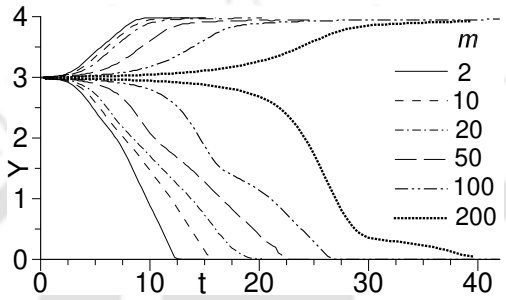

Figure 4.13: Time variation of spike front and bubble tip locations for various viscosity ratios with exponential variation of viscosity (rest of the parameters are: $\rho_r = 2$, $c_{p_r} = 2$, $k_r = 2$, $Re = 50$, $Pr = 1$, $Fr = 1$, $We = 150$ and $r_T = 3$).

observed that the other three types of viscosity variations follow similar trend of reduced rate of spike movement at higher viscosity ratio. For viscosity ratio more than 200, spike formation shows qualitative similarity with fluid column-like structure, irrespective of viscosity variations. With increasing viscosity ratio, time taken by the spike to strike the bottom wall is found to increase, for the four types of viscosity variations.

4.3.3 Effect of functional variations of viscosity with temperature for various density ratios

Effect of functional variation of viscosity with temperature on Rayleigh-Taylor instability is studied for density ratio in the range of 2 to 50. For density ratio 2, the evolution of instability and time variation of spike front and bubble tip locations for the four types of viscosity variations are presented in Fig. 4.1 and Fig. 4.2, respectively. The instability is found to be different from each other for the four types of viscosity variations which is already discussed in the above subsection for viscosity ratio 2. For density ratio 2, for exponential, linear constant and power law variations, the spike strikes the bottom wall at about dimensionless time $t = 12$, 18, 22 and 28, respectively. For power law variation, rate of spike movement is almost 2 times slower than that of exponential variation.

For density ratio 10, instability evolution is presented in Fig. 4.14 for the four types of viscosity variations. For constant and power law variations, a mushroom shaped spike forms with smaller head in size which eventually deforms and a thin elongated arm forms on both sides of the spike head.

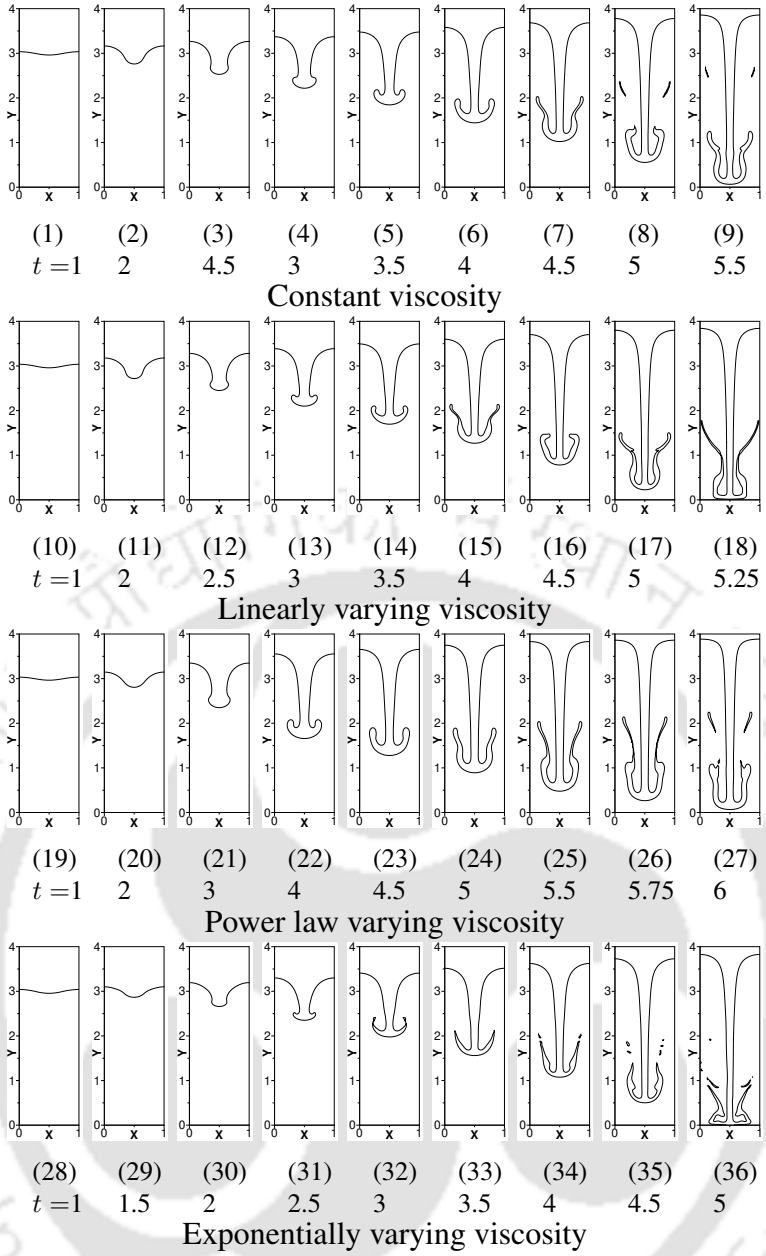

Figure 4.14: Instantaneous interface profiles for the four types of viscosity variations with density ratio $\rho_r = 10$ (rest of the parameters are: $m = 2$, $c_{p_r} = 2$, $k_r = 2$, $Re = 50$, $Pr = 1$, $Fr = 1$, $We = 150$ and $r_T = 3$).

For both the variations, the thin elongated arm breaks at the end portion as spike moves towards the bottom wall. For linear variation, the spike deforms and an elongated arm forms on both sides of the spike head which does not break, unlike the other types of viscosity variations. For exponential variation, the spike deforms and a smaller and thinner arm forms on both sides of the spike head. The spike movement becomes faster as density ratio is increased which is evident from the time variation of spike front and bubble tip locations, as shown in Fig. 4.15. For exponential, linear, constant and power law variations, the spike front strikes the bottom wall at about dimensionless time $t = 5$, 5.25, 5.5 and 6, respectively. For the four types of viscosity variations, time variation of spike front location shows small difference from each other.

With increasing density ratio, size of the spike head further reduces and the spike movement

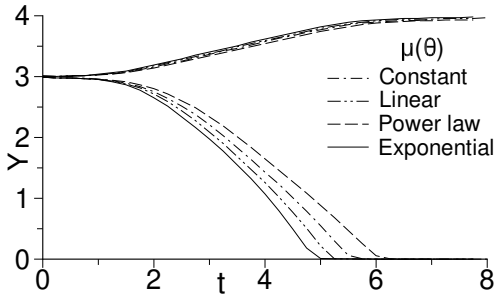

Figure 4.15: Time variation of spike front and bubble tip locations for the four types of viscosity variations with density ratio $\rho_r = 10$ (rest of the parameters are: $m = 2$, $c_{p_r} = 2$, $k_r = 2$, $Re = 50$, $Pr = 1$, $Fr = 1$, $We = 150$ and $r_T = 3$).

becomes faster for all type of viscosity variations. For density ratio 20, the instability evolution is presented in Fig. 4.16 for the four types of viscosity variations. For constant and power variations of viscosity, spike forms with smaller head and a thinner arm forms on the spike head. For linearly and exponential variation, spike-arm structure shows qualitative similarity. However, for linear variation the arm becomes relatively longer than that of exponential variation. Time variation of spike front and bubble tip locations is presented in Fig. 4.17. For exponential, linear, constant and power law variations, the spike strikes the bottom wall at about dimensionless time $t = 4.25$, 4.5, 4.75 and 4.75, respectively. Rate of spike movement shows marginal difference from each other for different types of viscosity variations.

Fig. 4.18 shows the instability evolution for the four types of viscosity variations for density ratio 50. The figure shows that the spike forms with smaller head, irrespective of type of viscosity variation. The smaller head spike moves towards the bottom wall rapidly with negligible length of arms. For density ratio 50, difference in the spike movement with time is found to be negligible for the different types of viscosity variations, as shown in Fig. 4.19. From the figure, it can be observed that for density ratio 50 or more, the spike strikes the bottom wall at about dimensionless time $t = 4$, almost same for all the four types of viscosity variations. Rate of spike movement is same for all the four types of viscosity variations. This means that for high density ratios, the instability is independent of type of viscosity variation.

For exponential variation, the time variation of spike front and bubble tip locations is shown in Fig. 4.20 for various density ratios. The figure shows that spike movement becomes relatively faster as density ratio is increased. Similar trend of spike movement is observed for the other three types of viscosity variations. At high density ratios, dynamics of the instability is almost same for the four types of viscosity variations.

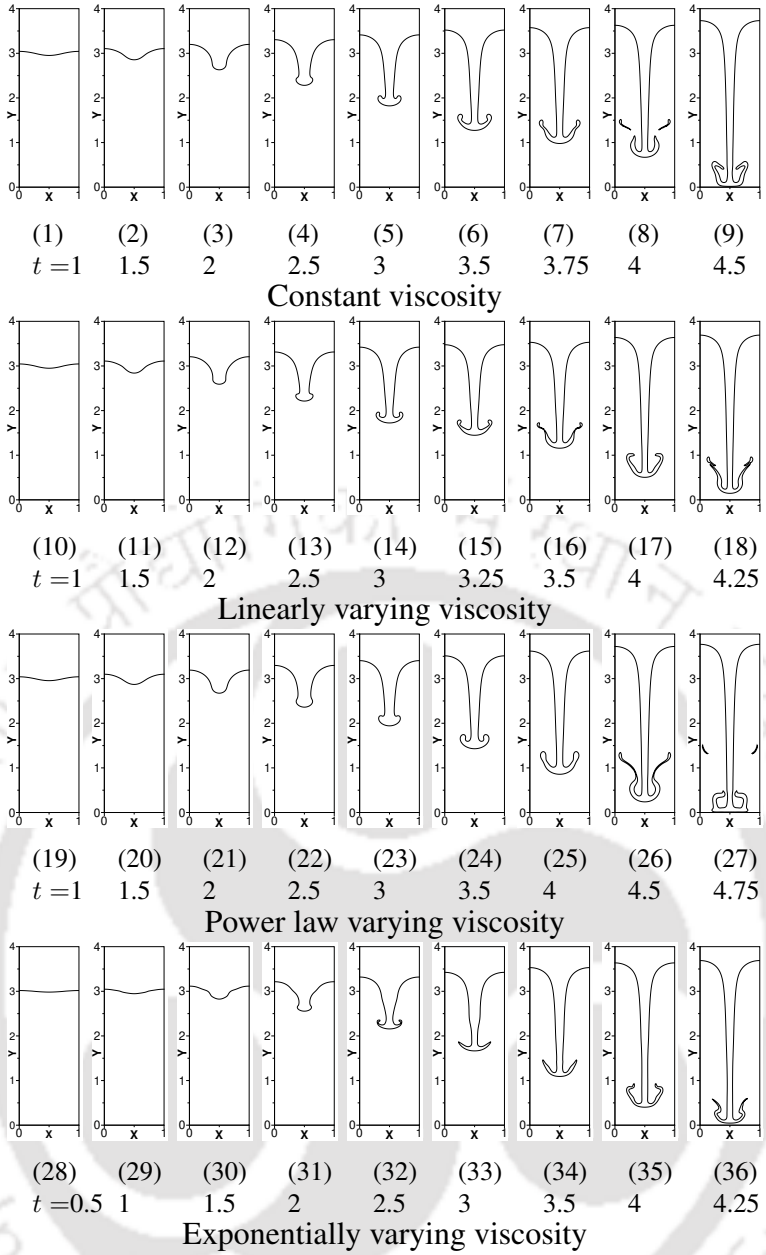

Figure 4.16: Instantaneous interface profiles for the four types of viscosity variations with density ratio $\rho_r = 20$ (rest of the parameters are: $m = 2$, $c_{p_r} = 2$, $k_r = 2$, $Re = 50$, $Pr = 1$, $Fr = 1$, $We = 150$ and $r_T = 3$).

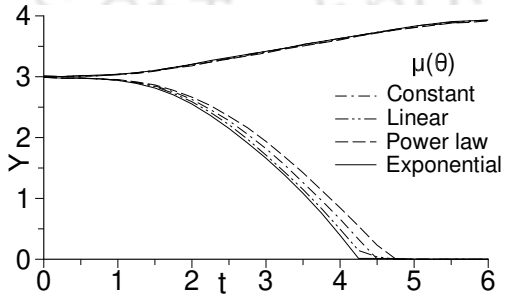

Figure 4.17: Time variation of spike front and bubble tip locations for the four types of viscosity variations with density ratio $\rho_r = 20$ (rest of the parameters are: $m = 2$, $c_{p_r} = 2$, $k_r = 2$, $Re = 50$, $Pr = 1$, $Fr = 1$, $We = 150$ and $r_T = 3$).

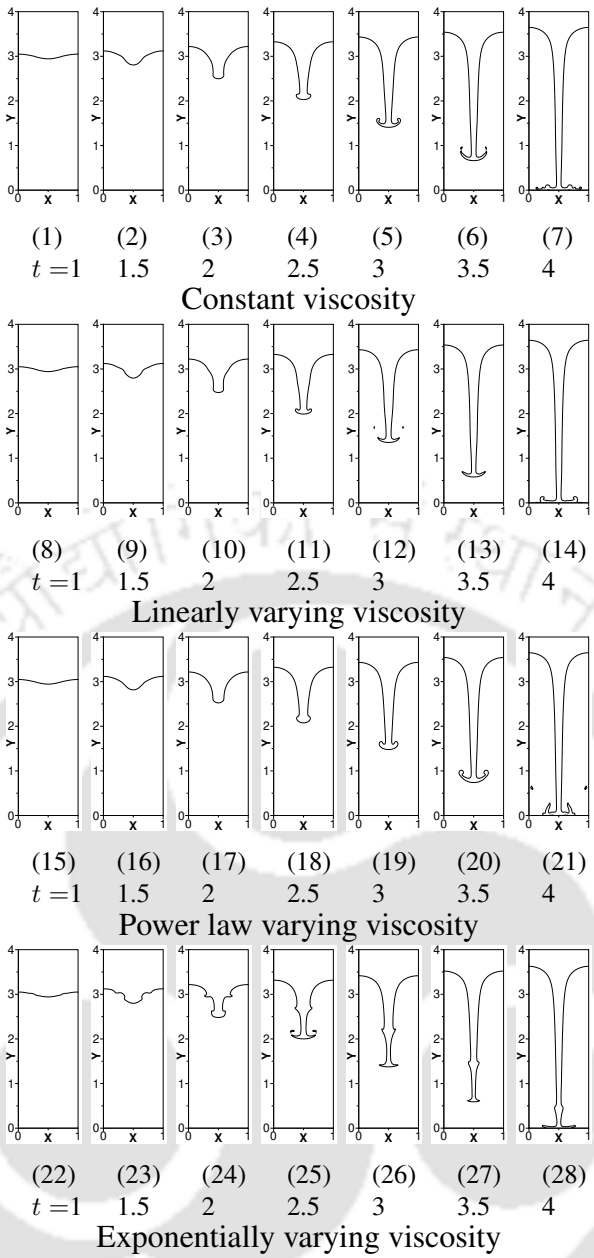

Figure 4.18: Instantaneous interface profiles for the four types of viscosity variations with density ratio $\rho_r = 50$ (rest of the parameters are: $m = 2$, $c_{p_r} = 2$, $k_r = 2$, $Re = 50$, $Pr = 1$, $Fr = 1$, $We = 150$ and $r_T = 3$).

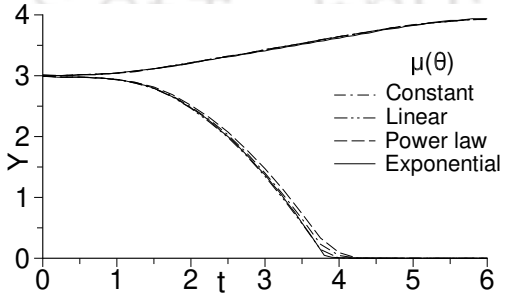

Figure 4.19: Time variation of spike front and bubble tip locations for the four types of viscosity variations with density ratio $\rho_r = 50$ (rest of the parameters are: $m = 2$, $c_{p_r} = 2$, $k_r = 2$, $Re = 50$, $Pr = 1$, $Fr = 1$, $We = 150$ and $r_T = 3$).

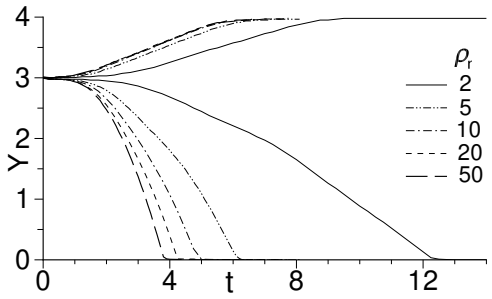

Figure 4.20: Time variation of spike front and bubble tip locations for various density ratios with exponential variation of viscosity (rest of the parameters are: $m = 2$, $c_{p_r} = 2$, $k_r = 2$, $Re = 50$, $Pr = 1$, $Fr = 1$, $We = 150$ and $r_T = 3$).

4.4 Conclusions

Rayleigh-Taylor instability is studied for viscosity stratification effect in 2-D rectangular configuration for four types of functional variations of viscosity with temperature. The four types of variations are constant, linear, power law and exponential variations. The study is carried out for various viscosity ratios in the range of 2 to 200 and density ratios in the range of 2 to 50. Type of viscosity variation shows strong effect on the instability at low viscosity ratios and low density ratios. For high viscosity ratios more than 100, spike forms into a fluid column like structure showing qualitative similarity for the four types of viscosity variations. For high density ratio about 50 or more, the dynamics of the instability become independent of type of viscosity variation. For a given type of viscosity variation, increasing viscosity ratio shows stabilizing effect and increasing density ratio shows destabilizing effect on the instability, all the four types of viscosity variations. Rate of spike movement is in the decreasing order of sequence of exponential, linear, constant and power law variations. This is because overall effective viscosity increases in the above order of sequence.

Chapter 5

Marangoni effect on Rayleigh-Taylor instability in viscosity stratified medium in 2-D rectangular coordinates

In this chapter, Marangoni effect on Rayleigh-Taylor instability is studied in viscosity stratified fluid layers in 2-D rectangular coordinates. Marangoni effect due to surface tension dependent on temperature is considered. Marangoni effect on the instability is studied for different functional dependencies of surface tension with temperature. Effect of Weber number and Froude number on the instability in the presence of Marangoni effect is also studied.

5.1 Physical system

In this chapter, physical system which is used for the study is described in subsection 2.1.1. Schematic of the physical system is as shown in Fig. 2.2.

5.2 Mathematical treatment

The numerical study presented in this chapter is carried out using Basilisk software. The software uses Volume of Fluid (VoF) method to solve multiphase flow in which an additional equation for volume fraction is solved. Hence, governing equations, which consist of equations for continuity, momentum, energy and volume fraction, are solved numerically.

5.2.1 Scaling parameters

For the study of Marangoni effect on the instability different reference scaling parameters are chosen. The reference scaling parameters for time, length, velocity, pressure, temperature and surface tension are chosen as $\tilde{L}_{\text{ref}}/\tilde{V}_{\text{ref}}$, $\tilde{L}_{\text{ref}}$, $\tilde{V}_{\text{ref}}$, $\tilde{\rho}_{\text{ref}}\,\tilde{V}^2_{\text{ref}}$, $\tilde{T}_{\text{ref}}$ and $\tilde{\sigma}_{\text{ref}}$, respectively. Reference velocity is taken equal to $\tilde{V}_{\text{ref}} = \beta_1\,\tilde{T}_{\text{ref}}/\tilde{\mu}_{\text{ref}}$. β_1 is constant in the expression of surface tension variation with temperature in dimensional form (see Eq. (2.28)). Here, β_1 is the rate of dimensional surface tension variation

with dimensional temperature at reference temperature ($\beta_1 = -d\tilde{\sigma}/d\tilde{T}|_{\tilde{T}_{\text{ref}}}$). Cold wall temperature is chosen as the reference temperature ($\tilde{T}_{\text{ref}} = \tilde{T}_2$). $\tilde{\sigma}_{\text{ref}} = \tilde{\sigma}_0$ is surface tension value at the reference temperature. The reference fluid properties are chosen to be of 'Fluid 2' layer fluid properties. The chosen reference scales are as following.

$$\begin{aligned} \tilde{\rho}_{\text{ref}} = \tilde{\rho}_2, \quad \tilde{\mu}_{\text{ref}} = \tilde{\mu}_2, \quad \tilde{k}_{\text{ref}} = \tilde{k}_2, \quad \tilde{c_p}_{\text{ref}} = \tilde{c_p}_2, \\ \tilde{L}_{\text{ref}} = \tilde{L}, \quad \tilde{T}_{\text{ref}} = \tilde{T}_2, \quad \tilde{\sigma}_{\text{ref}} = \tilde{\sigma}_0, \quad \tilde{V}_{\text{ref}} = \beta_1 \tilde{T}_2/\tilde{\mu}_2 \end{aligned} \tag{5.1}$$

Based on the above chosen reference scales, different dimensionless variables, as given by Eq. (2.14), become as following.

$$\begin{aligned} \rho = \frac{\tilde{\rho}}{\tilde{\rho}_2}, \quad \mu = \frac{\tilde{\mu}}{\tilde{\mu}_2}, \quad k = \frac{\tilde{k}}{\tilde{k}_2}, \quad c_p = \frac{\tilde{c_p}}{\tilde{c_p}_2}, \quad x = \frac{\tilde{x}}{\tilde{L}}, \quad y = \frac{\tilde{y}}{\tilde{L}}, \\ t = \frac{\tilde{t}\,\beta_1\,\tilde{T}_2}{\tilde{L}\,\tilde{\mu}_2}, \quad \mathbf{u} = \frac{\tilde{\mathbf{u}}}{\beta_1\,\tilde{T}_2/\tilde{\mu}_2}, \quad p = \frac{\tilde{p}}{\tilde{\rho}_2\,\beta_1^2\,\tilde{T}_2^2/\tilde{\mu}_2^2}, \quad \theta = \frac{\tilde{T}-\tilde{T}_2}{\tilde{T}_2}, \quad \sigma = \frac{\tilde{\sigma}}{\tilde{\sigma}_0} \end{aligned} \tag{5.2}$$

5.2.2 Governing equations

Using the above mentioned reference scales, the governing equations are non-dimensionalized which can be written as following.

Continuity equation

$$\nabla\cdot\mathbf{u} = 0 \tag{5.3}$$

Momentum equation

$$\rho\left(\frac{\partial\mathbf{u}}{\partial t} + \mathbf{u}\cdot\nabla\mathbf{u}\right) = -\nabla p + \frac{1}{Re}\nabla\cdot\mu\,\left(\nabla\mathbf{u} + \nabla\mathbf{u}^{\text{T}}\right) + \mathbf{F} \tag{5.4}$$

Energy equation

$$\rho\,c_p\left(\frac{\partial\theta}{\partial t} + \mathbf{u}\cdot\nabla\theta\right) = \frac{1}{Ma}\,\nabla\cdot\left(k\nabla\theta\right) \tag{5.5}$$

Volume fraction equation

$$\frac{\partial f}{\partial t} + \mathbf{u}\cdot\nabla f = 0 \tag{5.6}$$

Here, body force term in dimensionless form, which is given by Eq. (2.29), is expressed as

$$\mathbf{F} = \mathbf{F}_\sigma - \frac{\rho}{Fr}\mathbf{e}_j = \frac{\delta}{We}\left[\sigma(\theta)\,\kappa\,\mathbf{n} + \nabla_s\sigma(\theta)\right] - \frac{\rho}{Fr}\,\mathbf{e}_j \tag{5.7}$$

For the study of Marangoni effect presented in this chapter, a quadratic form of temperature dependent surface tension variation, which is also used in the studies of [73, 92], is considered. Surface tension expression in dimensional form, which is given by Eq. (2.28), is as following.

$$\tilde{\sigma}(\tilde{T}) = \tilde{\sigma_0} + \beta_1(\tilde{T} - \tilde{T}_{\text{ref}}) + \beta_2(\tilde{T} - \tilde{T}_{\text{ref}})^2 \tag{5.8}$$

Here, β_1 and β_2 are the surface tension constants in expression of surface tension variation with temperature which are defined equal to $-d\tilde{\sigma}/d\tilde{T}|_{\tilde{T}_{\text{ref}}}$ and $(1/2)d^2\tilde{\sigma}/d\tilde{T}^2|_{\tilde{T}_{\text{ref}}}$, respectively. The dimensionless form of surface tension expression, which is given by Eq. (2.31), is as following.

$$\sigma(\theta) = \tilde{\sigma}(\tilde{T})/\tilde{\sigma_0} = 1 - M_1\,\theta + M_2\,\theta^2 \tag{5.9}$$

Here, M_1 and M_2 are dimensionless surface tension constants which are defined as $\beta_1\,\tilde{T}_2/\tilde{\sigma_0}$ and $\beta_2\,\tilde{T}_2^2/\tilde{\sigma_0}$, respectively. Substituting the above surface tension (σ) expression in the Eq. (5.7), we get the body force term in the dimensionless form ($\mathbf{F}$) as following

$$\mathbf{F} = \frac{1}{We}\left[\kappa(1 - M_1\,\theta + M_2\theta^2)\,\delta\,\mathbf{n}\right] - \frac{(M_1 - 2\,M_2\theta)}{We}\left[\nabla\theta - (\nabla\theta\cdot\mathbf{n})\,\mathbf{n}\right]\delta_s - \frac{\rho}{Fr}\mathbf{e}_j \tag{5.10}$$

In the above equations, Reynolds number (Re), Froude number (Fr), Weber number (We) and Marangoni number (Ma) are defined as following.

$$Re = \frac{\beta_1\,\tilde{\rho}_2\,\tilde{T}_2\,\tilde{L}}{\tilde{\mu}_2^2},\; Fr = \frac{\beta_1^2\,\tilde{T}_2^2}{\tilde{g}\tilde{L}\,\tilde{\mu}_2^2},\; We = \frac{\tilde{\rho}_2\,\tilde{g}\,\tilde{L}^2}{\tilde{\sigma_0}},\; Ma = Re\,Pr = \frac{\beta_1\,\tilde{T}_2\,\tilde{\rho}_2\,\tilde{c_{p_2}}\,\tilde{L}}{\tilde{\mu}_2\,\tilde{k}_2},\; Pr = \frac{\tilde{\mu}_2\tilde{c_{p2}}}{\tilde{k}_2} \tag{5.11}$$

Expressions used for top and bottom layer fluid viscosities in dimensionless form, which are given by Eq. (2.25), are as following

$$\mu_1 = m\,e^{-\theta} \qquad \text{and} \qquad \mu_2 = e^{-\theta} \tag{5.12}$$

Here, m is the top to bottom layer fluid viscosity ratio at reference temperature, which is defined as $m = \mu_1(\tilde{T}_2)/\mu_2(\tilde{T}_2)$. Fluid properties such as density, heat capacity, viscosity and thermal conductivity in dimensionless form, as a function of f, are calculated according to Eq. (2.13).

$$\begin{aligned}
\rho &= \rho_1\,f + \rho_2\,(1-f)\\
\mu &= \mu_1\,f + \mu_2\,(1-f)\\
c_p &= c_{p_1}\,f + c_{p_2}\,(1-f)\\
k &= k_1\,f + k_2\,(1-f)
\end{aligned} \tag{5.13}$$

5.2.3 Initial and boundary conditions

For the study presented in this chapter, the initial and boundary conditions are given in subsection 2.2.2. In the same subsection, dimensions of the domain which is used for the study are also given.

5.2.4 Numerical methodology

The numerical methodology of Basilisk software is discussed in detail, in subsection 2.2.6. Usage of the software to study multiphase flow in 2-D rectangular coordinates in the presence of Marangoni effect is validated, and the validations are presented in the following subsection.

5.2.5 Validations

Before studying the Marangoni effect on the instability of the present study, usage of the software is validated for the simulations of Rayleigh-Taylor instability with and without surface tension along the interface for 2-D rectangular coordinates. The usage of the software is also validated for simulations of Marangoni effect in multiphase flows for 2-D rectangular coordinates. The validations carried out are as following.

5.2.5.1 Validations of solutions of Rayleigh-Taylor instability with constant viscosities of fluid layers in 2-D rectangular coordinates

The validation of usage of present software for the simulations of Rayleigh-Taylor instability without surface tension in 2-D rectangular domain is carried out. For the validation, Rayleigh-Taylor instability in 2-D rectangular domain without surface tension is solved using the present software and the obtained results are compared with those presented in Popinet and Zaleski [7]. The simulations are carried out for Rayleigh-Taylor instability in a rectangular domain of 1 m width and 4 m height. Top and bottom boundaries are solid walls and side boundaries are symmetric planes. Density and viscosity of the upper heavier fluid are 1.225 kg/m^3 and 0.00313 Pa·s, respectively. Density and viscosity of the bottom lighter fluid are 0.1694 kg/m^3 and 0.00313 Pa·s, respectively. In this problem, surface tension at the interface is set to zero. Acceleration of gravity is set to 9.81 m/s^2. At initial state, interface is located at 2 m from the bottom wall, which is perturbed by a perturbation of the form $0.05\ \cos(2\pi x)$. The interface profiles obtained from the present study results are compared with those presented in Popinet and Zaleski [7] for time instances 0.7 s, 0.8 s and 0.9 s in Fig. 5.1. The comparison shows good agreement of the present results with the reference results.

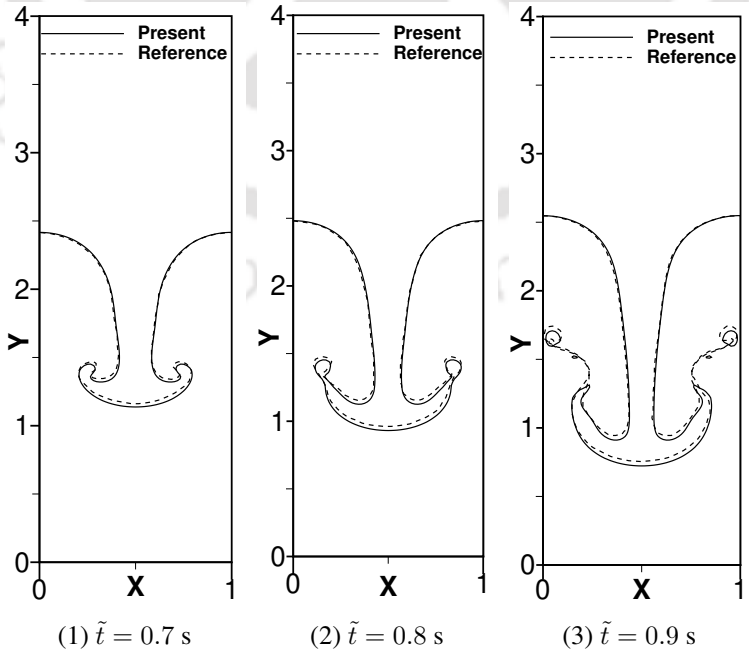

Figure 5.1: Comparison of interface profiles in Rayleigh-Taylor instability (without surface tension) obtained in the present simulations for various time instances with those of Popinet and Zaleski [7].

For the next validation of usage of the software, Rayleigh-Taylor instability including constant surface tension is solved, and the obtained results are compared with those presented in Salih and Maulik [9]. The instability is studied in a rectangular domain of dimensionless width and height of 1 and 3, respectively. The top and bottom boundaries of the domain are specified to be solid walls. The right and left side boundaries are specified to be symmetric planes. Density ratio of top heavier fluid density to bottom lighter fluid density is taken to be 5. Viscosity ratio of top heavier fluid viscosity to bottom lighter fluid viscosity is taken to be 10. Dimensionless numbers such as Reynolds number (Re) and Weber number (We) are defined based on the properties of heavier fluid and width of the domain. Values of Re and We are taken equal to 156.6 and 144, respectively. At the initial state, the interface is located at a dimensionless distance of 1.83 from the bottom wall. The interface is perturbed according to $0.03\ \cos(2\pi x)$. Instantaneous interface profiles obtained using present software are compared with those presented by Salih and Maulik [9] for instances of dimensionless time 2, 3 and 4 in Fig. 5.2. The present results show good agreement with those of the reference study results.

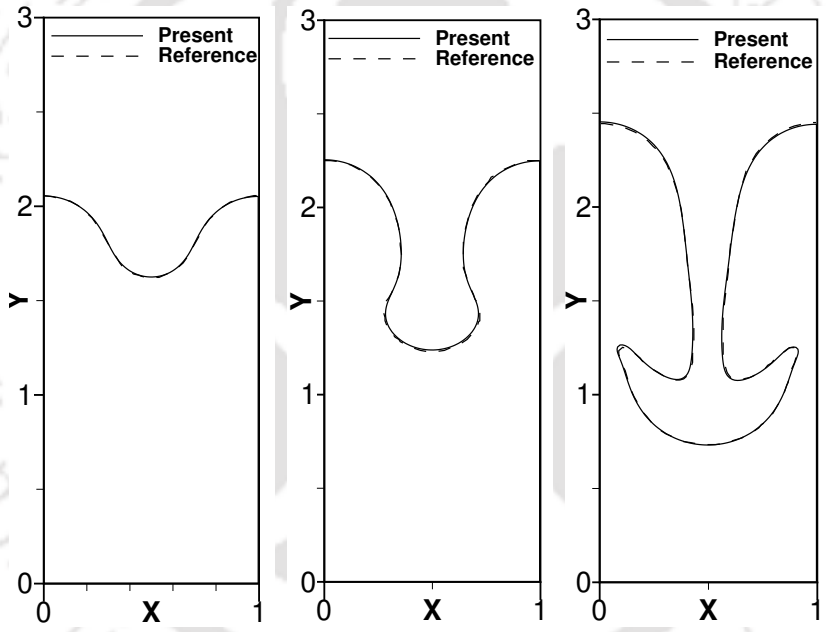

Figure 5.2: Comparison of interface profiles in Rayleigh-Taylor instability (with surface tension) obtained in the present simulations for various dimensionless time instances with those of Salih and Maulik [9].

5.2.5.2 Validation for Marangoni effect on a rising 2-D bubble in a surrounding fluid medium

Usage of the software is validated to perform multiphase flow simulations in the presence of Marangoni effect in 2-D rectangular coordinate configuration. For the validation, dynamics of a 2-D bubble in the presence of Marangoni effect under the absence of gravity is simulated using the present software and the obtained results are compared with those presented in Nas and Tryggvason [10]. The simulation is carried out for 2-D bubble of dimensionless radius 1 which is kept stationary in a rectangular domain of dimensionless size of 4×8 such that the center of the bubble is located at the center of the

rectangular domain. The remaining domain is filled with a surrounding fluid. Ratio of bubble fluid to surrounding fluid property ratios such as density, viscosity, heat capacity and thermal conductivity ratios, all are set to 0.5. Top and bottom boundaries of the domain are specified to be walls with hot and cold temperatures, respectively. Left and right side boundaries are specified to be periodic. At initial state, temperature in the domain is specified to vary in vertical direction with uniform temperature gradient from bottom cold wall to top hot wall. Surface tension is specified to vary linearly with temperature. Gravitational acceleration is set to zero. Dimensionless numbers, which are Reynolds number (Re), Marangoni number (Ma) and Capillary number (Ca), are defined based on the surrounding fluid properties and the bubble radius. Values of Re, Ma and Ca are set equal to 5, 20 and 0.01666, respectively. Marangoni forces arise in the presence of surface tension gradient due to temperature variation in vertical direction. Due to Marangoni forces the bubble moves in vertically upward direction in the absence of gravity. Velocity of the bubble in the absence of gravity is termed as migration velocity of the bubble. Variation of bubble migration velocity with time is obtained using the present software and compared with that presented by Nas and Tryggvason [10] in Fig. 5.3. The present study result shows good match with the reference study result.

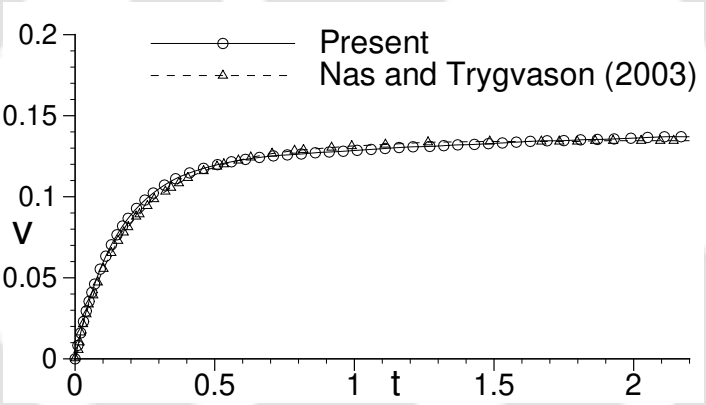

Figure 5.3: Comparison of bubble migration velocity variation with time which is obtained from the present software with that presented by Nas and Tryggvason [10].

5.2.6 Grid independence test

Before performing the numerical simulations to study Rayleigh-Taylor instability in viscosity stratified fluid medium in the presence of Marangoni effect in 2-D rectangular configuration grid independence test is carried out. The grid independence test is carried out at set of parameters at which the solution is expected to have highest sensitivity to grid variation. When surface tension approaches to zero the interface structure is expected to be complex and may undergo large deformation. When the interface structure is complex the solutions are expected to be sensitive to the grid variation. Hence, the grid independent test is carried out for surface tension approaching to zero (Weber number approaching to infinity). The other parameters chosen for the grid test are $\rho_r = 2$, $m = 2$, $k_r = 2$, $c_{p_r} = 2$, $Re = 50$, $Ma = 50$, $Fr = 1$ and $r_T = 2$ which are baseline parameter values. In Basilisk solver, to perform the simulations, domain is divided into 2^n number of cells in each direction, where

n is denoted as grid level in adaptive mesh refinement. For example, if the grid level of 9 is used in the simulation then it represents that 2^9=512 number of grids are used in one direction, and grid level of 9 represents the minimum grid spacing of 0.0078 in each direction. For the grid independent test, three different levels of grid 8, 9 and 10 are used which correspond to the minimum grid spacing of 0.0156, 0.0078 and 0.0039, respectively. The grid level and the corresponding minimum grid spacing are given in Table 5.1. Fig. 5.4 shows the comparison of instantaneous interface profiles obtained with different grids for Rayleigh-Taylor instability with Marangoni effect in 2-D rectangular coordinate configuration. Fig. 5.5 shows the comparison of spike front and bubble tip locations obtained with different grids. From the figures, it is found that the solutions of the problem do not vary with spacing when minimum spacing is 0.0078 or lower. Hence, the minimum grid spacing size of 0.0078, which corresponds to the grid level of 9, is used for the numerical simulations.

Table 5.1: The minimum grid spacing corresponds to different grid levels used in the grid independent test

Grid level	7	8	9	10
Minimum grid spacing $(\min(\Delta))$	0.03125	0.0156	0.0078	0.0039

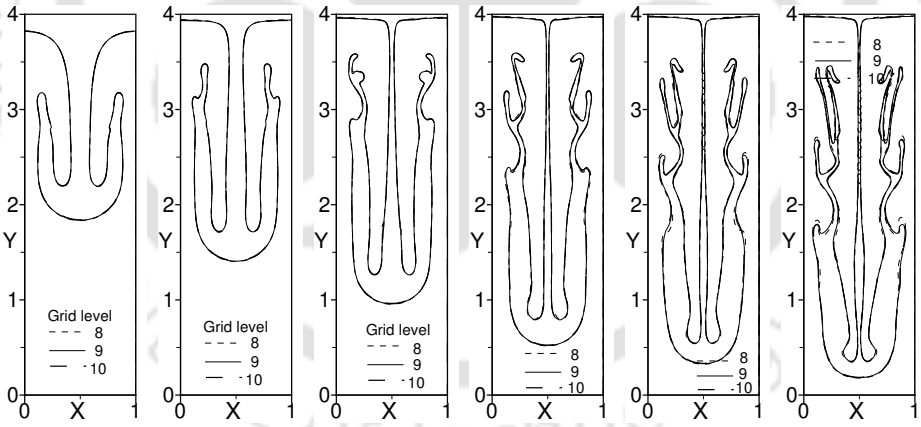

(1) t =8 (2) t =10 (3) t =12 (4) t =14 (5) t =15 (6) t =16

Figure 5.4: Comparison of instantaneous interface profiles of Rayleigh-Taylor instability in viscosity stratified fluid layers with Marangoni effect in 2-D rectangular coordinate configuration obtained with different grid sizes (rest of the parameters are: $\rho_r = 2$, $m = 2$, $k_r = 2$, $c_{p_r} = 2$, $Re = 50$, $Ma = 50$, $Fr = 1$, $We = \infty$ and $r_T = 2$).

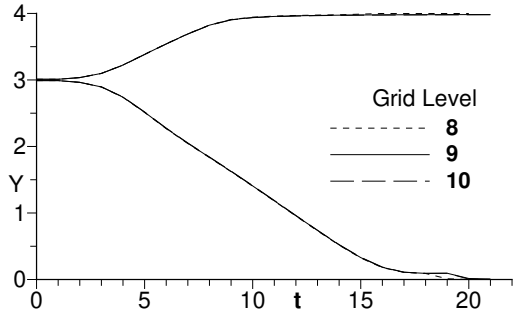

Figure 5.5: Comparison of time variation of spike front locations for various grid levels with Marangoni effect (rest of the parameters are: $\rho_r = 2$, $m = 2$, $k_r = 2$, $c_{p_r} = 2$, $Re = 50$, $Ma = 50$, $Fr = 1$, $We = \infty$ and $r_T = 2$).

5.3 Results and discussion

5.3.1 Baseline parameter values

In the present chapter, effect of various parameters on Rayleigh-Taylor instability is studied in the presence of Marangoni effect. The study is carried out for the effect of functional dependencies of surface tension on temperature, Weber number and Froude number at a baseline parameters values. The baseline parameter value are as following. Top heavier fluid to bottom lighter fluid density ratio (ρ_r), thermal conductivity ratio (k_r), viscosity ratio (m) and heat capacity ratio (c_{p_r}), all are chosen equal to 2. Temperature ratio (r_T) is chosen equal to 2. Froude number (Fr), Reynolds number (Re), Marangoni number (Ma) and Weber number (We) are chosen equal to 1, 50, 50, and 100, respectively. Parabolic surface tension dependency on temperature is chosen with values of $M_1 = 0.45$ and $M_2 = 0.225$ for the baseline values (for the studies other than the functional dependencies of surface tension on temperature). Effect of a particular parameter is studied by varying that particular parameter while the rest of the parameter values are kept at the corresponding above baseline parameter values.

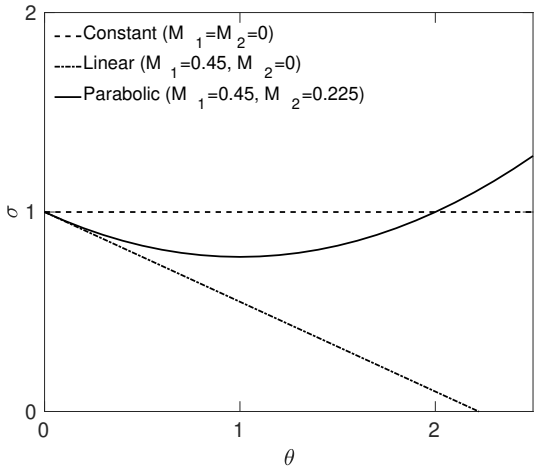

Figure 5.6: Variation of dimensionless surface tension (σ) with dimensionless temperature (θ).

5.3.2 Effect of functional dependency of surface tension on temperature

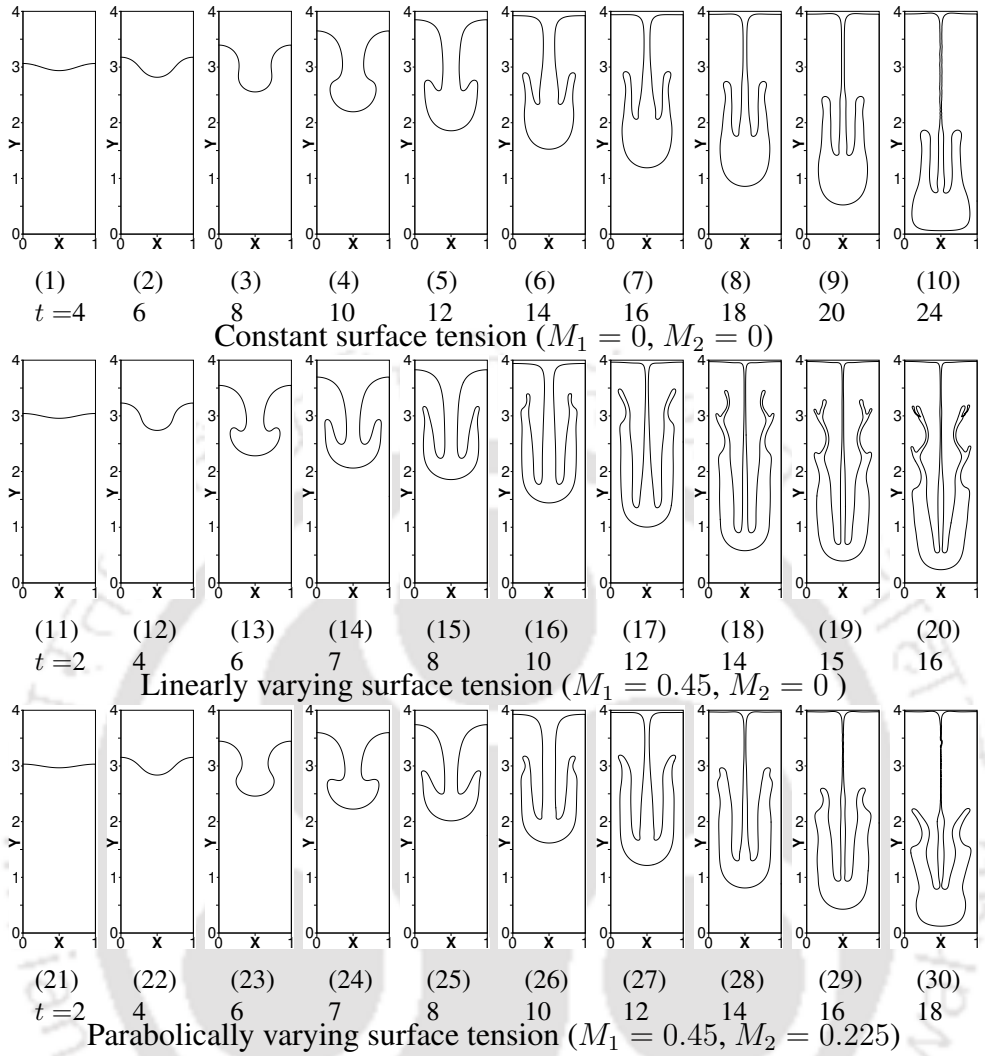

Figure 5.7: Instantaneous interface profiles for the three types of surface tension dependencies with temperature (rest of the parameters are: $\rho_r = 2$, $c_{p_r} = 2$, $k_r = 2$, $m = 2$, $r_T = 2$, $Ma = 50$, $Re = 50$ and $We = 100$).

Rayleigh-Taylor instability is studied for the effect of functional dependency of surface tension on temperature in viscous stratified fluid layers. A general form of expression of temperature dependent surface tension is given by Eq. (5.9). Three types of functional dependencies, which are constant, linear and parabolic dependencies, are considered for the study. For constant surface tension, M_1 and M_2, both are set to zero. For linearly varying surface tension, M_1 and M_2 are chosen equal to 0.45 and 0, respectively. For parabolically varying surface tension, M_1 and M_2 are chosen equal to 0.45 and 0.225, respectively. Surface tension coefficient (σ), in dimensionless form, varies with respect to dimensionless temperature differently for the three types of functional dependencies, as shown in Fig. 5.6. Hence, the instability is expected to be different from each other for the three types of functional dependencies of surface tension on temperature.

The instability is presented in Fig. 5.7 for the three types of functional dependencies of surface tension. In initial stage, the heavier fluid forms into a mushroom shaped spike, for the three types of

functional dependencies. In later stage, the spike undergoes deformation and an arm forms on both sides of the spike, which differs largely from each other as the types of functional dependencies of surface tension are changed. For constant surface tension, the spike forms with a thick and short arm on both sides of the spike which is maintained throughout the spike movement. For parabolically varying surface tension, an arm forms on both sides of the spike head which elongates more and becomes more wavy as the spike moves towards the bottom wall. For parabolically varying surface tension, the arms are found to be relatively longer and more wavy than that of constant surface tension. For linearly varying surface tension, a thin elongated arm forms on both sides of the spike head which eventually deforms more. With time, the arms become more thinner and irregular. For linear surface tension, spike undergoes larger deformation and moves relatively faster compared to that of constant and parabolically varying surface tension cases. This is because, for linear dependency of surface tension, overall effective surface tension is the lowest compared to that of the other two types of surface tension dependencies. For all the three types of surface tension dependencies, the spike-arm structure is found to be attached to the top wall with a thin stem.

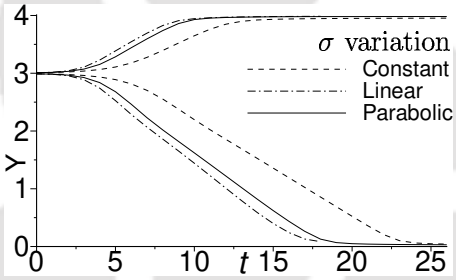

Figure 5.8: Time variation of spike front and bubble tip locations for the three types of surface tension dependencies with temperature (rest of the parameters are: $\rho_r = 2$, $c_{p_r} = 2$, $k_r = 2$, $m = 2$, $r_T = 2$, $Ma = 50$, $Re = 50$ and $We = 100$).

Time variation of spike front and bubble tip locations is presented in Fig. 5.8 for the three types of functional dependencies of surface tension. For constant, parabolic and linear dependencies of surface tension, the spike front strikes the bottom wall at about dimensionless time $t = 24$, 18 and 16, respectively. For linearly varying surface tension, rate of spike movement is almost 1.5 times compared to that of constant surface tension. Rate of spike movement is in increasing order of sequence of constant, parabolic and linear surface tension dependencies because the overall effective surface tension decrease in above order of sequence.

5.3.3 Effect of Weber number

Effect of surface tension on Rayleigh-Taylor instability is studied in the presence of Marangoni effect. The study is carried out by varying Weber number value, which is inversely proportional to the surface tension, in the range of 0 to infinity. Time evolution of interfacial instability is presented in Figs. 5.9-5.10. For Weber number less than critical value of 0.55, the configuration does not undergo instability. The surface tension along the interface acts similar to an elastic membrane. For Weber number of a

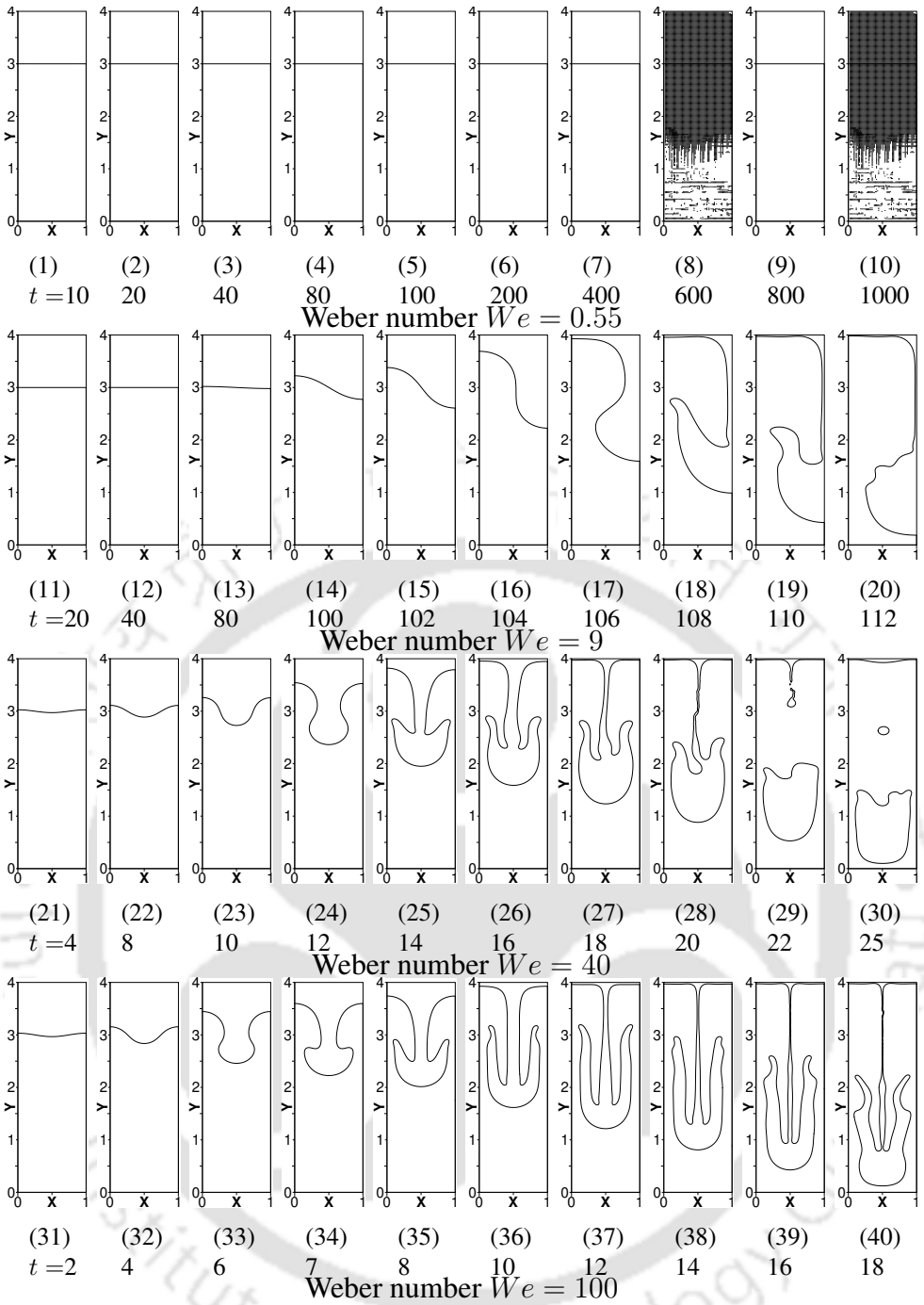

Figure 5.9: Instantaneous interface profiles for various Weber number in the range of We = 8-100 (rest of the parameters are: $\rho_r = 2$, $c_{p_r} = 2$, $k_r = 2$, $m = 2$, $r_T = 2$, $Ma = 50$, $Re = 50$, $M_1 = 0.45$ and $M_2 = 0.225$).

critical value or less, surface tension is large, strength of the elastic nature of the interface is strong enough to hold the heavier fluid layer over the lighter fluid layer. With increase in Weber number, surface tension decreases, the configuration undergoes instability.

For Weber number in the range of 0.55 to 35 (for example, see Fig. 5.9, for $We = 9$), the spike comes down along one of the side boundaries of the domain, instead of along the mid vertical plane of the domain. To find more about the results, for Weber number in the range of 0.55 to 35, simulations are carried out with domain of dimensionless width higher than unit width. With higher domain width, simulations are carried out with symmetry condition on left and right side boundaries, and the initial

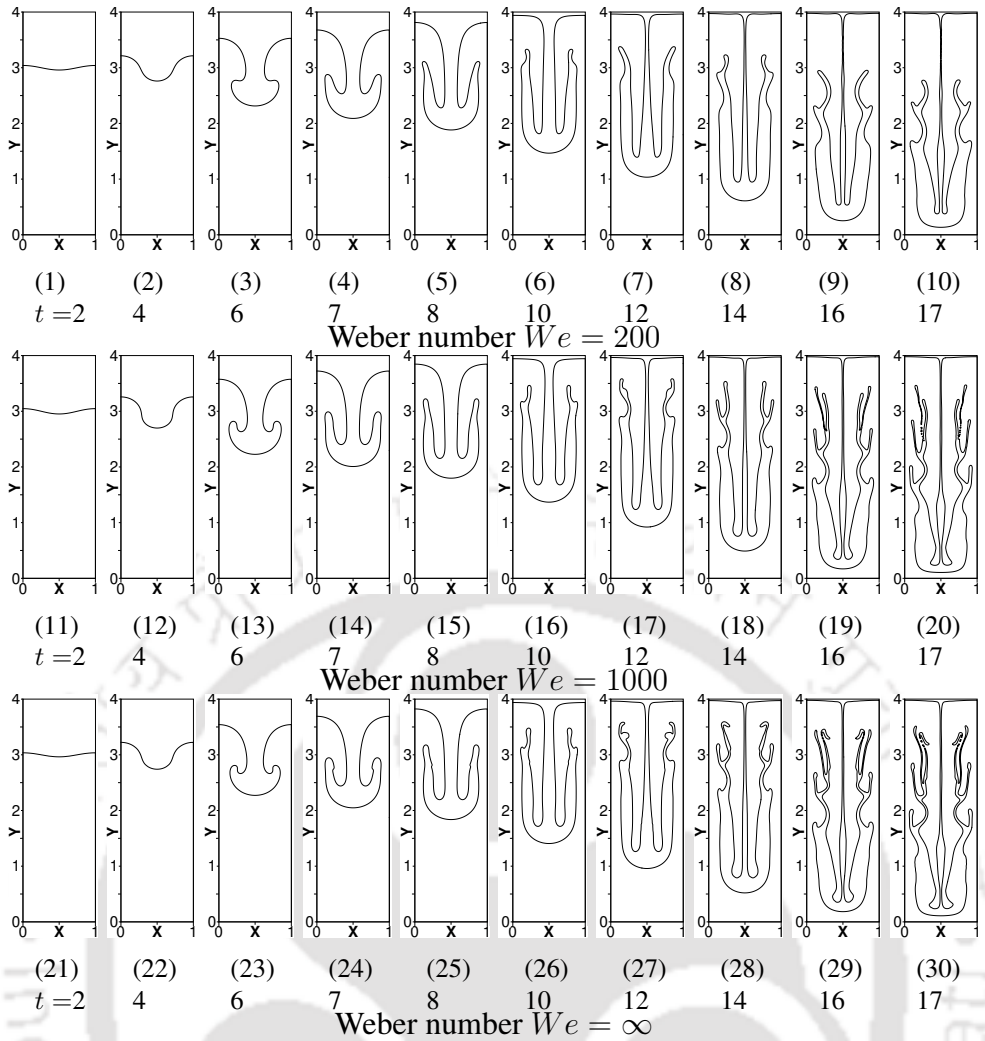

Figure 5.10: Instantaneous interface profiles for various Weber number in the range of $We = 200$ to infinity (rest of the parameters are: $\rho_r = 2$, $c_{p_r} = 2$, $k_r = 2$, $m = 2$, $r_T = 2$, $Ma = 50$, $Re = 50$, $M_1 = 0.45$ and $M_2 = 0.225$).

perturbation is specified according to $0.01\cos(2\pi x/L)$ (spatial periodicity of the initial perturbation is of one dimensionless unit). When the dimensionless domain width is increased to greater than a certain value, the solutions are found with spike coming down along the mid vertical plane. For example, for Weber number 35, when a domain of dimensionless width of about 1.2 or higher is used, the spike comes down along the mid vertical plane of the domain. This shows that for Weber number 35, the spatial periodicity of the instability is more than 1.2 times that of the initial perturbation. Similarly for Weber number 30, when a domain of dimensionless width of about 1.25 or higher is used, the spike comes down along the mid vertical plane. For Weber number 9, the spike comes down along the mid vertical plane in a domain of dimensionless width of about 2.1 or higher. This shows that for Weber number 30 and 9, the spatial periodicity of the instability is more than 1.25 and 2.1 times that of the initial perturbation, respectively. This infers that for Weber number in the range of 0.55-35, the spatial periodicity of the instability is higher than that of the initial perturbation.

With further increase in Weber number to more than 35, the spike comes down along the mid vertical plane of the domain (for example, see Fig. 5.9, for $We = 40$). This means for Weber number more than 35, the spatial periodicity of the instability is equal to the spatial periodicity of the initial

perturbation. For Weber number 40, a mushroom shaped spike comes down, which deforms into short and thick arms on both sides of the spike head. With time, stem of the spike breaks, and the spike strikes the bottom wall as a fluid droplet. With increasing Weber number, the spike undergoes larger deformation and moves relatively faster. For Weber number in the range of 100 to 200, the arms attached to the spike head become longer and more wavy. For Weber number 1000, the spike-arm structure deforms more, and the arm attached to the spike head becomes relatively thinner and more wavy. With time, both the arms split into multiple branches as the spike moves towards the bottom wall. For Weber number approaching infinity, surface tension approaching zero, spike-arm structure becomes more irregular, and with time, the arms on both sides of the spike head split into multiple branches. The formation of a non-smooth spike with multiple arms is due to the fact that surface tension is negligibly small, and rate of spike movement reaches to an asymptotic value. Such irregular spike-arm structure is expected to form at high Weber numbers, which represent low surface tension, as discussed by Sharp in [18].

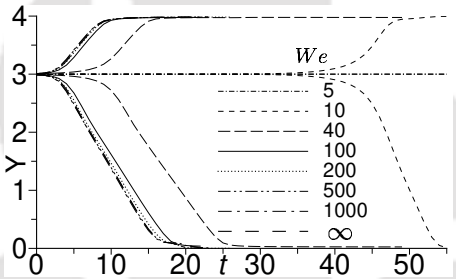

Figure 5.11: Time variation of spike front and bubble tip locations for various Weber numbers $We = 5$ to infinity (rest of the parameters are: $\rho_r = 2$, $c_{p_r} = 2$, $k_r = 2$, $m = 2$, $r_T = 2$, $Ma = 50$, $Re = 50$, $M_1 = 0.45$ and $M_2 = 0.225$).

Fig. 5.11 shows time variation of spike front and bubble tip locations for various Weber numbers. For Weber number 9, the heavier fluid spike strikes the bottom wall at about dimensionless time $t = 112$, and for Weber number approaching infinity, the heavier fluid spike strikes the bottom wall at the minimum asymptotic value of dimensionless time about $t = 17$, almost 6 times faster. Overall, increasing Weber number beyond the critical value shows destabilizing effect on the instability.

5.3.4 Effect of Froude number

Effect of Froude number on the instability is studied for various Froude numbers in the range of 0.5 to 11.5, in the presence of Marangoni effect. Figs. 5.12-5.13 show the instability evolution for various Froude numbers. For Froude number 0.5, the heavier fluid forms into a mushroom shaped spike which eventually deforms, and an elongated arm forms on both sides of the spike head. With time, the elongated arm splits into multiple branches as spike moves towards the bottom wall. For Froude number 0.75, the elongated arms become relatively smoother and simpler compared to those for Froude number 0.5. For Froude number in the range of 1 to 2, the arms on both sides of the spike head are relatively smoother and shorter than those of lower Froude numbers.

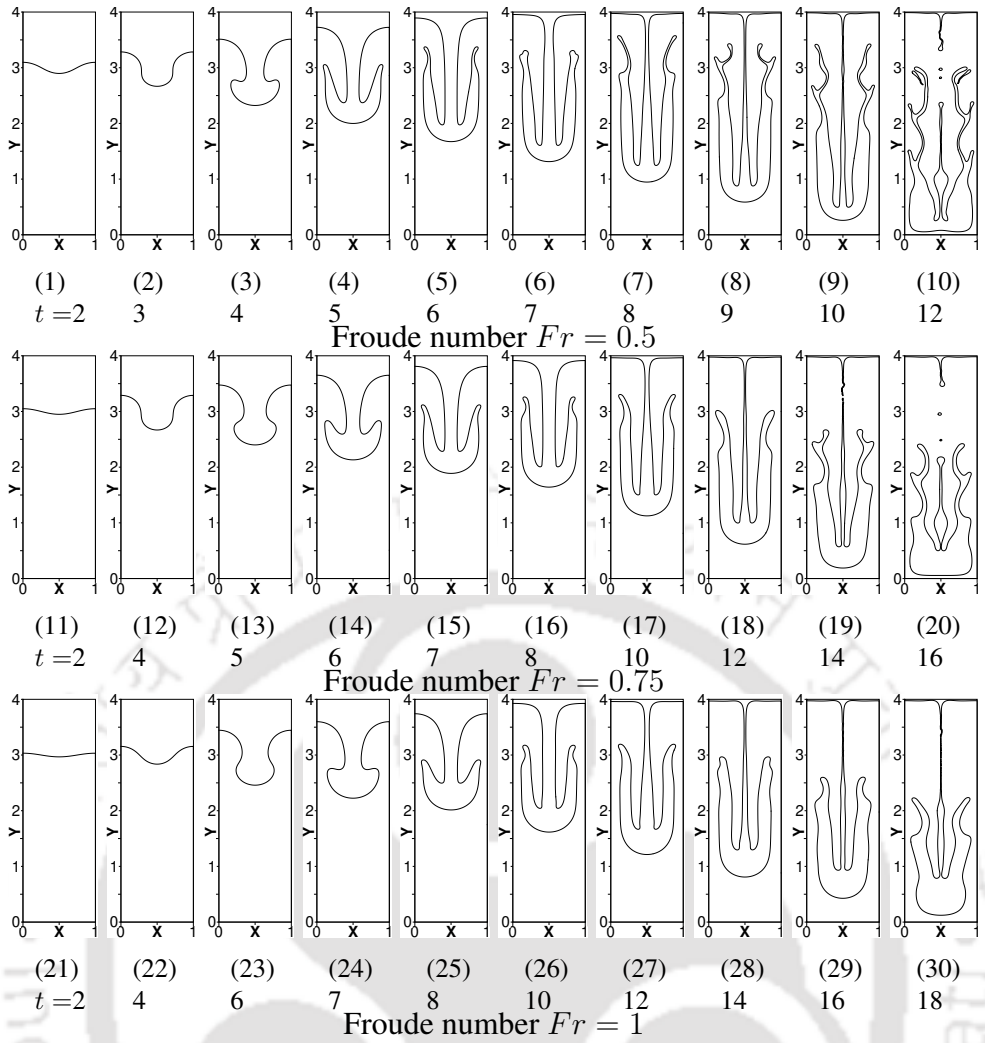

Figure 5.12: Instantaneous interface profiles for various Froude number in the range of $Fr = 0.5$-1 (rest of the parameters are: $\rho_r = 2$, $c_{p_r} = 2$, $k_r = 2$, $m = 2$, $r_T = 2$, $Ma = 50$, $Re = 50$, $We = 100$, $M_1 = 0.45$ and $M_2 = 0.225$).

With further increase in Froude number, relative gravitational effect reduces which shows an influential effect on the instability and rate of spike movement. For Froude number in the range of 2.75 to 11, the spike comes down along one of the side vertical boundaries of the domain, unlike for the lower Froude number cases for which spike comes down through mid vertical plane of the domain (for example, see Fig. 5.13, for $Fr = 2.75$). To find more inference of the results, for Froude number in the range of 2.75 to 11, simulations are carried out in the domain of dimensionless width higher than unit width. In such domain of higher width, simulations are carried out with symmetry conditions on both vertical side boundaries, and initially, the interface is specified to be perturbed according to $0.01\cos(2\pi x/L)$ (spatial periodicity of the initial perturbation is of one dimensionless unit). When the dimensionless domain width is increased to greater than a certain value, the solutions of the instability are found with spike coming down through mid vertical plane of the domain. For example, for Froude number 2.75, when a domain of dimensionless width of 1.2 or higher is used, the spike comes down through the mid vertical plane of the domain. This shows that for Froude number 2.75, spatial periodicity of the instability is found to be more than 1.2 times compared to that of the initial perturbation. This infers that for Froude number in this range ($Fr = 2.75$-11), the spatial periodicity

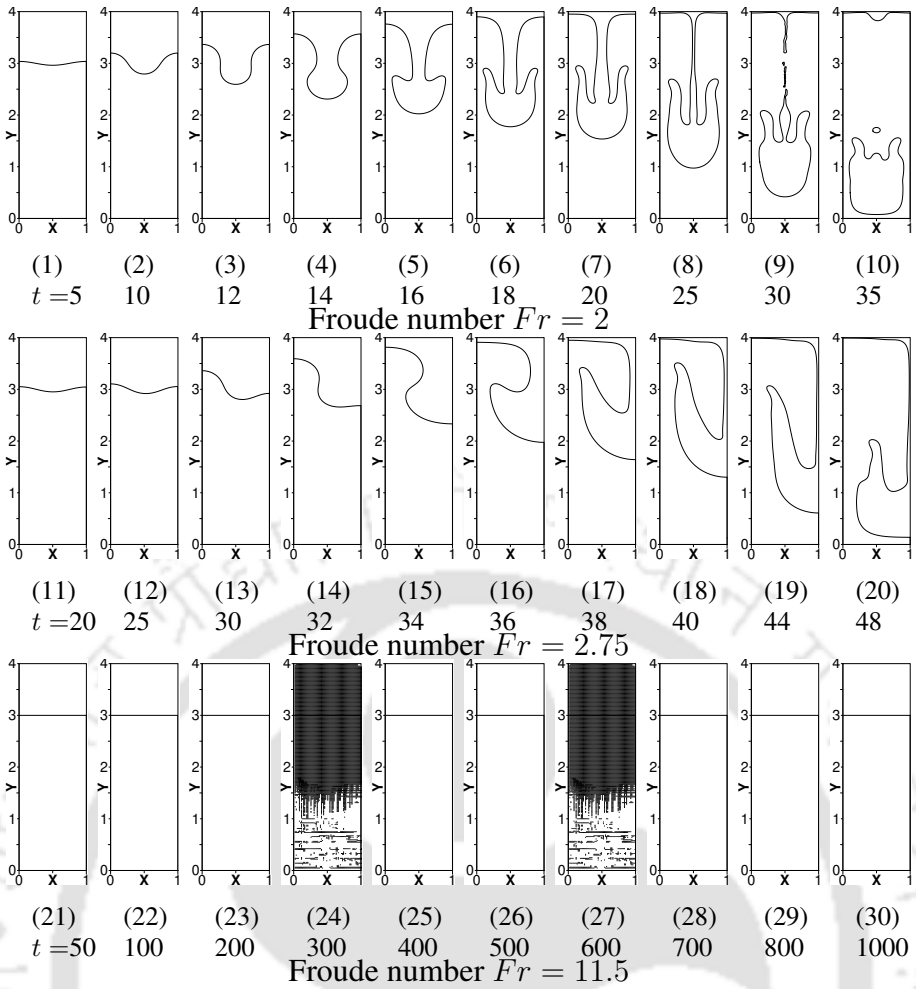

Figure 5.13: Instantaneous interface profiles for various Froude number in the range of $Fr = 2$-11.5 (rest of the parameters are: $\rho_r = 2$, $c_{p_r} = 2$, $k_r = 2$, $m = 2$, $r_T = 2$, $Ma = 50$, $Re = 50$, $We = 100$, $M_1 = 0.45$ and $M_2 = 0.225$).

of the instability is found to be higher than that of the initial perturbation. Increasing Froude number results into decreased relative gravitational effect, and the spike movement becomes relatively slower. Increase in Froude number shows stabilizing effect on the instability, and for Froude number value about 11.5 or more, the configuration does not undergo instability.

Fig. 5.14 shows time variation of spike front and bubble tip locations for various Froude numbers. For Froude number 0.5, spike strikes the bottom wall at about dimensionless time $t = 12$, and for Froude number 10, spike strikes the bottom wall at about dimensionless time $t = 250$, almost 20 times slower. This is due to the fact that with increasing Froude number value relative gravitational effect is reduced which turns into reduced rate of spike movement.

5.4 Conclusions

Marangoni effect on Rayleigh-Taylor instability in viscous stratified fluid layers is studied in 2-D rectangular coordinates. For the study, three types of functional dependencies of surface tension with temperature are considered which are constant, linear and parabolic dependencies. Rate of spike

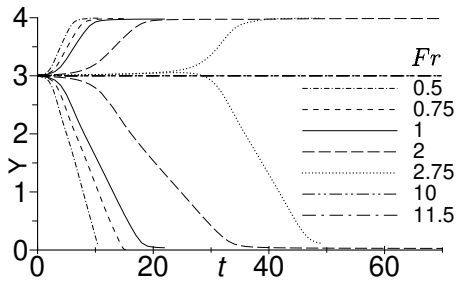

Figure 5.14: Time variation of spike front and bubble tip locations for various Froude numbers $Fr =$ 0.5-11.5 (rest of the parameters are: $\rho_r = 2$, $c_{p_r} = 2$, $k_r = 2$, $m = 2$, $r_T = 2$, $Ma = 50$, $Re = 50$, $We = 100$, $M_1 = 0.45$ and $M_2 = 0.225$).

movement is in the decreasing order of sequence of constant, parabolic and linear dependencies. This is because overall effective surface tension is the highest for constant and the lowest for linear dependencies. Critical value of Weber number is found to be 0.55, below which the configuration does not undergo instability. Increasing Weber number beyond the critical value shows destabilizing effect on the instability. For Weber number in the range of 0.55 to 35, the spike comes down through one of the side vertical boundaries of the domain representing higher value of spatial periodicity of the instability than that of the initial perturbation. For Weber number more than 35, the spike comes down through mid vertical plane representing that spatial periodicity of the instability is same as that of the initial perturbation. Increasing Froude number shows stabilizing effect on the instability, and for Froude number more than critical value of 11.5 or more, the configuration is stable.

Chapter 6

Rayleigh-Taylor instability in viscosity stratified medium in axisymmetric coordinates

In this chapter, Rayleigh-Taylor instability is studied in a temperature varying viscosity stratified fluid medium in axisymmetric configuration. Effect of viscosity stratification, viscosity ratio, temperature ratio, hot and cold wall locations and Weber number on the instability is studied under the influence of viscosity stratification.

6.1 Physical system

Physical system which is described in section 2.1.2 is used for the study presented in this chapter. Schematic diagram of the physical system is as shown in Fig. 2.3.

6.2 Mathematical treatment

In this present chapter, studies are performed by solving governing equations numerically using Basilisk software. The software uses Volume of Fluid (VoF) method. In VoF method an additional equation of volume fraction is solved to find the interface location. Hence, governing equations which consist of Navier-Stokes equations, energy equation and volume fraction equation are solved numerically.

6.2.1 Scaling parameters

For the present study, different scales are chosen to non-dimensionalize the governing equations. The reference scales for length, time, velocity, pressure, temperature and surface tension are taken equal to $\tilde{L}_{\text{ref}}$, $\tilde{L}_{\text{ref}}/\tilde{V}_{\text{ref}}$, $\tilde{V}_{\text{ref}}$, $\tilde{\rho}_{\text{ref}}\,\tilde{V}_{\text{ref}}^2$, $\tilde{T}_{\text{ref}}$ and $\tilde{\sigma}_{\text{ref}}$, respectively. Reference length is taken equal to $\tilde{L}$. Reference velocity is taken equal to $\left(\tilde{g}\,\tilde{L}_{\text{ref}}\right)^{1/2}$. Reference temperature is taken equal to cold wall temperature. Reference surface tension is taken equal to surface tension value ($\tilde{\sigma}_0$) at reference temperature. 'Fluid

2' fluid properties are taken as reference fluid properties ($\tilde{\rho}_2$, $\tilde{\mu}_2$, $\tilde{k}_2$, and $\tilde{c}_{p_2}$). The reference values are given as following.

$$\begin{gathered}\tilde{\rho}_{\text{ref}} = \tilde{\rho}_2, \quad \tilde{\mu}_{\text{ref}} = \tilde{\mu}_2, \quad \tilde{k}_{\text{ref}} = \tilde{k}_2, \quad \tilde{c}_{p_{\text{ref}}} = \tilde{c}_{p_2}, \\ \tilde{L}_{\text{ref}} = \tilde{L}, \quad \tilde{T}_{\text{ref}} = \min(\tilde{T}_1, \tilde{T}_2), \quad \tilde{\sigma}_{\text{ref}} = \tilde{\sigma}_0, \quad \tilde{V}_{\text{ref}} = \sqrt{\tilde{g}\,\tilde{L}}\end{gathered} \tag{6.1}$$

With the use of above reference values, definitions of dimensionless variables, which are given by Eq. (2.14), become

$$\begin{gathered}\rho = \frac{\tilde{\rho}}{\tilde{\rho}_2}, \quad \mu = \frac{\tilde{\mu}}{\tilde{\mu}_2}, \quad c_p = \frac{\tilde{c}_p}{\tilde{c}_{p_2}}, \quad k = \frac{\tilde{k}}{\tilde{k}_2}, \quad r = \frac{\tilde{r}}{\tilde{L}}, \quad z = \frac{\tilde{z}}{\tilde{L}}, \\ t = \frac{\tilde{t}}{\sqrt{\tilde{L}/\tilde{g}}}, \quad \mathbf{u} = \frac{\tilde{\mathbf{u}}}{\sqrt{\tilde{g}\,\tilde{L}}}, \quad p = \frac{\tilde{p}}{\tilde{\rho}_2\,\tilde{g}\,\tilde{L}}, \quad \theta = \frac{\tilde{T} - \min(\tilde{T}_1, \tilde{T}_2)}{\min(\tilde{T}_1, \tilde{T}_2)}, \quad \sigma = \frac{\tilde{\sigma}}{\tilde{\sigma}_0}\end{gathered} \tag{6.2}$$

6.2.2 Governing equations

Using the above dimensionless variables, governing equations are non-dimensionalized and given as following.

Continuity equation

$$\nabla\cdot\mathbf{u} = 0 \tag{6.3}$$

Momentum equation

$$\rho\left(\frac{\partial\mathbf{u}}{\partial t} + \mathbf{u}\cdot\nabla\mathbf{u}\right) = -\nabla p + \frac{1}{Re}\nabla\cdot\mu\,\left(\nabla\mathbf{u} + \nabla\mathbf{u}^{\mathrm{T}}\right) + \mathbf{F} \tag{6.4}$$

Energy equation

$$\rho\,c_p\left(\frac{\partial\theta}{\partial t} + \mathbf{u}\cdot\nabla\theta\right) = \frac{1}{Re\,Pr}\,\nabla\cdot(k\nabla\theta) \tag{6.5}$$

Volume fraction equation

$$\frac{\partial f}{\partial t} + \mathbf{u}\cdot\nabla f = 0 \tag{6.6}$$

The study presented in this chapter is carried out with constant surface tension. Hence, the dimensionless form of body force term ($\mathbf{F}$), which is given by Eq. (2.23), is given by

$$\mathbf{F} = \frac{1}{We}\,\kappa\,\delta\,\mathbf{n} - \frac{\rho}{Fr}\,\mathbf{e}_j \tag{6.7}$$

Expressions of dimensionless numbers in the above governing equations, which are given by Eq. (2.24), are as following.

$$Re = \frac{\tilde{\rho}_2\,\tilde{g}^{1/2}\,\tilde{L}^{3/2}}{\tilde{\mu}_2}, \quad Fr = 1, \quad We = \frac{\tilde{\rho}_2\,\tilde{g}\,\tilde{L}^2}{\tilde{\sigma}_0}, \quad Pr = \frac{\tilde{\mu}_2\tilde{c}_{p_2}}{\tilde{k}_2} \tag{6.8}$$

In this chapter, viscosity stratification effect is provided by varying the viscosity with temperature exponentially. Variations of viscosities in the fluid layers, as given by Eq. (2.25), are as following

$$\mu_1 = m\, e^{-\theta} \qquad \text{and} \qquad \mu_2 = e^{-\theta} \tag{6.9}$$

Here, m is top heavier to bottom lighter fluid viscosity ratio defined as $m = \mu_1(\tilde{T}_2)/\mu_2(\tilde{T}_2)$ at reference temperature. Dimensionless fluid properties (ρ, k, c_p and μ) are calculated using a function of volume fraction f, as given by Eq. (2.13).

$$\begin{aligned} \rho &= \rho_1\, f + \rho_2\, (1 - f) \\ \mu &= \mu_1\, f + \mu_2\, (1 - f) \\ c_p &= c_{p_1}\, f + c_{p_2}\, (1 - f) \\ k &= k_1\, f + k_2\, (1 - f) \end{aligned} \tag{6.10}$$

6.2.3 Initial and boundary conditions

For the study presented in this chapter, the initial and boundary conditions are given in subsection 2.2.3. The dimensions of the axisymmetric domain chosen for the study presented in this chapter are given in the same subsection.

6.2.4 Numerical methodology

The numerical methodology of Basilisk software is discussed in detail, in subsection 2.2.6. Usage of the software to solve multiphase flow in axisymmetric configuration is validated, and the validations are presented in the following subsection.

6.2.5 Validation for axisymmetric multiphase flow solution

Before studying viscosity stratification effect on the instability of the present study, usage of the software is validated for simulations of multiphase flow in constant viscosity fluid layers as well as in variable viscosity fluid layers for axisymmetric configuration. The validations are as following.

6.2.5.1 Bubble rise in constant viscosity medium: comparison with experimental study

Usage of the software for simulations of multiphase flow in constant viscosity fluid layers is validated by solving the dynamics of bubble rise in aqueous sugar solution using the present software and comparing the obtained results with those of experimental study results of Bhaga and Weber [11]. A bubble of dimensionless radius 1 is rising in a vertical circular tube of dimensionless radius 48. The dimensionless height of the tube is taken equal to 48. At initial state, spherical bubble is kept stationary such that its center is located on the axis of the circular tube and at a vertical dimensionless distance of 4 from the bottom of the domain. Axisymmetric condition is applied along the vertical axis. Free slip and no penetration conditions are applied at outer vertical side boundary. Free outflow and inflow conditions are applied on the top and bottom boundaries, respectively. Bubble fluid to

surrounding fluid density ratio is taken equal to 7.473×10^{-4} and viscosity ratio is taken equal 8.152 $\times$ 10^{-6}. Dimensionless numbers, which are Reynolds number (Re) and Weber number (We), are defined based on the radius of bubble and fluid properties of bubble. Various Reynolds numbers Re = 2.315, 3.094, 4.935 and 8.157, are chosen for the simulations. Weber number is set equal to We = 29. The simulations are carried out till the shape of the bubble reaches to terminal shape and does not further change with time. The terminal shapes obtained using the present software are compared with the terminal shapes presented by Bhaga and Weber [11] in Fig. 6.1. The terminal shapes of the bubble obtained using the present software show good match with those of the reference study.

(1) $Re = 2.315$ (2) $Re = 3.094$ (3) $Re = 4.935$ (4) $Re = 8.157$

Figure 6.1: Comparison of the terminal shapes of the bubble obtained by present software with the shapes found in Bhaga and Weber [11]. Solid line represents results with present software and dashed line represents the results of Bhaga and Weber [11].

6.2.5.2 Bubble rise in constant viscosity medium: comparison with numerical studies

The usage of software is validated with the various numerical studies of bubble rise dynamics for the constant viscosity case.

Validation for bubble rise dynamics with constant viscosity-1

The present axisymmetric results obtained using the present software is compared with 3-D numerical results of Tripathi and Sahu [12]. The physical system consists of a bubble of radius R rising in a long vertical circular tube of radius $48R$ which is filled with aqueous sugar solution. Dimensionless radius of the bubble is taken equal to $R = 1$. Dimensionless height of the tube taken equal to 48. Initially, the spherical bubble is placed such that its center is located on the vertical axis and at a vertical dimensionless distance of 4 from the bottom boundary of the tube. Vertical axis of the domain is applied with axisymmetric condition. Outer side vertical boundary is imposed with free slip and no-penetration condition. The bottom and top horizontal boundaries are imposed with free inflow and outflow conditions, respectively. Bubble fluid to surrounding fluid density ratio and viscosity ratio are taken equal to 7.473×10^{-4} and 8.152×10^{-6}, respectively. Dimensionless numbers such as Reynolds number (Re) and Weber number (We) are defined based on the bubble radius and the bubble fluid properties. The simulations are carried out for Reynolds number values of Re = 2.315, 3.094, 4.935 and 8.157. Weber number (We) is taken equal to 29. For the study of all the Reynolds numbers, simulations are carried out till the bubble reaches to its terminal shape where the bubble shape does

not further change with time. The terminal shapes obtained from the present software is compared with those Tripathi and Sahu [12] in Fig. 6.2 for various Reynolds numbers. The present results show good match with the reference results.

(1) $Re = 2.315$ (2) $Re = 3.094$ (3) $Re = 4.935$ (4) $Re = 8.157$

Figure 6.2: Comparison of the terminal shapes of bubble obtained from present software with those presented by Tripathi and Sahu [12]. Solid line represents the results of the present software and dashed line represents the results reference study results.

Validation for bubble rise dynamics in constant viscosity medium-2

In this, validation of usage of the present software is carried out by solving the bubble rise problem using the present software and comparing the obtained results with those presented by Sussman and Smereka [13]. Physical system consists a bubble rise in a surrounding fluid medium in an axisymmetric configuration. The system contains of a bubble of dimensionless radius of 1 rising in an axisymmetric domain of dimensionless height of 12. Dimensionless width is taken equal to 6. Initially, spherical shape bubble is kept stationary such that its center is located on axis at vertical dimensionless distance of 1.1 from the bottom boundary of the domain.

Axisymmetric condition is applied on axis and symmetry conditions are applied on outer vertical side boundary. No slip and no penetration conditions are applied on both top and bottom boundaries. Surrounding fluid to bubble fluid density ratio is taken to be 0.0011 and viscosity ratio is taken to be 0.0085. Dimensionless numbers such as Reynolds number (Re), Weber number (We) and Froude number (Fr) are defined based on bubble radius and bubble fluid properties. The values of dimensionless numbers are $Re = 9.8$, $We = 10$, and $Fr = 0.76$. The bubble shapes obtained using the present software at different time instance are compared with those presented by Sussman and Smereka [13] in Fig. 6.3. The present results show good match with the reference results.

The usage of the software is also validated for a rising bubble problem with breaking phenomena. For the breaking bubble phenomena, a bubble is taken of dimensionless radius of 1 rising in an axisymmetric domain of dimensionless height of 6. Dimensionless width of the domain is 6. Initially, spherical bubble is placed such that its center is located on vertical axis and at a dimensionless vertical height of 1.1 from the bottom boundary. Free slip condition is applied on the outer vertical boundary while axisymmetric condition is applied on the vertical axis. Top and bottom boundaries are specified with no slip and no penetration conditions (walls). Surrounding fluid to bubble fluid density ratio and viscosity ratio are taken equal to 0.001 and 0.01, respectively. Dimensionless numbers such as Reynolds number (Re), Weber number (We) and Froude number (Fr) are taken equal 100, 200, and

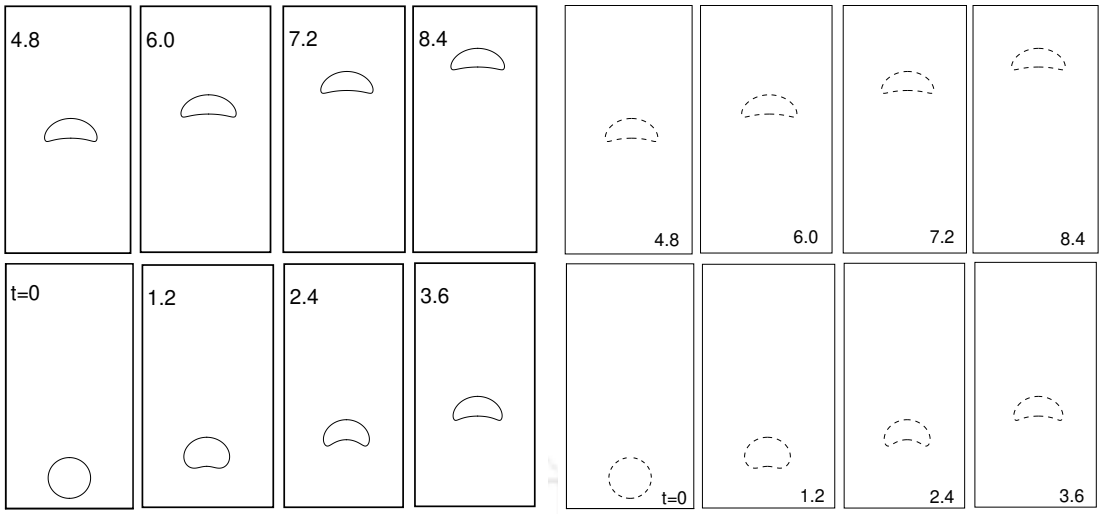

(1) Present (2) Sussman and Smereka [13]

Figure 6.3: Comparison of the instantaneous bubble shapes for constant viscosity case obtained from present software with those presented by Sussman and Smereka [13].

1, respectively. These dimensionless numbers are defined based on fluid properties of the bubble and radius of the bubble. Shapes of the breaking bubble at varios time instances are obtained using the software and compared with those presented by Sussman and Smereka [13] in Fig. 6.3. Present study results show good match with reference study results.

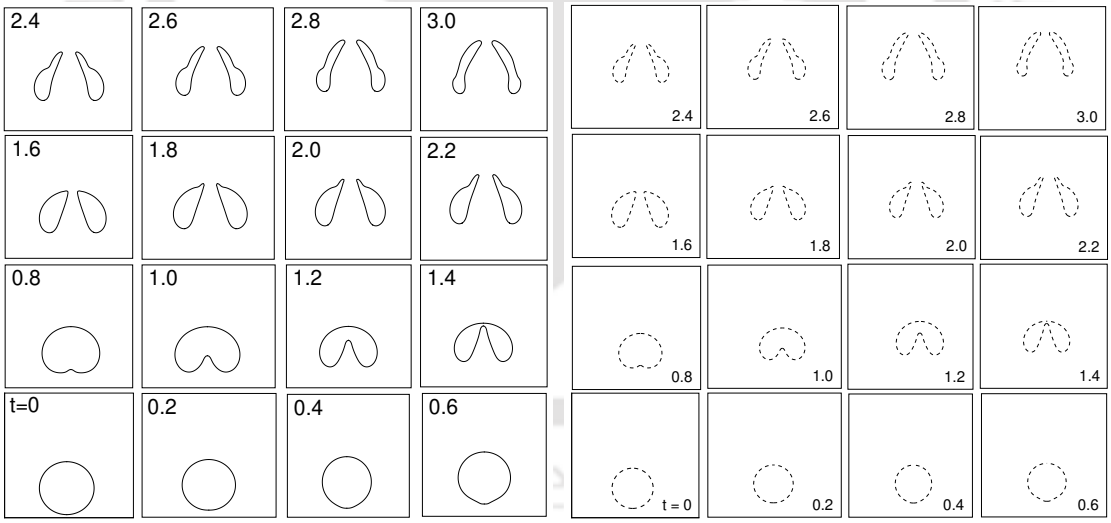

(1) Present (2) Sussman and Smereka [13]

Figure 6.4: Comparison of the instantaneous bubble shapes of breaking bubble obtained from present software with those presented by Sussman and Smereka [13].

Validation for bubble rise dynamics in constant viscosity medium-3

For the validation, dynamics of bubble rise is simulated using the present software and the obtained results are compared with those presented in Premlata et al. [14]. A bubble with a dimensionless diameter of 1 is rising in a surrounding fluid medium in an axisymmetric domain of size of 48×48.

Initially, the spherical bubble kept stationary such that its center is located on vertical axis at a vertical dimensionless distance of 4 from the bottom boundary. Surrounding fluid to bubble fluid density ratio and viscosity ratio are set to 1000 and 100, respectively. Reynolds number and Weber number are taken equal to $Re = 2.236$ and $We = 0.005$, respectively. For the comparison of bubble shape

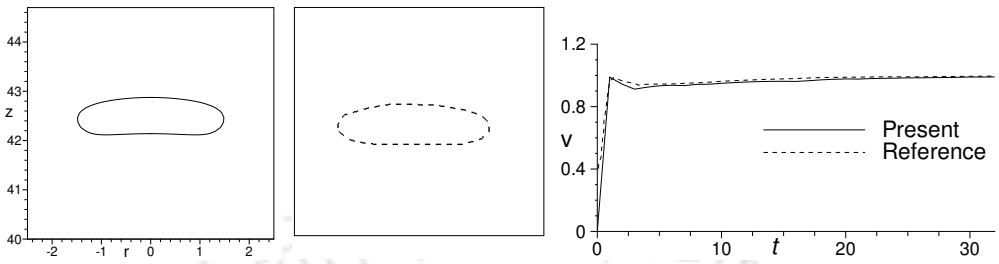

(1) Present (2) Premlata et al. [14] (3) Rise velocity

Figure 6.5: Comparison of present software results in the form of bubble shape at $t = 40$ for constant (Fig. 6.5(1)-6.5(2)) and bubble rise velocity variation with time (Fig. 6.5(3)) in surrounding fluid of constant viscosity with those presented by Premlata et al. [14].

at about dimensionless time $t = 40$, the shape of the bubble obtained from present software and those reported by Premlata et al. [14] are presented in Fig. 6.5(1) and Fig. 6.5(2), respectively. Time variation of bubble rise velocity is also compared and presented in Fig. 6.5(3). The results obtained from the present simulations show good match with those presented in Premlata et al. [14].

6.2.5.3 Validation for bubble rise dynamics in viscosity stratified medium

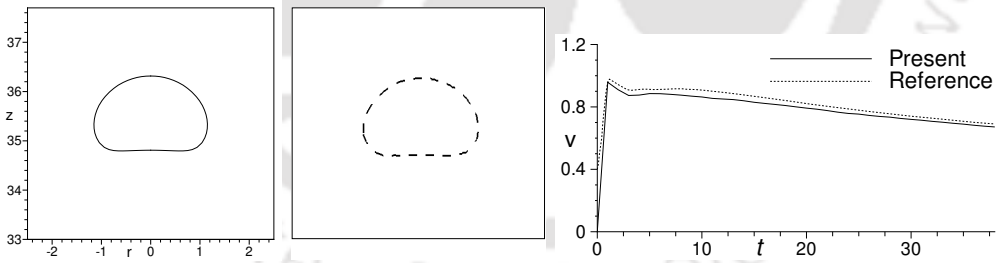

(1) Present (2) Premlata et al. [14] (3) Rise velocity

Figure 6.6: Comparison of present simulation results in the form of bubble shape at $t = 40$ (Fig. 6.6(1)-6.6(2)) and bubble rise velocity variation with time (Fig. 6.6(3)) in a viscosity-stratified medium with those presented by Premlata et al. [14].

The validation of axisymmetric simulations for prediction of viscosity stratified two phase flows is carried out using the results presented in Premlata et al. [14]. Premlata et al. [14] presented solutions for axisymmetric bubble rising inside a viscosity stratified fluid medium with an unbounded axisymmetric domain. The domain is of dimensionless size of 48×48. Dimensionless radius of the spherical bubble is taken equal to 1. At initial state, a spherical bubble is placed at a dimensionless distance of 4 from the bottom boundary. The center of the bubble is located on the vertical axis of the domain.

The dimensionless numbers Reynolds number (Re) and Weber number (We) are defined based on the bubble radius and properties of the bubble fluid. Values of $Re = 2.236$ and $We = 0.005$ are taken for the study. The outer fluid density to bubble density ratio and viscosity ratio are taken equal to 1000 and 100, respectively. Viscosity of the outer fluid is taken to be varying linearly with dimensionless elevation z according to $m\,(a_1 + a_2\,z)$. Here, m is the viscosity ratio and $a_1 = a_2$ =0.2. The shape of the bubble after it reaches to terminal velocity is compared with the result of Premlata et al. [14] in Fig. 6.6(1)-6.6(2). The variation of bubble velocity with time is compared with that presented in the reference study in Fig. 6.6(3). Comparison of the present simulation results show good agreement with those of Premlata et al. [14].

6.2.6 Grid independence test

Grid independence test is carried out before performing the numerical simulations to study Rayleigh-Taylor instability in viscosity stratified fluid medium in axisymmetric configuration. The grid independence test is carried out for the parameters $\rho_r = 2$, $m = 2$, $k_r = 2$, $c_{p_r} = 2$, $Re = 50$, $Pr = 1$, $Fr = 1$, $We = 500$ and $r_T = 3$, which are the baseline parameters of the study of the present chapter. The study is carried out using Basilisk software with uniform grid spacing in the both axial and radial coordinate directions. For the test, grid levels of 7, 8, 9 and 10 are chosen which correspond to the minimum grid spacing of 0.03125, 0.0156, 0.0078 and 0.0039, respectively, as given in Table 5.1. Comparison of instantaneous interface profiles of Rayleigh-Taylor instability and comparison of spike front location for different grids are presented in Fig. 6.7 and Fig. 6.8, respectively. Figures show that further decrease in the minimum grid spacing from 0.0078 or lower, the solutions do not show any significant change. Hence, the grid level of 9 which corresponds to the minimum grid spacing of 0.0078 is used for the numerical simulations.

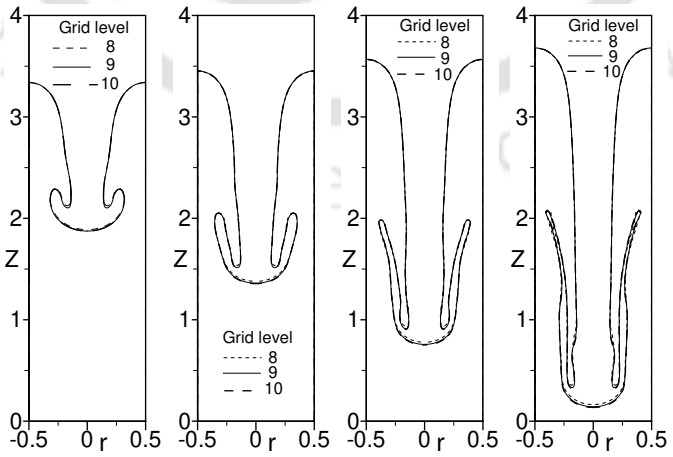

(1) t =6 (2) t =7 (3) t =8 (4) t =9

Figure 6.7: Comparison of instantaneous interface profiles of Rayleigh-Taylor instability in variable viscosity fluid layers in axisymmetric configuration obtained with different grid sizes (rest of the parameters are: $\rho_r = 2$, $m = 2$, $k_r = 2$, $c_{p_r} = 2$, $Re = 50$, $Pr = 1$, $Fr = 1$, $We = 500$ and $r_T = 3$).

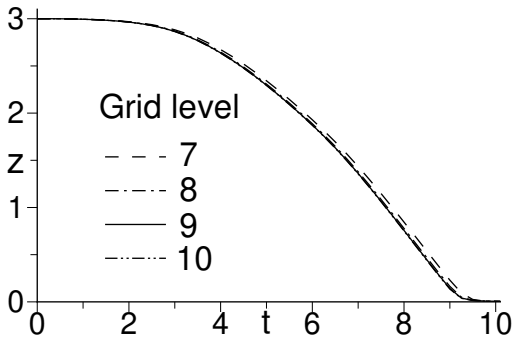

Figure 6.8: Comparison of time variation of spike front locations for various grid sizes in variable viscosity fluid layers (rest of the parameters are: $\rho_r = 2$, $m = 2$, $k_r = 2$, $c_{p_r} = 2$, $Re = 50$, $Pr = 1$, $Fr = 1$, $We = 500$ and $r_T = 3$).

6.3 Results and discussion

6.3.1 Baseline parameter values

In the present work, effect of various parameters such as viscosity ratio, temperature ratio, Prandtl number and Weber number on Rayleigh-Taylor instability is studied. All these studies are carried out at a set of baseline parameter values. The baseline parameter values are taken to be heavier fluid to lighter fluid viscosity ratio $m = 2$, density ratio ρ_r =2, thermal conductivity ratio $k_r = 2$, heat capacity ratio $c_{p_r} = 2$, Reynolds number $Re = 50$, Prandtl number $Pr = 1$, Froude number $Fr = 1$, Weber number $We = 500$ and temperature ratio $r_T = 3$. For the baseline configuration, top wall is heated and bottom wall is cooled. In the study of effect of any particular parameter, the parameter of focus is varied keeping all the other parameters at the above baseline values. For example, in the study of effect of viscosity ratio, the value of viscosity ratio is varied while keeping all other parameter values fixed at the above baseline values. Similarly, it is followed for the study of effect of other parameters.

6.3.2 Effect of viscosity variation with temperature

The effect of variable viscosity of fluid layers on the instability is examined comparing with that of fluid layers with constant viscosity. In the baseline Rayleigh-Taylor configuration of the present study, top wall is heated isothermally and bottom wall is cooled isothermally. The viscosity of fluid layers decreases exponentially with temperature. This results in temperature decreasing from top wall to bottom wall. Hence, the viscosity of bottom layer decreases from bottom wall to interface. In the top layer viscosity decreases from interface to top wall. Due to the viscosity variation within the individual fluid layers, Rayleigh-Taylor instability is expected to be different from that in fluid layers with constant viscosity.

To find out the effect of variable viscosity, Rayleigh-Taylor instability with variable viscosity fluid

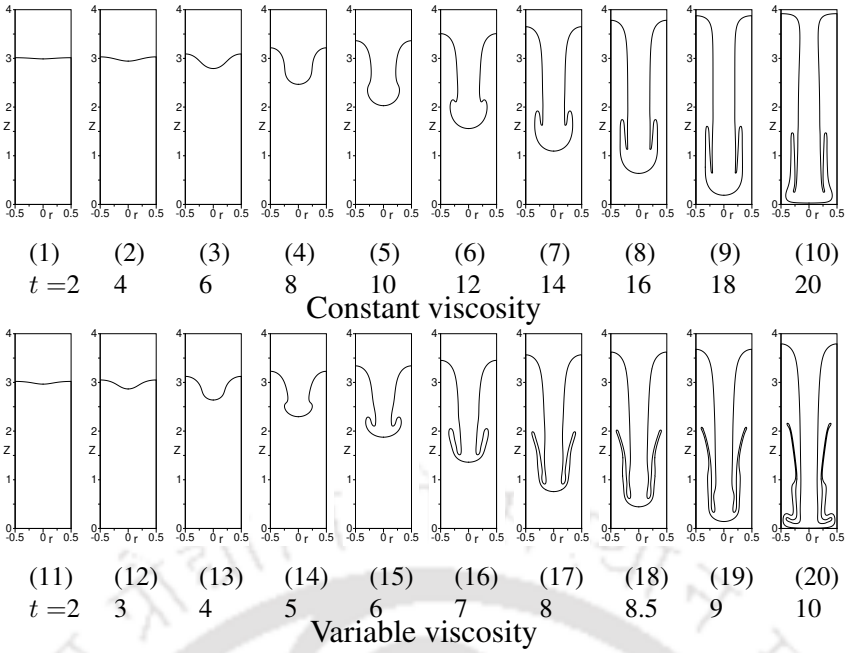

Figure 6.9: Instantaneous interface profiles for constant and variable viscosity of fluid layers for viscosity ratio $m = 2$ (rest of the parameters are: $\rho_r = 2$, $k_r = 2$, $c_{p_r} = 2$, $Re = 50$, $Pr = 1$, $Fr = 1$, $We = 500$ and $r_T = 3$).

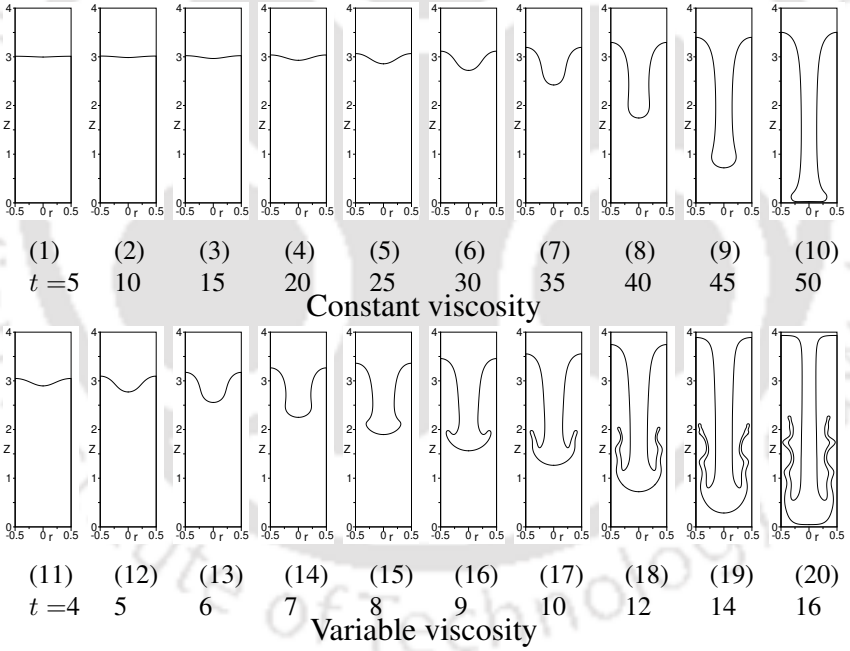

Figure 6.10: Instantaneous interface profiles for constant and variable viscosity of fluid layers for viscosity ratio $m = 20$ (rest of the parameters are: $\rho_r = 2$, $k_r = 2$, $c_{p_r} = 2$, $Re = 50$, $Pr = 1$, $Fr = 1$, $We = 500$ and $r_T = 3$).

layers is compared to that of constant viscosity fluid layers for various viscosity ratios in Figs. 6.9–6.12. The figures emphasize that temperature varying viscosity influences Rayleigh-Taylor instability to large extent compared to constant viscosity. In initial stage, the perturbation grows according to linear instability when the perturbation is small. This linear instability growth eventually converts into nonlinear growth when the disturbance grows to be larger. Once this stage begins, the interface deforms into a mushroom shape structure. With further time evolution, the upper fluid penetrates

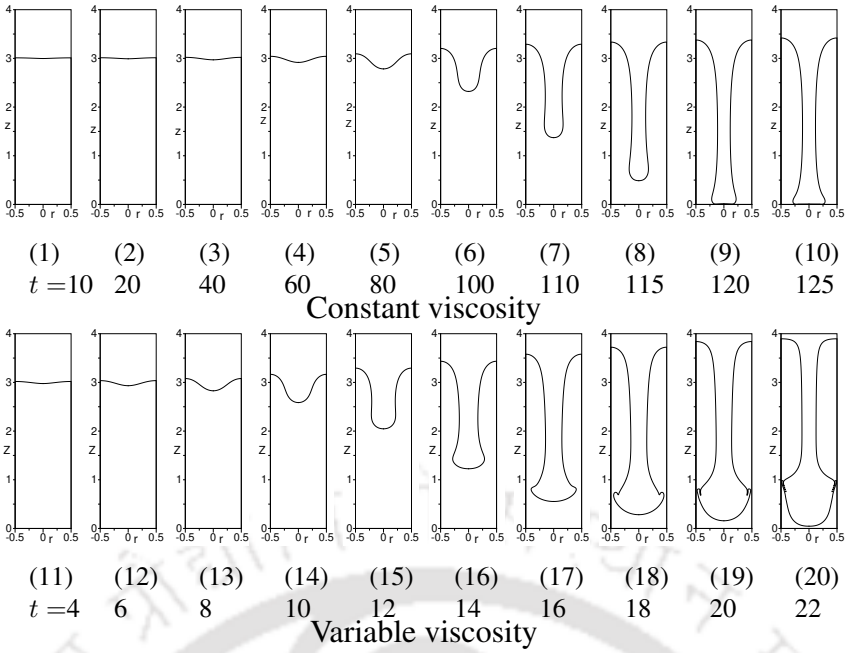

Figure 6.11: Instantaneous interface profiles for constant and variable viscosity of fluid layers for viscosity ratio $m = 60$ (rest of the parameters are: $\rho_r = 2$, $k_r = 2$, $c_{p_r} = 2$, $Re = 50$, $Pr = 1$, $Fr = 1$, $We = 500$ and $r_T = 3$).

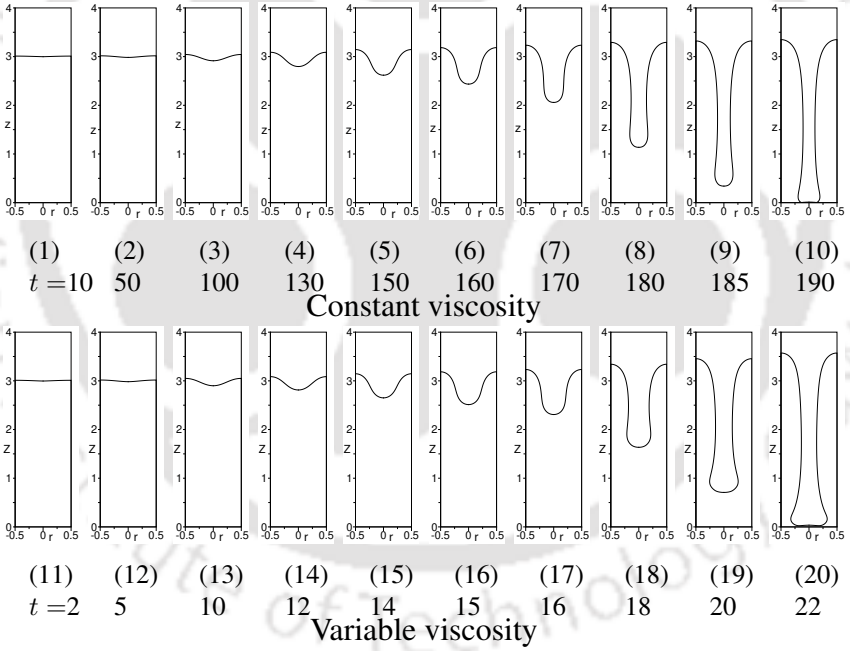

Figure 6.12: Instantaneous interface profiles for constant and variable viscosity of fluid layers for viscosity ratio m =100 (rest of the parameters are: $\rho_r = 2$, $k_r = 2$, $c_{p_r} = 2$, $Re = 50$, $Pr = 1$, $Fr = 1$, $We = 500$ and $r_T = 3$).

into the lower fluid in the form of a spike. The lower fluid rises in the form of a bubble. When the spike moves down and the bubble rises up, the velocities on either sides of the interface will be in opposite directions. This causes shearing action on the configuration around the interface. Such opposite flowing fluids lead to Kelvin-Helmholtz instability. Depending on the parameter values and the shear force distribution on both sides of the interface the spike undergoes further deformations and instabilities. In Rayleigh-Taylor instability for both varying viscosities and constant viscosities,

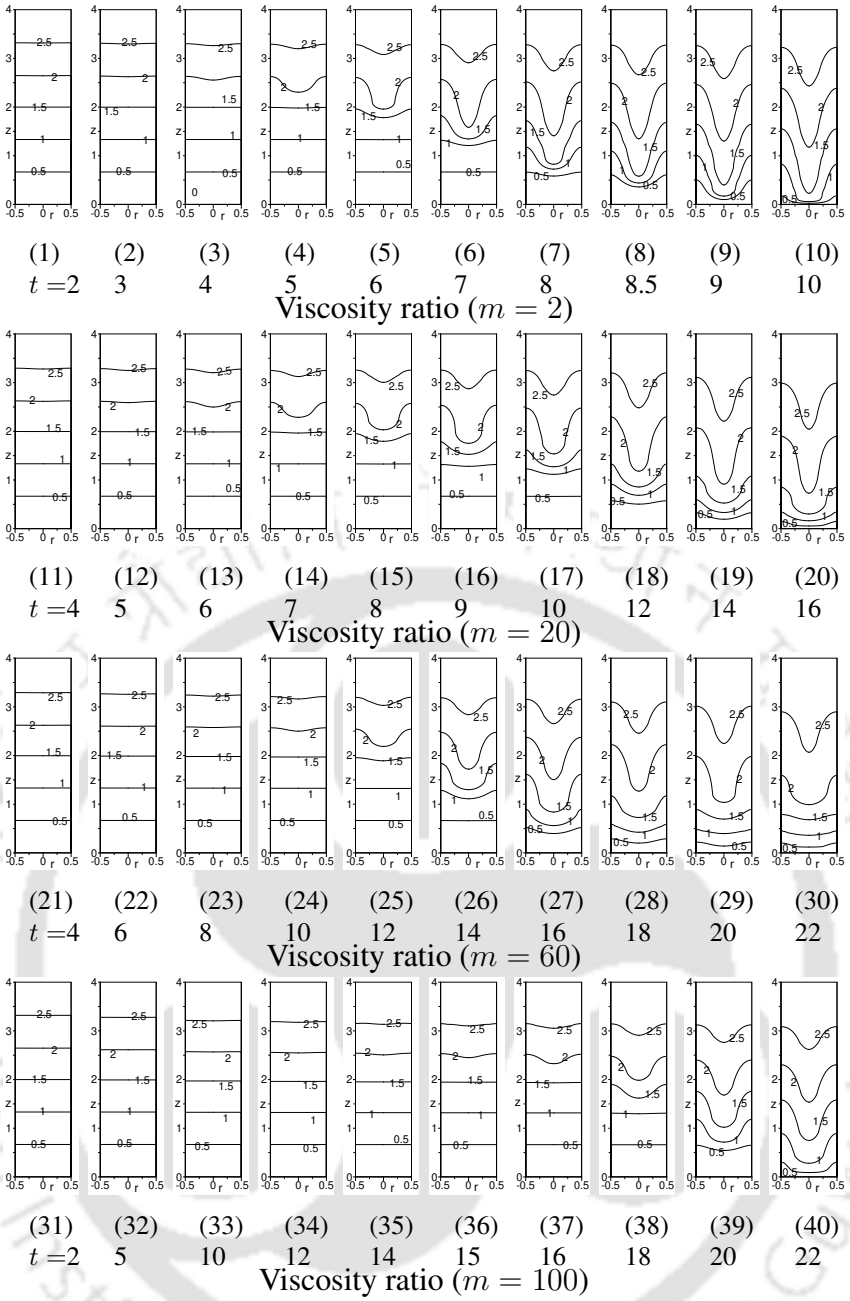

Figure 6.13: Temperature contours at different time instances for various viscosity ratios m =2, 20, 60 and 100 for variable viscosity fluid layers (rest of the parameters are: $\rho_r = 2$, $k_r = 2$, $c_{p_r} = 2$, $Re = 50$, $Pr = 1$, $Fr = 1$, $We = 500$ and $r_T = 3$).

the linear instability and mushroom forming stages are common for all sets of parameter values. However, at late stages after the mushroom shape formation, the deformation of spike and its structure vary significantly based on the parameter values and imposed conditions.

The interface profiles at various time instances for viscosity ratio 2 is shown in Fig. 6.9. Initially the disturbance grows linearly. At the later stages, in the nonlinear regime, the top fluid layer penetrates into bottom fluid layer in the form of mushroom shaped spike. Diameter of the spike for the case of constant viscosity is larger than that of variable viscosity. For the variable viscosity, a thin elongated skirt can be observed to form. The length of the skirt in constant viscosity fluid layers is much smaller than that of variable viscosity fluid layers. With variable viscosity, the penetration of

top fluid layer into bottom fluid layer happens with higher velocity. When viscosity in the fluid layers decreases with temperature, the viscous forces decrease. As viscous resistant forces decrease, the gravitational forces take dominant role resulting higher velocities of the fluid.

The instability for viscosity ratio 20 is shown in Fig. 6.10 for both variable and constant viscosity cases. For constant viscosity case the upper fluid penetrates into bottom fluid layer in the form of fluid column without any skirt. For variable viscosity case initially a mushroom shaped spike is formed and eventually the spike continues to have elongated wavy skirt. The thickness of the skirt is larger than that for viscosity ratio 2. The wavy structure is due to the fact, for higher viscosity ratios, the presence of higher viscous forces in the upper fluid makes the skirt to be more curvy.

Rayleigh-Taylor instability for viscosity ratio 60 is shown in Fig. 6.11. For constant viscosity case, the structure of the spike is similar to that of viscosity ratio 20. However, for variable viscosity case, the length of the skirt decreases and thicker spike head is formed. From this figure, a strong effect of variable viscosity on the instability can be observed compared to that of constant viscosity. The instability with variable viscosity is compared to that of constant viscosity for viscosity ratio m =100 in Fig. 6.12. For $m = 100$, for both constant and variable viscosity cases, the upper fluid penetrates into the lower fluid layer in the form of a fluid column. The shape of the interface structure is similar for both the cases. However, in the case of constant viscosity, the mushroom shape is formed at $t \geq 150$, whereas, for variable viscosity mushroom shape is formed at $t \geq$14. The variable viscosities prepones the onset of nonlinear instability regime very much compared to that with constant viscosities. It is evident that the dependence of viscosity on temperature increases the spike movement by more than 9 times.

Fig. 6.13 shows instantaneous temperature contours for viscosity ratios m =2, 20, 60 and 100 for viscosity varying temperature configuration. In initial stage, for all the viscosity ratios, temperature contours are parallel to horizontal walls. The formation of temperature contours parallel to horizontal walls represents heat transfer through conduction mode. As the velocities in the domain are very small in the linear instability stage, the temperature contours are oriented parallel to horizontal walls in this stage. In the nonlinear growth stage, temperature contours bend in the downward direction. The number of contours which bend downwards depends on the extent to which upper fluid layer penetrates into the lower fluid layer. Deeper the penetration, larger the number of contours bend downwards. It can be observed from the figure that with increasing viscosity ratio, the temperature contours stay horizontal for longer time duration. This is due to the fact that longer time is taken for the penetration with increasing viscosity ratio.

6.3.3 Effect of viscosity ratio

Figs. 6.14–6.16 show the instability evolution for viscosity ratio varying from 0.1 to 100 in the form of interface profiles for fluid layers with variable viscosity. At the beginning of the nonlinear stage of instability, the spike is formed with mushroom shape which is almost similar for all the cases of viscosity ratio. Whereas, in later stage of instability, spike formation is strongly affected by viscosity

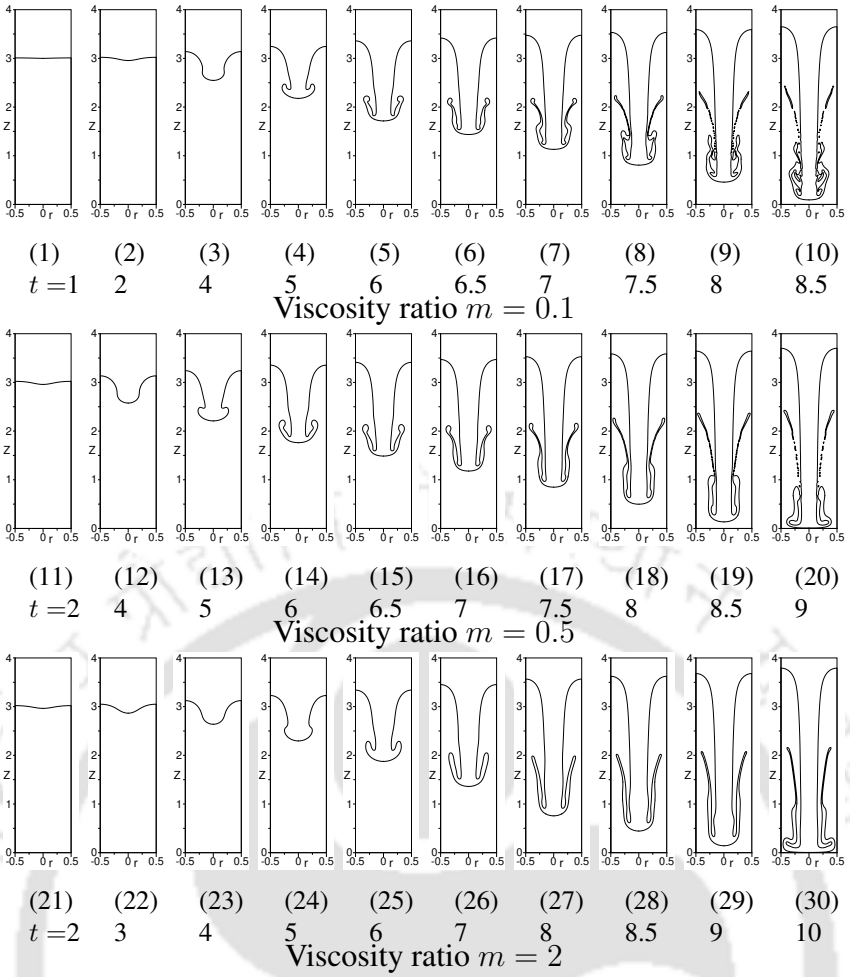

Figure 6.14: Instantaneous interface profiles for various viscosity ratios m = 0.1-2 (rest of the parameters are: $\rho_r = 2$, $k_r = 2$, $c_{p_r} = 2$, $Re = 50$, $Pr = 1$, $Fr = 1$, $We = 500$ and $r_T = 3$).

ratio. In this stage, heavy fluid spike penetrates into the lower fluid with increasing velocity with time. As the velocity of the spike increases viscous shear force between the two fluid layers increases. The distribution of shear on both sides of the interface dictates interface structures as the spike moves downwards.

Interface evolution is presented in Fig. 6.14 for low viscosity ratios in the range of 0.1 to 2. For this range of viscosity ratios mushroom shaped spike is formed after the linear growth stage. However, spike changes its shape and eventually a thin elongated skirt is formed in later stage of instability. For viscosity ratio 0.1, the skirt of the spike undergoes large deformations and more irregular shapes as the spike moves towards the bottom wall. With increasing viscosity ratio, the shape of the skirt becomes smoother.

Fig. 6.15 shows the interface evolution for the viscosity ratio in the range of 5 to 30. For viscosity ratio m = 5-20, at the later stage wavy skirt is formed. At viscosity ratio 30, the skirt becomes smoother with decreased length. This smoother shape of the skirt may be attributed to the increased viscosity of the upper fluid. This is due to fact that higher viscosity leads to decreased shape change results in smoother skirt. With further increase in viscosity ratio, the length of the skirt decreases and width of the spike head increases for viscosity ratios 40-60, as is shown in Fig. 6.16. It is evident from the figure that for viscosity ratio more than 80, the skirt disappears and the spike penetrates in a form

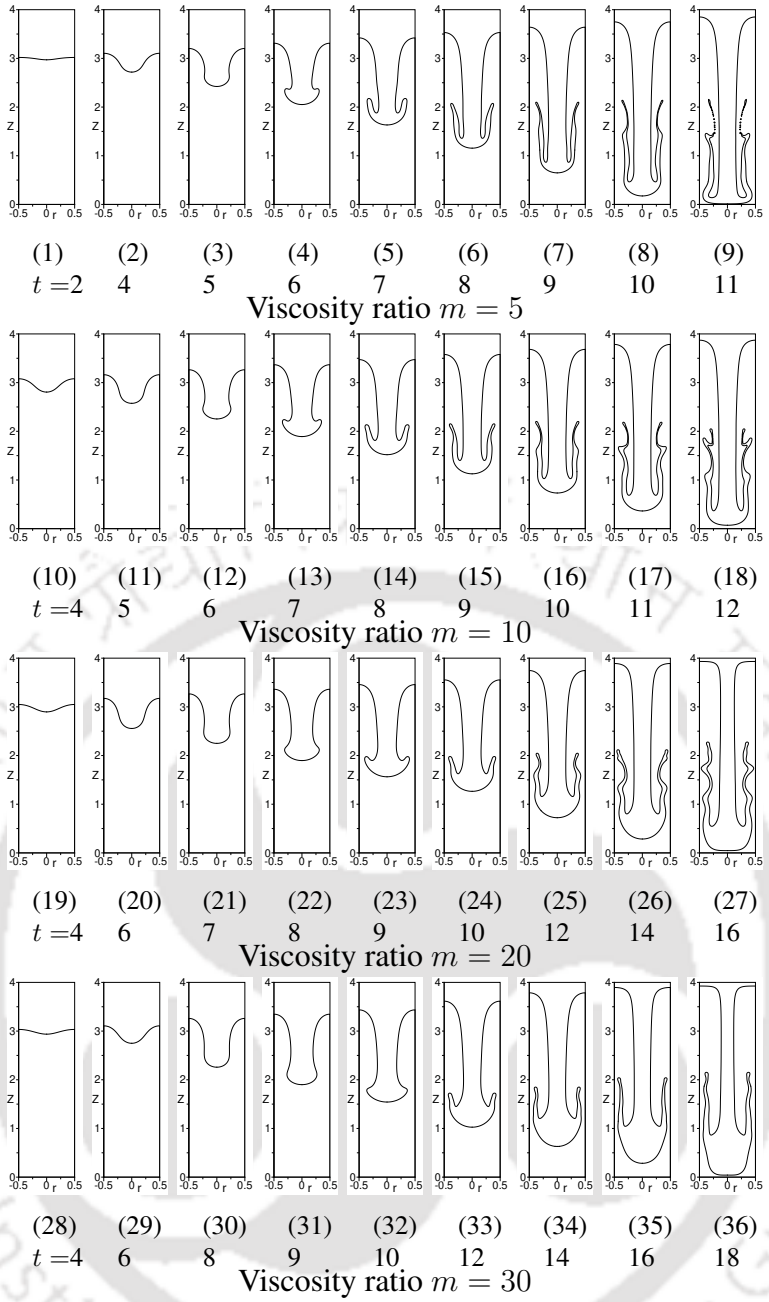

Figure 6.15: Instantaneous interface profiles for various viscosity ratios m = 5-30 (rest of the parameters are: $\rho_r = 2$, $k_r = 2$, $c_{p_r} = 2$, $Re = 50$, $Pr = 1$, $Fr = 1$, $We = 500$ and $r_T = 3$).

of liquid column. Such spike penetration in a form of liquid column in Rayleigh-Taylor instability, for high viscosity ratios, is also observed in the previous studies on Rayleigh-Taylor instability [9, 32, 168]. It is found that the fluid column structure spike formation occurs at higher viscosity ratios in case of temperature dependent viscosities compared to that of constant viscosities.

Fig. 6.17 shows the time variation of the spike and bubble locations for various viscosity ratios. In initial stage, the disturbance growth is observed to be similar for all the viscosity ratios. This is due to the fact that at the initial stage viscosity effect is weak as the velocities are small. However, in later stage, viscosity ratio shows strong influence. In the nonlinear stage of instability perturbation grows faster with time. With the increasing viscosity ratio, the rate of spike and bubble movement is observed to decrease. This is due to that increase in viscosity ratio restricts the fluid movement due

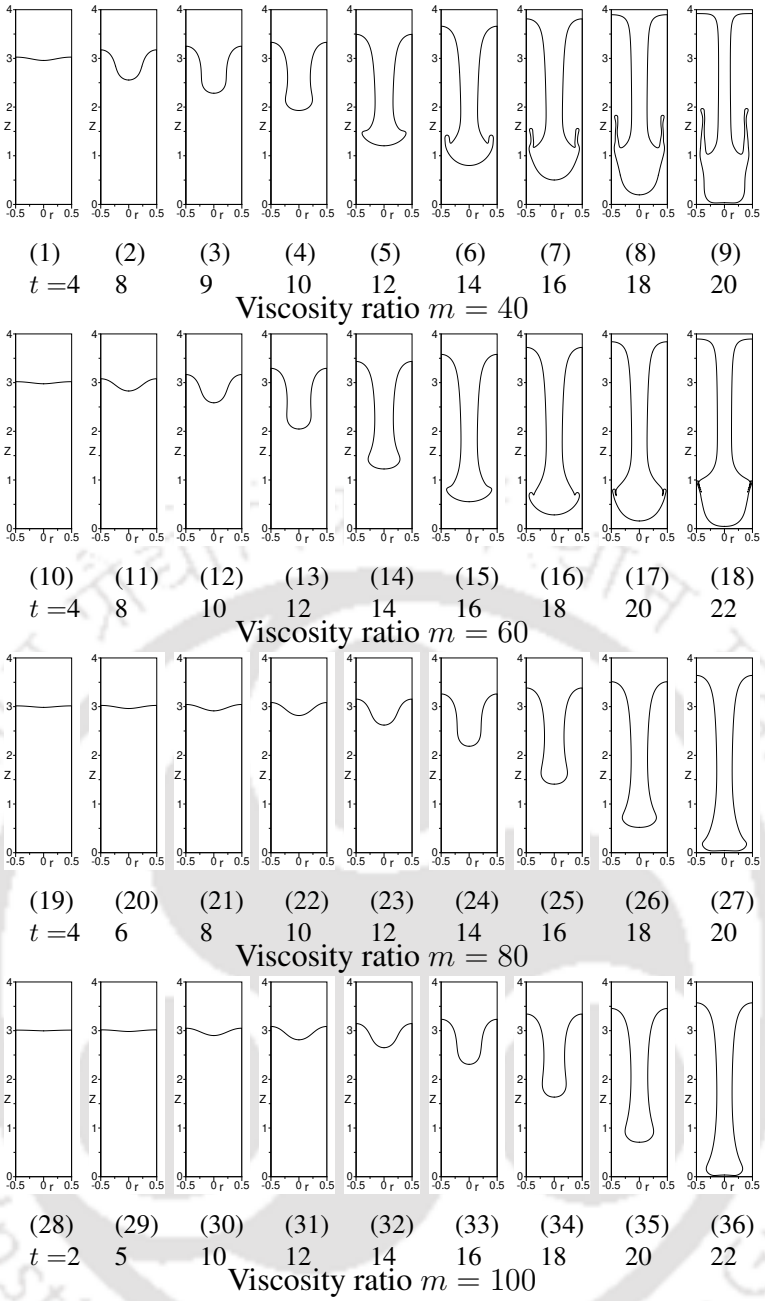

Figure 6.16: Instantaneous interface profiles for various viscosity ratios m = 40-100 (rest of the parameters are: $\rho_r = 2$, $k_r = 2$, $c_{p_r} = 2$, $Re = 50$, $Pr = 1$, $Fr = 1$, $We = 500$ and $r_T = 3$).

to increased viscous shear. Spike movement become slower by almost 3 times as the viscosity ratio is increased from 0.1 to 100.

6.3.4 Effect of temperature ratio

Effect of temperature ratio is studied in the range of r_T = 0-6. Higher the temperature ratio, larger the temperature variation in the individual fluid layers. Temperature ratio r_T =0 corresponds to constant viscosity fluid layers. With increasing temperature ratio, the viscosity decreases to a larger extent

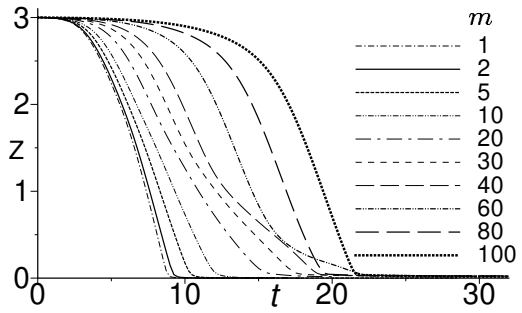

Figure 6.17: Time variation of spike front location for various viscosity ratios $m = 1$-100 (rest of the parameters are: $\rho_r = 2$, $k_r = 2$, $c_{p_r} = 2$, $Re = 50$, $Pr = 1$, $Fr = 1$, $We = 500$ and $r_T = 3$).

within the fluid layers and hence decreases viscous forces. Fig. 6.18 shows the effect of temperature ratio on Rayleigh-Taylor instability. At $r_T = 0$ (temperature independent viscosity), spike moves downwards with larger head and at later stage a skirt is formed. With increasing temperature ratio up to $r_T = 3$, elongated skirt becomes thinner and longer. For temperature ratios 5-6, the spike structure becomes more complex. In this range stem of the spike undergoes a complex deformation, as seen in Fig. 6.18(32)–Fig. 6.18(50). At the late stage, the skirt is broken. With increasing temperature ratio the instability takes place at faster rate.

Fig. 6.19 shows variation of locations of tips of the spike and bubble with time. In the early stage of instability the growth of spike and bubble show similarity irrespective of temperature ratio. However, with increasing temperature ratio bubble and spike move in a nonlinear trend with time. At higher temperature ratio the instability grows at faster rate. The time taken for the spike to strike the bottom at temperature ratio 6 is about 2 times lower compared to the case of temperature ratio 0.

6.3.5 Effect of hot and cold wall locations

The effect of hot and cold wall locations is studied by comparing Rayleigh-Taylor instability for the case of hot wall kept below and cold wall kept at top with the case of cold wall kept below and hot wall kept above. In both cases, cold and hot walls are kept at temperatures 0 and r_T, respectively. In the bottom heated top cooled wall configuration, viscosity in the bottom layer increases from bottom wall to interface and in the top layer viscosity increases from interface to top wall.

For both the heating configurations, the instability is compared in Fig. 6.20. The patterns of instability are similar in both the cases. However, in the top heated configuration the skirt is longer compared to that of bottom heated configuration. The formation of mushroom shaped spike-skirt structure takes place much earlier in top heated case than that of bottom heated case. By the time spike hits the bottom wall, spike-skirt structure is simpler in bottom heated configuration compare to that of top heated configuration. Fig. 6.21 shows the time variation of spike front location for the above mentioned heating configurations. In top heated configuration, Rayleigh-Taylor instability takes place at higher rate than that of the bottom heated configuration. Hence, the bottom heated configuration has stabilizing effect compared to that of top heated configuration.

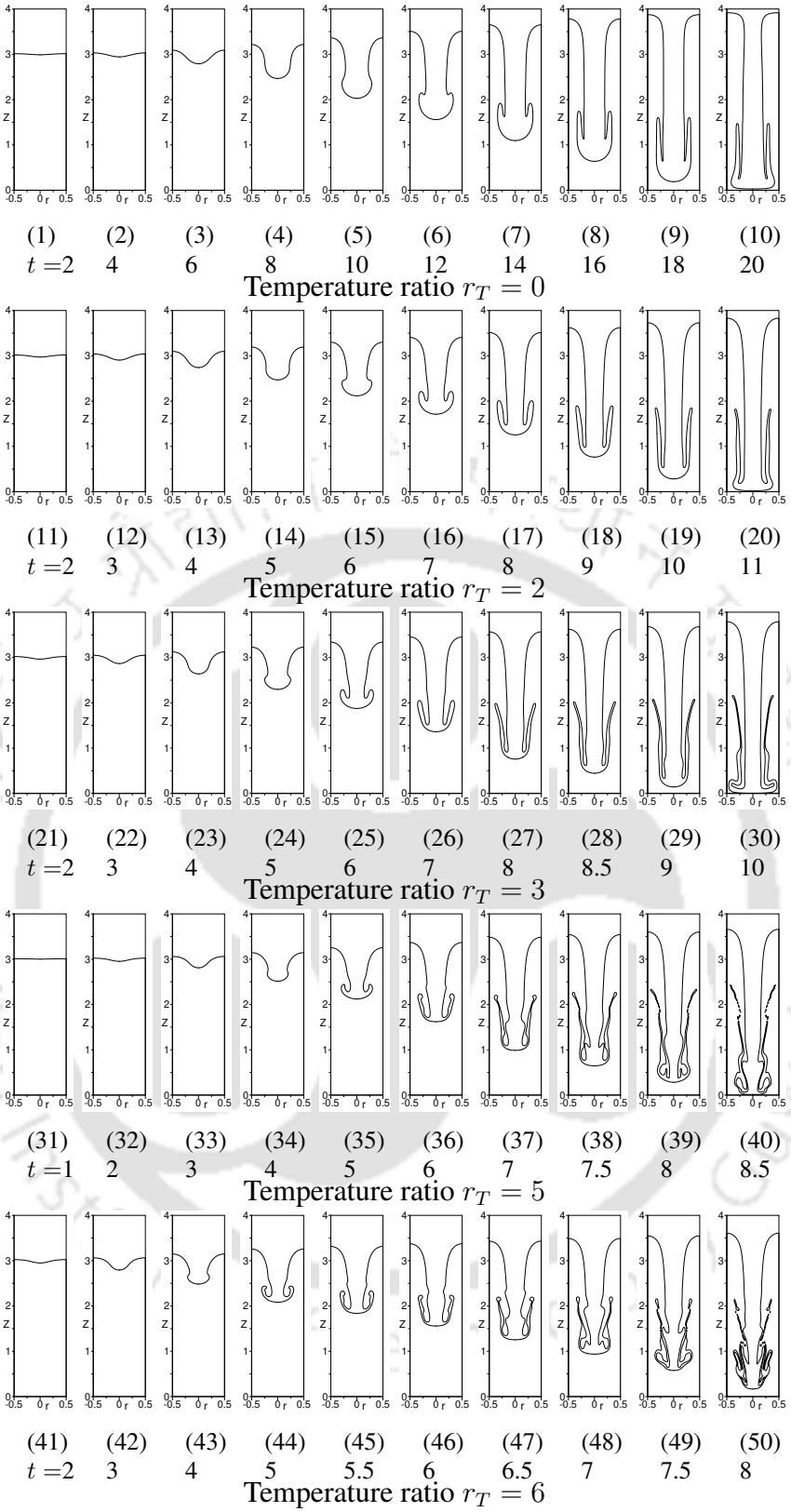

Figure 6.18: Instantaneous interface profiles for various temperature ratios r_T = 0-6 (rest of the parameters are: $\rho_r = 2$, $m = 2$, $k_r = 2$, $c_{p_r} = 2$, $Re = 50$, $Pr = 1$, $Fr = 1$ and $We = 500$).

6.3.6 Effect of Prandtl number

Effect of Prandtl number is studied in the range of 0.01 to 100. Interface profiles of the instability for different Prandtl numbers are shown in Fig. 6.22. Observation of the figure reveals that the instability

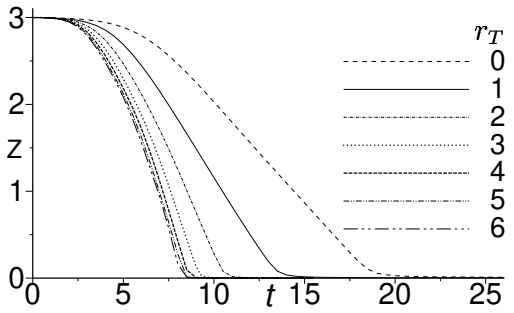

Figure 6.19: Time variation of spike front location for various temperature ratios r_T = 0-6 (rest of the parameters are: $\rho_r = 2$, $m = 2$, $k_r = 2$, $c_{p_r} = 2$, $Re = 50$, $Pr = 1$, $Fr = 1$ and $We = 500$).

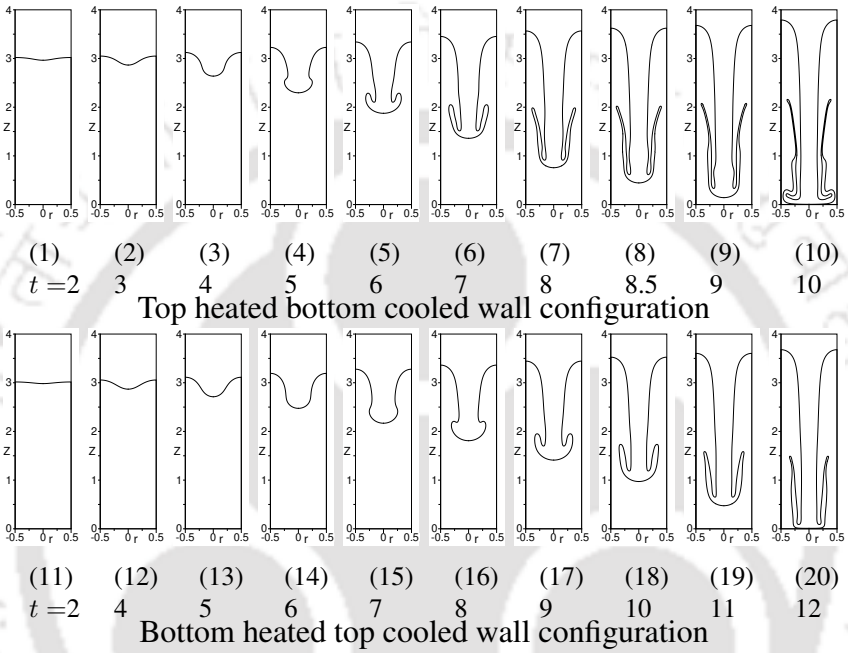

Figure 6.20: Instantaneous interface profiles for different hot and cold wall locations (rest of the parameters are: $\rho_r = 2$, $m = 2$, $k_r = 2$, $c_{p_r} = 2$, $Re = 50$, $Pr = 1$, $Fr = 1$, $We = 500$ and $r_T = 3$).

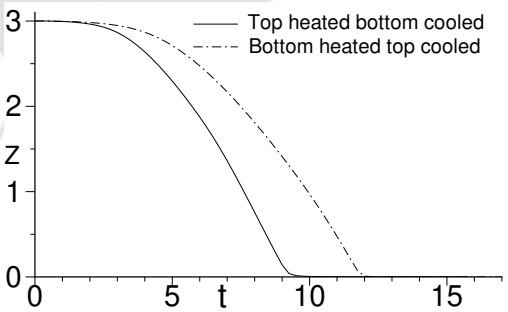

Figure 6.21: Time variation of spike front location for different hot and cold wall locations (rest of the parameters are: $\rho_r = 2$, $m = 2$, $k_r = 2$, $c_{p_r} = 2$, $Re = 50$, $Pr = 1$, $Fr = 1$, $We = 500$ and $r_T = 3$).

is almost unaffected by the Prandtl number values. This may be due to the fact that hydrodynamics happens in such a shorter time and diffusion of heat has negligible influence on the overall instability. The temperature affects only the effective viscosity of the fluid layers. The time variation of spike front location for various Prandtl numbers is shown in Fig. 6.23. The time variation is almost

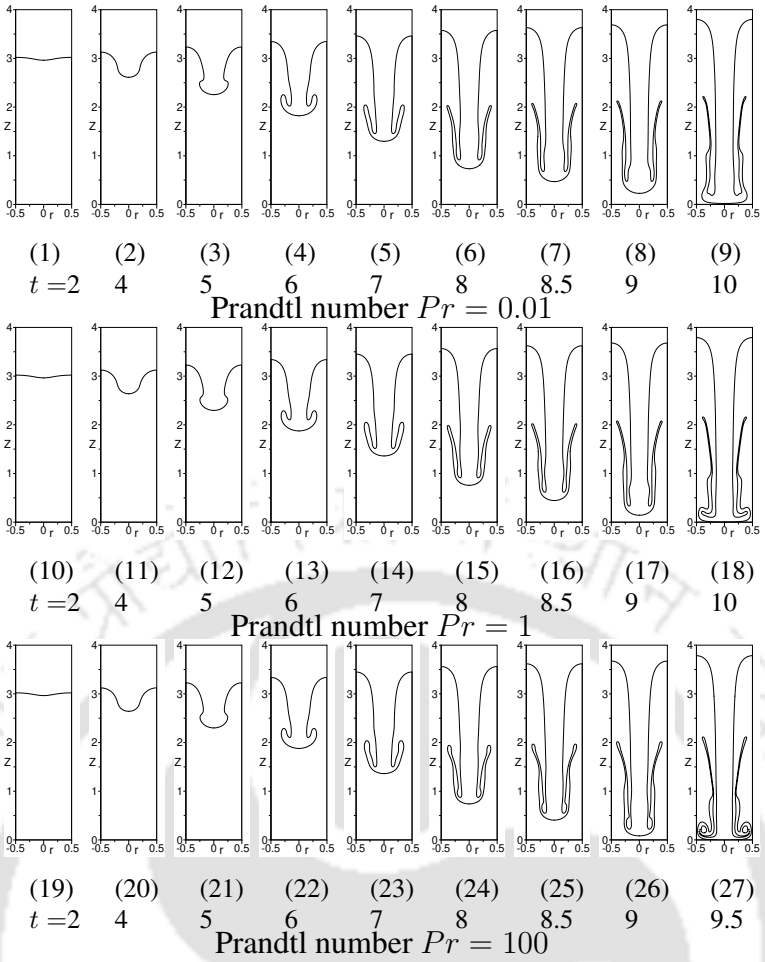

Figure 6.22: Instantaneous interface profiles for various Prandtl numbers (rest of the parameters are: $\rho_r = 2$, $m = 2$, $k_r = 2$, $c_{p_r} = 2$, $Re = 50$, $Fr = 1$, $We = 500$ and $r_T = 3$).

independent of Prandtl number.

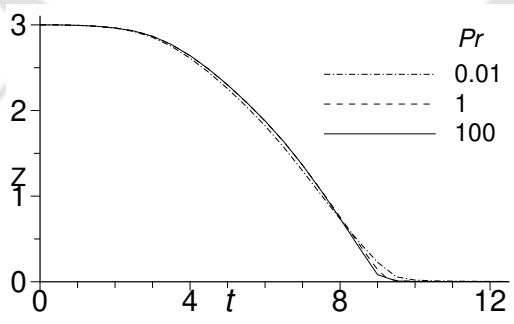

Figure 6.23: Time variation of spike front location for various Prandtl number values $Pr = 0.01$-100 (rest of the parameters are: ρ_r =2, m =2, k_r =2, c_{p_r} =2, Fr =1, Re =50, We =500 and r_T =3).

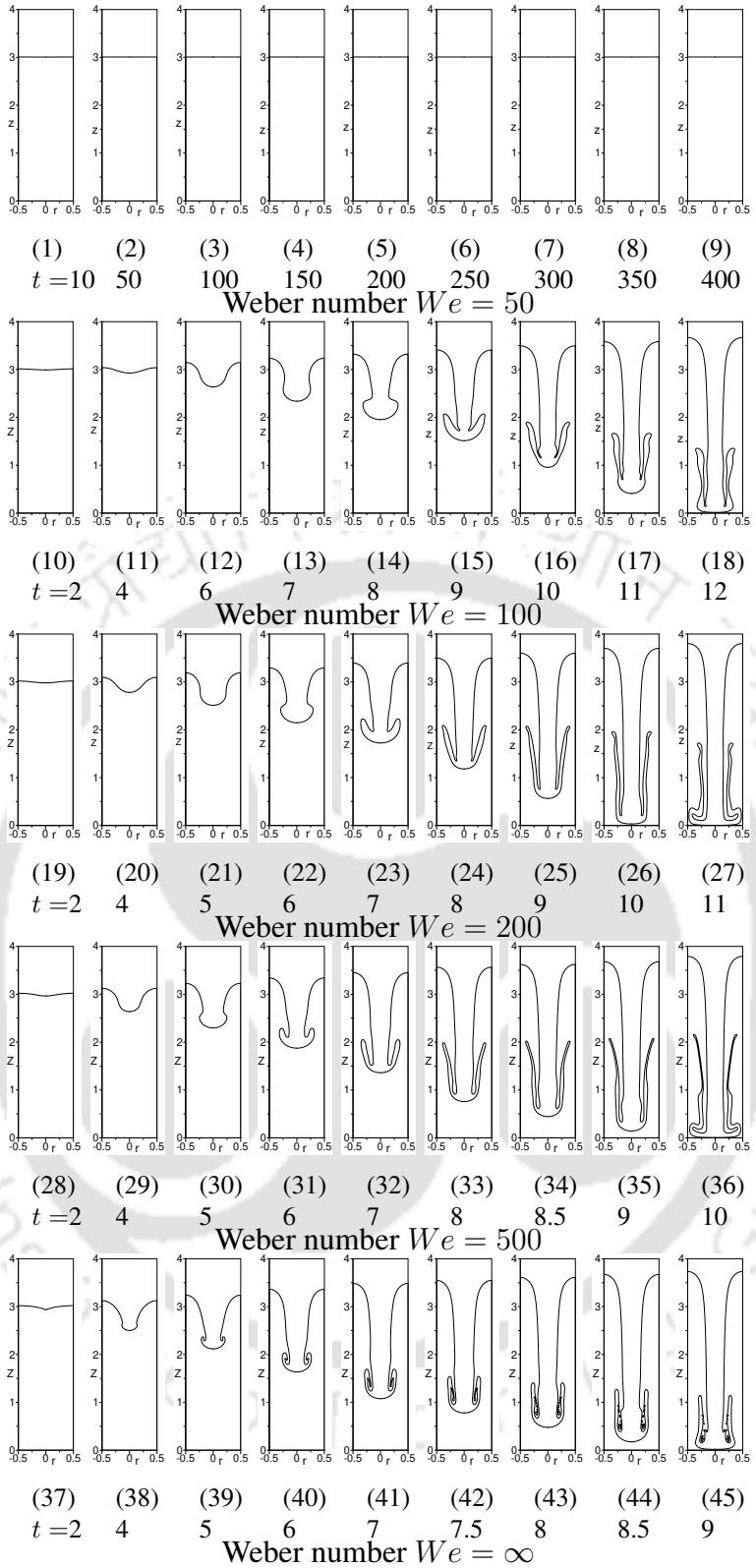

Figure 6.24: Instantaneous interface profiles for various Weber number values $We = 50$ to ∞ (rest of the parameters are: $\rho_r = 2$, $m = 2$, $k_r = 2$, $c_{p_r} = 2$, $Re = 50$, $Pr = 1$, $Fr = 1$ and $r_T = 3$).

6.3.7 Effect of Weber number

The effect of Weber number is studied in the range of 0 to ∞ on Rayleigh-Taylor instability. Weber number is inversely proportional to surface tension. The zero Weber number represents infinite sur-

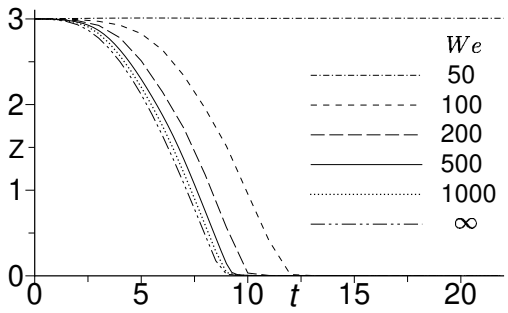

Figure 6.25: Time variation of spike front location for various Weber number values $We = 10$ to ∞ (rest of the parameters are: $\rho_r = 2$, $m = 2$, $k_r = 2$, $c_{p_r} = 2$, $Re = 50$, $Pr = 1$, $Fr = 1$, and $r_T = 3$).

face tension and infinite Weber number represents zero surface tension. Rayleigh-Taylor instability for various Weber numbers is shown in Fig. 6.24. For Weber number 50, the interface is stable and does not undergo instability. This means, Weber number 50 represents stronger surface tension sufficient to make the configuration stable. As the surface tension is large the interface behaves like an elastic membrane. This elastic membrane effect supports the top heavy fluid and makes the balance so that the fluid layers do not undergo instability. Suppression of Rayleigh-Taylor instability due to sufficiently large surface tension is also established in linear stability studies [20, 21, 39, 107]. The present study observations are in-line with the linear stability studies.

It is found that, for the parameters values of the present study, the interface is stable for Weber number in the range of 0-55. For Weber number about 55 or more, interface undergoes instability and displays the features of mushroom shaped spike and skirt formation. With increasing Weber number, the formation of mushroom shape spike takes place earlier. For Weber number in the range of 55 to 500, the mushroom shape spike undergoes deformation with thinner skirt. For Weber number in the range of 500 to 1000, instability patterns are similar. When Weber number is increases to infinity, surface tension decreases to zero, the generated skirt bends at the upper end inwards for some time duration. The skirt is oriented vertically upwards when the spike is about to reach the bottom.

The time variation of spike front location is shown in Fig. 6.25. Time variation of spike front location is significantly affected by the presence of surface tension force. For larger surface tension forces, Weber number below critical value ($We \leq$55), spike and bubble show no movement as interface is stable. For Weber number beyond the critical value, greater than 55, with increasing Weber number spike and bubble move faster. For Weber numbers more than 500, the time taken by the spike to strike to the bottom wall is almost similar for all higher Weber numbers.

6.4 Conclusions

Axisymmetric Rayleigh-Taylor instability with viscosity of fluid layers decreasing with temperature exponentially is studied. The decrease of viscosity due to temperature makes the flow to be more unstable. Due to temperature variation, the spike-skirt structure undergoes larger deformations compared to the fluid layers of constant viscosities. The occurrence of spike penetration in the form of a liquid column takes place at much higher viscosity ratio in variable viscosity layers compared to that

with constant viscosity fluid layers. At lower viscosity ratio skirt shows non-smooth structure. With increasing viscosity ratio skirt become smoother, thinner and shorter. Whereas, spike forms a thick finger like fluid column structure at high viscosity ratios. Increasing viscosity ratio slows down the perturbation growth showing stabilizing effect on the instability. Spike movement becomes almost 3 times slower as the viscosity ratio increased from 0.1 to 100. Increasing temperature ratio is found to show destabilizing effect with irregular spike at higher temperature ratios. Spike movement becomes 2 times faster as temperature ratio increased from 0 to 6. This is due to that higher temperature ratio results in lowered viscosity distribution in the fluid layers. Formation of mushroom shaped spike-skirt structure occurs earlier in the top wall heated configuration compared to that of bottom wall heated configuration. Top heated configuration is found to be more unstable with thinner and longer skirt than that of bottom heated configuration. Variation of Prandtl number is found to show no significant effect on the instability. For the parameters value of the study, the configuration is stable for Weber number less than 55. The evolution process of the instability is similar in the Weber number range of 55 to 500. Overall, surface tension shows stabilizing effect on the instability.

Chapter 7

Effect of functional variation of viscosity with temperature on Rayleigh-Taylor instability in axisymmetric coordinates

In the present chapter, effect of functional variation of viscosity with temperature on Rayleigh-Taylor instability is studied in axisymmetric configuration. The effect of functional variation of viscosity with temperature on the instability is studied for four types of functional variations of viscosity with temperature.

7.1 Physical system

Schematic of physical system used for the study presented in this chapter is shown in Fig. 2.3. The physical system is described in subsection 2.1.2.

7.2 Mathematical treatment

In this chapter, study of the instability is carried out using Basilisk software. The software uses Volume of Fluid (VoF) framework to find the interface location. The governing equations consist of Navier-Stokes equations, energy equation and volume fraction equation.

7.2.1 Scaling parameters

For the study reported in this chapter, different reference scales are chosen to non-dimensionalize the governing equations. The reference scales for velocity, length, time, pressure, temperature and surface tension are taken equal to $\tilde{V}_{\text{ref}}$, $\tilde{L}_{\text{ref}}$, $\tilde{L}_{\text{ref}}/\tilde{V}_{\text{ref}}$, $\tilde{\rho}_{\text{ref}}\,\tilde{V}_{\text{ref}}^2$, $\tilde{T}_{\text{ref}}$ and $\tilde{\sigma}_{\text{ref}}$, respectively. Reference velocity is taken equal to $\tilde{V}_{\text{ref}} = \sqrt{\tilde{g}\,\tilde{L}}$. The reference length is taken equal to $\tilde{L}$. Reference temperature is taken equal to cold wall temperature ($\tilde{T}_2$). Reference surface tension is taken equal to $\tilde{\sigma}_0$, which is surface tension value at reference temperature. Reference fluid properties are taken equal to 'Fluid 2'

properties ($\tilde{\rho}_2$, $\tilde{\mu}_2$, $\tilde{k}_2$, and $\tilde{c}_{p2}$). The reference variables for various parameters are given as following.

$$\begin{aligned} &\tilde{\rho}_{\text{ref}} = \tilde{\rho}_2, \quad \tilde{\mu}_{\text{ref}} = \tilde{\mu}_2, \quad \tilde{k}_{\text{ref}} = \tilde{k}_2, \quad \tilde{c}_{p_{\text{ref}}} = \tilde{c}_{p2}, \\ &\tilde{L}_{\text{ref}} = \tilde{L}, \tilde{V}_{\text{ref}} = \sqrt{\tilde{g}\,\tilde{L}}, \quad \tilde{\sigma}_{\text{ref}} = \tilde{\sigma}_0, \quad \tilde{T}_{\text{ref}} = \tilde{T}_2 \end{aligned} \tag{7.1}$$

With the use of the above reference variables, the definitions of dimensionless variables, as given by Eq. (2.14), become

$$\begin{aligned} &\rho = \frac{\tilde{\rho}}{\tilde{\rho}_2}, \quad \mu = \frac{\tilde{\mu}}{\tilde{\mu}_2}, \quad c_p = \frac{\tilde{c}_p}{\tilde{c}_{p2}}, \quad k = \frac{\tilde{k}}{\tilde{k}_2}, \quad r = \frac{\tilde{r}}{\tilde{L}}, \quad z = \frac{\tilde{z}}{\tilde{L}}, \\ &t = \frac{\tilde{t}}{\sqrt{\tilde{L}/\tilde{g}}}, \quad \mathbf{u} = \frac{\tilde{\mathbf{u}}}{\sqrt{\tilde{g}\,\tilde{L}}}, \quad p = \frac{\tilde{p}}{\tilde{\rho}_2\,\tilde{g}\,\tilde{L}}, \quad \theta = \frac{\tilde{T} - \tilde{T}_2}{\tilde{T}_2}, \quad \sigma = \frac{\tilde{\sigma}}{\tilde{\sigma}_0} \end{aligned} \tag{7.2}$$

7.2.2 Governing equations

With the use of the above dimensionless variables, the governing equations are non-dimensionalized and given as following.

Continuity equation

$$\nabla\cdot\mathbf{u} = 0 \tag{7.3}$$

Momentum equation

$$\rho\left(\frac{\partial\mathbf{u}}{\partial t} + \mathbf{u}\cdot\nabla\mathbf{u}\right) = -\nabla p + \frac{1}{Re}\nabla\cdot\mu\left(\nabla\mathbf{u} + \nabla\mathbf{u}^{\mathrm{T}}\right) + \mathbf{F} \tag{7.4}$$

Energy equation

$$\rho\, c_p\left(\frac{\partial\theta}{\partial t} + \mathbf{u}\cdot\nabla\theta\right) = \frac{1}{Re\,Pr}\nabla\cdot(k\nabla\theta) \tag{7.5}$$

Volume fraction equation

$$\frac{\partial f}{\partial t} + \mathbf{u}\cdot\nabla f = 0 \tag{7.6}$$

Here, surface tension is considered to be constant. Hence, the body force term ($\mathbf{F}$) in dimensionless form, as given by Eq. (2.23), is expressed as

$$\mathbf{F} = \frac{1}{We}\,\kappa\,\delta\,\mathbf{n} - \frac{\rho}{Fr}\,\mathbf{e}_j \tag{7.7}$$

Dimensionless numbers in the above governing equations, as given by Eq. (2.24), are given by

$$Re = \frac{\tilde{\rho}_2\,\tilde{g}^{1/2}\,\tilde{L}^{3/2}}{\tilde{\mu}_2}, \quad We = \frac{\tilde{\rho}_2\,\tilde{g}\,\tilde{L}^2}{\tilde{\sigma}_0}, \quad Fr = 1, \quad Pr = \frac{\tilde{\mu}_2\tilde{c}_{p2}}{\tilde{k}_2} \tag{7.8}$$

7.2.3 Functional variations of viscosity with temperature in the fluid layers

In the present study, four different types of functional variations of viscosity with temperature are considered for the fluid layers. These functional variations of viscosity with temperature are chosen

based on the past studies [12, 52, 53, 64–72, 74–76], which are given as following. Constant viscosity, which was used in the past [7, 32, 37, 71, 72, 74], is expressed as

$$\mu_1 = m \qquad \text{and} \qquad \mu_2 = 1 \tag{7.9}$$

Linearly varying temperature dependent viscosity, which was used in the studies of Dhiman and Sharma [76], Tripathi et al. [73] and Wall and Wilson [67], is expressed as

$$\mu_1 = m\,(a + b\,\theta) \qquad \text{and} \qquad \mu_2 = (a + b\,\theta) \tag{7.10}$$

Here, $a = 1$ and $b = -0.2$. Power law varying temperature dependent viscosity, also used in the studies of Nahme [64], Tripathi and Sahu [12] and Balla et al. [75], is expressed as

$$\mu_1 = m\,(a + b\,\theta^{3/2}) \qquad \text{and} \qquad \mu_2 = (a + b\,\theta^{3/2}) \tag{7.11}$$

Here, a and b are constants whose values are taken equal to 1 and 0.2, respectively. In Eq. (7.10) and Eq. (7.11), values of a and b are chosen such that both the fluid viscosities (μ_1 and μ_2) are positive throughout the domain. Exponentially varying temperature dependent viscosity, which was also used in the studies of [52, 53, 64–67, 69, 70], is expressed as

$$\mu_1 = m\,e^{-\theta} \qquad \text{and} \qquad \mu_2 = e^{-\theta} \tag{7.12}$$

Here, $m = \mu_1(\tilde{T}_2)/\mu_2(\tilde{T}_2)$ is top heavier fluid to bottom lighter fluid viscosity ratio at reference temperature. In VoF method, dimensionless fluid properties such as density (ρ), viscosity (μ), thermal conductivity (k) and heat capacity (c_p) are calculated as a function of volume fraction (f), as given by Eq. (2.13), according to the following expressions

$$\begin{aligned} \rho &= \rho_1\,f + \rho_2\,(1 - f) \\ \mu &= \mu_1\,f + \mu_2\,(1 - f) \\ c_p &= c_{p1}\,f + c_{p2}\,(1 - f) \\ k &= k_1\,f + k_2\,(1 - f) \end{aligned} \tag{7.13}$$

7.2.4 Initial and boundary conditions

The initial and boundary conditions used for the study of the present chapter are described in subsection 2.2.3. Details of the dimensions of axisymmetric domain used for the present study are presented in the same subsection.

7.2.5 Numerical methodology

Numerical methodology of the software is discussed in detail in subsection 2.2.6. The validations carried out for the usage of the software for simulation of multiphase flow in axisymmetric configuration are given in subsection 6.2.5.

7.3 Results and discussions

7.3.1 Baseline parameter values

Axisymmetric Rayleigh-Taylor instability in two viscous fluid layers is studied for four types of functional variations of viscosity with temperature, which are constant, linear, power law and exponential variations. A set of baseline parameter values are chosen for the study, which are given as following. The baseline values of heavier fluid to lighter fluid density ratio (ρ_r), viscosity ratio (m) heat capacity ratio (c_{p_r}) and thermal conductivity ratio (k_r) all are chosen equal to 2. Temperature ratio (r_T) is chosen equal to 3. The values of Froude number, Prandtl number, Reynolds number, Weber number are chosen equal to 1, 1, 50 and 150, respectively. The effect of functional variation of viscosity with temperature on the instability is studied for various viscosity ratios and density ratios. Effect of a particular parameter is studied by varying the value of that particular parameter and keeping the remaining parameter values at the above mentioned baseline values.

7.3.2 Effect of functional variation of viscosity with temperature for various viscosity ratios

The effect of the four types of functional variations of viscosity with temperature on the instability is studied for various viscosity ratios in the range of 0.5 to 100. The results are plotted in the form of interface profiles and time variation of spike front location and compared the instability for the four types of viscosity variations for corresponding viscosity ratio, as shown in Figs. 7.1-7.12.

For the different types of viscosity variations, fluid viscosities in both top and bottom layers vary differently with temperature based on the type of viscosity variation. For example, for constant viscosity, viscosities of top and bottom layer fluids are constant, independent of temperature. For linear viscosity variation, fluid viscosity decreases linearly with increasing temperature according to Eq. (7.10). For power law viscosity variation, fluid viscosity increases with increasing temperature according to Eq. (7.11). For exponential viscosity variation, fluid viscosity decreases exponentially with increasing temperature according to Eq. (7.12). Since, bottom wall is maintained at lower temperature and top wall is maintained at higher temperature, the temperature increases from the bottom wall to interface and it increases again from interface to the top wall. Since, viscosity decreases with temperature in linear and exponential viscosity variations, for these variations, viscosity in bottom layer decreases from the bottom wall to interface and it again decreases from interface to the top wall. As viscosity increases with temperature in power law viscosity variation, fluid viscosity in bottom layer increases from the bottom wall to interface and it again increases from interface to the top wall. Due to such difference in viscosity variations for different types of functional variations of viscosity, the instability may largely differ for different viscosity variations.

In initial stage, the top heavier fluid forms a mushroom shaped spike showing qualitative similarity, for the four types of viscosity variations. Whereas in later stage, the spike undergoes deformation differently for the different types of viscosity variations. The instability evolution is presented in

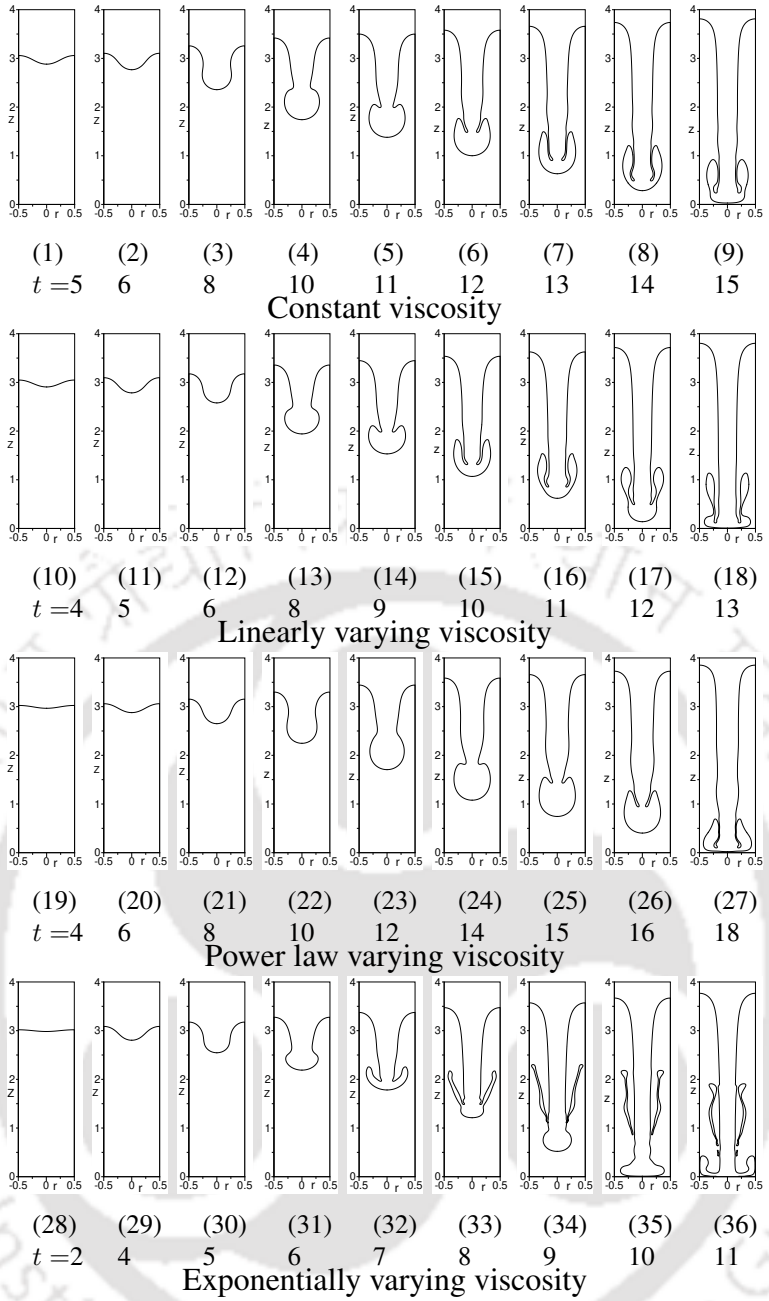

Figure 7.1: Instantaneous interface profiles for the four types of viscosity variations with viscosity ratio $m = 0.5$ (rest of the parameters are: $\rho_r = 2$, $c_{p_r} = 2$, $k_r = 2$, $Re = 50$, $Pr = 1$, $Fr = 1$, $We = 150$ and $r_T = 3$).

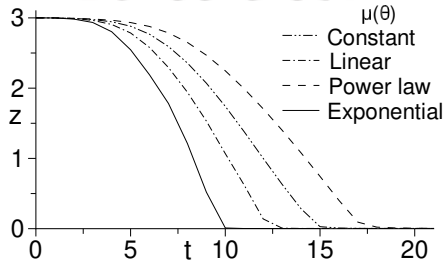

Figure 7.2: Time variation of spike front location for the four types of viscosity variations with viscosity ratio $m = 0.5$ (rest of the parameters are: $\rho_r = 2$, $c_{p_r} = 2$, $k_r = 2$, $Re = 50$, $Pr = 1$, $Fr = 1$, $We = 150$ and $r_T = 3$).

Fig. 7.1 for the four types of viscosity variations for viscosity ratio 0.5. For constant and linear viscosity variations, the spike undergoes deformation, and with time, a thick skirt forms on the spike head. However, for linear variation, length of the skirt is found to be relatively longer than that of constant viscosity. For power law variation, the spike forms with bigger head and short skirt. For exponential variation, the spike forms with a thin skirt attached to its head, and eventually the distance between the spike head and skirt location increases as spike moves towards the bottom wall. With time, the skirt get detached from the spike as the spike strikes the bottom wall. For exponential variation, skirt forms relatively longer than that of the other three types of viscosity variations. Fig. 7.2 shows time variation of spike front location for the four types of viscosity variations for viscosity ratio 0.5. For exponential, linear, constant and power law variations, spike strikes the bottom wall at about dimensionless time $t = 10$, 13, 15 and 18, respectively. For exponential variation, the spike strikes the bottom wall almost 2 times earlier than that of power law variation.

Fig. 7.3 shows the instability evolution for the four types of viscosity variations for viscosity ratio 2. For constant viscosity, the heavier fluid spike deforms and short skirt is formed as it moves towards the bottom wall. For linear variation, the spike-skirt formation shows a qualitative similarity with that of constant viscosity. However, for linear viscosity, the skirt forms relatively longer than that of constant viscosity. For exponential variation, the heavier fluid spike forms with relatively thinner and longer skirt compared to that of linear variation. For power law variation, the heavier fluid spike forms with suppressed skirt, and with time the spike moves towards the bottom wall in the form of a thick finger like pattern with bigger head. Fig. 7.4 shows time variation of spike front location for different types of viscosity variations for viscosity ratio 2. For exponential, linear, constant and power law viscosity variations, the spike strikes the bottom wall at about dimensionless time $t = 11$, 18, 22 and 28, respectively. For power law variation, rate of spike movement is almost 3 times slower than that of exponential variation.

Fig. 7.5 shows instability evolution for the four types of viscosity variations for viscosity ratio 5. For constant viscosity, spike forms with a small skirt on both the sides of spike head. For power law variation of viscosity, the spike shows qualitative similarity with suppressed skirt. For linear variation of viscosity, top heavier fluid forms into a mushroom shaped spike with relatively longer skirt compared to that of constant and power law variations of viscosity. For exponential variation of viscosity, the skirt forms on the spike head with a relatively thicker and larger form than that of other types of viscosity variations. Fig. 7.6 shows time variation of the spike front locations for the four types of viscosity variations for viscosity ratio 5. For exponential, linear, constant and power law viscosity variations, the spike strikes the bottom wall at about dimensionless time $t = 12$, 22, 30 and 40, respectively. Exponential variation shows almost 3 times faster spike movement than that of power law variation. Fig. 7.7 shows the instability evolution for the four types of viscosity variations for viscosity ratio of 20. Formation of spike shows qualitative similarity for constant, linear and power

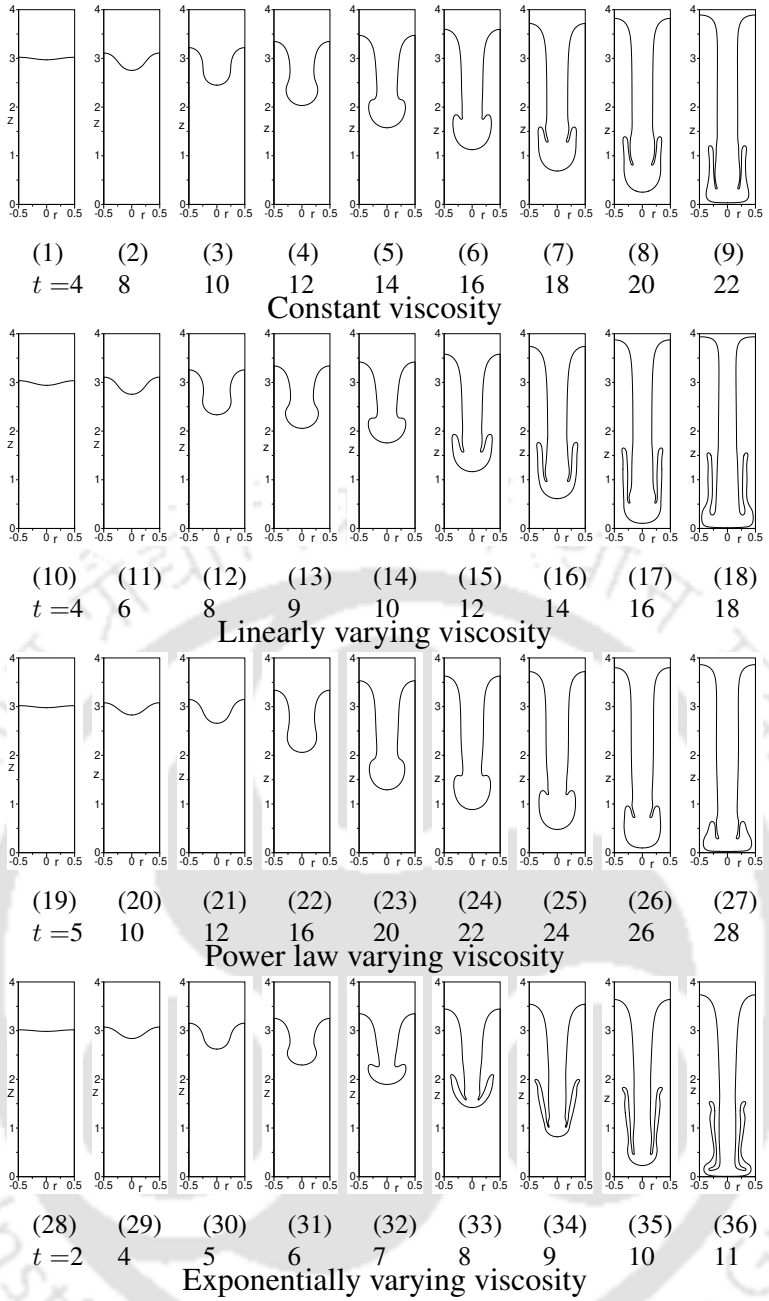

Figure 7.3: Instantaneous interface profiles for the four types of viscosity variations with viscosity ratio $m = 2$ (rest of the parameters are: $\rho_r = 2$, $c_{p_r} = 2$, $k_r = 2$, $Re = 50$, $Pr = 1$, $Fr = 1$, $We = 150$ and $r_T = 3$).

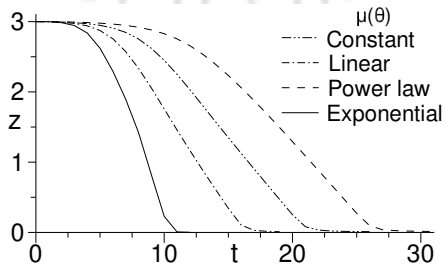

Figure 7.4: Time variation of spike front location for the four types of viscosity variations with viscosity ratio $m = 2$ (rest of the parameters are: $\rho_r = 2$, $c_{p_r} = 2$, $k_r = 2$, $Re = 50$, $Pr = 1$, $Fr = 1$, $We = 150$ and $r_T = 3$).

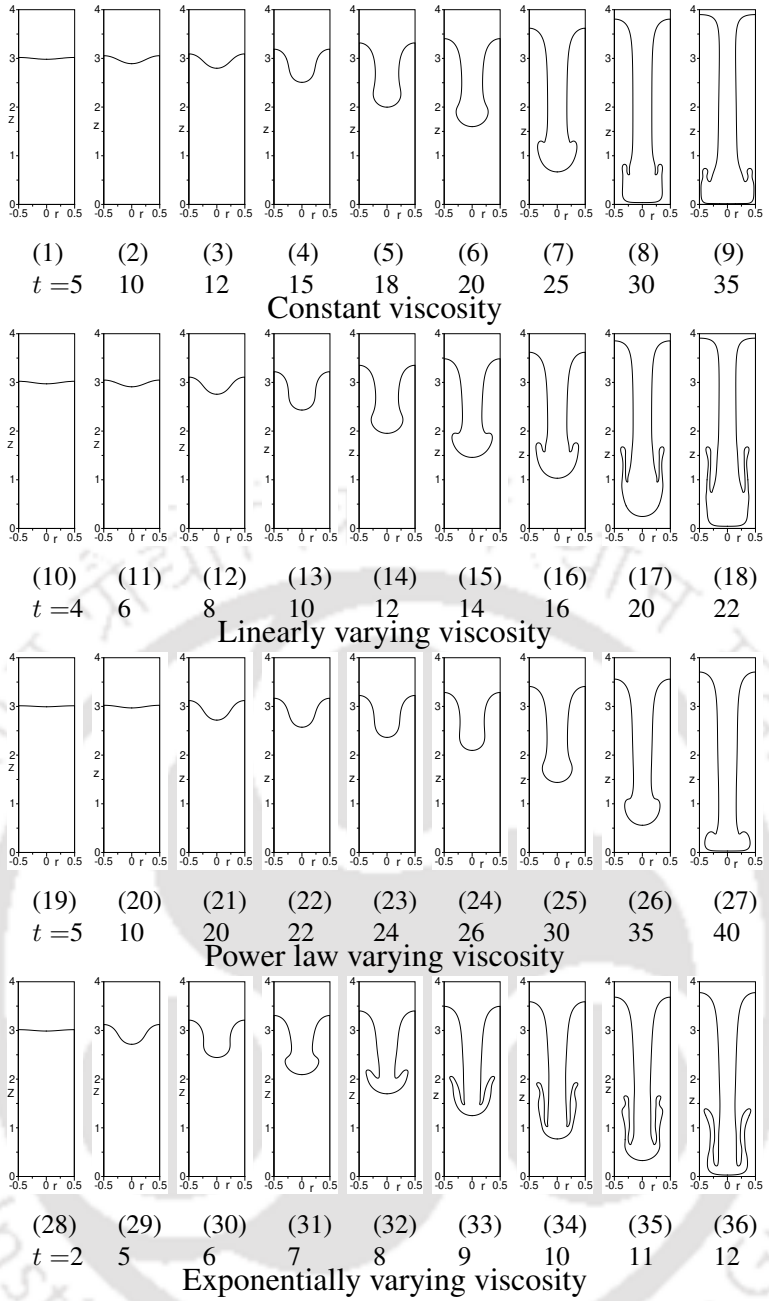

Figure 7.5: Instantaneous interface profiles for the four different types of viscosity variations for viscosity ratio $m = 5$ (rest of the parameters are: $\rho_r = 2$, c_{p_r} =2, k_r =2, Re =50, Pr =1, Fr =1, We =150 and r_T =3).

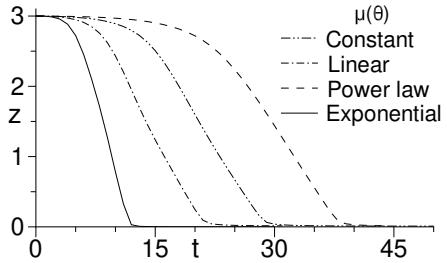

Figure 7.6: Time variation of spike front location for the four types of viscosity variations for viscosity ratio $m = 5$ (rest of the parameters are: $\rho_r = 2$, $c_{p_r} = 2$, $k_r = 2$, $Re = 50$, $Pr = 1$, $Fr = 1$, $We = 150$ and $r_T = 3$).

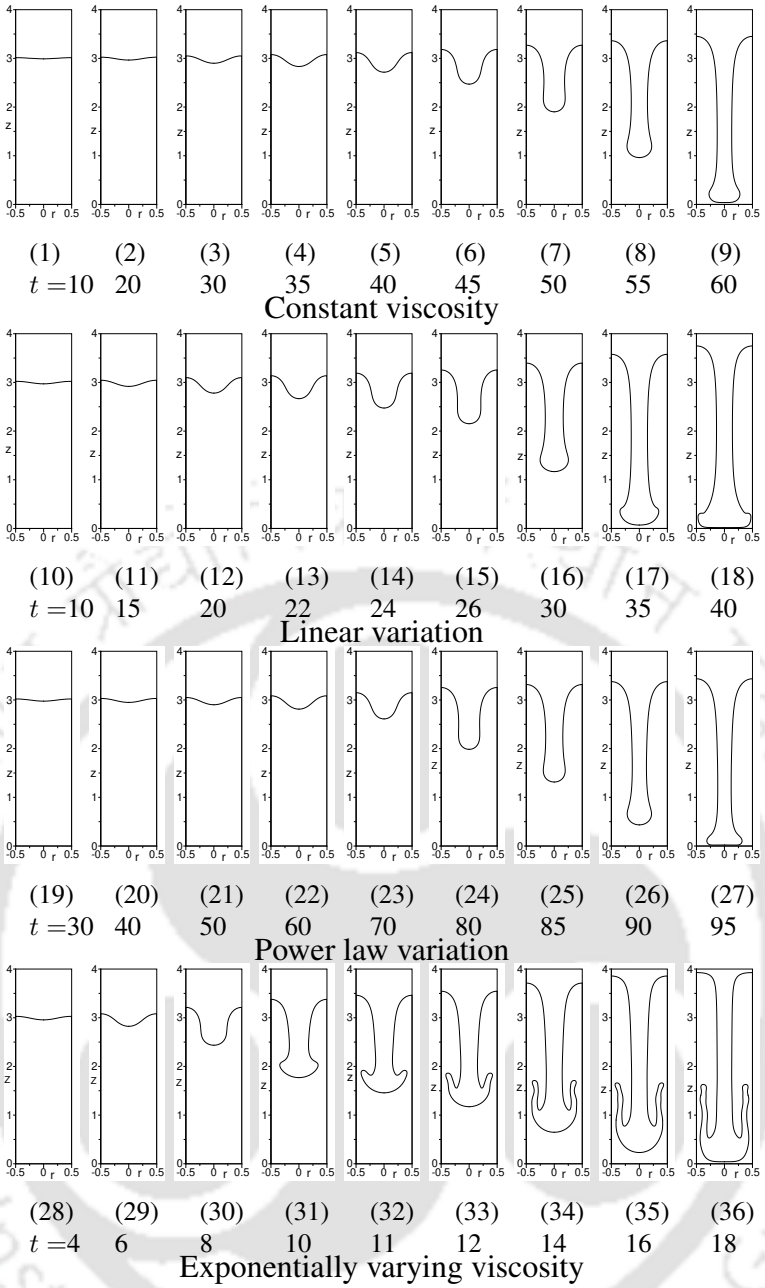

Figure 7.7: Instantaneous interface profiles for the four types of viscosity variations with viscosity ratio $m = 20$ (rest of the parameters are: $\rho_r = 2$, $c_{p_r} = 2$, $k_r = 2$, $Re = 50$, $Pr = 1$, $Fr = 1$, $We = 150$ and $r_T = 3$).

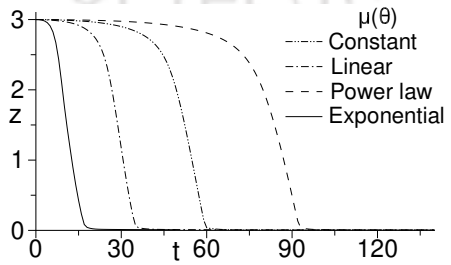

Figure 7.8: Time variation of spike front location for the four types of viscosity variations for viscosity ratio $m = 20$ (rest of the parameters are: $\rho_r = 2$, $c_{p_r} = 2$, $k_r = 2$, $Re = 50$, $Pr = 1$, $Fr = 1$, $We = 150$ and $r_T = 3$).

law viscosity variations. For these three types of viscosity variations, the spike forms in a thick finger like pattern. For exponential variation, the spike forms with an elongated skirt. Time variation of spike front location is presented in Fig. 7.8 for viscosity ratio 20. For exponential, linear, constant and power law variations, the spike strikes the bottom wall at about dimensionless time $t = 18$, 35, 60 and 95, respectively. For power law variation, rate of spike movement is almost 5 times slower than that of exponential variation.

Fig. 7.9 shows instability evolution for the four types of viscosity variations for viscosity ratio 60. With increased viscosity ratio, viscosity of top layer fluid increases which slows down the spike movement, and deformation of spike is found to be reduced for all the four types of viscosity variations. The heavier fluid spike does not undergo large deformation, and the spike moves towards the bottom wall in the form of a fluid column structure, irrespective of type of viscosity variation. This spike resembles a thick finger like pattern. However, for exponential variation, the spike forms in a thick finger like pattern with a bigger head than that of the other types of viscosity variations. Change in type of viscosity variation shows negligible effect on variation of spike shape at high viscosity ratios. However, rate of spike movement is found to be affected significantly by the type of viscosity variation which is evident from the time variation of spike front location shown in Fig. 7.10. For exponential, linear, constant and power law viscosity variations, the spike strikes the bottom wall at about dimensionless time $t = 26$, 80, 160 and 240, respectively. For exponential variation, rate of spike movement is almost 9 times compared to that of power law variation.

Fig. 7.11 shows the instability evolution for the four types of viscosity variations for viscosity ratio 100. For viscosity ratio 100, the spike forms a thick finger like pattern and the variation of spike shape with time is found to be qualitatively similar, for the four types of viscosity variations. The finger like pattern is due to the fact that with increased viscosity ratio, relative viscosity of top fluid layer increases which results into significantly reduced deformation of the spike. With increased viscosity ratio, viscous drag also increases which results into relatively slower spike movement. The slower spike movement turns into reduced instability which is evident from the time variation of spike front location shown in Fig. 7.12. Time taken by the spike to strike to the bottom wall is arranged in the increasing order of sequence of about dimensionless time $t = 28$, 125, 250 and 390, for power law, constant, linear and exponential variations, respectively. For exponential variation, time taken by the spike to strike the bottom wall is almost 14 times lower than that of power law variation.

With increasing viscosity ratio, rate of spike movement decreases for all the four types of viscosity variations. For exponential variation, time variation of spike front location is presented in Fig. 7.13 for various viscosity ratios. The figure shows that spike strikes the bottom wall at about dimensionless time $t = 10$ and 26 for viscosity ratio 0.5 and 100, respectively. For viscosity ratio 100, time taken by the spike to strike the bottom wall is almost three times compare to that of viscosity ratio 0.5. Similar trend is observed for the other three types of viscosity variations for increasing viscosity ratio. At low viscosity ratio, spike-skirt formation are found to be different for the four types of viscosity

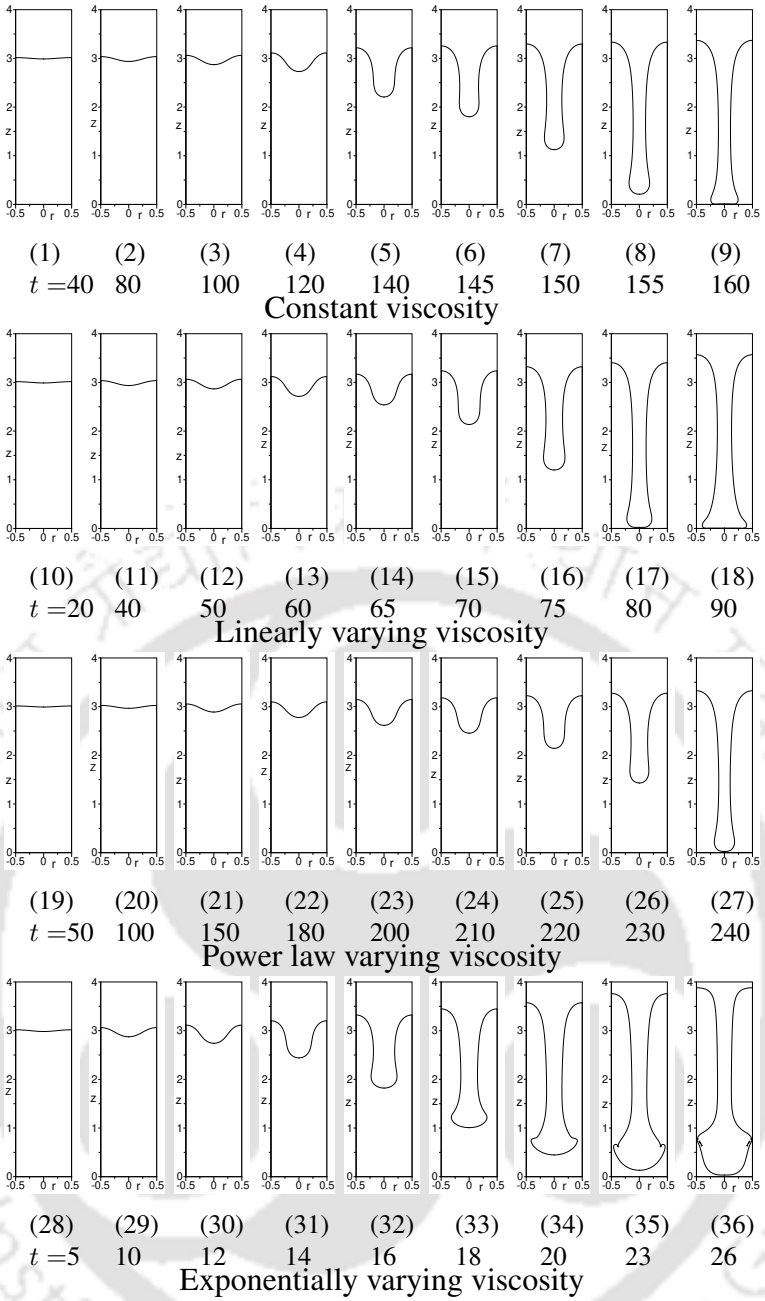

Figure 7.9: Instantaneous interface profiles for the four types of viscosity variations with viscosity ratio $m = 60$ (rest of the parameters are: $\rho_r = 2$, $c_{p_r} = 2$, $k_r = 2$, $Re = 50$, $Pr = 1$, $Fr = 1$, $We = 150$ and $r_T = 3$).

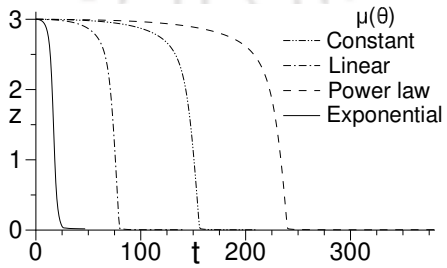

Figure 7.10: Time variation of spike front location for the four types of viscosity variations with viscosity ratio $m = 60$ (rest of the parameters are: $\rho_r = 2$, $c_{p_r} = 2$, $k_r = 2$, $Re = 50$, $Pr = 1$, $Fr = 1$, $We = 150$ and $r_T = 3$).

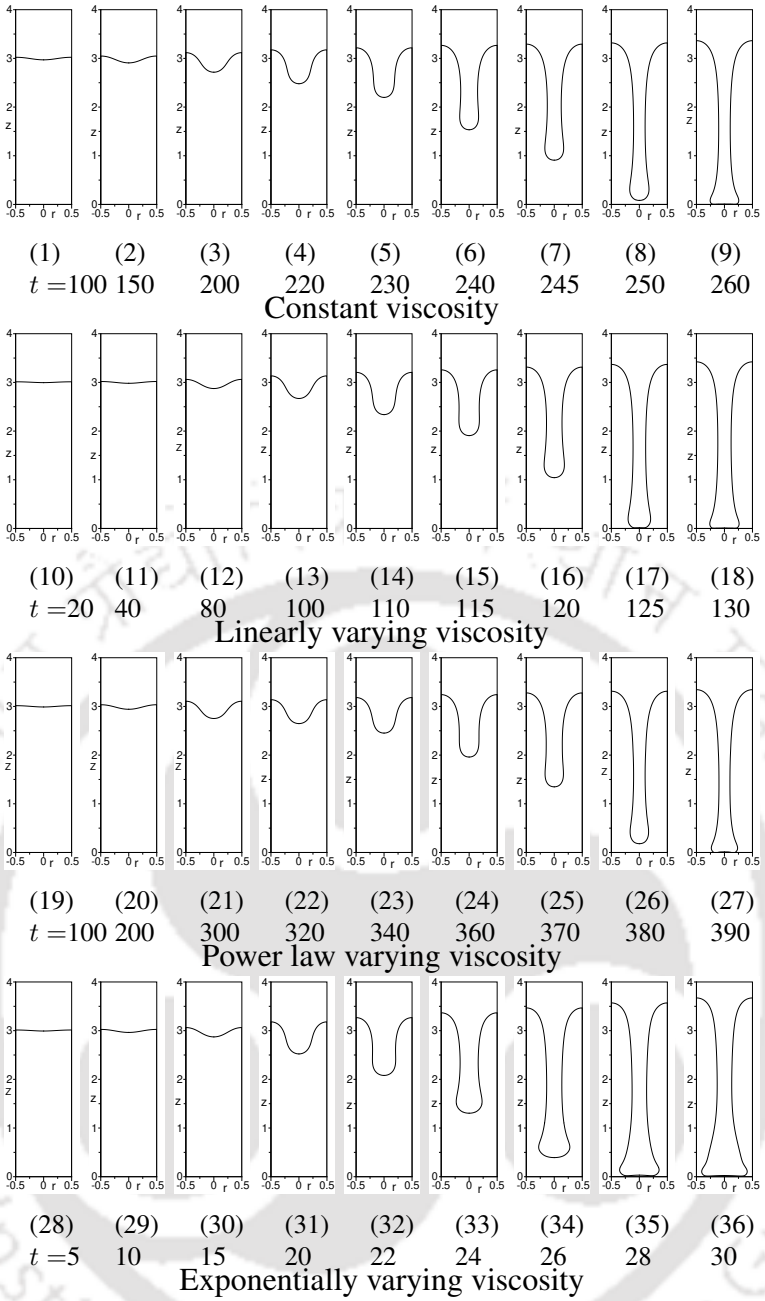

Figure 7.11: Instantaneous interface profiles for the four types of viscosity variations for viscosity ratio $m = 100$ (rest of the parameters are: $\rho_r = 2$, $c_{p_r} = 2$, $k_r = 2$, $Re = 50$, $Pr = 1$, $Fr = 1$, $We = 150$ and $r_T = 3$).

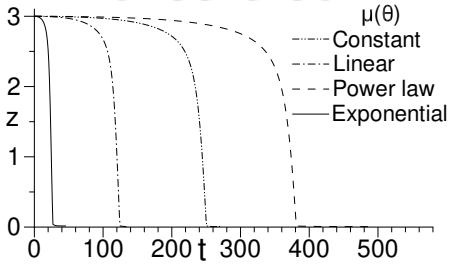

Figure 7.12: Time variation of spike front location for the four types of viscosity variations with viscosity ratio $m = 100$ (rest of the parameters are: $\rho_r = 2$, $c_{p_r} = 2$, $k_r = 2$, $Re = 50$, $Pr = 1$, $Fr = 1$, $We = 150$ and $r_T = 3$).

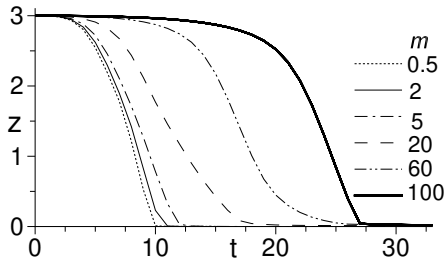

Figure 7.13: Time variation of spike front location for various viscosity ratios with exponential variation of viscosity (rest of the parameters are: $\rho_r = 2$, $c_{p_r} = 2$, $k_r = 2$, $Re = 50$, $Pr = 1$, $Fr = 1$, $We = 150$ and $r_T = 3$).

variations. However, at high viscosity ratios, spike forms into a fluid column like structure without any skirt, irrespective of type of viscosity variation.

Overall, for power law viscosity variation, interface deformation is relatively lower, and for exponential viscosity variation, interface deformation is relatively higher. Rate of spike movement is found to be strongly affected by type of viscosity variation, and time taken by the spike to strike the bottom wall is arranged in the decreasing order of sequence of power law, constant, linear and exponential variations, for all the viscosity ratios. This is due to the fact that overall effective viscosity varies in the increasing order of sequence of exponential, linear, constant and power law variations. Power law variation shows relatively more stabilizing effect, and exponential variation shows relatively more destabilizing effect on the instability.

7.3.3 Effect of functional variation of viscosity with temperature for various density ratios

In this part of the study, the instability is studied for the four types of viscosity variations for density ratios in the range of 1.5 to 20. Fig. 7.14 shows the instability evolution for the four types of viscosity variations for density ratio 1.5. For constant and power law variations, a mushroom shaped spike forms without any skirt showing qualitative similarity. For linear variation, the mushroom shaped spike deforms and a skirt is formed as the spike moves towards the bottom wall. For exponential variation, the mushroom shaped spike forms with a skirt attached to its head which eventually deforms more, and with time, the skirt detaches from the spike head as the spike moves towards the bottom wall. Fig. 7.15 shows time variation of spike front location for the four different types of viscosity variations for density ratio 1.5. For exponential, linear, constant and power law variations, spike strikes the bottom wall at about dimensionless time $t = 22$, 45, 60 and 80, respectively. For power law variation, rate spike movement is almost 4 times slower than to that of exponential variation.

The instability evolution and time variation of spike front location are presented in Fig. 7.3 and Fig. 7.4, respectively, for the four types of viscosity variations for density ratio 2. The instability is found to be different from each other for the four types of viscosity variations which is already discussed in the above subsection for viscosity ratio 2. For power law variation, rate of spike movement is almost 3 times slower compared to that of exponential variation. Fig. 7.16 shows the instability

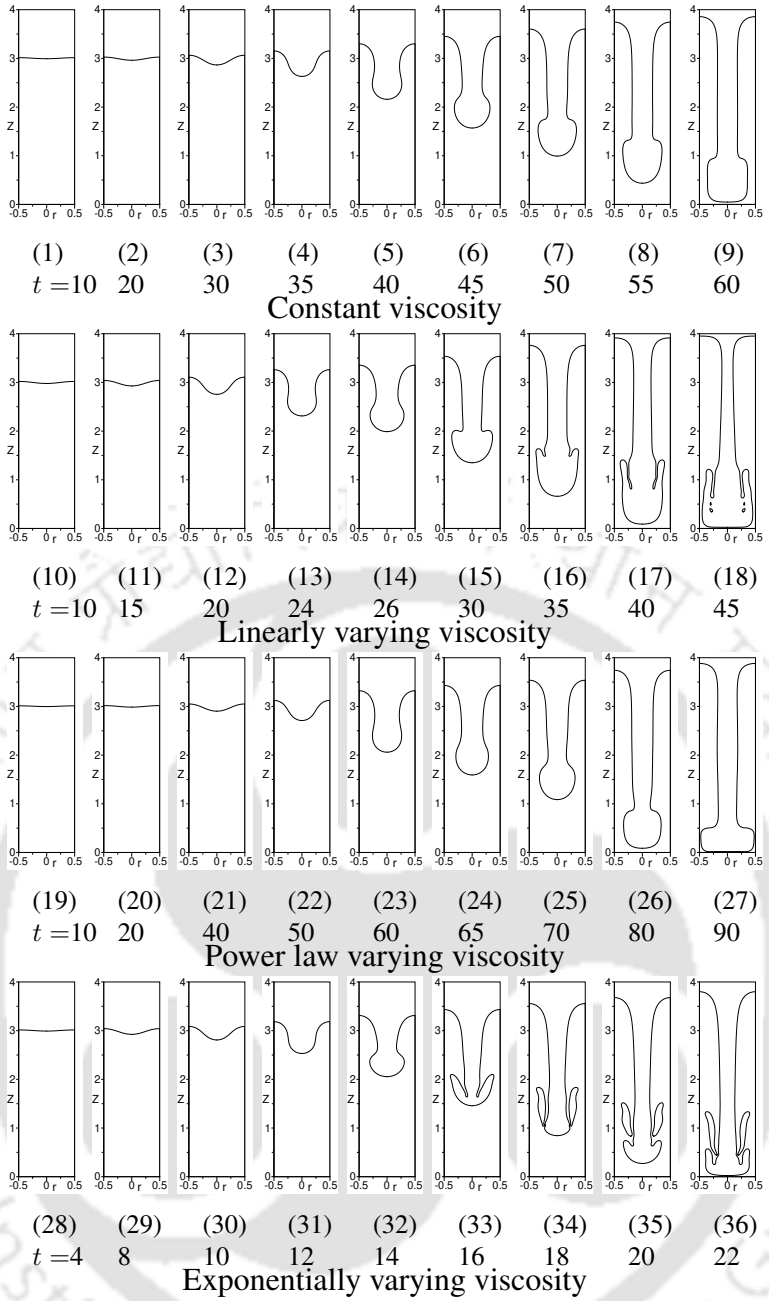

Figure 7.14: Interface profiles for different functional variation of viscosity with temperature for density ratio $\rho_r = 1.5$ (rest of the parameters are: $m = 2$, $k_r = 2$, $c_{p_r} = 2$, $Re = 50$, $Pr = 1$, $Fr = 1$, $We = 150$ and $r_T = 3$).

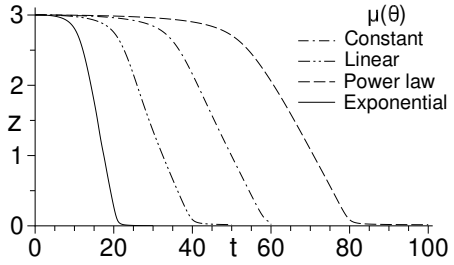

Figure 7.15: Time variation of spike front location for the four types of viscosity variations with density ratio $\rho_r = 1.5$ (rest of the parameters are: $m = 2$, $k_r = 2$, $c_{p_r} = 2$, $Re = 50$, $Pr = 1$, $Fr = 1$, $We = 150$ and $r_T = 3$).

evolution for the four types of viscosity variations for density ratio 4. For constant, power law and linear variations, top heavier fluid forms a mushroom shaped spike which eventually deforms, and a thick skirt is forms which is attached to the spike head. For these three variations, the spike-skirt structure shows qualitative similarity. For exponential variation, spike forms with longer and thinner skirt attached to spike head. For exponential variation, length of the skirt is relatively longer than that of the other viscosity variations. Time variation of spike front location is presented in Fig 7.17 for the four types of viscosity variations for density ratio 4. For exponential, linear, constant and power law variations, the spike strikes the bottom wall at about dimensionless time $t = 6$, 7.5, 9 and 11, respectively. For exponential variation, rate of spike movement is almost 2 times that of power law variation.

Interfacial instability for density ratio 10 is presented in Fig. 7.18 for the four types of viscosity variations. From the figure it is observed that formation of spike shows qualitative similarity for constant, power law and linear variations. For these three types of variations, the skirt on the spike head forms relatively smaller. For exponential variation, the skirt on the spike head forms relatively thinner and longer than that of the other three variations. Time variation of spike front location is presented in Fig. 7.19 for density ratio 10. For exponential, linear, constant and power law variations, the spike strikes the bottom wall at about dimensionless time $t = 4.5$, 5, 5.5 and 6, respectively, which shows marginal difference between the four types of viscosity variations.

Fig. 7.20 shows the instability for the four types of viscosity variations for density ratio 20. The heavier fluid spike shows qualitative similarity and the spike forms with smaller head, irrespective of type of viscosity variation. For density ratio 20 or higher, effect of type of viscosity variation on the instability is found to be negligible. Time taken by the spike to strike the bottom wall shows negligible difference for the four types of viscosity variations, which can be observed from the time variation of the spike front location shown Fig. 7.21. For all the four types of viscosity variations, spike strikes the bottom wall almost at the same time instance at about dimensionless time $t = 4$. For high density ratios, the instability become independent of type of viscosity variations. This is evident from the structure of the spike and time variation of the spike front locations presented in Fig. 7.20 and Fig. 7.21, respectively.

With increasing density ratio, the quantitative difference in the instability due to different types of viscosity variations is found to be decreased, which can be observed from the spike-skirt formations and time variation of spike front location. For exponential variation, time variation of spike front location for various density ratios is presented in Fig. 7.22 for various density ratios. The figure shows that rate of spike movement becomes relatively faster as density ratio is increased. For density ratio 20 or more, spike movement is found to be almost same with negligible difference. Similar trends of increasing destabilizing effect on the instability with increasing density ratio is observed for the other types of viscosity variations. At high density ratios, size of the spike head is found

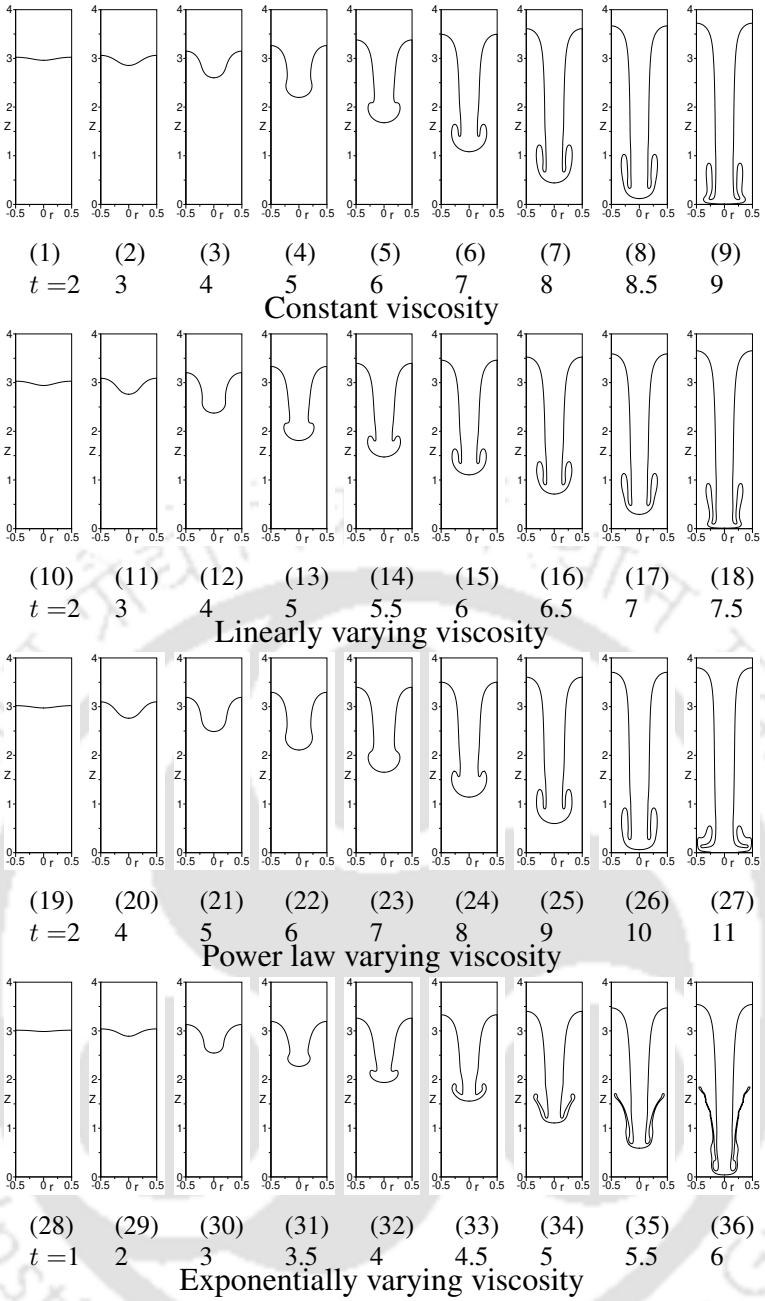

Figure 7.16: Interface profiles for different functional variations of viscosity with temperature for density ratio $\rho_r = 4$ (rest of the parameters are: $m = 2$, $k_r = 2$, $c_{p_r} = 2$, $Re = 50$, $Pr = 1$, $Fr = 1$, $We = 150$ and $r_T = 3$).

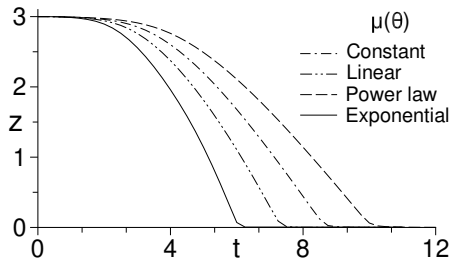

Figure 7.17: Time variation of spike front location for the four types of viscosity variations with density ratio $\rho_r = 4$ (rest of the parameters are: $m = 2$, $k_r = 2$, $c_{p_r} = 2$, $Re = 50$, $Pr = 1$, $Fr = 1$, $We = 150$ and $r_T = 3$).

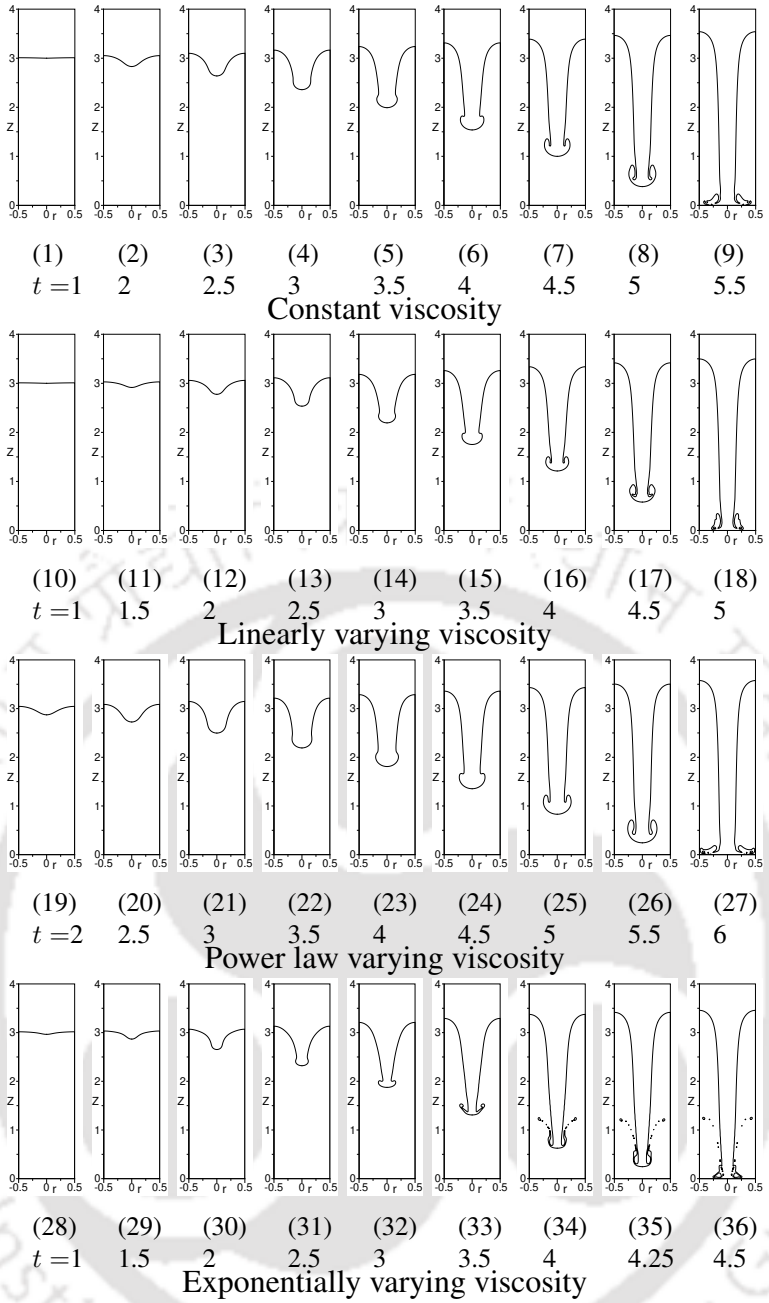

Figure 7.18: Interface profiles for different functional variations of viscosity with temperature for density ratio $\rho_r = 10$ (rest of the parameters are: $m = 2$, $k_r = 2$, $c_{p_r} = 2$, $Re = 50$, $Pr = 1$, $Fr = 1$, $We = 150$ and $r_T = 3$).

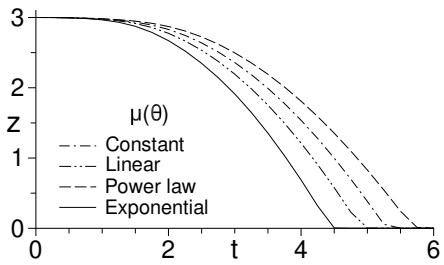

Figure 7.19: Time variation of spike front location for the four types of viscosity variations with density ratio $\rho_r = 10$ (rest of the parameters are: $m = 2$, $k_r = 2$, $c_{p_r} = 2$, $Re = 50$, $Pr = 1$, $Fr = 1$, $We = 150$ and $r_T = 3$).

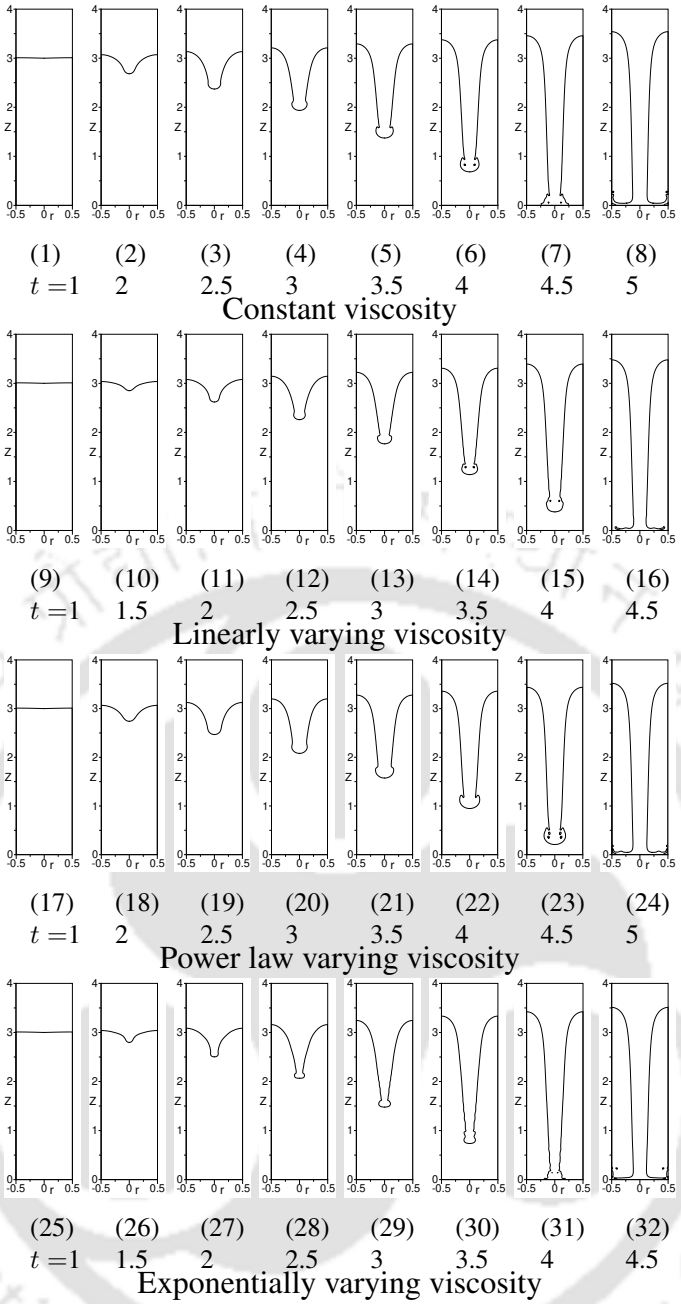

Figure 7.20: Interface profiles for different functional variations of viscosity with temperature for density ratio $\rho_r = 20$ (rest of the parameters are: $m = 2$, $k_r = 2$, $c_{p_r} = 2$, $Re = 50$, $Pr = 1$, $Fr = 1$, $We = 150$ and $r_T = 3$).

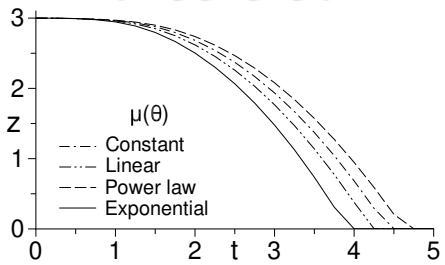

Figure 7.21: Time variation of spike front location for the four types of viscosity variations with density ratio $\rho_r = 20$ (rest of the parameters are: $m = 2$, $k_r = 2$, $c_{p_r} = 2$, $Re = 50$, $Pr = 1$, $Fr = 1$, $We = 150$ and $r_T = 3$).

to be relatively smaller, irrespective of viscosity variations. Overall, increase in density ratio shows destabilizing effect on the instability with smearing off the effect of viscosity variations.

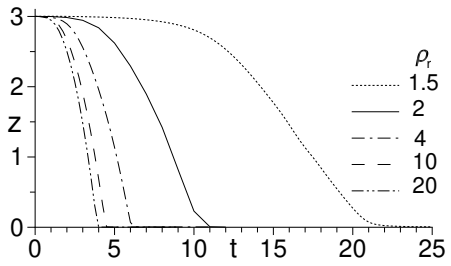

Figure 7.22: Time variation of spike front location for various density ratios with exponential variation of viscosity (rest of the parameters are: $m = 2$, $k_r = 2$, $c_{p_r} = 2$, $Re = 50$, $Pr = 1$, $Fr = 1$, $We = 150$ and $r_T = 3$).

7.4 Conclusions

Effect of functional variations of viscosity with temperature on axisymmetric Rayleigh-Taylor instability is studied for four types of functional variations, which are constant, linear, power law and exponential variations. Effect of functional variation of viscosity on the instability is studied for various viscosity ratios in the range of 0.5 to 100 and density ratios in the range of 1.5 to 20, respectively. Type of viscosity variation shows an strong effect on the instability at low density ratios and low viscosity ratios. For viscosity ratio about 60 or more, spike forms into a fluid column like structure, irrespective of viscosity variations. For density ratio about 20 or more, a smaller spike head is formed, for all the four types of viscosity variations. At high density ratio, the instability and rate of spike movement becomes independent of viscosity variation. The instability becomes almost independent of density ratio for density ratio higher than 20. Rate of spike movement is decreased with increasing viscosity ratio and increased with increasing density ratio, for all the four types of viscosity variations. Rate of spike movement is in increasing order of sequence of power law, constant, linear and exponential variations because the overall effective viscosity decreases in the order of above sequence.

Chapter 8

Marangoni effect on Rayleigh-Taylor instability in viscosity stratified medium in axisymmetric coordinates

Marangoni effect on Rayleigh-Taylor instability is studied in temperature varying viscosity stratified fluid layers in axisymmetric configuration. The Marangoni effect is due to temperature varying surface tension. Marangoni effect on the instability is studied for different functional dependencies of surface tension with temperature. Effect of Weber number, temperature ratio and Froude number on the instability in the presence of Marangoni effect is also studied.

8.1 Physical system

Physical system in axisymmetric coordinates used for the study presented in this chapter is shown in Fig. 2.3. The physical system is described in subsection 2.1.2.

8.2 Mathematical treatment

In this present chapter, studies are performed by solving governing equations numerically using Basilisk software. The software uses Volume of Fluid (VoF) method. In VoF method an additional equation of volume fraction is solved to find the interface location. The governing equations consist of continuity, momentum, energy and volume fraction equations.

8.2.1 Scaling parameters

Reference scales chosen to non-dimensionalize the governing equations are as following. The reference scales for length, time, velocity, pressure, temperature and surface tension are taken to be $\tilde{L}_{\text{ref}}$, $\tilde{L}_{\text{ref}}/\tilde{V}_{\text{ref}}$, $\tilde{V}_{\text{ref}}$, $\rho_{\text{ref}}\,\tilde{V}_{\text{ref}}^2$, $\tilde{T}_{\text{ref}}$ and $\tilde{\sigma}_{\text{ref}}$, respectively. Reference length is taken as $\tilde{L}_{\text{ref}} = \tilde{L}$. Reference velocity is taken as $\tilde{V}_{\text{ref}} = \beta_1\,\tilde{T}_{\text{ref}}/\tilde{\mu}_{\text{ref}}$. β_1 is a constant in the expression of surface tension variation

with temperature in dimensional form (see Eq. 2.28). Here, β_1 is the rate of dimensional surface tension variation with dimensional temperature at reference temperature ($\beta_1 = -d\tilde{\sigma}/d\tilde{T}|_{\tilde{T}_{\text{ref}}}$). Reference temperature is taken equal to cold wall temperature. Reference surface tension is taken as $\tilde{\sigma}_{\text{ref}} = \tilde{\sigma}_0$, which is surface tension value at reference temperature. Reference scales for fluid properties such as density, viscosity, specific heat and thermal conductivity are chosen to be the respective properties of 'Fluid 2'. The chosen reference scales to non-dimensionlize the governing equations are

$$\begin{aligned} \tilde{\rho}_{\text{ref}} = \tilde{\rho}_2, \quad \tilde{\mu}_{\text{ref}} = \tilde{\mu}_2, \quad \tilde{k}_{\text{ref}} = \tilde{k}_2, \quad \tilde{c_p}_{\text{ref}} = \tilde{c_p}_2, \\ \tilde{L}_{\text{ref}} = \tilde{L}, \quad \tilde{T}_{\text{ref}} = \tilde{T}_2, \quad \tilde{\sigma}_{\text{ref}} = \tilde{\sigma}_0, \quad \tilde{V}_{\text{ref}} = \beta_1 \tilde{T}_2/\tilde{\mu}_2 \end{aligned} \tag{8.1}$$

Based on the above reference scaling parameters, the different dimensionless variables, as given by Eq. (2.14), become as follows.

$$\begin{aligned} \rho = \frac{\tilde{\rho}}{\tilde{\rho}_2}, \quad \mu = \frac{\tilde{\mu}}{\tilde{\mu}_2}, \quad k = \frac{\tilde{k}}{\tilde{k}_2}, \quad c_p = \frac{\tilde{c_p}}{\tilde{c_p}_2}, \quad r = \frac{\tilde{r}}{\tilde{L}}, \quad z = \frac{\tilde{z}}{\tilde{L}}, \\ t = \frac{\tilde{t}\,\beta_1\,\tilde{T}_2}{\tilde{L}\,\tilde{\mu}_2}, \quad \mathbf{u} = \frac{\tilde{\mathbf{u}}}{\beta_1\,\tilde{T}_2/\tilde{\mu}_2}, \quad p = \frac{\tilde{p}}{\tilde{\rho}_2\,\beta_1^2\,\tilde{T}_2^2/\tilde{\mu}_2^2}, \quad \theta = \frac{\tilde{T}-\tilde{T}_2}{\tilde{T}_2}, \quad \sigma = \frac{\tilde{\sigma}}{\tilde{\sigma}_0} \end{aligned} \tag{8.2}$$

8.2.2 Governing equations

Using the above mentioned reference scaling parameters, the governing equations, which consist of continuity, momentum, energy and volume fraction equations, are non-dimensionalized and written as following.

Continuity equation

$$\nabla\cdot\mathbf{u} = 0 \tag{8.3}$$

Momentum equation

$$\rho\left(\frac{\partial\mathbf{u}}{\partial t} + \mathbf{u}\cdot\nabla\mathbf{u}\right) = -\nabla p + \frac{1}{Re}\nabla\cdot\mu\,\left(\nabla\mathbf{u} + \nabla\mathbf{u}^{\mathrm{T}}\right) + \mathbf{F} \tag{8.4}$$

Energy equation

$$\rho\,c_p\left(\frac{\partial\theta}{\partial t} + \mathbf{u}\cdot\nabla\theta\right) = \frac{1}{Ma}\nabla\cdot(k\nabla\theta) \tag{8.5}$$

Volume fraction equation

$$\frac{\partial f}{\partial t} + \mathbf{u}\cdot\nabla f = 0 \tag{8.6}$$

Here, dimensionless body force term including Marangoni effect is given by

$$\mathbf{F} = \frac{\delta}{We}\left[\sigma(\theta)\,\kappa\,\mathbf{n} + \nabla_s\,\sigma(\theta)\right] - \frac{\rho}{Fr}\,\mathbf{e}_j \tag{8.7}$$

For the study of Marangoni effect presented in this chapter, a quadratic form of temperature dependent surface tension variation, which is also used in the studies of [73, 92], is considered. Surface tension

expression in dimensional form, which is given by Eq. (2.28), is as following.

$$\tilde{\sigma}(\tilde{T}) = \tilde{\sigma_0} + \beta_1(\tilde{T} - \tilde{T}_{\text{ref}}) + \beta_2(\tilde{T} - \tilde{T}_{\text{ref}})^2 \tag{8.8}$$

Here, β_1 and β_2 are the surface tension coefficients dependent on temperature which are defined equal to $-d\tilde{\sigma}/d\tilde{T}|_{\tilde{T}_{\text{ref}}}$ and $(1/2)d^2\tilde{\sigma}/d\tilde{T}^2|_{\tilde{T}_{\text{ref}}}$, respectively. Expression of dimensionless surface tension varying with dimensionless temperature, as given by Eq. (2.31), is given as following

$$\sigma(\theta) = \tilde{\sigma}(\tilde{T})/\tilde{\sigma_0} = 1 - M_1\,\theta + M_2\,\theta^2 \tag{8.9}$$

Here, $M_1 = \beta_1\,\tilde{T}_{\text{ref}}/\tilde{\sigma_0}$ and $M_2 = \beta_2\,\tilde{T}^2_{\text{ref}}/\tilde{\sigma_0}$ are the dimensionless constants of surface tension expression. Substituting expression of dimensionless surface tension ($\sigma(\theta)$), given by Eq. (8.9), in Eq. (8.7) we get body force term as

$$\mathbf{F} = \frac{1}{We}\left[\kappa(1 - M_1\,\theta + M_2\theta^2)\,\delta\,\mathbf{n}\right] - \frac{(M_1 - 2\,M_2\theta)}{We}\left[\nabla\theta - (\nabla\theta\cdot\mathbf{n})\,\mathbf{n}\right]\delta_s - \frac{\rho}{Fr}\mathbf{e}_j \tag{8.10}$$

In the above governing equations, definitions of Reynolds number (Re), Froude number (Fr), Weber number (We) and Marangoni number (Ma), as given by Eq. (2.24), are as following.

$$Re = \frac{\beta_1\,\tilde{\rho}_2\,\tilde{T}_2\,\tilde{L}}{\tilde{\mu}_2^2},\; Fr = \frac{\beta_1^2\,\tilde{T}_2^2}{\tilde{g}\tilde{L}\,\tilde{\mu}_2^2},\; We = \frac{\tilde{\rho}_2\,\tilde{g}\,\tilde{L}^2}{\tilde{\sigma_0}},\; Ma = Re\,Pr = \frac{\beta_1\,\tilde{T}_2\,\tilde{\rho}_2\,\tilde{c_{p2}}\,\tilde{L}}{\tilde{\mu}_2\,\tilde{k}_2},\; Pr = \frac{\tilde{\mu}_2\tilde{c_{p2}}}{\tilde{k}_2} \tag{8.11}$$

Variation of viscosities of top and bottom fluid layers in dimensionless form, is given by Eq. (2.25), is as following.

$$\mu_1 = m\,e^{-\theta} \qquad \text{and} \qquad \mu_2 = e^{-\theta} \tag{8.12}$$

Here, m is top heavier to bottom lighter fluid viscosity ratio ($m = \mu_1(\tilde{T}_2)/\mu_2(\tilde{T}_2)$). Here, $\mu_1(\tilde{T}_2)$ and $\mu_2(\tilde{T}_2)$ are top and bottom layer fluid viscosities at reference temperature, respectively. In VoF method, dimensionless fluid properties such as viscosity, density, thermal conductivity and heat capacity are calculated using a function of f, given by Eq. (2.13), are expressed as following

$$\begin{aligned}
\rho &= \rho_1\,f + \rho_2\,(1-f)\\
\mu &= \mu_1\,f + \mu_2\,(1-f)\\
c_p &= c_{p1}\,f + c_{p2}\,(1-f)\\
k &= k_1\,f + k_2\,(1-f)
\end{aligned} \tag{8.13}$$

8.2.3 Initial and boundary conditions

For the study presented in this chapter, initial and boundary conditions used are given in subsection 2.2.3. The dimensions of axisymmetric domain used in the study of this chapter are given in the same subsection.

8.2.4 Numerical methodology

Numerical methodology of the Basilisk software is discussed in subsection 2.2.6. The validations of usage of the software is presented in the next subsection.

8.2.5 Validation for Marangoni effect in axisymmetric configuration

Before studying the Marangoni effect on the instability of the present study, usage of the software is validated for simulations of Marangoni effect due to variable surface tension on multiphase flow for axisymmetric configuration. The validations carried out are as following.

8.2.5.1 Bubble rise in fluid medium with spatially varying surface tension

For the validation, dynamics of a spherical bubble in the presence of Marangoni effect and in the absence of gravity is simulated using the software and the obtained results are compared with those presented in Muradoglu and Tryggvason [93]. The simulation is carried out for a spherical bubble with dimensionless radius of 0.5 which is kept stationary on the axis of a vertical tube such that its center is located at dimensionless vertical distance of 1.5 from the bottom boundary of the vertical tube. The tube with dimensionless radius of 2.5 and dimensionless height of 7.5 is filled with quiescent fluid. Densities of inner and outer fluids both are set to 0.2. Viscosities of inner and outer fluids both are set to 0.1. Surface tension is specified to vary with space in vertical direction. Due to surface tension variation in the vertically upward direction, surface tension forces vary asymmetrically along the bubble interface. Due to such asymmetric surface tension forces, the bubble migrates in the vertical direction. Young et al. [86] obtained theoretical terminal migration velocity of the bubble for the same problem using theoretical analysis. The bubble migration velocities obtained from present software and reference study are normalized with the theoretical terminal bubble migration velocity obtained by Young et al. [86]. Fig. 8.1 shows the comparison of variation of the normalized bubble migration velocity obtained from present software with that of Muradoglu and Tryggvason [93]. In the figure normalized terminal bubble migration velocity is also plotted. The present result shows good agreement with the reference study result.

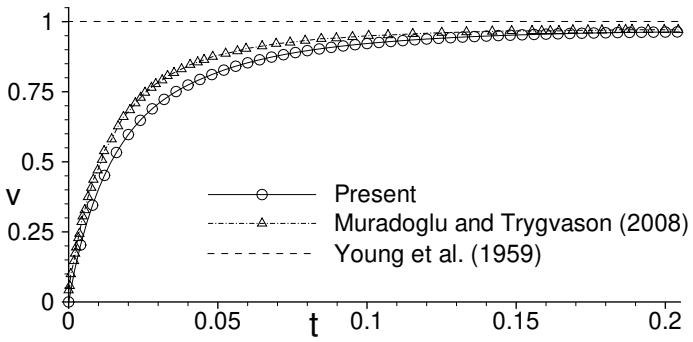

Figure 8.1: Time variation of migration velocity of the bubble in the presence of variable surface tension.

8.2.5.2 Bubble rise in fluid medium with temperature varying surface tension

For the next validation, solution of dynamics of 2-D bubble in the presence of temperature dependent surface tension and in the absence of gravity is obtained using Basilisk software which is compared with the solution presented by Ma and Bothe [15]. A bubble with dimensionless diameter of 1 is placed at the center of a square domain of dimensionless size of 2×2. The bubble is surrounded by an outer fluid medium in the domain. Top and bottom horizontal boundaries of the domain are hot and cold walls, respectively. Side vertical boundaries are of symmetric nature. The bubble fluid to outer fluid density ratio, viscosity ratio, heat capacity ratio and thermal conductivity ratio, all are set equal to 0.5. The outer ambient fluid properties are taken as reference fluid properties. Surface tension is specified to vary linearly with temperature. At the initial state, $t = 0$, temperature is specified to vary with a uniform temperature gradient in vertical direction from bottom wall to top wall. The values of capillary number (Ca), Marangoni number (Ma) and Reynolds number (Re) are set equal to 0.0576, 0.72 and 0.72, respectively.

Due to temperature variation from bottom to top wall, the surface tension along the bubble interface will be asymmetric with respect to mid horizontal plane. Due to the asymmetric surface tension forces, the bubble migrates towards the upper hot wall. The time variation of migration velocity of bubble obtained in the present simulation is compared with that presented by Ma and Bothe [15], in Fig. 8.2. The comparison shows that the present results are in good agreement with the reference results.

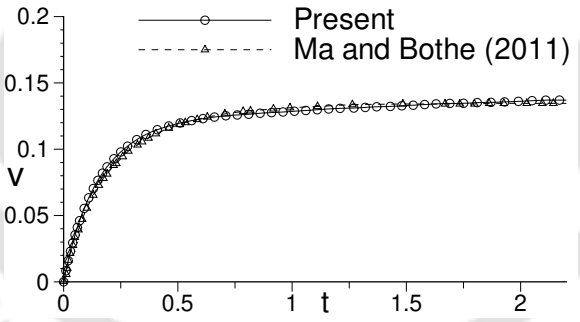

Figure 8.2: Time variation of migration velocity of the bubble in the presence of variable surface tension is compared with reference study results of Ma and Bothe [15].

8.2.6 Grid independence test

Grid independence test is carried out before performing the numerical simulations to study Rayleigh-Taylor instability in viscosity stratified fluid medium with Marangoni effect in axisymmetric configuration. When Weber number approaches to infinity (surface tension approaches to zero), the interface structure is expected to be complex and may undergo large deformation. When the interface structure is complex and undergo large deformation, the solutions are expected to be sensitive to the grid variation. Hence, the grid independent test results are carried out for Weber number (We) value approaching to infinity. The other parameters are taken equal to $\rho_r = 2$, $m = 2$, $k_r = 2$, $c_{p_r} = 2$,

$Re = 50$, $Ma = 50$, $Fr = 1$ and $r_T = 5$, which are the baseline parameters of the study presented in the chapter. Surface tension is specified to vary with temperature parabolically. For the test, different grid levels such as 8, 9 and 10 are chosen which correspond to the minimum grid spacing of 0.0156, 0.0078 and 0.0039, respectively, as given in Table 5.1. It can be seen from Fig. 8.3– 8.4 that with the use of minimum grid spacing of 0.0078 or less, present study results do not show any significant differences qualitatively and quantitatively. Hence, the numerical simulations are carried out with the grid level of 9 which corresponds to the minimum grid spacing of 0.0078.

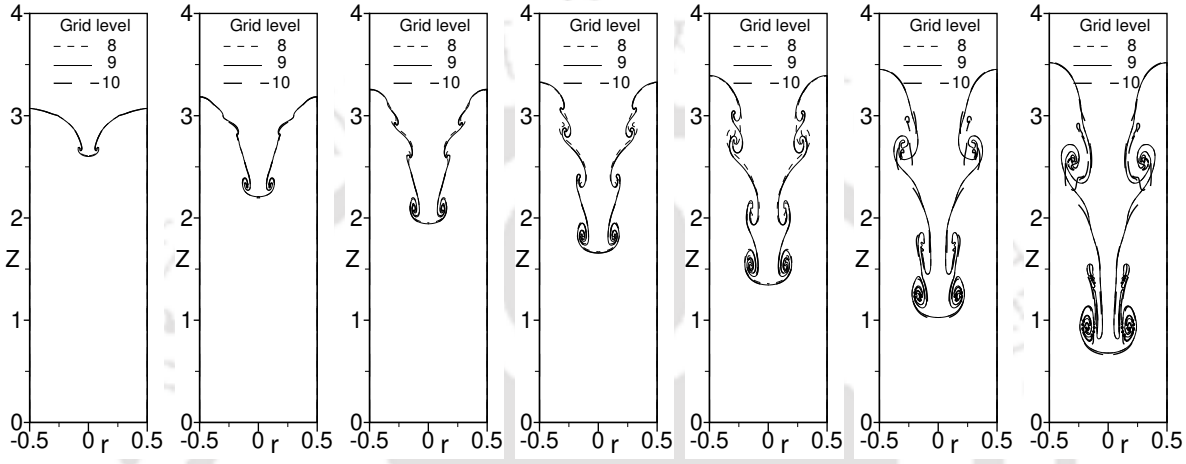

Figure 8.3: Comparison of instantaneous interface profiles of Rayleigh-Taylor instability in variable viscosity fluid layers with Marangoni effect in axisymmetric configuration obtained with different grid sizes (rest of the parameters are: $\rho_r = 2$, $m = 2$, $k_r = 2$, $c_{p_r} = 2$, $Re = 50$, $Ma = 50$, $Fr = 1$, $We = \infty$ and $r_T = 5$).

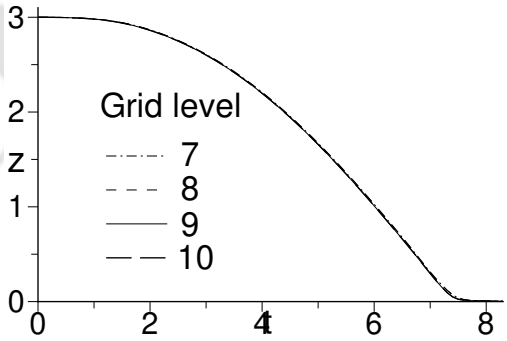

Figure 8.4: Comparison of time variation of spike front locations for various grid sizes in variable viscosity fluid layers with Marangoni effect (rest of the parameters are: $\rho_r = 2$, $m = 2$, $k_r = 2$, $c_{p_r} = 2$, $Re = 50$, $Ma = 50$, $Fr = 1$, $We = \infty$ and $r_T = 5$).

8.3 Results and discussion

8.3.1 Baseline parameter values

In the present chapter, effect of various parameters on Rayleigh-Taylor instability is studied in the presence of Marangoni effect. Effect of functional dependencies of surface tension on temperature, Weber number, temperature ratio and Froude number on the instability is studied in the presence of Marangoni effect. The studies are carried out at the following baseline parameter values. Baseline values of heavier fluid to lighter fluid density ratio (ρ_r), viscosity ratio (m), heat capacity ratio (c_{p_r}), thermal conductivity ratio (k_r) are chosen to be equal to 2, 2, 2 and 2, respectively. Temperature ratio (r_T) is chosen equal to 5. The values of Weber number (We), Froude number (Fr), Reynolds number (Re) and Marangoni number ($Ma = Re\,Pr$) are chosen to be equal to 100, 1, 50 and 50, respectively. $M_1 = 0.15$ and $M_2 = 0.075$ are chosen for baseline values (except for the study of surface tension functional dependency on temperature presented in section 8.3.2). Effect of a particular parameter is studied by varying the value of that particular parameter and keeping the remaining parameter values at the above mentioned baseline values.

8.3.2 Effect of functional dependency of surface tension on temperature

Rayleigh-Taylor instability is studied for the effect of functional dependency of surface tension on temperature. A generalized expression for surface tension dependency on temperature is given by Eq. (2.31). With $M_1 = M_2 = 0$, the expression represents constant (temperature independent) surface tension. When $M_2 = 0$ along with nonzero M_1 value, the expression represents linear variation of surface tension with temperature. When both M_1 and M_2 are chosen to be nonzero, the expression represents parabolic variation of surface tension with temperature (self-rewetting fluids). Comparison of functional dependency of surface tension on temperature is carried out for constant, linear and parabolic variation. The comparison is carried out by taking $M_1 = M_2 =$0 for constant surface tension, $M_1 = 0.15$, $M_2 = 0$ for linearly varying surface tension and $M_1 = 0.15$, $M_2 = 0.075$ for parabolically varying surface tension.

The instability evolution for the three types of functional dependencies is shown in Fig. 8.5. In all the three types, initially mushroom-shaped spike forms which eventually evolves into a spike with a skirt. However, in later stage, the instability differs from each other for different functional dependencies. For constant surface tension case, a skirt forms initially at tip of the spike head, and the distance between spike head and skirt location increases as spike moves towards the bottom wall. With time, the skirt detaches from the spike stem for a short period of time and it reattaches to the stem which again detaches from the stem. From the observation of the intermediate time frames of interface profile, it is confirmed that a sequence of detachment, attachment, and again detachment of the skirt from the spike stem occurs in the range of dimensionless time span about $t = 9 - 13$, as seen in Figs. 8.5(5)-8.5(9). The detached skirt moves in the wake created by spike head and stem in such a way that the skirt reattaches and again detaches from the spike stem. Whereas for linearly

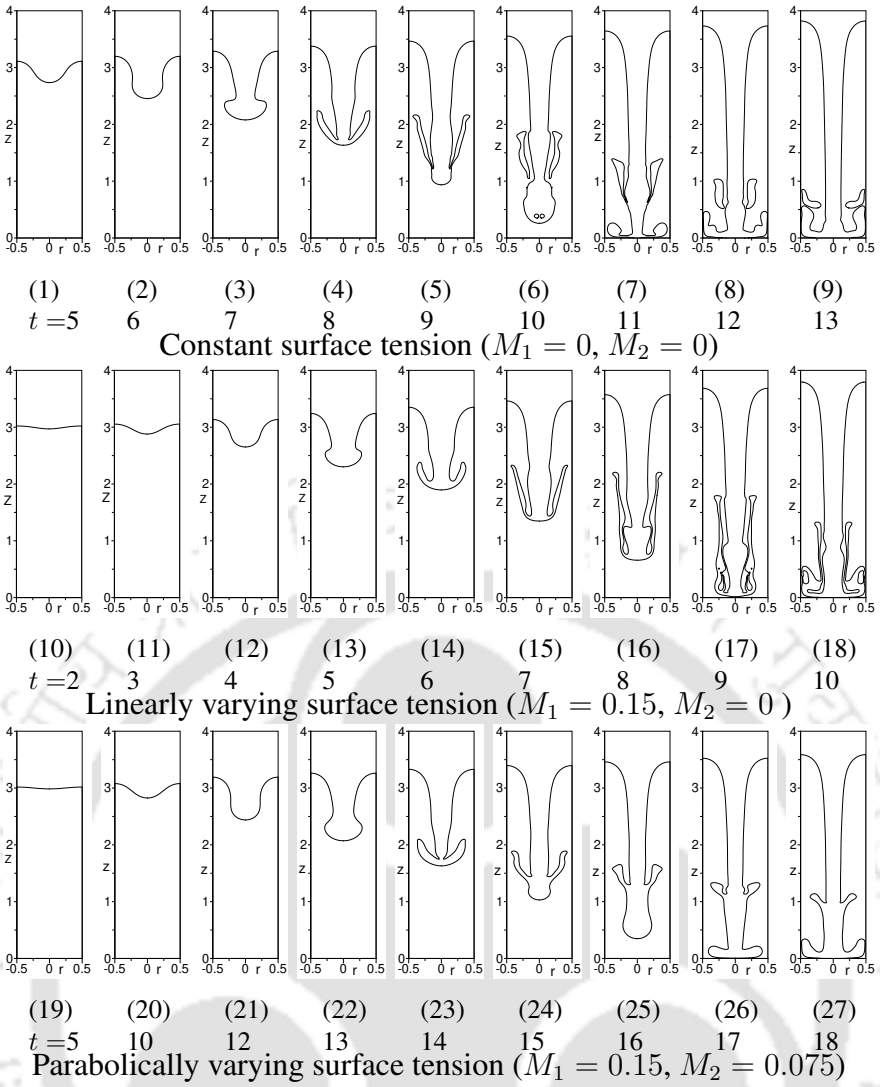

Figure 8.5: Instantaneous interface profiles for three types of surface tension variation with temperature (rest of the parameters are: $\rho_r = 2$, $m = 2$, $k_r = 2$, $c_{p_r} = 2$, $Re = 50$, $Ma = 50$, $Fr = 1$, $We = 100$ and $r_T = 5$).

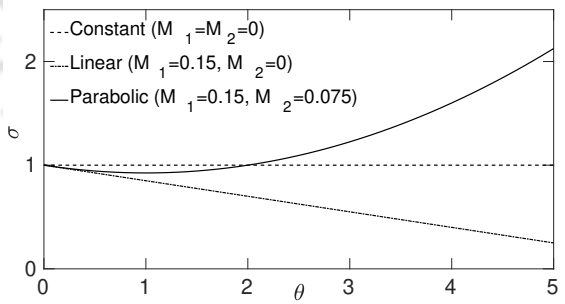

Figure 8.6: Dimensionless surface tension (σ) variation with dimensionless temperature (θ).

varying surface tension case, the spike moves relatively faster towards the bottom wall with thinner and longer skirt. With time, shape of the spike and the skirt become more irregular. For parabolically varying surface tension case, the spike moves relatively slower with smaller skirt compared to the other cases of surface tension variation. For parabolic surface tension, distance between the spike head and location of the skirt increases with time, and length of the skirt decreases as spike moves

towards the bottom wall. For linear and parabolic surface tension, the skirt is found to be attached with the spike all the time while the spike moves towards the bottom wall unlike for constant surface tension.

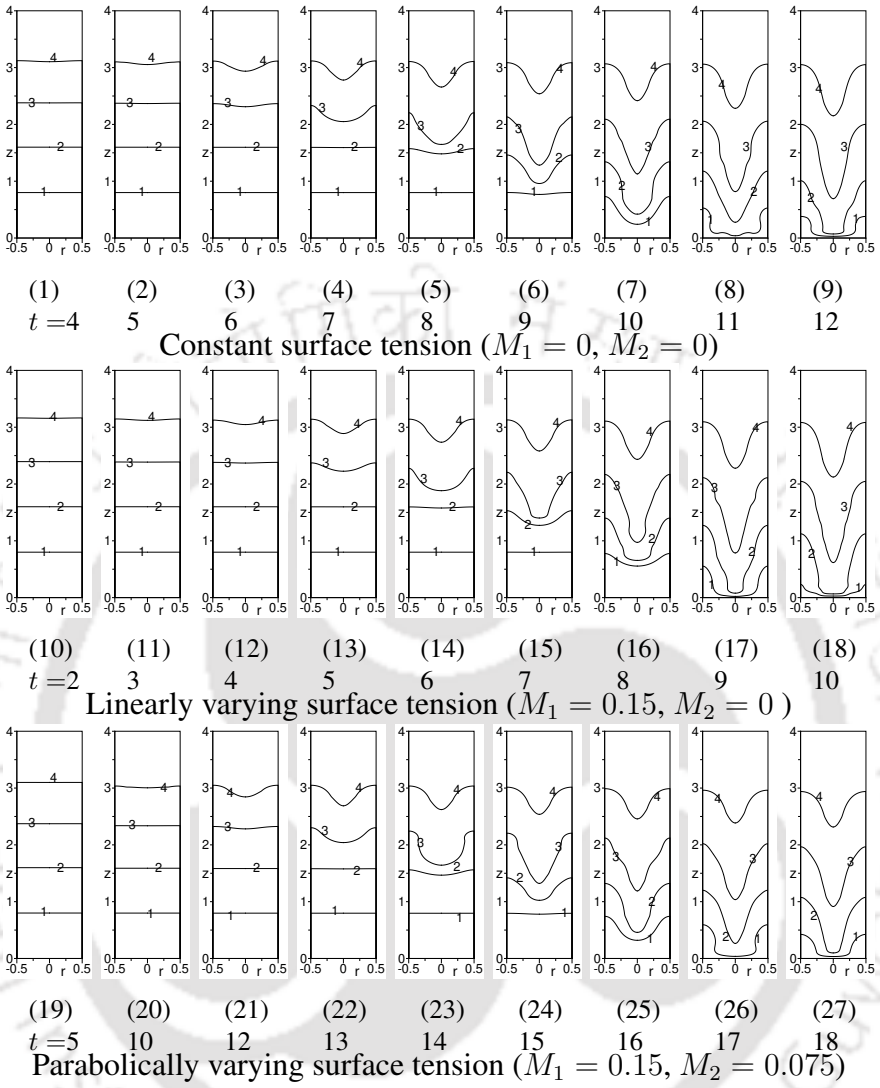

Figure 8.7: Instantaneous temperature contours for three types of surface tension variation with temperature (rest of the parameters are: $\rho_r = 2$, $m = 2$, $k_r = 2$, $c_{p_r} = 2$, $Re = 50$, $Ma = 50$, $Fr = 1$, $We = 100$ and $r_T = 5$).

The difference in interfacial movement and its structure is due to the fact that variation of surface tension differs largely for the three types of functional dependencies. The reason for difference in the instability can be understood by comparing the variation of surface tension with temperature for the three types of variations. The comparison of surface tension variations is shown in Fig. 8.6. From the figure it can be seen that for the constant case, the effective surface tension is equal to 1 throughout the domain, irrespective of hot and cold wall temperatures. For linear dependency, the surface tension varies linearly from a maximum value of $\sigma = 1$ at the bottom cold wall to a minimum value of $\sigma = 0.25$ at the top hot wall. Hence, in the sense of on an average, the overall effective surface tension for linear dependency would be lower than that of constant surface tension. For the parabolic dependency, the surface tension is slightly less than 1 for dimensionless temperature range

of 0 to 2. For dimensionless temperature beyond 2 the surface tension values are much higher than 1 which reaches to a maximum value of $\sigma = 2.125$ at hot wall. In the sense of on an average, the overall effective surface tension for parabolic dependency would be higher than that of constant surface tension. For linear dependency, the lowest effective surface tension results into an irregular spike-skirt structure with longer skirt which moves relatively faster. For parabolic dependency, the highest effective surface tension results into a smooth spike-skirt structure with shorter skirt which moves relatively slower. Due to the fact that the overall effective surface tension is in the increasing order of linear, constant and parabolic dependency, the rate of spike movement follows the reverse order of the effective surface tension.

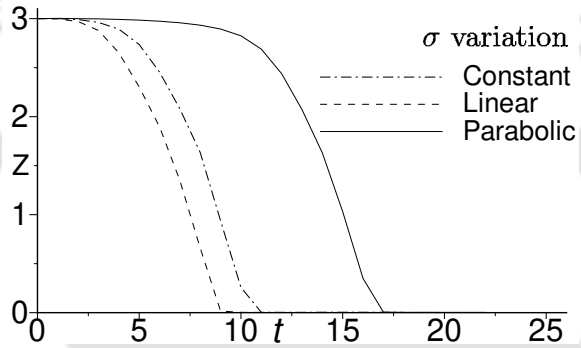

Figure 8.8: Time variation of spike front location for three types of surface tension variation (rest of the parameters are: $\rho_r = 2$, $m = 2$, $k_r = 2$, $c_{p_r} = 2$, $Re = 50$, $Ma = 50$, $Fr = 1$, $We = 100$ and $r_T = 5$).

Fig. 8.7 shows temperature contours of the instability evolution for the three types of surface tension variations. Temperature contours form penetrative in nature following the interfacial movement. Temperature contours show similarity among the three types of surface tension variations. Fig. 8.8 shows time variation of location of spike front (elevation of spike which is the value of $Z-$coordinate) for the three types of functional dependencies. The instability differs largely for the three types of surface tension dependencies which is evident from the time variation of spike front location. For constant surface tension, the spike strikes the bottom wall at about dimensionless time $t = 11$. For linearly varying surface tension, the spike strikes the bottom wall at about dimensionless time $t = 9$. Whereas for parabolically varying surface tension, the spike strikes the bottom wall at about dimensionless time $t = 17$ which is about two times slower compared to that of linearly varying surface tension.

In the following subsections (subsections 8.3.3-8.3.5), effect of temperature ratio, Weber number and Froude number on the instability is studied for the parabolic variation of surface tension with temperature at the baseline parameter values mentioned in subsection 8.3.1.

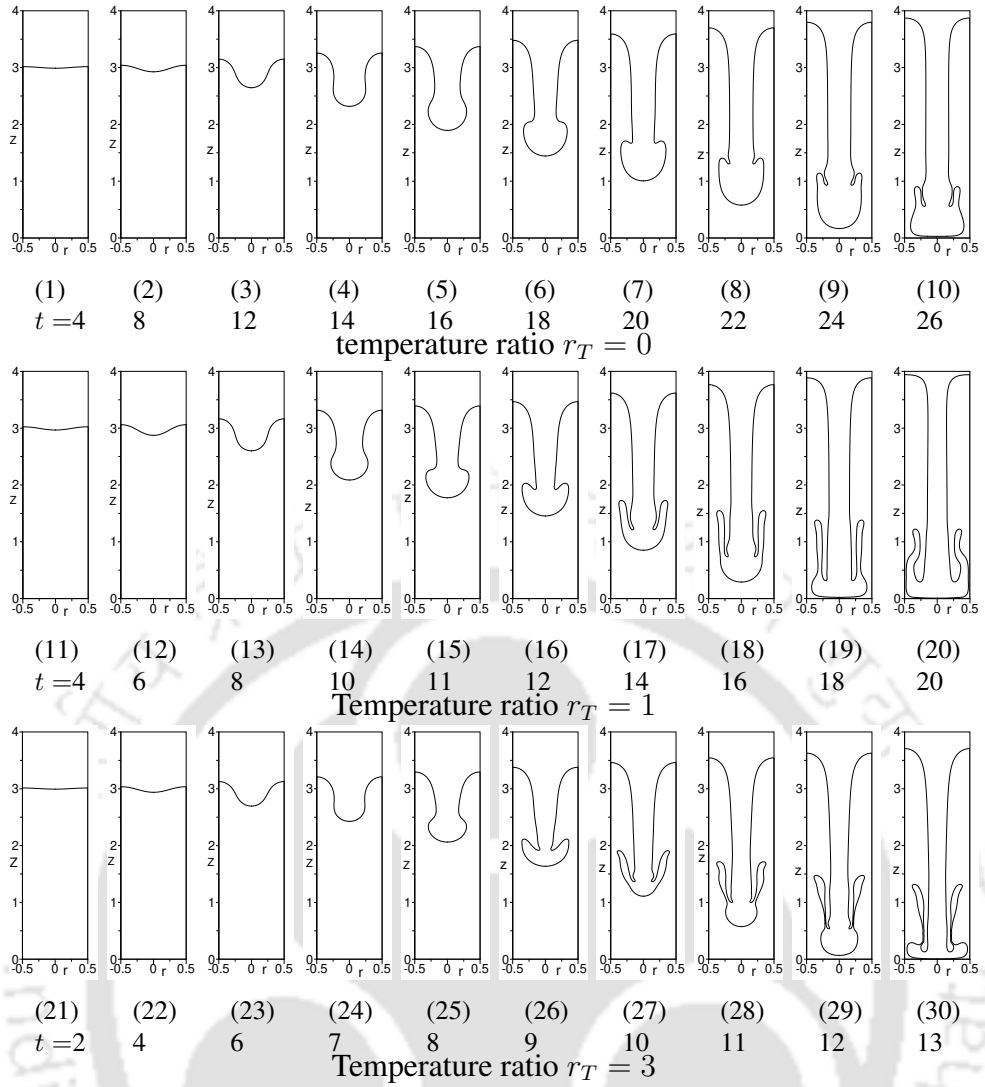

Figure 8.9: Instantaneous interface profiles for temperature ratios in the range of r_T = 0-3 (rest of the parameters are: $\rho_r = 2$, $m = 2$, $k_r = 2$, $c_{p_r} = 2$, $Re = 50$, $Ma = 50$, $Fr = 1$, $We = 100$, $M_1 = 0.15$ and $M_2 = 0.075$).

8.3.3 Effect of temperature ratio

Effect of temperature ratio on the instability is studied for temperature ratio in the range of 0 to 5.27. The instability evolution for various temperature ratios is presented in Figs. 8.9- 8.10. Temperature ratio 0 corresponds to constant temperature throughout the domain, which represents constant surface tension and constant viscosity. For temperature ratio 0, initially a spike with mushroom shaped head is formed and the shape of the spike head is retained all the time till the spike strikes the bottom wall. When temperature ratio is increased to 1, the spike eventually deforms and a skirt is formed before striking the bottom wall. When the temperature ratio is increased from 1 to 3, an elongated skirt forms on the spike head. For temperature ratio more than 3, increase in temperature ratio results into a shorter skirt with slower spike movement. For temperature ratio in the range of 4 to 5, a skirt forms on the spike head, and with time the distance between the skirt location and spike head increases as spike moves towards the bottom wall. With further increase in temperature ratio beyond 5.27, it is found that configuration becomes stable with denser fluid resting on top of the lighter fluid. Hence,

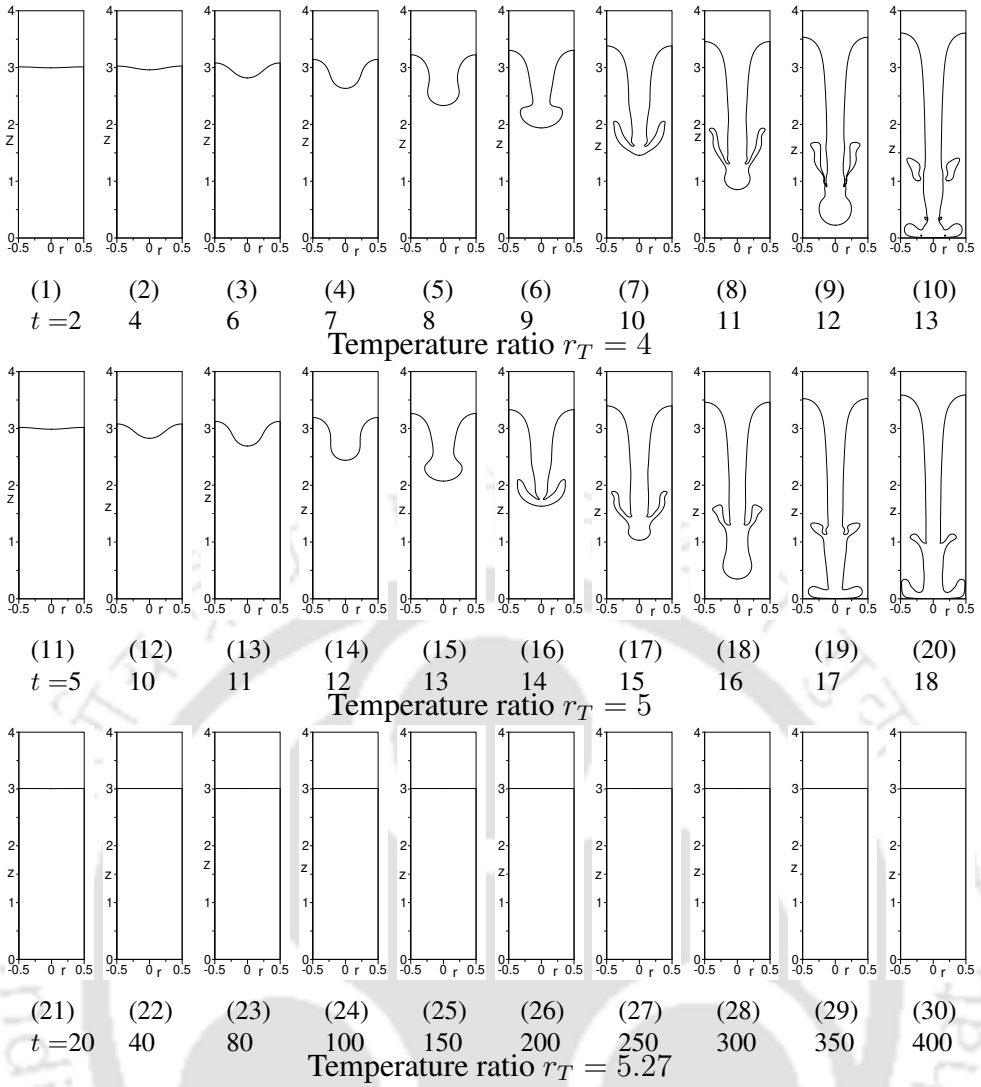

Figure 8.10: Instantaneous interface profiles for temperature ratios in the range of $r_T = 4$-5.27 (rest of the parameters are: $\rho_r = 2$, $m = 2$, $k_r = 2$, $c_{p_r} = 2$, $Re = 50$, $Ma = 50$, $Fr = 1$, $We = 100$, $M_1 = 0.15$ and $M_2 = 0.075$).

critical temperature ratio is 5.27, below which the configuration is stable.

With the increasing temperature ratio from 0 to 3, time taken by the spike to strike the bottom wall decreases, whereas for temperature ratio increased beyond 3, it increases. The decreasing and increasing trend of spike movement with temperature ratio can be seen from the fact that increasing temperature ratio decreases the overall effective viscosity and increases the overall effective surface tension. The decrease in overall effective viscosity results into destabilizing effect and the increase in overall effective surface tension results into stabilizing effect on the instability. Due to the opposite competing effects on the instability with increasing temperature ratio, the resultant spike movement shows increasing and decreasing trend.

The time variation of spike front location for different temperature ratios is shown in Fig. 8.11. With increasing temperature ratio in the range of 0 to 3, time taken by the spike to strike the bottom wall reduces as spike movement becomes relatively faster. For temperature ratio 3, the spike strikes the bottom wall at about dimensionless time $t = 12$ which is almost 2 times faster comparing to that

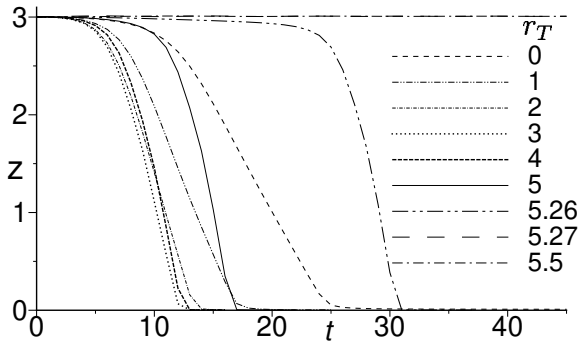

Figure 8.11: Time variation of spike front location for various temperature ratios (rest of the parameters are: $\rho_r = 2$, $m = 2$, $k_r = 2$, $c_{p_r} = 2$, $Re = 50$, $Ma = 50$, $Fr = 1$, $We = 100$, $M_1 = 0.15$ and $M_2 = 0.075$).

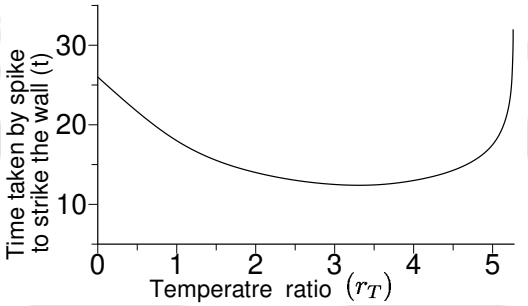

Figure 8.12: Variation of time taken by spike front to strike the bottom wall with temperature ratio (rest of the parameters are: $\rho_r = 2$, $m = 2$, $k_r = 2$, $c_{p_r} = 2$, $Re = 50$, $Ma = 50$, $Fr = 1$, $We = 100$, $M_1 = 0.15$ and $M_2 = 0.075$).

of the temperature ratio 0 in which spike strikes the bottom wall at about dimensionless time $t = 26$. With increasing temperature ratio beyond 3, time taken by the spike to strike the bottom wall increases as spike movement becomes relatively slower. For temperature ratio 5.26, the spike strikes the bottom wall at about dimensionless time $t = 32$, almost 2.5 times slower comparing to that of temperature ratio 3. For temperature ratio beyond critical value of 5.27, the configuration does not undergo instability. Fig. 8.12 shows variation of time taken by the spike to strike the bottom wall with temperature ratio. The curve shows non-monotonic variation of time taken by the spike with temperature ratio which indicates decreasing and increasing trend of spike movement with temperature ratio. For the given set of parameter values, the minimum time taken by the spike to strike the bottom wall is for temperature ratio about 3.5 which represents the fastest occurrence of the instability.

8.3.4 Effect of Weber number

In this part of the section, the effect of Weber number on Rayleigh-Taylor instability is studied in the range of 10 to infinity. Weber number is inversely proportional to surface tension and hence, increasing Weber number represents decreasing surface tension. Figs. 8.13-8.14 show the interfacial instability evolution for various Weber numbers in the range of 0 to infinity. From the figure it can be

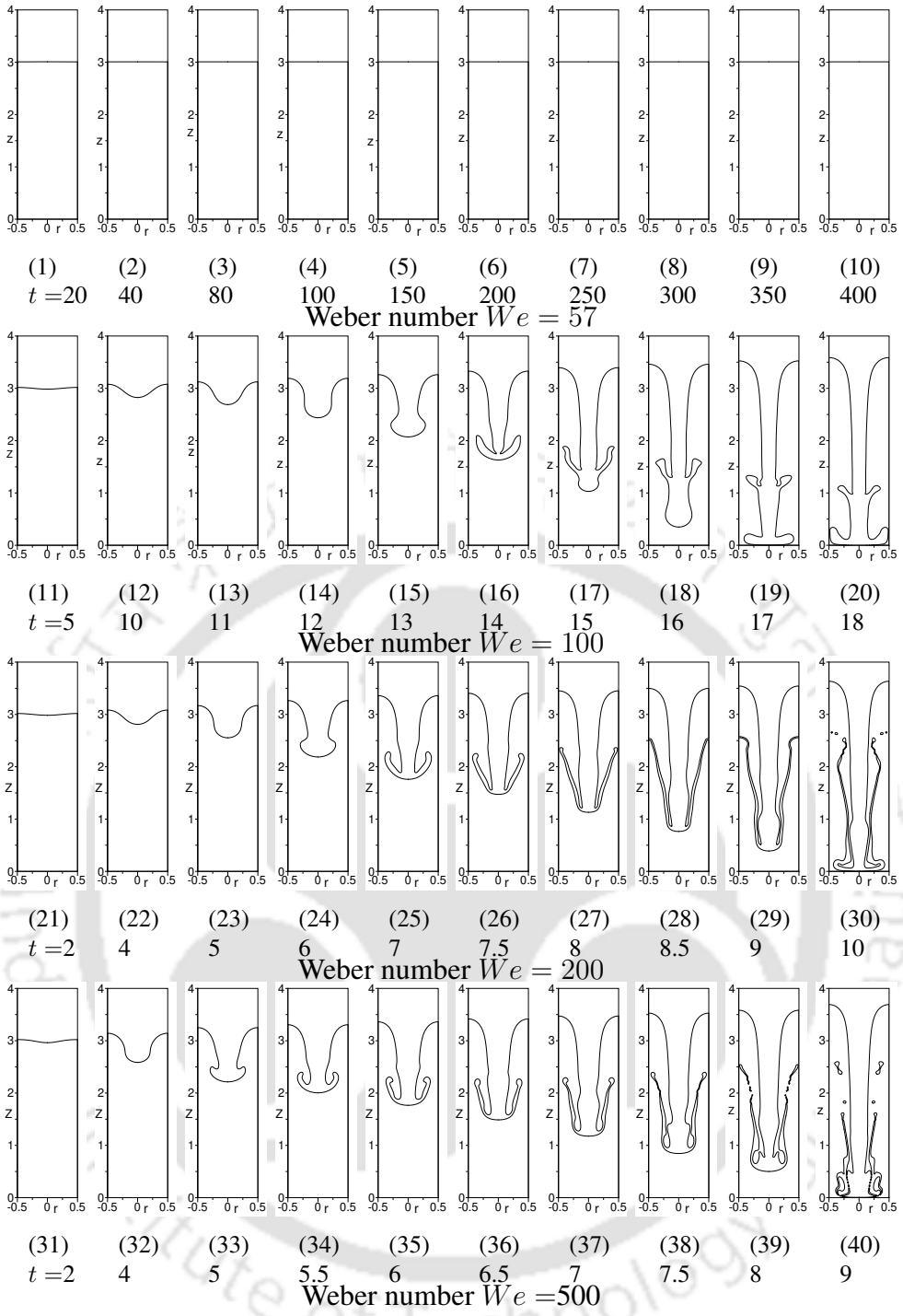

Figure 8.13: Interface profiles for Weber numbers in the range of $We = 57$-500 (rest of the parameters are: $\rho_r = 2$, $m = 2$, $k_r = 2$, $c_{p_r} = 2$, $Re = 50$, $Ma = 50$, $Fr = 1$, $r_T = 5$, $M_1 = 0.15$ and $M_2 = 0.075$).

observed that configuration does not undergo instability for Weber number 57. It is found that for the set of parameters of the study, the critical Weber number value is 57, below which the configuration does not undergo instability. This is due to the fact that for Weber number less than 57, surface tension is sufficiently large to make the configuration stable. With increase in Weber number beyond 57, the configuration becomes unstable and undergoes instability. From the figures it can be seen that a mushroom shaped spike is formed in initial stage of instability which is similar for all the Weber numbers in the range of 100 to infinity. However, in later stage of instability, interface profiles and

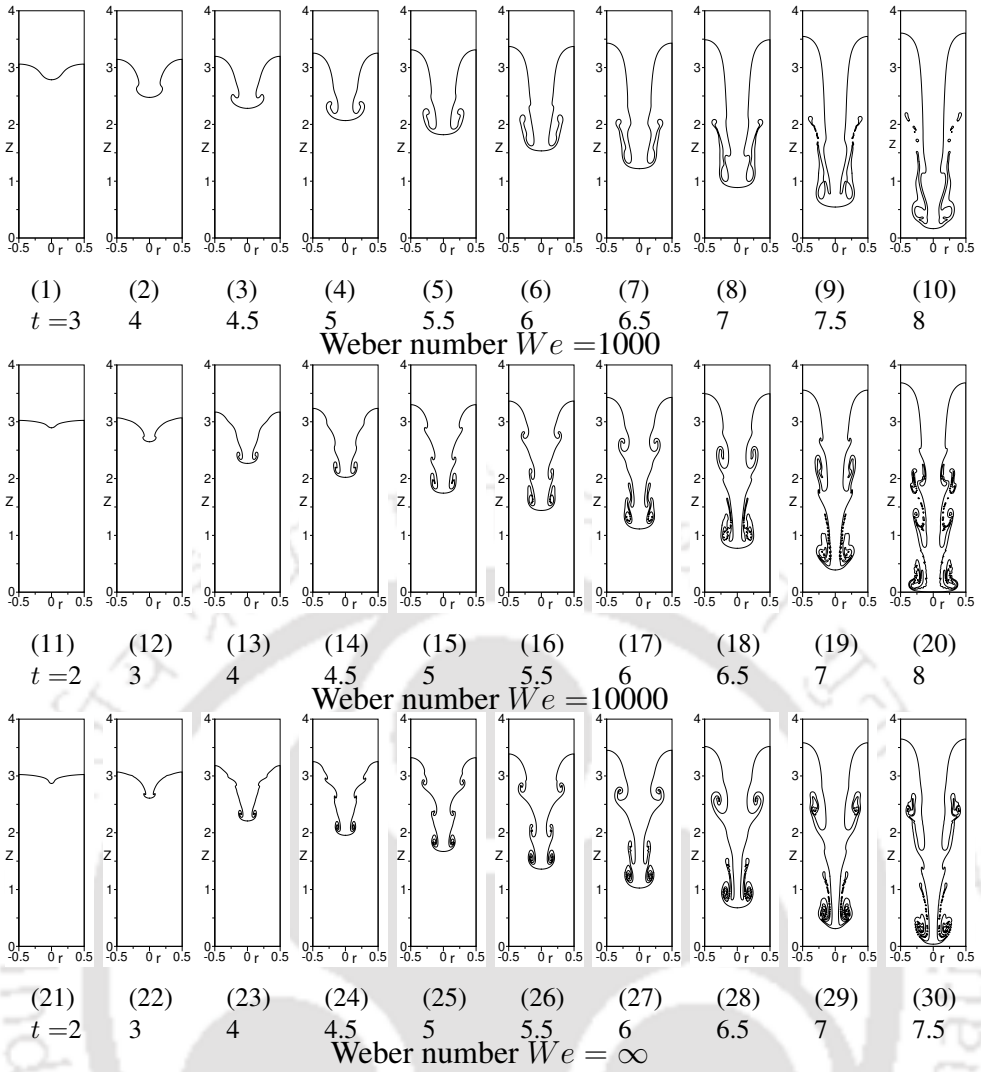

Figure 8.14: Interface profiles for Weber numbers in the range of $We = 1000$ to ∞ (rest of the parameters are: $\rho_r = 2$, $m = 2$, $k_r = 2$, $c_{p_r} = 2$, $Re = 50$, $Ma = 50$, $Fr = 1$, $r_T = 5$, $M_1 = 0.15$ and $M_2 = 0.075$).

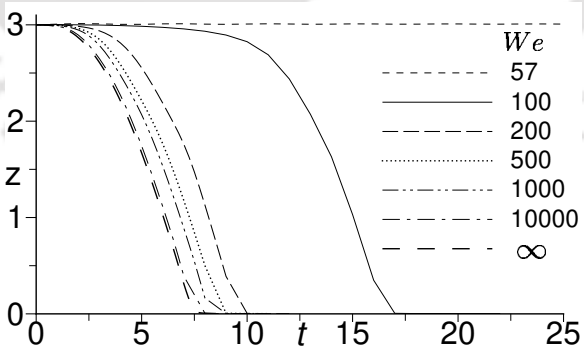

Figure 8.15: Time variation of spike front location for various Weber numbers (rest of the parameters are: $\rho_r = 2$, $m = 2$, $k_r = 2$, $c_{p_r} = 2$, $Re = 50$, $Ma = 50$, $Fr = 1$, $r_T = 5$, $M_1 = 0.15$ and $M_2 = 0.075$).

spike movement show significant difference from each other for different Weber numbers. For Weber number 100, heavier fluid forms a mushroom shaped spike with a short skirt attached to its spike head. With time, the distance between skirt location and spike head increases as the spike moves

towards the bottom wall. Spike moves faster and spike-skirt structure deforms more with increasing Weber number as surface tension decreases. For Weber number 200, the skirt becomes thinner and longer, and all the time the skirt is attached to the spike head unlike for Weber number 100 in which skirt moves away from spike head. With further increase of Weber number, the spike moves faster. For Weber number in the range of 500-1000, end portion of the skirt is broken into smaller pieces as the spike moves towards the bottom wall. For Weber number in the range of 10000 to infinity, multiple roll up structures form on the stem of the spike. These roll up skirt structures resemble the Kelvin-Helmholtz instability structure. The value of Weber number tending to infinity, surface tension tending to zero, represents an asymptotic behavior of the instability for low surface tension values. At high Weber number, representing low surface tension, such kind of Kelvin-Helmholtz instability structure is expected to form as discussed by Sharp in [18]. Overall, increasing Weber number beyond the critical value shows destabilizing effect on the instability.

Fig. 8.15 shows time variation of spike front location for various Weber numbers. Figure shows that beyond the critical value of Weber number 57, spike movement becomes faster with increasing Weber number. For example, for Weber number 100, the spike strikes the bottom wall at about dimensionless time $t = 17$, and for Weber number tends to infinity, the spike strikes the bottom wall at an asymptotic value at about dimensionless time $t = 7.5$ which is about 2.5 times faster. This confirms that beyond the critical value increasing Weber number shows destabilizing effect on the instability.

8.3.5 Effect of Froude number

The evolution of Rayleigh-Taylor instability for various Froude numbers in the range of 0.25 to 1.07 is presented in Fig. 8.16. From the figure, it can be observed that for Froude number 0.25, the top heavier fluid forms a mushroom-shaped spike. Later on, a thin elongated skirt attached to the tip of spike head forms. With time, the spike-skirt structure becomes more complex as the spike moves towards the bottom wall. Increase in Froude number results in a smoother spike-skirt structure with slower spike movement. For Froude number 0.5, a mushroom-shaped spike forms in initial stage of the instability. In later stage of the instability, the spike deforms into a thin and elongated skirt. With time, the skirt elongates more and covers more than half of the domain height, as seen in Figs. 8.16(17)-8.16(18).

Further increase in Froude number brings further changes in spike-skirt structure and its movement. For Froude number 0.75, skirt is formed on the spike head and the distance between spike head and skirt increases with time. With further increase in Froude number, the skirt becomes smaller in length and spike takes longer time to strike the bottom. This is due to fact that increase in Froude number represents decreased relative gravitational effect. The structure of the spike and skirt shows qualitative similarity for Froude numbers in the range of 0.75-1.06. For Froude number 1.07 or more, the configuration becomes stable. Hence, critical Froude number is 1.07, beyond which configuration does not undergo instability. Overall, increasing Froude number shows stabilizing effect on the instability.

Time variation of spike front location for various Froude numbers is shown in Fig. 8.17. The

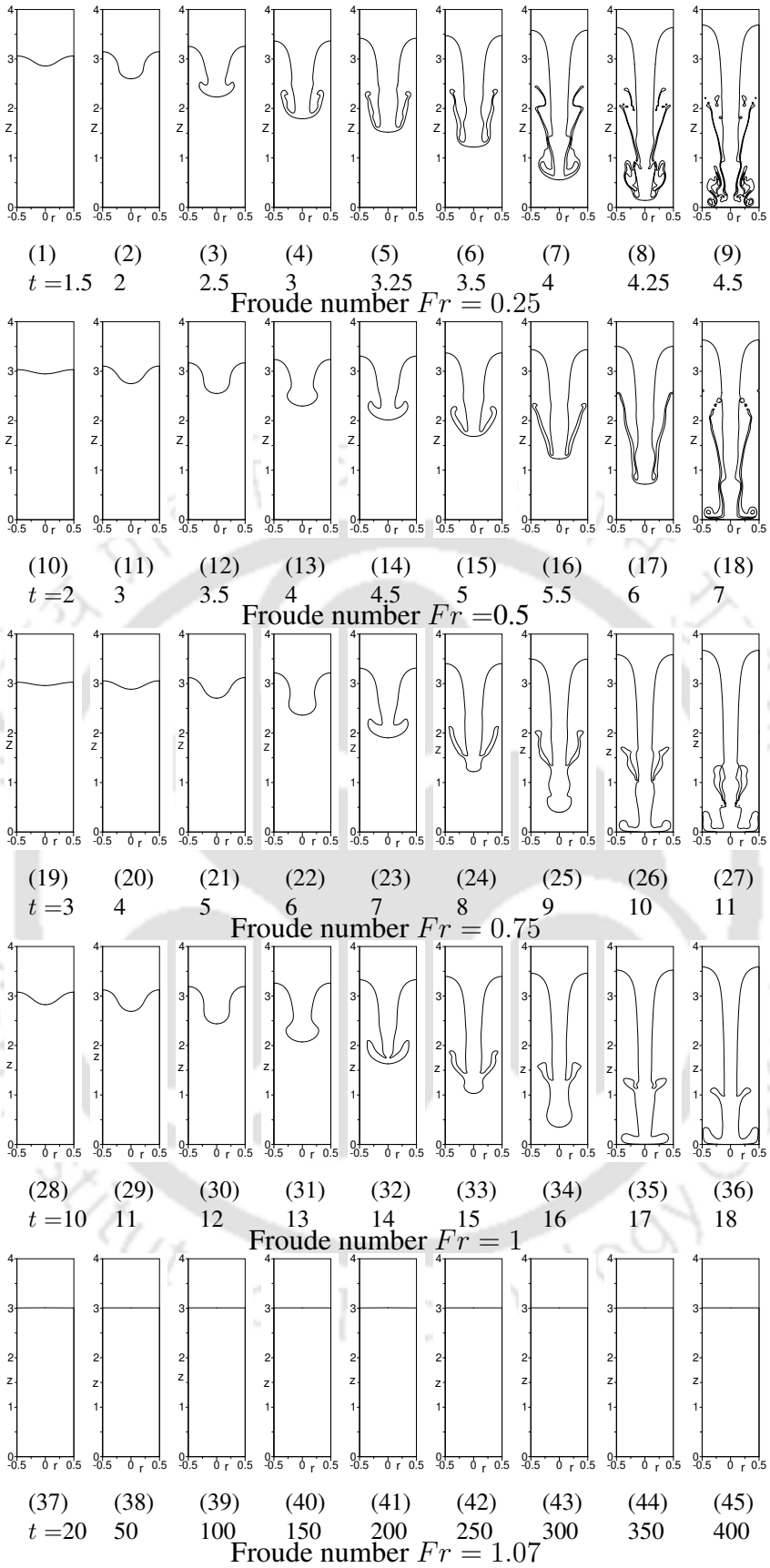

Figure 8.16: Instantaneous interface profiles for Froude numbers in the range of $Fr = 0.25$-1.07 (rest of the parameters are: $\rho_r = 2$, $m = 2$, $k_r = 2$, $c_{p_r} = 2$, $Re = 50$, $Ma = 50$, $We = 100$, $r_T = 5$, $M_1 = 0.15$ and $M_2 = 0.075$).

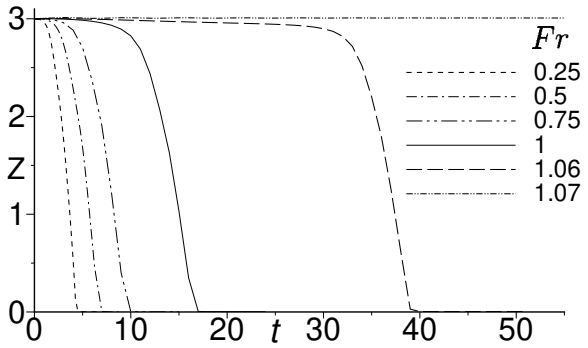

Figure 8.17: Time variation of spike front location for various Froude numbers (rest of the parameters are: $\rho_r = 2$, $m = 2$, $k_r = 2$, $c_{p_r} = 2$, $Re = 50$, $Ma = 50$, $We = 100$, $r_T = 5$, $M_1 = 0.15$ and $M_2 = 0.075$).

figure shows that the disturbance growth is found to be low in initial stage. In later stage of the instability, disturbance growth increases drastically and spike moves at faster rate. With increase in Froude number, time taken by the spike to strike the bottom wall increases and spike takes longer time to strike the bottom wall. For example, for Froude number 0.25 spike strikes the bottom wall at about dimensionless time $t = 4$, and for Froude number 1.06 spike strikes the bottom wall at about dimensionless time $t = 39$ which is almost 10 times slower.

8.4 Conclusions

Marangoni effect on axisymmetric Rayleigh-Taylor instability is studied in viscosity stratified fluid layers. Three types of functional dependency of surface tension on temperature, which are constant, linear and parabolic dependency, are considered for the study. The time taken by the spike to strike the bottom wall for the three types of surface tension dependency on temperature is found in the decreasing order of sequence of parabolic, constant and linear surface tension variation due to that the overall effective surface tension decreases in the above order of sequence. For the set of parameters of the study, time taken by the spike to strike the bottom wall decreases with temperature ratio in the range of 0 to 3, beyond which it increases. For temperature ratio more than 5.27, the configuration does not undergo instability. The non-monotonic variation of time variation of spike to strike the bottom wall with temperature ratio is due to the opposing stabilizing and destabilizing effects through increasing effective surface tension and decreasing effective viscosity, respectively, with increasing temperature ratio. For Weber number less than critical value of 57, the configuration is found to be stable. Above the critical value of Weber number, increasing Weber number results in destabilizing effect on the instability. For Weber number approaching infinity, multiple roll up structures resembling the Kelvin-Helmholtz instability structure is formed. Increasing Froude number shows stabilizing effect on Rayleigh-Taylor instability, and for Froude number greater than 1.07, the configuration does not undergo instability.

Chapter 9

Conclusions and future scope

In the present work, study of Rayleigh-Taylor instability in viscosity stratified fluid medium is carried out. The instability is studied for two dimensional rectangular as well as axisymmetric coordinate configurations using numerical simulations. In both the configurations, two viscous fluid layers, a heavier fluid layer is superposed over a lighter fluid layer, are sandwiched between two parallel isothermal solid walls. Out of the two walls, one wall is isothermally heated, while the other wall is isothermally cooled. In particular, the effect of stratification due to viscosity varying exponentially with temperature on the instability is studied. Effect of functional variation of viscosity with temperature on the instability is studied for both the configurations. Marangoni effect on the instability is studied under the influence of viscous stratification for both the configurations. From the observations of the results obtained from the present work, the major conclusions from various studies are as following.

9.1 Rayleigh-Taylor instability in viscosity stratified medium in 2-D rectangular coordinates

Rayleigh-Taylor instability is studied in viscous stratified two fluid layers in 2-D rectangular coordinates. Viscosity stratification effect on the instability is studied for fluid viscosity varying exponentially with temperature. Effect of viscosity ratio, temperature ratio, Weber number, Prandtl number and hot and cold wall locations on the instability is studied under the influence of viscosity stratification. Important conclusions drawn from the study are as following.

1. The configuration is more unstable in viscosity stratified fluid layers compared to that in constant viscosity fluid layers. This is because fluid viscosity decreases with temperature, making the flow more unstable.

2. In variable viscosity fluid layers, spike forms as a fluid column structure for viscosity ratio about 150 or higher, whereas in constant viscosity fluid layers, it occurs for viscosity ratio about 20 or higher.

3. An increase in viscosity ratio shows stabilizing effect on the instability. For example, for viscosity ratio 200, time taken by the spike to strike the bottom wall is increased to almost 4 times

compared to that of viscosity ratio 1.

4. For high temperature ratios, spike undergoes larger deformation and moves faster compared to that of low temperature ratios. For example, time taken by the spike to strike the bottom wall is reduced to almost half as temperature ratio is increased from 0 to 3.

5. Top heated wall configuration is more unstable than that of bottom heated wall configuration. In top heated wall configuration, rate of spike movement is almost 1.5 times faster than that in bottom heated wall configuration.

6. Effect of Prandtl number variation on the instability is negligible.

7. Critical Weber number value is about 0.1, below which configuration does not undergo instability. With increasing Weber number beyond the critical value, the instability occurs at faster rate.

8. For Weber number in the range of 0.1 to 39, the configuration undergoes instability and the spike comes down through one of the side vertical boundaries of the domain. In this range of Weber numbers, spatial periodicity of the instability is higher than that of the initial perturbation.

9. For Weber number beyond 39, the spike comes down through the mid vertical plane of the domain. In this range of Weber number, spatial periodicity of the instability is same as that of the initial perturbation.

9.2 Effect of functional variation of viscosity with temperature on Rayleigh-Taylor instability in 2-D rectangular coordinates

Rayleigh-Taylor instability is studied for the effect of four types of functional variation of viscosity with temperature in 2-D rectangular coordinates, which are constant, linear, power law and exponential variations. The study is carried out for viscosity ratios ranging from 2 to 200 and density ratios ranging from 2 to 50. Some of the important conclusions from the study are as following.

1. Type of viscosity variation with temperature shows strong effect on the instability at low viscosity ratios and low density ratios.

2. With increasing viscosity ratios and density ratios, effect of type of viscosity variation on the instability decreases.

3. For viscosity ratio about 100 or more, the spike structure is independent of type of viscosity variation.

4. For density ratio about 50 or more, the instability becomes independent of type of viscosity variation.

5. For a given type of viscosity variation, rate of spike movement increases with increasing density ratio and decreases with increasing viscosity ratio.

6. Rate of spike movement is in increasing order of sequence of power law, constant, linear and exponential variations, irrespective of viscosity ratios and density ratios. This is due to the fact that overall effective viscosity is in the decreasing order of sequence of power law, constant, linear and exponential variations.

9.3 Marangoni effect on Rayleigh-Taylor instability in viscosity stratified medium in 2-D rectangular coordinates

Marangoni effect on Rayleigh-Taylor instability in viscosity stratified fluid layers is studied in 2-D rectangular coordinates. Marangoni effect is studied for three types of functional dependencies of surface tension with temperature which are constant, linear and parabolic dependencies. The effect of Weber number and Froude number on the instability is studied in the presence of Marangoni effect. The major conclusions drawn from the study are as following.

1. Time taken by the spike to strike the bottom wall is in the decreasing order of sequence of constant, parabolic and linear dependencies. This trend is due to the fact that overall effective surface tension is highest for constant and lowest for linear dependencies.

2. Critical value of Weber number is about 0.55, below which the configuration is stable. This is because, for Weber number sufficiently small, strength of surface tension is sufficiently large for which the interface holds the heavier fluid layer over the lighter fluid layer. For Weber number beyond critical value, increasing Weber number shows destabilizing effect on the instability.

3. For Weber number in the range of 0.55 to 35, the spike comes down through one of the side vertical boundaries of the domain. In this range of Weber number, the spatial periodicity of the instability is higher than the spatial periodicity of the initial perturbation.

4. For Weber number higher than 35, the spike comes down through mid vertical plane of the domain. In this range of Weber number, the spatial periodicity of the instability is same as that of the initial perturbation.

5. For Weber number approaching infinity, the spike strikes the bottom wall at about a minimum asymptotic value of dimensionless time $t = 17$, which is almost 6 times lower than that of Weber number 9 which is about dimensionless time $t = 112$.

6. For Weber number number approaching infinity, surface tension approaches to zero, the spike forms with multiple branches of arms which resembles the Kelvin-Helmholtz instability like structure. Such irregular spike-arm structure is expected to form at high Weber numbers, represents low surface tension values, and is inline with the results in the literature.

7. For Froude number 0.5 or less, the spike forms with multiple branches of arms resembling the Kelvin-Helmholtz instability like structure. This results are in-line with the results in the literature.

8. Increasing Froude number shows stabilizing effect on the instability. Critical value of Froude number is about 11.5 above which the configuration does not undergo instability.

9.4 Rayleigh-Taylor instability in viscosity stratified medium in axisymmetric coordinates

Study of axisymmetric Rayleigh-Taylor instability is carried out in viscous stratified two fluid layers. Viscosity stratification effect on the instability is studied for viscosity varying exponentially with temperature. The instability is studied for the effect of different parameters such as viscosity ratio, temperature ratio, Weber number, Prandtl number and hot and cold wall locations under the influence of viscosity stratification. The major conclusions drawn from the study are as following.

1. The configuration is more unstable in viscosity stratified fluid layers compared to that in constant viscosity fluid layers. This is because fluid viscosity decreases with temperature which makes the flow more unstable.

2. The occurrence of spike penetration in the form of liquid column takes place at much higher viscosity ratio in temperature varying viscosity fluid layers compared to that in constant viscosity fluid layers.

3. Time taken by the spike to strike the bottom wall increases with increasing viscosity ratio showing stabilizing effect on the instability. For viscosity ratio 100, the time taken by the spike to strike the bottom wall is almost 3 times that of viscosity ratio 0.1.

4. Spike-skirt deformation and rate of spike movement increases with increasing temperature ratio. For temperature ratio 6, the spike strikes the bottom wall almost 2 times earlier than that of temperature ratio 0.

5. For top heated configuration, skirt on the spike head forms relatively thinner and longer, and configuration is more unstable than that of bottom heated configuration.

6. Effect of Prandtl number variation is negligible on the instability.

7. Critical Weber number value is about 55, below which the configuration does not undergoes instability. An increase in Weber number beyond the critical value shows destabilizing effect on the instability.

9.5 Effect of functional variation of viscosity with temperature on Rayleigh-Taylor instability in axisymmetric coordinates

Effect of functional variation of viscosity with temperature on axisymmetric Rayleigh-Taylor instability is studied for four types of functional variations of viscosity with temperature, which are constant, linear, power law and exponential variations. The study is carried out for viscosity ratios ranging from 0.5 to 100 and density ratios ranging from 1.5 to 20. The important conclusions drawn from the study are as following.

1. Type of viscosity variation with temperature shows strong effect on the instability at low density ratios and low viscosity ratios.
2. At high viscosity ratios, spike structure becomes independent of type of viscosity variation.
3. At high density ratios, the dynamics of instability become independent of type of viscosity variation.
4. For a given type of viscosity variation, increasing viscosity ratio shows stabilizing effect and increasing density ratio shows destabilizing effect on the instability.
5. Rate of spike movement is in decreasing order of sequence of exponential, linear, constant and power law variations for various viscosity and density ratios. This is because overall effective viscosity for the different types of viscosity variations are in increasing order of the above sequence.

9.6 Marangoni effect on Rayleigh-Taylor instability in viscosity stratified medium in axisymmetric coordinates

Marangoni effect on Rayleigh-Taylor instability is studied in viscosity stratified fluid layers in axisymmetric configuration. Marangoni effect is studied for three types of functional dependencies of surface tension with temperature which are constant, linear and parabolic dependencies. The effect of temperature ratio, Weber number and Froude number on the instability is studied in the presence of Marangoni effect. The major conclusions drawn from the study are as following.

1. The time taken by the spike to strike the bottom wall is in the decreasing order of sequence of parabolic, constant and linear dependencies due to that overall effective surface tension decreases in the above order of sequence.
2. Rate of spike movement increases with temperature ratio in the range of 0 to 3, beyond which it decreases. The non-monotonic variation of instability with temperature ratio is due to the opposing stabilizing and destabilizing effects through increasing effective surface tension and decreasing effective viscosity, respectively, with increasing temperature ratio.
3. Critical temperature ratio is about 5.27, beyond which the configuration is stable.

4. Critical Weber number is about 57, below which the configuration is stable. Beyond the critical Weber number, increasing Weber number shows destabilizing effect on the instability.

5. For Weber number approaching infinity, multiple roll-up structures resembling the Kelvin-Helmholtz instability structure are formed. This result is inline with the observation made in literature.

6. Increasing Froude number shows stabilizing effect on Rayleigh-Taylor instability. Critical Froude number is about 1.07, beyond which the configuration does not undergo instability.

9.7 Future scope

For the physics aspects of the work, the present study can be extended to the following studies.

1. Two dimensional Rayleigh-Taylor instability studies in rectangular coordinates can be extended to three dimensional rectangular coordinates.

2. Axisymmetric Rayleigh-Taylor instability studies can be extended to three dimensional cylindrical coordinates $(r - \theta - z)$.

3. Experimental studies can be carried out for Rayleigh-Taylor instability in viscosity stratified fluid layers.

4. Rayleigh-Taylor instability study in 2-D rectangular and axisymmetric coordinate configurations can be extended for visco-elastic fluid layers.

5. The study can be extended for Rayleigh-Taylor instability with mass transfer across the interface.

6. In the present work, Rayleigh-Taylor instability is carried out in 2-D rectangular coordinates with single mode of disturbance. Study can be extended for Rayleigh-Taylor instability with multi mode of disturbance in viscosity stratified fluid layers.

7. The effect of presence of magnetic and electrical fields on Rayleigh-Taylor instability is studied using linear stability analysis in various studies [27, 45, 46, 113]. Fully nonlinear Rayleigh-Taylor instability can be studied in the presence of magnetic and electrical fields using numerical simulations.

8. Rayleigh-Taylor instability in multiple fluid layers were carried out in various studies [120, 151, 176, 238]. Rayleigh-Taylor instability in multiple fluid layers with viscosity stratification can be studied in 2-D rectangular and axisymmetric coordinates.

9. Density stratification has shown a strong influence on Rayleigh-Taylor instability with turbulence for mixing effect [171]. Similarly, viscous stratification effect study on Rayleigh-Taylor instability with turbulence mixing can be carried out.

10. Rayleigh-Taylor instability in viscous fluid layers with oscillatory movement is known as Faraday instability which was studied in various studies in past [238–241]. Faraday instability in viscous stratified fluid layers can be studied.

In the present work, a code is developed for the solutions of multiphase flows. Simulations of some parts of the present study is carried out using the present developed code. The development of the present code can be extended to the following.

1. The present developed code can be extended to include the capabilities of Marangoni effect.
2. Multigrid method can be implemented to accelerate the solver to decrease the simulation time.
3. Present code is developed for 2-D rectangular coordinates. A code can be developed for axisymmetric coordinates.
4. The present code can also be extended for the simulations of three dimensional multiphase flows in rectangular as well as cylindrical coordinates.

References

[1] A. Salih, S. G. Moulic, Some numerical studies of interface advection properties of level set method, Sadhana 32 (2) (2009) 271–298.

[2] S. Vincent, J. P. Caltagirone, Test-case no 17: Dam-break flow on dry and wet surfaces, Multiphase Sci. Tech. 16 (2004) 273–280.

[3] J. K. Patel, G. Natarajan, A novel consistent and well-balanced algorithm for simulations of multiphase flows on unstructured grids, J. Comput. Phys. 350 (2017) 207–236.

[4] M. Sussman, P. Smereka, S. Osher, A level set approach for computing solutions to incompressible two-phase flow, J. Comput. Phys. 114 (1994) 146–159.

[5] S. Hysing, S. Turek, D. Kuzmin, N. Parolini, E. Burman, S. Ganesan, L. Tobiska, Quantitative benchmark computations of two-dimensional bubble dynamics, Int. J. Numer. Meth. Fluids 60 (2009) 1259–1288.

[6] L. Strubelj, I. Tiselj, Numerical simulation of Rayleigh–Taylor instability with two fluid model and interface sharpening, Proceedings of FEDSM, ASME Fluids Engineering Conference 2008 55063 (2008) 1–10.

[7] S. Popinet, S. Zaleski, A front tracking algorithm for accurate representation of surface tension driven interfacial flows, Int. J. Numer. Methods Fluids 30 (6) (1999) 775–793.

[8] E. G. Puckett, A. S. Almgren, J. B. Bell, D. L. Marcus, W. J. Rider, A high-order projection method for tracking fluid interfaces in variable density incompressible flows, J. Comput. Phys. 130 (1997) 269–282.

[9] A. Salih, S. G. Moulic, Simulation of Rayleigh–Taylor instability using level set method, Proceedings of NCFMFP2006, 3rd International Conference on Fluid Mechanics and Fluid Power IIT Bombay, India, December 7-9, 2006 55063 (2006) 1–10.

[10] S. Nas, G. Tryggvason, Thermocapillary interaction of two bubbles or drops, Int. J. Multiphase Flow 29 (2003) 1117–1135.

[11] D. Bhaga, M. E. Weber, Bubbles in viscous liquids: Shapes, wakes and velocities, J. Fluid Mech. 105 (1981) 61–85.

[12] M. K. Tripathi, K. C. Sahu, Motion of an air bubble under the action of thermocapillary and buoyancy forces, Comp. Fluids 177 (2018) 58–68.

[13] M. Sussman, P. Smereka, Axisymmetric free boundary problems, J. Fluid Mech. 341 (1997) 269–294.

[14] A. R. Premlata, M. K. Tripathi, K. C. Sahu, Dynamics of rising bubble inside a viscosity-stratified medium, Phys. Fluids 27 (2015) 1–15.

[15] C. Ma, D. Bothe, Direct numerical simulation of thermocapillary flow based on the volume of fluid method, Int. J. Multiphase Flow 37 (2011) 1045–1058.

[16] L. Rayleigh, Investigation of the character of the equilibrium of an incompressible heavy fluid of variable density, Proc. London Math. Soc. 14 (1883) 170–177.

[17] G. I. Taylor, The instability of liquid surfaces when accelerated in a direction perpendicular to their planes, Proc. R. Soc. London, Ser. A 201 (1065) (1950) 192–196.

[18] D. H. Sharp, An overview of Rayleigh–Taylor instability, Physica D 12 (1984) 3–18.

[19] S. B. Dalziel, Rayleigh–Taylor instability: experiments with image analysis, Dyn. Atmos. Oceans 20 (1993) 127–153.

[20] J. M. Burgess, A. Juel, W. D. McCormick, J. B. Swift, H. L. Swinney, Suppression of dripping from a ceiling, Phys. Rev. Lett. 86 (2001) 1–4.

[21] P. G. Drazin, Introduction to hydrodynamic stability, Cambridge University Press, London, (2002).

[22] S. A. Colgate, R. H. White, The hydrodynamic behavior of supernovae explosions, Astrophys. J. 143 (1966) 626–681.

[23] M. Zingale, S. E. Woosley, C. A. Rendleman, M. S. Day, J. B. Bell, Three-dimensional numerical simulations of Rayleigh–Taylor unstable flames in type ia supernovae, Astrophys. J. 632 (2005) 1021–1034.

[24] N. J. Hammer, H. T. Janka, E. Muller, Three-dimensional simulations of mixing instabilities in supernova explosions, Astrophys. J. 714 (2010) 1371–1385.

[25] B. Olson, Rayleigh–Taylor instability and fusion, http://large.stanford.edu/courses/2011/ph241/olson2/, [Online; accessed 20-April-2022] (2011).

[26] W. H. Cabot, A. W. Cook, Reynolds number effects on Rayleigh–Taylor instability with possible implications for type-Ia supernovae, Nature Phys. 2 (2006) 562–568.

[27] A. Hillier, The magnetic Rayleigh–Taylor instability in solar prominences, Rev. Mod. Plasma Phys. 2 (2018) 1–47.

[28] D. Telloni, F. Carbone, A. Bemporad, E. Antonucci, Evidence for Rayleigh–Taylor plasma instability at the front of solar coronal mass ejections, Atmosphere 10 (2019) 1–19.

[29] R. E. Marrs, K. Wira, Electromagnetic implosion of metal liners, J. Appl. Phys. 53 (1982) 230–236.

[30] Q. Sun, Y. Jia, Z. Zhang, W. Qin, N. Zhang, R. Zhou, W. Liu, Y. Chi, Q. Tian, B. Wei, X. Zhao, Z. Liu, Cylindrical metal liner implosion at extremes of pressure and material velocity on an intense pulsed power facility-FP-2, Rev. Sci. Instrum. 93 (2022) 1–13.

[31] X. He, R. Zhang, S. Chen, G. D. Doolen, On the three-dimensional Rayleigh–Taylor instability, Phys. Fluids 11 (1999) 1143–1152.

[32] S. N. Yakovenko, The effects of density difference and surface tension on the development of Rayleigh–Taylor instability of an interface between fluid media, Fluid Dyn. 49 (2014) 748–760.

[33] U. Alon, J. Hecht, D. Ofer, D. Shvarts, Power laws and similarity of Rayleigh–Taylor and Richtmyer-Meshkov mixing fronts at all density ratios, Phys. Rev. Lett. 74 (1995) 534–543.

[34] D. Oron, L. Arazi, D. Kartoon, A. Rikanati, U. Alon, D. Shvarts, Dimensionality dependence of the Rayleigh–Taylor and Richtmyer-Meshkov instabilitylate-time scaling laws, Phys. Plasmas 8 (6) (2001) 2883–2889.

[35] G. Dimonte, Dependence of turbulent rayleigh-taylor instability on initial perturbations, Phys. Rev. Lett. 69 (056305) (2004) 1–14.

[36] S. I. Sohn, Simple potential-flow model of Rayleigh–Taylor and Richtmyer-Meshkov instabilities for all density ratios, Phys. Rev. E 67 (2003) 1–5.

[37] B. J. Daly, Numerical study of two fluid Rayleigh–Taylor instability, Phys. Fluids 10 (297) (1967) 1–11.

[38] S. I. Sohn, S. Baek, Bubble merger and scaling law of the Rayleigh–Taylor instability with surface tension, Phys. Lett. A 381 (2017) 3812–3817.

[39] S. Chandrasekhar, Hydrodynamic and Hydromagnetic Stability, Oxford University Press, London, (1961).

[40] X. L. Li, Study of three dimensional Rayleigh–Taylor instabilities in compressible fluids through level set method and parallel computation, Phys. Fluids 5 (1993) 1–10.

[41] D. Livescu, Compressibility effects on the Rayleigh–Taylor instability growth between immiscible fluids, Phys. Fluids 16 (2004) 118–127.

[42] F. Chen, A. Xu, G. Zhang, Viscosity, heat conductivity and Prandtl number effects in Rayleigh–Taylor instability, Front. Phys. 11 (2016) 1–14.

[43] A. Mitra, R. Roychoudhury, M. Khan, Stabilization of Rayleigh–Taylor instability in the presence of viscosity and compressibility: A critical analysis, Phys. Plasmas 23 (2016) 1–6.

[44] D. Hartmann, T. Colonius, A projection approach for multiphase flows, Proceedings of AIAACFD2011, 20th AIAA Computational Fluid Dynamics Conference, Honolulu, Hawaii, June 27–30, 2011 3831 (2011) 1–12.

[45] L. L. Barannyk, D. T. Papageorgiou, P. G. Petropoulos, Suppression of Rayleigh–Taylor instability using electric fields, Math. Comput. Simul. 82 (2012) 1008–1016.

[46] M. K. Awasthi, D. Yadav, G. S. Agrawal, Viscous potential flow analysis of electrohydrodynamic Rayleigh–Taylor instability, J. Appl. Fluid Mech. 7 (2014) 209–216.

[47] F. Yang, A. Khodak, H. A. Stone, The effects of a horizontal magnetic field on the Rayleigh–Taylor instability, Nucl. Mater. Energy 18 (2019) 175–181.

[48] G. Dimonte, P. Ramaprabhu, M. J. Andrews, Rayleigh–Taylor instability with complex acceleration history, Phys. Rev. E 72 (2007) 1–6.

[49] D. Aslangil, A. Banerjee, Numerical investigation of initial condition effects on Rayleigh–Taylor instability with acceleration reversals, Phys. Rev. E 94 (2016) 1–16.

[50] D. Livescu, Turbulence with large thermal and compositional density variations, Annu. Rev. Fluid Mech. 52 (2020) 309–41.

[51] D. Aslangil, D. Livescu, A. Banerjee, Effects of atwood and reynolds numbers on the evolution of buoyancy-driven homogeneous variable-density turbulence, J. Fluid Mech. 895 (2020) 12–34.

[52] A. Sameen, R. Govindarajan, The effect of wall heating on instability of channel flow, J. Fluid Mech. 577 (2007) 417–442.

[53] V. T. S. R. K. Reddy, V. M. Janardhanan, K. C. Sahu, Effects of wall-heating on the linear instability characteristics of pressure-driven two-layer channel flow, Chem. Eng. Sci. 66 (2011) 6272–6279.

[54] J. J. Riley, M. P. Lelong, Fluid motions in the presence of strong stable stratification, Annu. Rev. Fluid Mech. 32 (2000) 613–657.

[55] C. Beal, The viscosity of air, water, natural gas, crude oil and its associated gases at oil field temperatures and pressures, Trans. AIME 65 (1946) 94–115.

[56] A. G. Nouri, P. Givi, D. Livescu, Modeling and simulation of turbulent nuclear flames in type Ia supernovae, Prog. Aerosp. Sci. 108 (2019) 156–179.

[57] T. V. Gerya, D. A. Yuen, Rayleigh–Taylor instabilities from hydration and melting propel cold plumes at subduction zones, Earth Planet. Sci. Lett. 212 (2003) 47–62.

[58] M. L. Rudolph, V. Leki, C. L. Bertelloni, Viscosity jump in Earth's mid-mantle, Science 350 (2015) 1349–1952.

[59] L. Landau, D. Lifshitz, Fluid Mechanics, Pergamon, New York, 1959.

[60] O. A. Hougen, K. M. Watson, Chemical Process Principles Charts, Wiley, New York, (1960).

[61] F. M. White, Viscous Fluid Flow, McGraw-Hill, New Delhi, 2016.

[62] Y. A. Cengel, J. M. Cimbala, Fluid Mechanics: Fundamental and Applications, Mcgraw-Hill, New Delhi, (2012).

[63] F. M. White, Fluid Mechanics, McGraw-Hill, New Delhi, 2016.

[64] R. Nahme, Beitrage zur hydrodynamischen theorie der lagerreibung, Ingenieur Arch. 11 (1940) 191–209.

[65] A. Costa, G. Macedonio, Viscous heating effects in fluids with temperature-dependent viscosity: triggering of secondary flows, J. Fluid Mech. 540 (2005) 21–38.

[66] A. Pinarbasi, A. Liakopoulos, The role of variable viscosity in the stability of the channel flow, Int. Comm. Heat Mass Transfer 22 (1995) 837–847.

[67] D. P. Wall, S. K. Wilson, The linear stability of channel flow of fluid with temperature-dependent viscosity, J. Fluid Mech. 323 (1996) 107–132.

[68] M. T. Ghannam, M. N. Esmail, Rheological properties of carboxymethyl cellulose, J. Appl. Polym. Sci. 64 (1997) 289–305.

[69] K. C. Sahu, O. K. Matar, Stability of plane channel flow with viscous heating, ASME J. Fluids Eng. 132 (2010) 1–7.

[70] R. Govindarajan, K. C. Sahu, Instabilities in viscosity-stratified flow, Annu. Rev. Fluid Mech. 46 (2014) 331–353.

[71] P. Ramaprabhu, G. Dimonte, P. Woodward, C. Fryer, G. Rockefeller, K. Muthuraman, P. H. Lin, J. Jayaraj, The late-time dynamics of the single-mode Rayleigh–Taylor instability, Phys. Fluids 24 (074107) (2012) 1–21.

[72] P. Ramaprabhu, V. Karkhanis, R. Banerjee, H. Varshochi, M. Khan, A. G. W. Lawrie, Evolution of the single-mode Rayleigh–Taylor instability under the influence of time-dependent accelerations, Phys. Rev. E 93 (2016) 1–17.

[73] M. K. Tripathi, K. C. Sahu, G. Karapetsas, K. Sefiane, O. K. Matar, Non-isothermal bubble rise: non-monotonic dependence of surface tension on temperature, J. Fluid Mech. 763 (2015) 82–108.

[74] R. Betti, J. Sanz, Bubble acceleration in the ablative Rayleigh–Taylor instability, Phys. Rev. Lett. 97 (205002) (2006) 1–4.

[75] M. Balla, M. K. Tripathi, K. C. Sahu, G. Karapetsas, O. K. Matar, Non-isothermal bubble rise dynamics in a self-rewetting fluid: three-dimensional effects, J. Fluid Mech. 858 (2019) 689–713.

[76] J. S. Dhiman, N. Sharma, Effect of temperature dependent viscosity on thermal convection of nanofluids: Steady case, J. Thermophys Heat Transfer 29 (2015) 90–101.

[77] K. C. Sahu, R. Govindarajan, Instabilities in viscosity-stratified flow, Annu. Rev. Fluid Mech. 46 (2014) 331–353.

[78] S. Bair, Pressure-viscosity behavior of lubricants to 1.4 GPa and its relation to EHD traction, Tribol. Transac. 43 (2000) 91–99.

[79] S. Bair, A critical evaluation of film thickness-derived pressure-viscosity coefficients, Lubricat Sci. 27 (2015) 337–346.

[80] J. M. Tsangaris, R. B. Martin, Viscosities of aqueous solutions of di-polar ions, Arch. Biochem. Biophys. 112 (1965) 267–272.

[81] T. S. Banipal, S. Gagandeep, Effect of temperature and concentration on the viscosity of aqueous solutions of 3-amino propanoic acid, 4-amino butanoic acid, 5-amino pentanoic acid, 6-amino hexanoic acid, Thermochim. Acta. 412 (2004) 63–83.

[82] C. M. Romero, A. Beltrn, Effect of temperature and concentration on the viscosity of aqueous solutions of 3-amino propanoic acid, 4-amino butanoic acid, 5-amino pentanoic acid, 6-amino hexanoic acid, Rev. Colomb. Qum. 41 (2012) 123–131.

[83] J. R. A. Pearson, Mechanics of Polymer Processing, Elsevier, London, (1985).

[84] J. C. Beale, R. D. Reitz, Modeling spray atomization with the Kelvin-Helmholtz/Rayleigh–Taylor hybrid model, Atomization Sprays 9 (1999) 623–650.

[85] J. E. Smith, C. R. W. Gillham, Effects of solute concentration-dependent surface tension on unsaturated flow: Laboratory sand column experiments, Water Resour. Res. 35 (1999) 973–982.

[86] N. O. Young, J. S. Goldstein, M. J. Block, The motion of bubbles in a vertical temperature gradient, J. Fluid Mech. 6 (1959) 350–356.

[87] H. H. Hariri, Q. Shi, A. Borhan, Thermocapillary motion of deformable drops at finite Reynolds and Marangoni numbers, Phys. Fluids 9 (1997) 845–855.

[88] M. Herrmann, J. M. Lopez, P. Brady, M. Raessi, Thermocapillary motion of deformable drops and bubbles, Proceedings of the 2008 Summer Program Center for Turbulence Research, Center for Turbulence Research Conference 2008 (2008) 155–170.

[89] Y. Sui, Moving towards the cold region or the hot region? thermocapillary migration of a droplet attached on a horizontal substrate, Phys. Fluids 26(092102) (2014) 1–19.

[90] I. Seric, S. Afkhami, L. Kondic, Direct numerical simulation of variable surface tension flows using a volume-of-fluid method, J. Comput. Phys. 352 (2018) 615–636.

[91] P. T. Brady, M. Herrmann, J. M. Lopez, Confined thermocapillary motion of a three-dimensional deformable drop, Phys. Fluids 23 (022101) (2011) 1–11.

[92] M. Balla, M. K. Tripathi, K. C. Sahu, G. Karapetsas, O. K. Matar, Non-isothermal bubble rise dynamics in a self-rewetting fluid: three-dimensional effects, J. Fluid Mech. 858 (2019) 689–713.

[93] M. Muradoglu, G. Tryggvason, A front-tracking method for computation of interfacial flows with soluble surfactants, J. Comput. Phys. 227 (2008) 2238–2262.

[94] N. Adami, H. Caps, Capillary-driven two-dimensional buoyancy in vertical soap films, Europhys. Lett. 106 (2014) 1–5.

[95] G. Petre, M. A. Azouni, Experimental evidence for the minimum of surface tension with temperature at aqueous alcohol solution air interfaces, J. Colloid Interface Sci. 98 (1984) 261–263.

[96] Y. Abe, A. Iwaski, K. Tanaka, Microgravity experiments on phase change of self-rewetting fluids, Ann. New York Acad. Sci. 1027 (2004) 269–285.

[97] A. D. Myshkis, V. G. Babskii, N. D. Kopachevskii, L. A. Slobozhanin, A. D. Tyuptsov, Low Gravity Fluid Mechanics, Springer-Verlag, Berlin, (1987).

[98] J. B. Fournier, A. M. Cazabat, Tears of wine, Europhys. Lett. 20 (1992) 517–522.

[99] M. S. Plesset, C. G. Whipple, Viscous effects in Rayleigh–Taylor instability, Phys. Fluids 17 (1974) 1–7.

[100] H. Takabe, K. Mima, L. Montierth, R. L. Morse, Self-consistent growth rate of the Rayleigh–Taylor instability in an ablatively accelerating plasma, Phys. Fluids 3676 (1985) 1–7.

[101] L. A. D. Orozco, J. E. A. Rosas, Rayleigh–Taylor instability of a continuously stratified fluid under a general rotation field, Phys. Fluids 1 (1989) 1192–1199.

[102] R. Banerjee, L. Mandal, S. Roy, M. Khan, M. R. Gupta, Combined effect of viscosity and vorticity on single mode Rayleigh–Taylor instability bubble growth, Phys. Plasmas 18 (2011) 1–5.

[103] A. Kord, J. Capecelatro, Optimal perturbations for controlling the growth of a Rayleigh–Taylor instability, J. Fluid Mech. 876 (2019) 150–185.

[104] R. Menikoff, R. C. Mjolsness, D. H. Sharp, C. Zemach, Unstable normal mode for Rayleigh–Taylor instability in viscous fluids, Phys. Fluids 20 (2000) 1–5.

[105] P. Clavin, F. Williams, Asymptotic spike evolution in Rayleigh–Taylor instability, J. Fluid Mech. 525 (2005) 105–113.

[106] S. Gerashchenko, D. Livescu, Viscous effects on the Rayleigh–Taylor instability with background temperature gradient, Phys. Plasmas 23 (2016) 1–14.

[107] S. I. Sohn, Effects of surface tension and viscosity on the growth rates of Rayleigh–Taylor and Richtmyer-Meshkov instabilities, Phys. Rev. E 80 (2009) 1–5.

[108] K. O. Mikaelian, Exact, approximate, and hybrid treatments of viscous Rayleigh–Taylor and Richtmyer-Meshkov instabilities, Phys. Rev. E 99 (2019) 1–20.

[109] N. Rudraiah, R. D. Mathod, H. Betigeri, The Rayleigh–Taylor instability of a viscous fluid layer with viscosity stratification, Curr. Sci. 72 (1997) 391–395.

[110] A. R. Piriz, O. D. Cortzar, J. J. L. Cela, N. A. Tahir, The Rayleigh–Taylor instability, Am. J. Phys. 74 (2006) 1095–1098.

[111] C. Xie, J. Tao, J. Li, Viscous Rayleigh–Taylor instability with and without diffusion effect, Int. J. Appl. Math. Mech. -Engl. Ed. 38 (2017) 263–270.

[112] F. E. M. Silveira, H. I. Orlandi, Viscous-resistive layer in Rayleigh–Taylor instability, Phys. Plasmas 24 (2017) 1–6.

[113] Y. B. Sun, C. Wang, Viscous Rayleigh–Taylor and Richtmyer-Meshkov instabilities in the presence of a horizontal magnetic field, Phys. Rev. E 101 (2020) 1–12.

[114] H. Yu, D. Livescu, Rayleigh–Taylor instability in cylindrical geometry with compressible fluids, Phys. Fluids 20 (2008) 104–103.

[115] J. R. Lister, R. C. Kerr, N. J. Russel, A. Crosby, Rayleigh–Taylor instability of an inclined buoyant viscous cylinder, J. Fluid Mech. 671 (2011) 313–338.

[116] G. Balestra, N. Kofman, P. T. Brun, B. Scheid, F. Gallaire, Three-dimensional Rayleigh–Taylor instability under a unidirectional curved substrate, J. Fluid Mech. 837 (2018) 19–47.

[117] Y. Zheng, Y. Lai, Y. Hu, S. Cai, Rayleigh–Taylor instability in in a confined elastic soft cylinder, J. Mech. Phys. Solids 131 (2019) 221–229.

[118] D. Y. Hsieh, Interfacial stability with mass and heat transfer, Phys. Fluids 21 (1978) 745–748.

[119] S. P. Ho, Linear Rayleigh–Taylor stability of viscous fluids with mass and heat transfer, J. Fluid Mech. 101 (1980) 111–128.

[120] S. Parhi, G. Nath, A sufficient criterionn for Rayleigh–Taylor instability of incompressible viscous three layer flow, Int. J. Engng Sci. 29 (1991) 1439–1450.

[121] K. A. Khodaparast, M. Kawaji, B. N. Antar, The Rayleigh–Taylor and Kelvin–Helmholtz stability of a viscous liquid–vapor interface with heat and mass transfer, Phys. Fluids 7 (1995) 202–208.

[122] M. K. Awasthi, V. K. Srivastava, Study on electrohydrodynamic Rayleigh–Taylor instability with heat and mass transfer, Sci. World J. 2014 (2014) 1–8.

[123] V. V. Konovalov, D. V. Lyubimov, T. P. Lyubimova, The Rayleigh–Taylor instability of the externally cooled liquid lying over a thin vapor film coating the wall of a horizontal plane heater, Phys. Fluids 28 (2016) 1–34.

[124] V. N. Goncharov, Analytical model of nonlinear, single-mode, classical Rayleigh–Taylor instability at arbitrary Atwood numbers, Phys. Rev. Lett. 13 (2002) 1–4.

[125] D. Layzer, On the instability of superposed fluids in a gravitational field, Astrophys. J. 122 (1955) 1–12.

[126] M. K. Awasthi, Viscous corrections for the viscous potential flow analysis of Rayleigh-Taylor instability with heat and mass transfer, ASME J. Heat Transfer 135 (071701) (2013) 1–8.

[127] D. Y. Hsieh, Interfacial stability with mass and heat transfer, Phys. Fluids 22 (1979) 1435–1439.

[128] D. Y. Hsieh, S. P. Ho, Rayleigh–Taylor stability with mass and heat transfer, Phys. Fluids 24 (1981) 202–208.

[129] M. K. Awasthi, R. Asthana, G. S. Agrawal, Viscous potential flow analysis of nonlinear Rayleigh–Taylor instability with heat and mass transfer, Microgravity Sci. Technol. 24 (2012) 351–363.

[130] A. R. Seadwy, K. E. Rashidy, Nonlinear Rayleigh–Taylor instability of the cylindrical fluid flow with mass and heat transfer, Pramana J. Phys. 87 (2016) 1–9.

[131] M. R. Gupta, L. Mandal, S. Roy, M. Khan, Effect of magnetic field on temporal development of Rayleigh–Taylor instability induced interfacial nonlinear structure, Phys. Plasmas 17 (2010) 1–12.

[132] K. I. Read, Experimental investigation of turbulent mixing by Rayleigh–Taylor instability, Physica D 12 (1984) 45–58.

[133] D. L. Youngs, Numerical simulation of turbulent mixing by Rayleigh–Taylor instability, Physica D 12 (1989) 32–34.

[134] J. Andrews, D. B. Spalding, A simple experiment to investigate two-dimensional mixing by Rayleigh–Taylor instability, Phys. Fluids 2 (922) (1990) 1–6.

[135] G. Dimonte, M. Schneider, Density ratio dependence of Rayleigh–Taylor mixing for sustained and impulsive acceleration histories, Phys. Fluids 12 (2) (2000) 1–21.

[136] S. B. Dalziel, M. D. Patterson, C. P. Caulfield, I. A. Coomaraswamy, Mixing efficiency in high-aspect-ratio Rayleigh–Taylor experiments, Phys. Fluids 20 (2008) 1–14.

[137] D. H. Olson, J. W. Jacobs, Experimental study of Rayleigh–Taylor instability with a complex initial perturbation, Phys. Fluids 21 (034103) (2009) 1–13.

[138] M. J. Andrews, S. B. Dalziel, Small Atwood number Rayleigh–Taylor experiments, Phil. Trans. R. Soc. A 368 (2010) 1663–1679.

[139] K. A. Baldwin, M. M. Scase, R. J. A. Hill, The inhibition of the Rayleigh–Taylor instability by rotation, Sci. Rep. 5 (2002) 117–126.

[140] V. Tsiklashvili, P. E. R. Colio, O. A. Likhachev, J. W. Jacobs, An experimental study of small Atwood number Ryleigh-Taylor instability using the magnetic levitation of paramagnetic fluids, Phys. Fluids 24 (2012) 1263–1273.

[141] R. V. Morgan, O. A. Likhachev, J. W. Jacobs, Rarefaction-driven Rayleigh–Taylor instability. Part 2. Diffuse-interface linear stability measurements and theory, J. Fluid Mech. 791 (2016) 34–60.

[142] R. V. Morgan, W. H.Cabot, J. A. Greenough, J. W. Jacobs, Rarefaction-driven Rayleigh–Taylor instability. Part 2. Experiments and simulations in the nonlinear regime, J. Fluid Mech. 838 (2018) 320–355.

[143] A. Blair, N. Metropolis, J. Neuman, A. H. Taub, M. Tsingou, A study of a numerical solution to a two-dimensional hydrodynamic problem, Proc. Am. Math. Soc. 13 (145) (1959) 1–10.

[144] G. Tryggvason, S. O. Unverdi, Computations of three-dimensional Rayleigh–Taylor instability, Phys. Fluids 2 (1990) 656–665.

[145] L. A. Newhouse, C.Pozrikids, The Rayleigh–Taylor instability of a viscous liquid layer resting on a plane wall, J. Fluid Mech. 217 (1990) 615–638.

[146] X. L. Li, B. X. Jin, J. Glimm, Numerical study for the three-dimensional Rayleigh–Taylor instability through the TVD/AC scheme and parallel computation, J. Comput. Phys. 169 (1996) 343–355.

[147] J. Glimm, J. W. Grove, X. L. Li, W. Oh, D. H. Sharp, A critical analysis of Rayleigh–Taylor growth rates, J. Comput. Physics 169 (2001) 652–677.

[148] A. Celani, A. Mazzino, P. M. Ginanneschi, L. Vozella, Phase-field model for the Rayleigh–Taylor instability of immiscible fluids, J. Fluid Mech. 622 (2009) 115–134.

[149] N. J. Mueschke, O. Schilling, Investigation of Rayleigh–Taylor turbulence and mixing using direct numerical simulation with experimentally measured initial conditions. I. comparison to experimental data, Phys. Fluids 21 (2009) 1–19.

[150] A. Banerjee, M. J. Andrews, 3D simulations to investigate initial condition effects on the growth of Rayleigh–Taylor mixing, Int. J. Heat Mass Transfer 52 (2009) 3906–3917.

[151] H. G. Lee, K. Kim, J. Kim, On the long time simulation of the Rayleigh-Taylor instability, Int. J. Numer. Meth. Engng 85 (2011) 1633–1647.

[152] S. Popinet, A quadtree-adaptive multigrid solver for the Serre-Green-Naghdi equations, J. Comput. Phys. 302 (2015) 336–358.

[153] G. R. Baker, D. I. Meiron, S. A. Orszag, Vortex simulations of the Rayleigh–Taylor instability, Phys. Fluids 23 (1980) 1485–1490.

[154] G. Birkhoff, D. Carter, Rising plane bubbles, J. Math. Mech. 6 (1951) 769–779.

[155] P. Ramaprabhu, G. Dimonte, Single-mode dynamics of the rayleigh-taylor instability at any density ratio, Phys. Rev. E 71 (036314) (2005) 1–9.

[156] N. N. Anuchina, V. I. Volkov, V. A. Gordeychuk, N. S. Eskov, O. S. Ilyutina, O. M. Kozyrev, Numerical simulations of Rayleigh–Taylor and Richtmyer-Meshkov instability using MAH-3 code, J. Comput. Appl. Math. 168 (2004) 11–20.

[157] H. G. Lee, J. Kim, Numerical simulation of the three-dimensional Rayleigh–Taylor instability, Comput Math Appl. 66 (2013) 1466–1474.

[158] K. O. Mikaelian, Reshocks, rarefactions, and the generalized Layzer model for hydrodynamic instabilities, Phys. Fluids 21 (2009) 1–16.

[159] J. P. Wilkinson, J. W. Jacobs, Experimental study of the single-mode three-dimensional Rayleigh–Taylor instability, Phys. Fluids 19 (124102) (2007) 1–11.

[160] H. J. Kull, Theory of the Rayleigh–Taylor instability, Phys. Reports 206 (1991) 197–325.

[161] S. I. Abarzhi, Review of theoretical modelling approaches of Rayleigh–Taylor instabilities and turbulent mixing, Phil. Trans. R. Soc. A 368 (2010) 1809–1828.

[162] G. Boffetta, A. Mazzino, Incompressible Rayleigh–Taylor turbulence, Annu. Rev. Fluid Mech. 49 (2017) 119–143.

[163] Y. Zhou, Rayleigh–Taylor and Richtmyer-Meshkov instability induced flow, turbulence, and mixing I, Phys. Reports 720–722 (2017) 1–136.

[164] Y. Zhou, Rayleigh–Taylor and Richtmyer-Meshkov instability induced flow, turbulence, and mixing II, Phys. Reports 723–725 (2017) 1–160.

[165] C. P. Caulfield, Layering, instabilities, and mixing in turbulent stratified flows, Annu. Rev. Fluid Mech. 53 (2021) 113–145.

[166] A. Banerjee, Rayleigh–Taylor instability: A status review of experimental designs and measurement diagnostics, ASME J. Fluids Eng. 142 (2020) 1–17.

[167] N. J. Mueschke, M. J. Andrews, O. Schilling, Experimental characterization of initial conditions and spatio-temporal evolution of a small Atwood number Rayleigh–Taylor mixing layer, J. Fluid Mech. 567 (2006) 27–63.

[168] A. Elgowainy, N. Ashgriz, The Rayleigh–Taylor instability of viscous fluid layers, Phys. Fluids 9 (1997) 1635–1649.

[169] H. Sweeney, R. R. Kerswell, T. Mullin, Rayleigh–Taylor instability in a finite cylinder: linear stability analysis and long-time fingering solutions, J. Fluid Mech. 734 (2013) 338–362.

[170] J. T. Waddell, C. E. Niederhaus, J. W. Jacobs, Experimental study of Ryleigh-Taylor instability: Low Atwood number liquid systems with single-mode initial perturbations, Phys. Fluids 13 (2001) 1263–1273.

[171] M. S. D. Wykes, S. B. Dalziel, Efficient mixing in stratified flows: experimental study of a Rayleigh–Taylor unstable interface within an otherwise stable stratification, J. Fluid Mech. 756 (2014) 1027–1057.

[172] Y. Wang, C. Shu, L. M. Yang, An improved multiphase lattice Boltzmann flux solver for three-dimensional flows with large density ratio and high Reynolds number, Phys. Fluids 302 (2015) 41–58.

[173] S. J. Walters, L. K. Forbes, Fully 3-D Rayleigh–Taylor instability in a Boussinesq fluid, Anjiam J. 0 (2019) 1–6.

[174] X. Bian, H. Aluie, D. Zhao, H. Zhang, D. Livescu, Revisiting the late-time growth of single-mode Rayleigh–Taylor instability and the role of vorticity, Physica D 132250 (2019) 1–22.

[175] Y. N. Young, H. Tufo, A. Dubey, R. Rosner, On the miscible Rayleigh–Taylor instability: two and three dimensions, J. Fluid Mech. 447 (2001) 377–408.

[176] H. Li, Y. Yap, J. Lou, Z. Shang, Numerical investigation of heat transfer in three-fluid stratified flows, Int. J. Heat Mass Transfer 89 (2015) 576–587.

[177] K. V. Manu, P. Deshmukh, S. Basu, Rayleigh–Taylor instability in a thermocline based thermal storage tank, Int. J. Therm. Sci. 100 (2016) 333–345.

[178] H. Z. Yuan, C. Shu, Y. Wang, S. Shu, A simple mass-conserved level set method for simulation of multiphase flows, Phys. Fluids 30 (2018) 1–13.

[179] H. Liang, X. Hu, X. Huang, J. Xu, Direct numerical simulations of multi-mode immiscible Rayleigh–Taylor instability with high reynolds numbers, Phys. Fluids 31 (2019) 1–14.

[180] D. L. Youngs, Three-dimensional numerical simulation of turbulent mixing by Rayleigh–Taylor instability, Phys. Fluids A 3 (5) (1991) 1312–1320.

[181] J. L. Guermond, L. Quartapelle, A projection FEM for variable density incompressible flows, J. Comput. Phys. 165 (2000) 167–188.

[182] P. H. Chiu, Y. T. Lin, A conservative phase field method for solving incompressible two-phase flows, J. Comput. Phys. 230 (2011) 185–204.

[183] E. E. Meshkov, S. I. Abarzhi, Group theory and jellys experiment of Rayleigh–Taylor instability and Rayleigh–Taylor interfacial mixing, Fluid Dyn. Res. 51 (2019) 1–34.

[184] Y. Wang, C. Shu, H. B. Huang, C. J. Teo, Multiphase lattice Boltzmann flux solver for incompressible multiphase flows with large density ratio, J. Comput. Phys. 280 (2015) 404–423.

[185] G. Liu, Z. Guo, Effects of prandtl number on mixing process in miscible Rayleigh–Taylor instability, Int. J. Numer. Methods Heat Fluid Flow 23 (2013) 176–188.

[186] Y. J. Chou, F. C. Wu, W. R. Shih, Toward numerical modeling of fine particle suspension using a two-way coupled Euler-Euler model: Part 2: Simulation of particle-induced Rayleigh–Taylor instability, Int. J. Multiphase Flow 64 (2014) 44–54.

[187] A. Hamzehloo, P. Bartholomew, S. Laizet, Direct numerical simulations of incompressible Rayleigh–Taylor instabilities at low and medium atwood numbers, Phys. Fluids 33 (2021) 1–23.

[188] A. G. W. Lawrie, S. B. Dalziel, Rayleigh–Taylor mixing in an otherwise stable stratification, J. Fluid Mech. 688 (2011) 507–527.

[189] A. A. Gonzalez, L. M. G. Gutierrez, Effects of a semi-infinite stratification on the Rayleigh–Taylor instability in an interface with surface tension, AIP Adv. 7 (2017) 1–19.

[190] D. Aslangil, D. Livescu, A. Banerjee, Variable-density buoyancy-driven turbulence with asymmetric initial density distribution, Phys. D: Nonlinear Phenom. 406 (2020) 132–144.

[191] D. M. Snider, M. J. Andrews, Rayleigh–Taylor and shear driven mixing with an unstable thermal stratification, Phys. Fluids 6 (1994) 3324–3334.

[192] P. Ramaprabhu, V. Karkhanis, A. G. W. Lawrie, Rayleigh–Taylor instability driven by an accel-decel-accel profile, Phys. Fluids 25 (2020) 1–33.

[193] D. Aslangil, Z. Farley, A. G. Lawrie, A. Banerjee, Rayleigh–Taylor instability with varying periods of zero acceleration, ASME J. Fluids Eng. 142 (2020) 1–12.

[194] S. A. Wieland, P. E. Hamlington, S. J. Reckinger, D. Livescu, Effects of isothermal stratification strength on vorticity dynamics for single-mode compressible Rayleigh–Taylor instability, Phys. Rev. Fluids 4 (2019) 1–28.

[195] J. D. Gibbon, Variable density model for the Rayleigh–Taylor instability and its transformation to the diffusive, inhomogeneous, incompressible navier-stokes equations, Phys. Rev. Fluids 6 (2021) 1–7.

[196] C. S. Yih, Instability due to viscosity stratification, J. Fluid Mech. 27 (1967) 337–352.

[197] S. G. Yiantsios, B. G. Higgins, Linear stability of plane poiseuille flow of two superposed fluids, Phys. Fluids 31 (1988) 3225–3238.

[198] Q. Cao, A. L. Ventresca, K. R. Sreenivas, A. K. Prasad, Instability due to viscosity stratification downstream of a centerline injector, Can. J. Chem. Eng. 81 (2003) 1027–1057.

[199] K. C. Sahu, P. Valluri, P. D. M. Spelt, O. K. Matar, Linear instability of pressure-driven channel flow of a newtonian and a herschel-bulkley fluid, Phys. Fluids 19 (2007) 1–11.

[200] K. C. Sahu, R. Govindarajan, Instability of a free-shear layer in the vicinity of a viscosity-stratified layer, J. Fluid Mech. 752 (2014) 626–648.

[201] R. Govindarajan, S. Jose, K. C. Sahu, Instabilities in viscosity and density stratified flow, IUTAM Symposium on Helicity, structures and singularity in fluid and plasma dynamics, 11-15 April 2016, Venice, Italy (2016) 1–10.

[202] P. Ern, F. Charru, P. Luchini, Stability analysis of a shear flow with strongly stratified viscosity, J. Fluid Mech. 496 (2003) 295–312.

[203] S. V. Malik, A. P. Hooper, Linear stability and energy growth of viscosity stratified flows, Phys. Fluids 17 (2005) 1–8.

[204] A. P. Hooper, W. G. C. Boyd, Shear-flow instability at the interface between two viscous fluids, J. Fluid Mech. 128 (1983) 507–528.

[205] N. Harnik, E. Heifetz, O. M. Umuran, F. Lott, A buoyancy-vorticity wave interaction approach to stratified shear flow, J. Atmos. Sci. 65 (2008) 2615–2630.

[206] H. Srivastava, A. Dalal, K. C. Sahu, G. Biswas, Temporal linear stability analysis of an entry flow in a channel with viscous heating, Int. J. Heat Mass Transf. 109 (2017) 922–929.

[207] S. M. Churilov, Stability analysis of stratified shear flows with a monotonic velocity profile without inflection points. Part 2. Continuous density variation, J. Fluid Mech. 617 (2008) 301–326.

[208] A. Defina, S. Lanzoni, F. M. Susin, Stability of a stratified viscous shear flow in a tilted tube, Phys. Fluids 11 (1999) 344–355.

[209] J. Duan, J. Gong, H. Yao, T. Deng, J. Zhou, Numerical modeling for stratified gasliquid flow and heat transfer in pipeline, Appl. Energy 115 (2014) 83–94.

[210] J. Duan, H. Liu, J. Gong, G. Jiao, Heat transfer for fully developed stratified wavy gasliquid two-phase flow in a circular cross-section receiver, Sol. Energy 118 (2015) 338–349.

[211] D. Aslangil, A. Banerjee, A. Lawrie, Numerical investigation of initial condition effects on Rayleigh–Taylor instability with acceleration reversals, Phys. Rev. E. 94 (2016) 1–46.

[212] P. Schafer, H. Herwig, Stability of plane poiseuille flow with temperature dependent viscosity, Int. J. Heat Mass Transfer 36 (1993) 2441–2448.

[213] R. Deissler, A. Oron, Stable localized patterns in thin liquid films, Phys. Rev. Lett. 68 (19) (1992) 1–4.

[214] S. Krishnamoorthy, B. Ramaswamy, S. W. Joo, Spontaneous rupture of thin liquid films due to thermocapillarity: A full-scale direct numerical simulation, Phys. Fluids 7 (1995) 2291–2293.

[215] Y. O. Kabova, A. Alexeev, T. G. Roisman, P. Stephan, Marangoni-induced deformation and rupture of a liquid film on a heated microstructured wall, Phys. Fluids 18 (2006) 1–15.

[216] P. H. Trinh, H. Kim, N. Hammoud, P. D. Howell, S. J. Chapman, H. A. Stone, Curvature suppresses the Rayleigh–Taylor instability, Phys. Fluids 26 (051704) (1914) 1–7.

[217] E. Shabalina, A. Berut, M. Cavelier, A. S. Jalmes, I. Cantat, Rayleigh–Taylor-like instability in a foam film, Phys. Rev. Fluids 4 (124001) (2019) 1–20.

[218] D. Q. Nguyen, R. P. Fedkiw, M. Kang, A boundary condition capturing method for incompressible flame discontinuities, J. Comput. Phys. 172 (2001) 71–98.

[219] G. Son, V. K. Dhir, A level set method for analysis of film boiling on an immersed solid surface, Numer. Heat Transfer, Part B 52 (2) (2007) 153–177.

[220] S. Popinet, Numerical models of surface tension, Annu. Rev. Fluid Mech. 50 (2018) 1–28.

[221] S. Popinet, An accurate adaptive solver for surface tension driven interfacial flows, J. Comput. Phys. 228 (2009) 5838–5886.

[222] M. A. A. Saud, S. Popinet, H. Tchelepi, A conservative and well-balanced surface tension model, J. Comput. Phys. 317 (2018) 896–913.

[223] Z. Ge, J. C. Loiseau, O. Tammisola, L. Brandt, An efficient mass-preserving interface-correction level set/ghost fluid method for droplet suspensions under depletion forces, J. Comput. Phys. 353 (2018) 435–459.

[224] C. W. Shu, S. J. Osher, Efficient implementation of essentially non-oscillatory shock capturing schemes, J. Comput. Phys. 77 (1988) 439–471.

[225] X. D. Liu, S. Osher, T. Chan, Weighted essentially nonoscillatory schemes, J. Comput. Phys. 115 (1994) 200–212.

[226] C. W. Shu, Essentially non-oscillatory and weighted essentially non-oscillatory schemes for hyperbolic conservation laws, in High-Order Methods for Computational Physics , T. J. Barth and H. Deconinck , editors , Lect. Notes Comput. Sci. 9 (1999) 439–582.

[227] S. Osher, R. Fedkiw, Level set methods: An overview and some recent results, J. Comput. Phys. 169 (2001) 463–502.

[228] S. Osher, R. Fedkiw, Level set methods and dynamic implicit surfaces, Springer, New York, 2003.

[229] S. V. Patankar, Numerical Heat Transfer and Fluid Flow, McGraw-Hill, New York, 1981.

[230] H. K. Versteeg, W. Malalasekera, An Introduction to Computational Fluid Dynamics, Pearson Education Limited, Harlow, England, (2008).

[231] A. Harten, High resolution schemes for hyperbolic conservation laws, J. Comput. Phys. 49 (1983) 357–393.

[232] J. Blazek, Computational Fluid Dynamics, Elsevier limited, Oxford, UK, (2015).

[233] S. Popinet, Basilisk, http://basilisk.fr, [Online; accessed 5-May-2022] (2022).

[234] J. U. Brackbill, D. B. Kothe, C. Zemach, A continuum method for modeling surface tension, J. Comput. Phys. 100 (1992) 335–354.

[235] M. M. Francois, S. J. Cummins, E. D. Dendy, D. B. Kothe, J. M. Sicilian, M. W. Williams, A balanced force algorithm for continuous and sharp interfacial surface tension models within a volume tracking framework, Int. J. Numer. Methods Fluids 213 (2006) 141–173.

[236] P. G. Drazin, W. H. Reid, Hydrodynamic stability, Cambridge University Press, London, (2004).

[237] L. Strubelj, I. Tiselj, Numerical simulations of basic interfacial instabilities with incompressible two-fluid model, Nucl. Eng. Des. 241 (2011) 1018–1023.

[238] K. Ward, F. Zoueshtiagh, R. Narayanan, Faraday instability in double-interface fluid layers, Phys. Rev. Fluids 4 (2019) 1–24.

[239] M. Bestehorn, A. Pototsky, Faraday instability and nonlinear pattern formation of a two-layer system: A reduced model, Phys. Rev. Fluids 1 (063905) (2016) 1–24.

[240] K. Kumar, Linear theory of faraday instability in viscous liquids, Proc. R. Soc. London, Ser. A 452 (1996) 1113–1126.

[241] G. Bevilacqua, X. Shao, J. R. Saylor, J. B. Bostwick, P. Ciarletta, Faraday waves in soft elastic solids, Proc. R. Soc. London, Ser. A 476 (2020) 1–19.